# A low energy Ion Scattering Spectroscopy study of clean and adsorbed Cu(100) and Ni(100) surfaces.

by

D.J. Godfrey B.Sc.

A thesis submitted for the degree of Doctor of Philosophy of the University of Warwick.

December 1979

Memorandum.

The work reported in this thesis is my own, except where specifically acknowledged as otherwise, and was carried out in the Department of Physics of the University of Warwick. The model calculations for elastic scattering and ion-atom neutralisation were performed by Dr. D.P. Woodruff.

Part of the contents of Chapter 5 has been published in Surface Sci. 89, 76 (1979). Much of the remainder of this chapter has also been submitted for publication. It is intended to submit the work reported in Chapters 3 and 4 in the near future. References cited in each chapter have been listed at the end of the thesis.

D.C. Godfrey.

Acknowledgements.

I would like to express my gratitude to Dr. D.P. Woodruff for his excellent supervision during the experimental stage of this work and for his continued assistance during the completion of this thesis, particularly with respect to the model calculations reported in this work. I would also like to thank Prof. A.J. Forty for the provision of facilities within the Department of Physics.

Thanks are due to the members of the Surface Physics group, particularly to Drs. J.H. Onuferko and P.D. Johnson, for their help and encouragement during the course of this work. The excellent technical support of C.S. Simpson and J.V. Edwards is gratefully acknowledged.

The work was carried out under a C.A.S.E. award with Phillips Research Laboratories (Redhill). Thanks are extended to Dr. B.A. Joyce for his cooperation and assistance during this project.

I would like to extend my most sincere thanks to my family for their support during this work, particularly to my wife, Sharon, and to my father, L.G. Godfrey, for their practical assistance in the completion of this thesis.

## Abstract.

A complete Ultra High Vacuum (U.H.V.) system has been developed to study the adsorption of gases on single crystal surfaces. Three surface sensitive techniques, namely Low Energy Electron Diffraction (LEED), Auger Electron Spectroscopy (AES) and Ion Scattering Spectroscopy (ISS), are included in the apparatus. The three techniques are available within the same experimental chamber. This allows the experimental techniques to be applied sequentially to the same surface.

This experimental system has been used to study the adsorption of oxygen on Cu(100) and Ni(100) and ethylene on Ni(100). The ISS results obtained cannot be interpreted using elastic scattering arguements. The other major factor determining ion yields is neutralisation. Thus, a model of localised neutralisation has been developed. If the surface structure is taken as known, this model can be used to interpret successfully the ISS data from the Ni(100)($\sqrt{2}$x$\sqrt{2}$)R45° -O and Ni(100)(2x2)-C surfaces. The same model of localised neutralisation has been applied to the oxygen adsorption on Cu(100). The model does not allow unambiguous surface structure analysis to be performed. However, qualitative interpretation can be achieved by consideration of the differences between the ISS data obtained from the three surface systems. The best agreement with the experimental data is found for a Cu(100)($\sqrt{2}$x2$\sqrt{2}$)R45° -O surface with a combination of two fold and four fold adsorbed oxygen atoms. However, the level of agreement is not sufficient for more than tentative acceptance of this structure.

The major implication of this work for the use of ISS in surface structure analysis is that localised neutralisation effects dominate for the (100) surface. Previous surface structural studies using ISS have been successful on the (110) crystal face, where the 'ridged' surface makes structural interpretation less sensitive to the shadowing model. Thus, for a complete understanding of the factors determining the relative ion yields, both ion neutralisation and elastic scattering must be considered.

## Contents.

## Preface.

There are many phenomena which occur in materials that can be described in a satisfactory way only by examining in detail the electronic and atomic structure of the surface. Examples of such processes are oxidation, catalysis and thermionic emission. There are a number of reasons for expecting the surface region to have different properties from the bulk. One reason is that the loss of three dimensional periodicity will effect the electronic states near the surface. The surface electronic structure will influence the chemical reactivity of the material. Thus, the study of solid surfaces is of both theoretical and technological interest.

In order to gain understanding in these areas, a large amount of work has been performed on 'ideal' surfaces, such as single crystal metals. This has the advantage of simplifying the analysis, compared with the relative complexity of surfaces found, for example, in practical catalysis. There are a number of basic requirements for the performance of surface studies. Firstly, it must be possible to produce clean surfaces which can be studied. Secondly, the surface should remain clean for the duration of the experiments. Thirdly, experimental techniques which are particularly sensitive to the surface region must be applied. In this work, clean and adsorbed single crystal metal surfaces have been studied in a purpose built Ultra High Vacuum (U.H.V.) system using three surface sensitive techniques.

There are a number of methods for obtaining clean surfaces. For example, inert gas ion bombardment and cleavage in a vacuum have been used (1). The appropriate manner of cleaning is dependent on the sample surface to be studied. The particular method of cleaning used in this present work was inert gas ion bombardment. In addition to being clean, the surface of the crystal also needs to be well-ordered. To achieve this, the crystal may require high

temperature annealing after cleaning.

Once a clean well-ordered surface has been prepared, an U.H.V. environment is required. Working in U.H.V. conditions leads to a reduction in the rate at which molecules of the residual gases of the chamber collide with the target. The kinetic theory of gases (2) shows that the rate of arrival of N molecules of molecular weight M at a temperature T °K upon a square centimetre of a surface at a pressure P torr is given by

$$N = 2.9 \times 10^{22} \; P(MT)^{-\frac{1}{2}} \quad \text{molecules cm}^{-2} \; \text{s}^{-1}$$

For a base pressure of $2 \times 10^{-10}$ torr of nitrogen at room temperature, this gives approximately $6 \times 10^{14}$ molecules $\text{cm}^{-2} \; \text{s}^{-1}$. The interatomic distance is typically 0.3 nm. Thus, a monolayer of atoms corresponds to approximately $1 \times 10^{15}$ atoms $\text{cm}^{-2}$. If each molecule sticks to the surface, a monolayer will be formed in 5 hours. Clearly, for experiments involving clean surfaces, only a fraction of a monolayer is sufficient to change significantly the system being studied. However, it is unlikely that each molecule will in fact stick to the surface. Hence, for periods of less than one hour, problems of contamination are negligible at a pressure of $2 \times 10^{-10}$ torr.

Having studied a clean, well-ordered surface, adsorption can be considered. There are two basic types of adsorption - physical and chemical. In physical adsorption (or physisorption), an adsorbed molecule is bound by a weak Van der Waals type bond. This type of bond requires no charge transfer. The binding energies of physisorbed molecules are typically 0.25 eV or less (3). In chemisorption, an electron is exchanged between the adsorbed molecule and the surface. The range of binding energies is quite large, varying between 0.5 eV and 8.5 eV (3). In the present work, it is chemisorption which is studied.

In order to examine the effect of adsorption on a surface, it

is necessary to use techniques which are sensitive only to the first few atomic layers. In this work, three such techniques, namely Low Energy Electron Diffraction (LEED), Auger Electron Spectroscopy (AES) and Ion Scattering Spectroscopy (ISS) have been used. In Chapter 1, a brief description of the theory and use of each technique, as is relevant to the present study, is given. Chapter 2 includes a detailed description of ISS with particular reference to surface structure analysis. The roles of elastic scattering and ion neutralisation in determining the ion yield are discussed. Previous surface structure analysis using ISS has assumed an ion neutralisation rate which is independent of the azimuthal angle of the surface. Azimuthal variations in the ion yield have been interpreted in terms of elastic shadowing. Two methods of obtaining surface structure analysis are described which have been used by other workers ((4) and (5)). Also, experimental evidence of oscillatory ion neutralisation (6), where the neutralisation rate is dependent upon the particular ion-atom combination, is dealt with.

Chapter 3 details the complete experimental system which has been developed for this study. The system consists of two experimental levels which allow LEED, AES and ISS to be performed within the same vacuum chamber. This has the advantage that all three techniques can be applied to the same surface within the same experimental run. The LEED display system consists of a 3 grid retarding field analyser with an axial LEED gun. The ISS and AES instrumentation uses a common 120° azimuthal sector cylindrical mirror analyser (C.M.A.). The ions or electrons may be analysed by changing the polarity of the ramps for the analyser and the voltages on the detection system. The detection system consists of two channel plate multipliers mounted in series. The ion gun required for ISS is based on a commercial quadrupole mass spectrometer. Using this arrangement, it has been possible to perform routine analysis of clean and

adsorbed surfaces by applying the three surface sensitive techniques available.

Chapter 4 reports the results obtained from the experimental system. The Cu(100) surface was used for characterisation of the equipment. It was found that the mass resolution of the ISS system was sufficient to allow studies of gas atom adsorption on metal surfaces. One major limitation of the system was that the scattering angle used for ISS could only be changed by letting the system up to atmospheric pressure. The scattering angles available were approximately 48°, 90° and 120°. The majority of the experiments which were carried out with the aim of performing surface structure analysis used scattering angles of 48° and 90° with 1.0 keV helium ions. The results obtained with ISS from the Cu(100)($\sqrt{2}$x$\sqrt{2}$)R45°-O surface are not readily explicable when analysed by the methods reported in Chapter 2. Hence, it was necessary to carry out an ISS study of a known surface structure using these experimental conditions.

Thus, Chapter 5 deals in detail with ISS from the Ni(100)($\sqrt{2}$x$\sqrt{2}$)R45°-O surface. This surface was one of the first surfaces for which LEED I(V) analysis was successful in determining surface structure (7). The structure for this surface places the oxygen atoms 0.9 Å above the four fold hollows in the Ni(100) surface. Again, the ISS data from this adsorbed surface was not explicable using the approaches tested in Chapter 2. However, a theory of neutralisation which takes into account the localised neutralisation has been developed to interpret the results. This ion-atom neutralisation model includes the effect of adsorbing the gas atom on to the substrate atom, thereby effecting the neutralisation due to the latter. The agreement obtained between this theoretical model and the experimental data is, in most cases, satisfactory. The Ni(100)(2x2)-C system was also studied. The ISS

experiments performed were similar to those used for the oxygen adsorbed Ni(100) and Cu(100) surfaces. The Ni(100)(2x2)-C surface has been subjected to LEED I(V) analysis at the University of Warwick and the preferred site for the carbon was shown to be a near coplanar four fold site (8). Again, the experimental ISS data could not be interpreted by considering purely elastic scattering effects. The ion-atom model was applied to this surface structure. The agreement obtained between theory and experiment was improved by applying a simple approximation for the effect of adsorption on neutralisation. This model does not include elastic shadowing and the approximation used to incorporate the effect of adsorption is simplistic.

In Chapter 6, the Cu(100)($\sqrt{2}$x$\sqrt{2}$)R45°-O and ($\sqrt{2}$x2$\sqrt{2}$)R45°-O surfaces are discussed. Recent experiments by other workers ((9), (10), (11), (12) and (13)) on these surfaces are reported here. It is not possible to establish with confidence the surface site by using these studies. Recent LEED I(V) data from these surfaces, performed at the Surface Physics group at the University of Warwick, are also included (14). The surface structure suggested from that work for the Cu(100)($\sqrt{2}$x2$\sqrt{2}$)R45°-O surface consists of a mix of two fold and four fold sites. This complex structure is unlikely to be completely formed. The ion-atom neutralisation model is applied to a number of possible adsorbate sites for the Cu(100)($\sqrt{2}$x$\sqrt{2}$)R45°-O surface. The agreement obtained with the experimental data is poor for all the sites which were considered. This may be due to the complex nature of the surface obtained from oxygen adsorbed on Cu(100). Qualitative interpretation of the ISS data is possible by comparison with the data obtained from the Ni(100)($\sqrt{2}$x$\sqrt{2}$)R45°-O and (2x2)-C surfaces. This allows tentative support to be given to the structure suggested by Onuferko et al (14). However, with the present level of understanding of the ion-atom neutralisation model, it is not

possible to perform quantitative surface structure analysis.

Chapter 7 summarises the major conclusions of this present work. The role of ion-atom neutralisation in determining the detected ion yield is crucial for the experimental ISS conditions used in this work on the (100) crystal face. Suggestions for further theoretical and experimental work are included in this chapter. These include the need to develop a more complete understanding of the processes involved in ISS. The theoretical model used in this work could be generalised by including elastic shadowing effects and by using a less crude approximation for the effect of adsorbing species on to clean surfaces. Experimentally, the ISS conditions which lead to localised neutralisation dominating the ion yield should be investigated.

# Chapter 1.

# Low Energy Electron Diffraction (LEED), Auger Electron Spectroscopy (AES) and Ion Scattering Spectroscopy (ISS).

## Introduction.

Three surface sensitive techniques have been used in this work to study the structure of adsorbate atoms on single crystal metal surfaces. The three techniques are Low Energy Electron Diffraction (LEED), Auger Electron Spectroscopy (AES) and Ion Scattering Spectroscopy (ISS). A brief description of the theory and use of each technique, as is relevant to this work, will be given in turn. ISS will be dealt with in considerably more detail in Chapter 2, as this has been the major technique used in this work.

## 1.1. Low Energy Electron Diffraction (LEED).

When a monoenergetic beam of electrons is incident on a solid metal surface, the secondary electron energy distribution is as shown in Figure 1.1. The secondary electron analyser used in this work was a cylindrical mirror analyser (C.M.A.). This produces an output which is proportional to the product of the number of electrons at a given energy and their actual energy, that is E.N(E). This has the effect that the signal due to low energy electrons is suppressed. However, the N(E) spectrum allows the processes involved in the distribution to be understood more readily. Figure 1.1 shows both the N(E) and the E.N(E) secondary electron distributions obtained from 1.0 keV electrons from Cu(100).

The N(E) spectrum can be understood by separating it into three regions. Firstly, a large broad maximum occurs at low energies. This is due to secondary electrons which are emitted as a result of cascade processes in the solid (1). The next region includes a number of emissions at characteristic energies and a

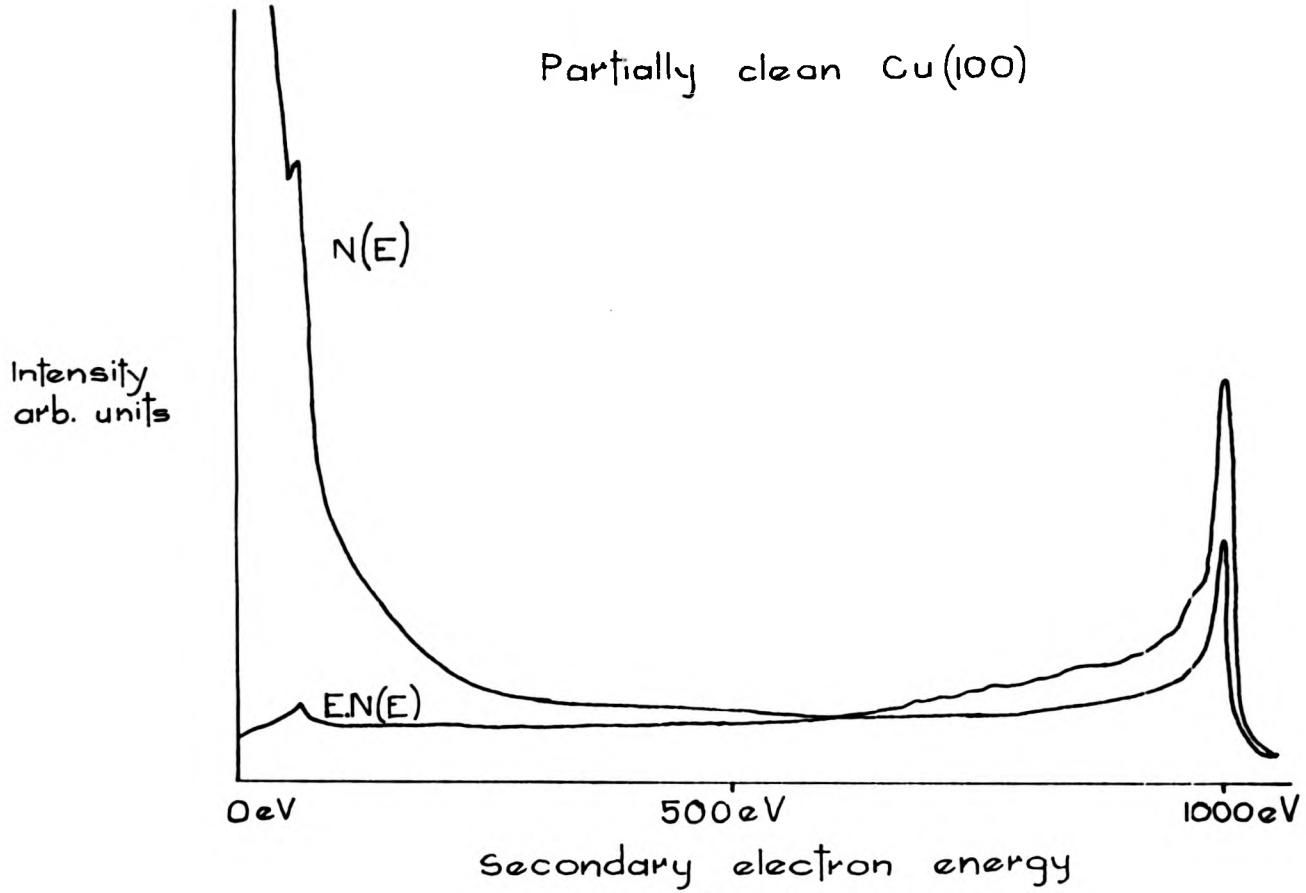
Partially clean Cu(100)
N(E)
Intensity
arb. units
E.N(E)
0eV
500eV
1000eV
Secondary electron energy

Figure 1.1.

slowly varying background. The latter is caused by inelastic scattering of the primary beam. The third region includes the peak obtained at the energy of the beam. This is comprised of elastically scattered electrons and 'quasi-elastic' electrons that have lost a small amount of energy (approximately 0.02 eV) by phonon scattering. It is the spatial distribution of this third region which is studied in LEED.

The first LEED experiments of Davisson and Germer (2) illustrated the wave-like nature of the electron. Their observations provided experimental evidence of the de Broglie relation

$$\lambda = \frac{h}{p} \simeq (150/E)^{1/2} \quad \text{Å}$$

where the electron energy, E, is measured in electron volts. At a low energy (below about 300 eV), the wavelength of the electrons will be comparable with the lattice spacings of the crystal. Thus, diffraction of the low energy electrons by the crystal lattice will occur. The spatial distribution of these electrons is a representation, in reciprocal space, of the real surface net. It is this distribution which is displayed in a LEED pattern.

X-ray diffraction has been used to obtain bulk structures of many crystals. The atomic scattering cross-section for X-rays is weak, and, therefore, they are able to penetrate deeply into the crystal. As a result, the sensitivity of X-rays to the surface layer is low and information concerning the bulk of the crystal is obtained. Since the probability of single scattering is very small, the probability of detecting multiple scattering is extremely low. Thus, a simple kinematic theory can be used to interpret X-ray diffraction.

Unlike X-rays, electrons with energies between 0 eV and 300 eV have a high probability of being scattered, typically between 10% and 50% (3). This has the result that LEED is extremely surface sensitive. Whereas the symmetry of the bulk can be deduced from

X-ray diffraction, LEED gives information on surface structure. A spot pattern from Ni(100) using 60 eV electrons and the corresponding surface atom arrangement are shown in Figure 1.2. It is generally found that low index metal surfaces are essentially simple truncations of the corresponding bulk structure. Although the arrangement of the surface atoms is the same as the bulk, the spacing between the top layer and the underlying layer is often slightly modified (4).

When an active gas is adsorbed on to a metal surface, the chemisorbed atoms usually take up preferred sites. If the adsorbate layer is ordered with a periodicity different from that of the clean surface, this will give rise to further diffraction spots. Some of these spots will be coincident with the spots produced by the metal surface. However, if the adsorbate coverage is less than one monolayer or the symmetry of the adsorbate atoms different from that of the metal atoms, other diffraction spots will appear in the pattern. This can be seen in Figure 1.3 where a Ni(100)($\sqrt{2}$x$\sqrt{2}$)R45°-O diffraction pattern for 60 eV electrons is shown. Some possible atom arrangements are also shown in this figure. The structure of the overlayer can be placed in a number of positions with respect to the crystal lattice (c.f. positions a, b and c in Figure 1.3). Each of these sites will lead to the same diffraction pattern. Thus, the symmetry of the diffraction pattern does not allow the positions of the adsorbate atoms to be known. Only the translational symmetry of the layer can be determined.

In order to obtain information concerning the actual position of the atoms, the variation of the spot intensity with the beam energy must be measured. This measurement is generally called an I(V) spectrum. This can be achieved most readily by using a spot photometer to measure the light intensity produced on a phosphor screen. Alternatively, a Faraday cup, which measures the electron

Ni (100)

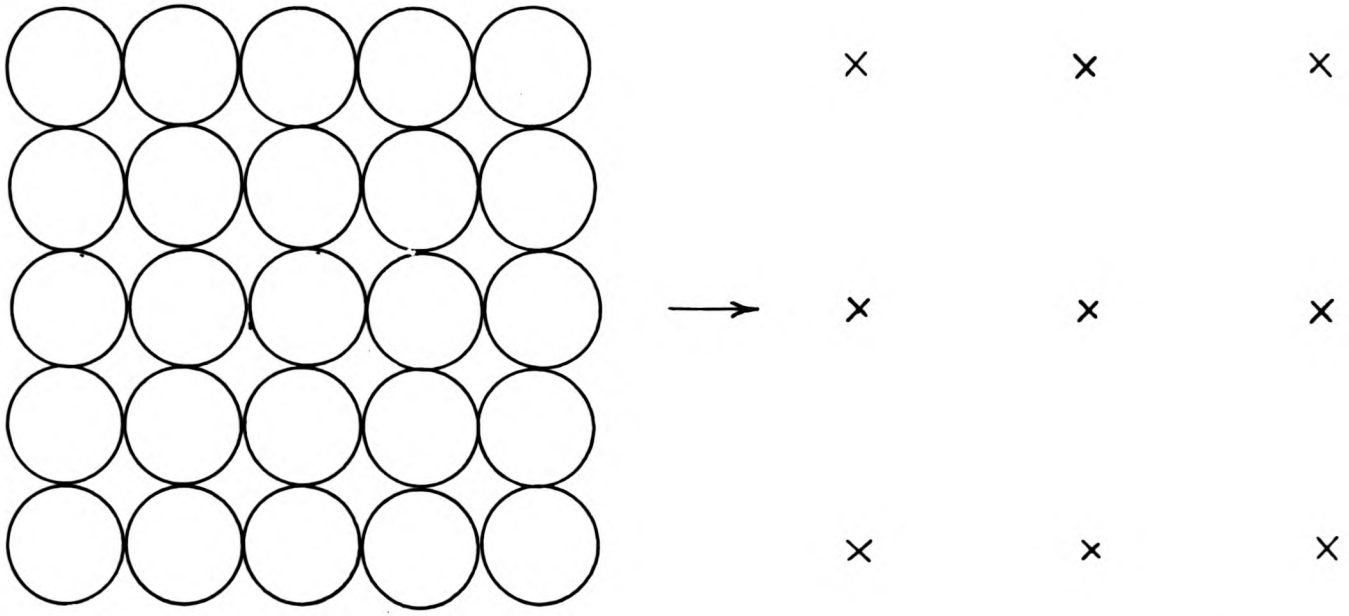

Atomic Arrangement of Top Atom Layer

60 eV LEED pattern

Figure 1.2.

Ni (100) $(\sqrt{2} \cdot \sqrt{2})R45° - O$

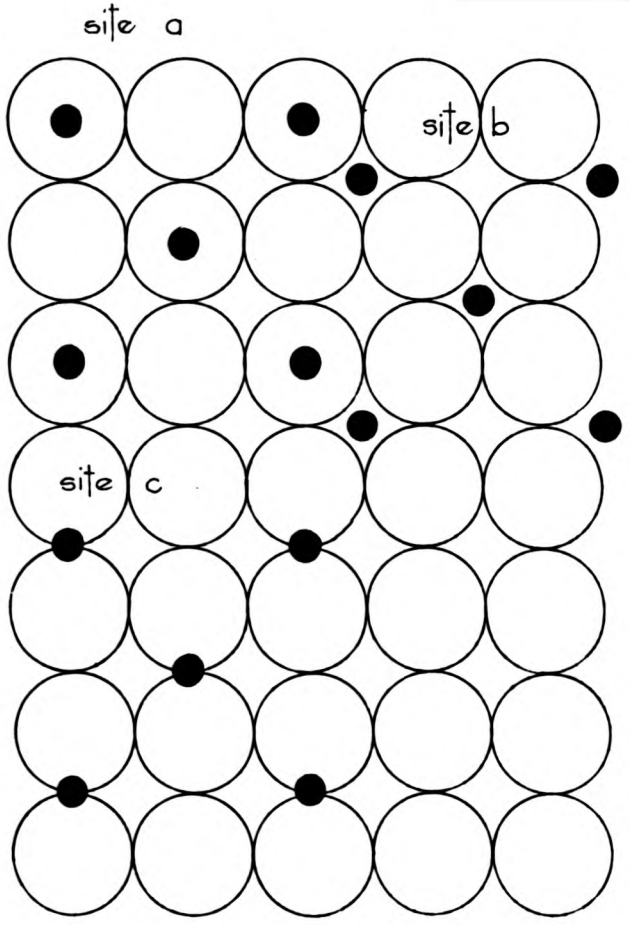


Atomic Arrangement

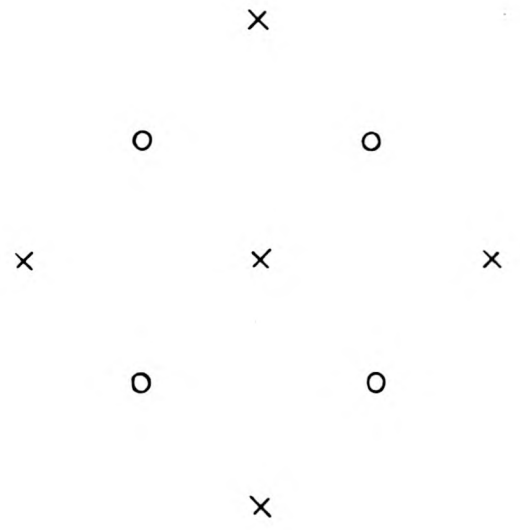

x clean surface spots

o extra spots

60 eV LEED pattern

**Figure 1.3.**

beam intensity directly, can be used. It is not possible to use a simple kinematic theory, as in X-ray diffraction, to interpret these data. The large scattering cross-section for electrons means that electrons can be multiply scattered and emerge with measureable intensity from the lattice. For a full description of LEED, the amplitude and phases of all the waves must be taken into consideration. This type of theory is called a dynamical theory. If this theory is used, large amounts of computer time are required to calculate I(V) curves for different model structures. A second method of dealing with LEED I(V) data is to attempt to subtract the contribution due to multiple scattering (5). This has the advantage of using less computer time. However, the successful application of these techniques is limited because of the difficulty of isolating the effect of singly scattered electrons.

LEED has been successfully used to study a number of adsorbate covered metal surfaces. These studies have been restricted in the main to the low index faces of metals and single atom adsorbates. The reasons for this are both experimental and theoretical. At present, the typical experimental arrangement for measuring I(V) spectra has a number of disadvantages. Recording the I(V) spectrum of one LEED spot over a range of 300 volts typically requires a time of about ten minutes. Thus only six such beams can be measured within one hour. After this length of time, it is possible that the surface has been contaminated and so must be recleaned before further data can be taken. Hence, only relatively simple systems have been studied in detail with these types of experimental arrangements. In order to increase the scope of LEED, a more efficient method of data collection must be achieved. A number of experimental systems are being developed where the intensities of all the diffraction spots are measured at the same time (6). This has the added advantage that the total electron current incident

on the sample is also greatly reduced. This allows the study of adsorbates, such as organic molecules, which would be desorbed by the electron doses previously required to obtain LEED I(V) data.

The theory used to interpret LEED I(V) data requires model structures to be chosen. A computer programme is used to predict the I(V) spectra which would be given by this structure. The model structure is refined until the agreement between the calculated I(V) spectra and the experimental data is acceptable. This process requires large amounts of computer time. The complexity of the adsorbate system to be studied and the number of model structures considered are also limited by the amount of computer time available.

In spite of these limitations, LEED is probably the most reliable technique for surface structure analysis which is at present in use. If the large amount of time needed for both data collection and computer modelling is available, then good agreement can be found between the experimental results and the model calculations (7). It was hoped that one advantage of combining ISS with LEED would be that the number of model structures which must be considered would be reduced. For example, we shall see that ISS should give a clear indication as to whether an adsorbate atom is positioned above the surface or below the level of the surface.

## 1.2. Auger Electron Spectroscopy (AES).

Auger Electron Spectroscopy (AES) is a method of studying the composition of the first few layers of the surface of a solid. The technique consists of bombarding the surface with a beam of energetic electrons (usually 1.0 to 3.0 keV) and analysing the energies of the ejected electrons. Auger electrons were first discovered by Pierre Auger (8). However, it was not until Harris (9) demonstrated the advantages of electronically differentiating

the ejected energy distribution, that the high sensitivity attainable and the practicability of the technique for surface analysis were noted.

Auger electrons are produced by the process shown in Figure 1.4. Auger emission occurs after an atomic level has been ionised by incident photons or electrons. The hole caused in the inner shell is filled by one electron from a less tightly bound level and a second electron escapes into the vacuum with the remaining kinetic energy. This energy of the Auger electron is approximately

$$E \approx E_{K} - E_{L_1} - E_{L_2,3}$$

for the transition shown in Figure 1.4. This is because $E_{K} - E_{L_1}$ is the amount of energy released by an electron falling from the initial hole in the shell. The escaping electron requires $E_{L_2,3}$ to overcome its binding energy. Hence, the emitted electron has an energy which is characteristic of the material it came from and which is independent of the exciting beam energy.

In order to obtain a more accurate value for the Auger energy, the effect of removing an electron from $E_{L_1}$, thereby increasing the binding energy of $E_{L_2,3}$, must be taken into consideration. However, it is difficult to calculate this effect accurately. This is because such effects are not easily solved analytically and intuitive, empirical estimates are usually used (10). A number of formulae are available which can be applied with an accuracy of the order of 5 eV (11).

As previously stated, the primary beam energy used in AES of solids is usually between 1.0 keV and 3.0 keV. Auger electrons will be generated up to a penetration depth of between 500 Å and 1000 Å, which is the penetration depth of these beams (10). However, the depth from which Auger electrons are detected will be much less than this. This is because any Auger electrons suffering an energy loss of more than a few electron volts will be scattered out of the Auger peak

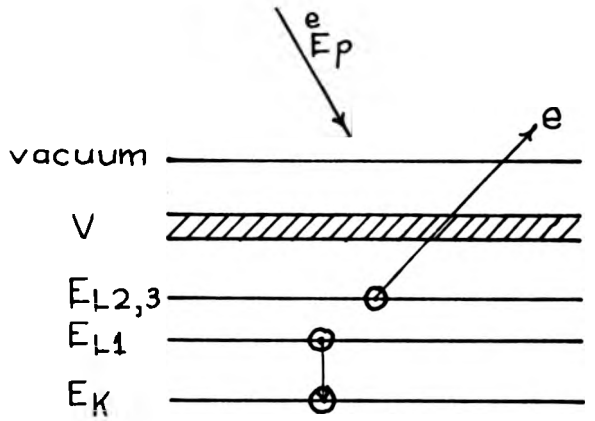


Figure 1.4.

into the general background. Thus, the escape depth will be approximately equal to the mean free path for the most probable inelastic electron-electron interaction. For transitions between 10 eV and 1000 eV, the mean escape depth is between 3 Å and 30 Å (3). The surface sensitivity of AES is dependent on the value of the mean escape depth. This is also an important factor in the surface sensitivity of LEED.

It is this surface sensitivity which makes quantitative analysis with AES difficult. One reason for this is that it is unlikely that the impurities will be evenly distributed within the first few atomic layers of the surface. Thus, the concentration of an impurity species may be different in the second, third and lower atomic layers. The peak size obtained for a given concentration will be attenuated with successive atomic layers. Hence, quantitative analysis can only be attempted if the distribution of the impurity is known and the relative attenuation can be calculated.

A number of quantitative studies have been attempted using AES, (for example, see ref. (12)). These studies show that there is a linear relationship between the Auger peak height and the coverage of less than one monolayer. In these studies, the surface coverage is calibrated by means of another technique, such as radioactive tracers. The minimum amount of an element which can produce a detectable Auger signal is found to be about 1% of a monolayer (13). The actual value obtained will be dependent on the relative strengths of the Auger transitions and the particular experimental arrangement.

AES is probably the most widely used surface sensitive technique. There are a number of reasons for this. Firstly, it is sensitive to small amounts of individual elements. Also, tabulated Auger energies and representative Auger spectra are available for

the majority of elements (14). These allow quick identification of the atomic species in the surface region. Another advantage is that AES is relatively straight forward experimentally. This is because electron beams with high current densities are readily available. The experimental arrangement used in LEED can easily be adapted for use in AES. This aided the adoption of AES as a standard technique for surface analysis. The use of cylindrical mirror analysers (C.M.A.) has enabled the achievable sensitivity to be greatly increased (15). This has the benefit that either the time required for analysis can be shortened or the electron beam current density can be lowered.

Thus, AES is an extremely useful technique for the characterisation of experimental systems. In this work its application has been limited to allowing clean surfaces to be prepared reproducibly and to the estimation of surface coverages.

## 1.3 Ion Scattering Spectroscopy.

When inert gas ions ($He^+$, $Ne^+$ and $Ar^+$) of energy less than a few keV are incident on a solid surface, the interaction is mainly with the top atomic layer. Therefore, these ions are well suited for investigating the physical properties of the surface. Ion Scattering Spectroscopy (ISS), that is, the spectroscopy of the energy of the backscattered ions, allows analysis of the outermost atomic layer. Thus, ISS is, in principle, a more surface sensitive technique than either LEED or AES.

The basic measurements of low energy ion scattering for surface analysis are relatively straight forward. A monoenergetic beam of ions with energy between approximately 0.1 and 5.0 keV strikes the target surface, and the energy distribution of the ions scattered off at a particular angle is measured. The energy spectrum obtained provides information on the mass, or chemical

identity, of the surface atom through the energy position of the ISS peak. The magnitude of the ISS peak is related to the number of surface atoms of the given species. In the case of single crystal targets, surface structural information may be derived from the positions and relative strengths of the different ISS peaks as the angle of incidence, the azimuthal angle and the scattering angle are varied.

These different types of information are obtained with varying degrees of accuracy and ease. Mass identification is quite straight forward. The peaks from higher masses occur at a higher energy in a manner predicted by simple conservation of energy and momentum considerations. Quantitative determination of the number of surface atoms is not straight forward. This is because the scattered ion yield depends on the scattering cross-section, the level of neutralisation and any shadowing effects. None of these effects are completely understood, and a detailed treatment of each is given in Chapter 2.

Low energy ion scattering is useful for qualitative and semi-quantitative composition analysis on a wide variety of materials. It is particularly advantageous where extreme surface sensitivity is required. Quantitative study is only possible where calibration against standard measurements is available. In order to obtain quantitative analysis directly from ISS, an understanding of the neutralisation probability and the differential scattering cross-section is required. Progress has been made in these areas, but much further study is required. In surface structure analysis, solutions to adsorbate covered metal systems have been achieved on the (110) surface using simple elastic shadowing arguements. Theoretical and experimental studies of ions scattered from chains of atoms have been carried out (16). These give information not only on surface structure, but also on surface defects.

The experimental requirements of ISS are compatible with other surface sensitive techniques. The advantages of using a number of techniques in a complementary way are of great importance in the study of surface structure. This is because none of the experimental methods used in surface physics is able to give a completely reliable determination of a surface structure. Thus, the use of more than one technique on a given problem is desireable.

At present, far fewer surface systems have been investigated using ISS than using LEED. However, in the few cases where both techniques have been used, there has been a good agreement between the surface structure found (17). The sensitivity of ISS varies with the mass of the analysed target atom. A typical value for a light element on a heavy substrate is approximately $10^{-3}$ monolayers. With high masses, mass resolution is difficult to achieve. In comparison to other techniques for surface analysis, ISS provides an outstanding specific sensitivity to the outermost atomic layer. This makes the method particularly promising for the investigation of adsorbate systems and ordered surface structures.

# Chapter 2.

## The Theory and Application of Ion Scattering Spectroscopy (ISS).

### Introduction.

Ion Scattering Spectroscopy (ISS) is not so fully developed as a surface sensitive technique when compared with either LEED or AES. As a result, most studies using ISS are not only applications of the technique, but also lead to further understanding of the processes involved in the technique. Since ISS has been the major experimental method used for surface structural analysis in this work, and because it has not been so widely used as LEED or AES, it will be dealt with in greater detail than the other two techniques.

This chapter aims to provide a survey of the theory previously used to interpret ISS data for surface structural analysis. However, in order to understand the ISS data in this work, it has been necessary to extend the theoretical treatment of ISS, especially in the area of ion neutralisation. The need for this will be shown in Chapters 4 and 5 where the results of studies on the Cu(100)($\sqrt{2}$x$\sqrt{2}$)R45°-O and the Ni(100)($\sqrt{2}$x$\sqrt{2}$)R45°-O structures are presented. The details of the new treatment of the role of ion neutralisation in surface structure determination is given in Chapter 5 where it is applied to the Ni(100)($\sqrt{2}$x$\sqrt{2}$)R45°-O structure.

### 2.1. Development of ISS.

The major processes present when an ion interacts with a surface are shown in Figure 2.1. In ISS, only the positively charged ions which are reflected from the surface are detected. These fall into two main categories; backscattered ions and sputtered ions. It is the elastically backscattered ions which form the basis of ISS.

Scattering of ions can be used for the analysis of solid

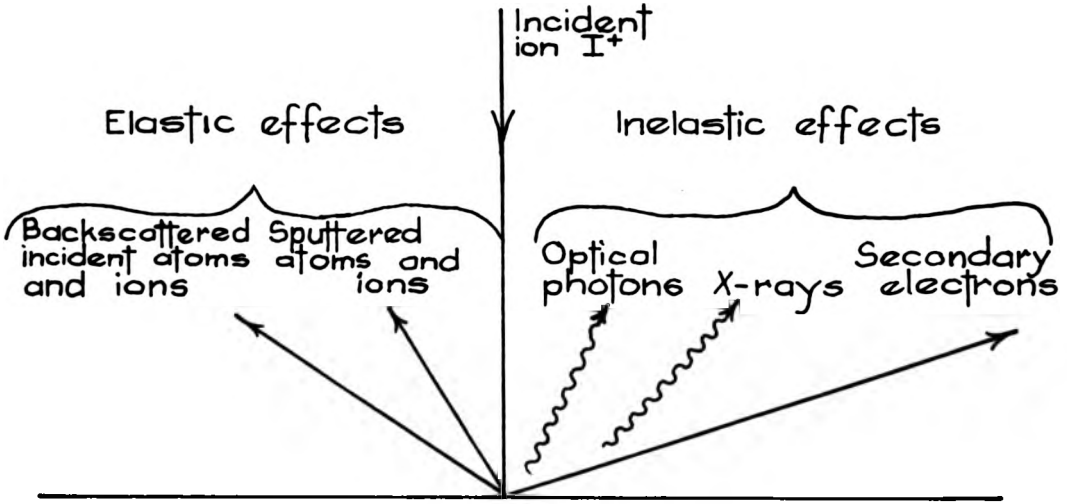
Incident
ion $I^+$
Elastic effects
Inelastic effects
Backscattered incident ions
Sputtered atoms and ions
Optical photons
X-rays
Secondary electrons

Figure 2.1.

surfaces by recording the energy spectrum of the scattered ions at a particular scattering angle. Panin (1) bombarded several metal surfaces with 7.5 keV to 80 keV ions, including helium and argon. It was found that as the energy of the ions was lowered, the spectra became more simple and approached the spectra expected from an ion scattered fom a single atom. Investigations using ion energies above 30 keV continued and reviews of this high energy work are available (2). However, the emphasis of this high energy work was in understanding scattering phenomena rather than in surface analysis.

The first demonstration of low energy ion scattering as a surface analytical technique was provided by the work of Smith (3). He used beams of $He^+$, $Ne^+$ and $Ar^+$ at energies between 0.5 keV and 3.0 keV on single crystal Ni and polycrystalline Mo and Ni. Using these beams, he obtained sharp peaks corresponding to ions back scattered from substrate surface atoms and also from adsorbate atoms of O and C. From the relative peak heights of the C and O peaks, he inferred structural information for CO adsorbed on nickel. Thus, low energy ion scattering was shown to allow chemical composition and surface structure to be studied.

## 2.2. Binary Collision Model.

An important conclusion from this early work was that the prominent features in low energy ion scattering spectra result from simple two-body collisions between the incident ion and a single atom. Here the remainder of the lattice plays little or no part. Thus, the interaction can be described by a simple binary collision model. This is possible because the interaction time between an incident ion and a surface atom is small, (about $10^{-13}$ sec. (4)), within the energy range used for ISS. Therefore, an ion can be viewed as interacting with one surface atom at a time.

For each collision there is a probability that the ion will be neutralised. For inert gas ions, the neutralisation probability is high (greater than 99.99% for 1.0 keV helium ions (5)). Hence, interactions between incident ions and one single target atom will predominate in the reflected ion yield. The advantage of single scattering conditions is illustrated in Figure 2.2 by contrasting the scattering of $He^+$ ions to that of $H^+$ ions (6).

The energy of an ion after a single collision with a target atom can be found by solving the equations of the conservation of energy and momentum for the collision. A schematic diagram of the geometry of the collision is given in Figure 2.3. The target atom is assumed to be initially at rest. The result obtained is

$$\frac{E_1}{E_0} = \frac{1}{(1 + M_2 / M_1)^2} \left\{ \cos \vartheta_1 \pm \left[ (M_2/M_1)^2 - \sin^2 \vartheta_1 \right]^{1/2} \right\}^2 \qquad (1)$$

where $E_1$ is the energy of the scattered ion of mass $M_1$, with a primary energy $E_0$ into a laboratory scattering angle $\vartheta_1$ by a target atom of mass $M_2$. If the mass and the energy of the primary ion and the scattering angle of the collision are known, then the resultant energy of the scattered ion is dependent on the mass of the target atom. Thus, the energy scale of the reflected ion spectrum becomes a mass scale for the target atoms at the surface, with higher energy indicating larger mass. In the collision, energy is transferred to the target atom,

$$E_2 = \frac{E_0 4A}{(1 + A)^2} \cos \vartheta_2 \qquad (2)$$

where $A = \frac{M_2}{M_1}$. This shows that the lattice is likely to be damaged in ISS experiments.

These relationships have been proved experimentally to be valid for the energy range E = 0.1 keV to 2.0 keV with noble gas ions $He^+$, $Ne^+$ and $Ar^+$ (3). If the binary collision model is assumed, a number of important parameters can be calculated. For example,

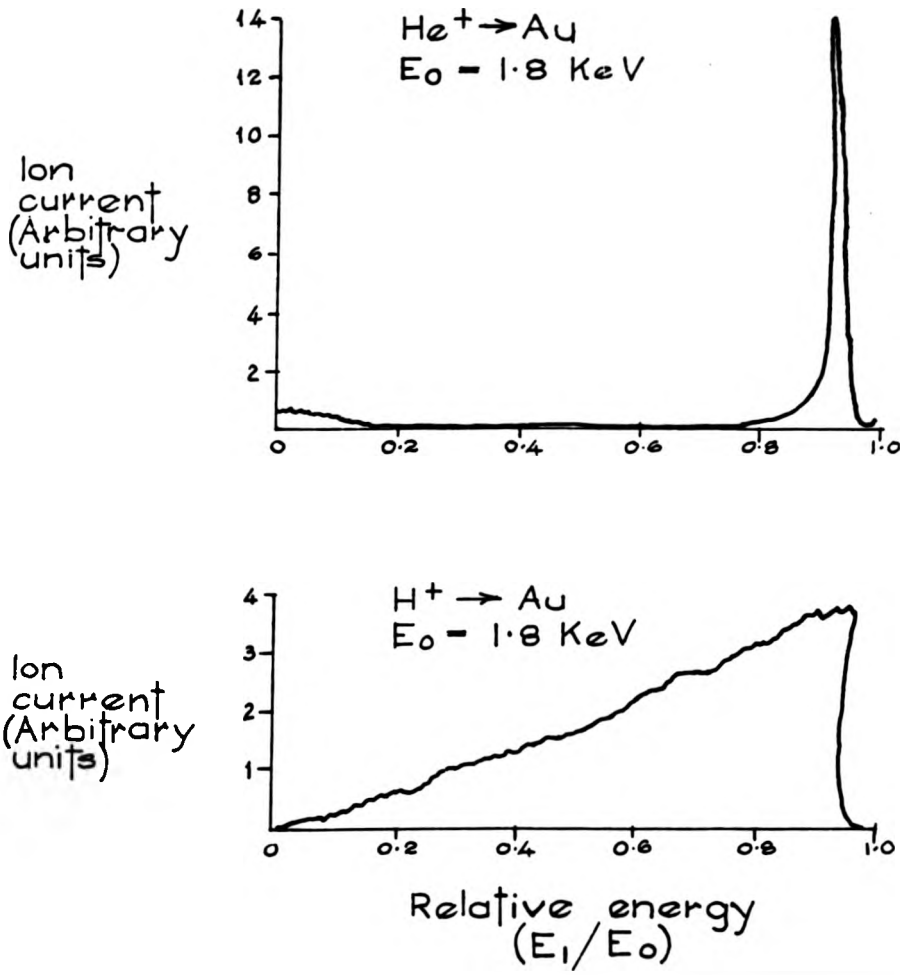
He+ → Au
E0 = 1·8 KeV
Ion current (Arbitrary units)
14
12
10
8
6
4
2
0
0·2
0·4
0·6
0·8
1·0
H+ → Au
E0 = 1·8 KeV
Ion current (Arbitrary units)
4
3
2
1
0
0·2
0·4
0·6
0·8
1·0
Relative energy (E1/E0)

**Figure 2.2.**

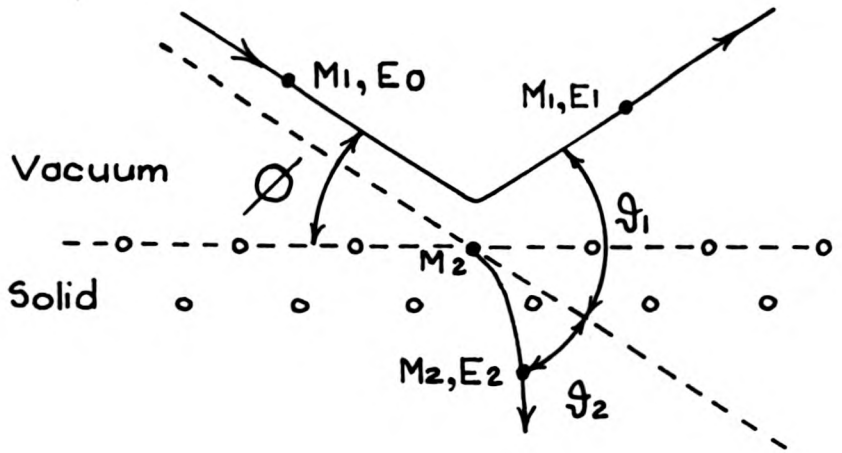


Figure 2.3.

from Eqtn. (1) the mass resolution as a function of the scattering angle and energy resolution can be found.

$$\frac{M_2}{\Delta M_2} = \frac{E_1}{\Delta E_1} \cdot \frac{2A}{A+1} \cdot \frac{A + \sin^2\vartheta_1 - \cos\vartheta_1 (A^2 - \sin^2\vartheta_1)^{1/2}}{A^2 - \sin^2\vartheta_1 + \cos\vartheta_1 (A^2 - \sin^2\vartheta_1)^{1/2}}$$

The mass resolution as a function of the scattering angle is shown in Figure 2.4. The values shown in the figure for A and $\frac{E}{\Delta E}$ are those found in this work. It can be seen that the best mass resolution is obtained if the ion and target mass are approximately equal. For heavy target atoms, good mass resolution is difficult to achieve. Below a scattering angle of 90°, the mass resolution decreases drastically. Also, the mass resolution increases proportionately with energy resolution. However, increasing the energy resolution will decrease the detected signal, thereby requiring a compromise to be made.

The range of scattering angles which will be included in the detected signal is dependent upon the acceptance angle of the analyser. The electrostatic energy analyser used for detecting the ISS signal was a 120° azimuthal sector cylindrical mirror analyser (C.M.A.). The C.M.A. has an acceptance angle of $\pm$ 6°, and so the scattering angle becomes $\vartheta_1 \pm 6°$. Table 2.1 shows the maximum possible range of masses which will result in the same value of $E_1/E_0$ for the main experimental conditions used in this present work. It can be seen that the effect on the mass resolution of the large acceptance angle is greatest for the smallest scattering angle. The total peak width for 90° scattering with 1.0 keV helium ions on copper, calculated from the angular acceptance, is approximately 22 eV. However, the experimental resolution is dependent upon the full width at half maximum peak height (F.W.H.M). For these experimental conditions in the present work, the F.W.H.M. is approximately 24 eV (see Figure 4.6). Thus, the resolution of the experimental system is similar to that 'suggested' by Table 2.1.

Mass resolution as a function of the laboratory scattering angle $\theta_1$

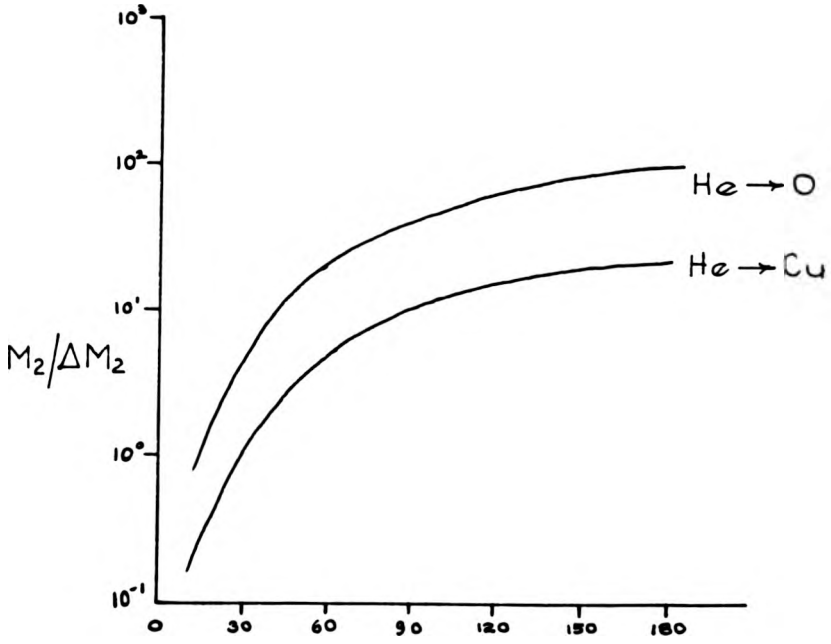


**Figure 2.4.**

The effect of the acceptance angle of the C.M.A. for $He^+$ scattering

| | | | | |
|---|---|---|---|---|
| $\vartheta_1 = 90°$ | $M_2 = 63.5$ | $E_1/E_0 = 0.88$ | $M_2 = 16.0$ | $E_1/E_0 = 0.60$ |
| $\vartheta_1 + 6°$ | $M_2 = 70.0$ | | $M_2 = 17.5$ | |
| $\vartheta_1 - 6°$ | $M_2 = 57.0$ | | $M_2 = 14.5$ | |
| $\vartheta_1 = 48°$ | $M_2 = 63.5$ | $E_1/E_0 = 0.96$ | $M_2 = 16.0$ | $E_1/E_0 = 0.85$ |
| $\vartheta_1 + 6°$ | $M_2 = 78.5$ | | $M_2 = 20.0$ | |
| $\vartheta_1 - 6°$ | $M_2 = 49.0$ | | $M_2 = 12.5$ | |

**Table 2.1.**

A number of other factors affect the practical mass identification when using ISS. For example, an ion can undergo two or more collisions in a row with surface atoms until it is finally backscattered with a total scattering angle $\vartheta_1$. As a number of angles combine to give the angle $\vartheta_1$, the energy retained by the ion is greater than the energy retained in a single scattering event. The energy of multiply scattered ions is not easy to calculate as the scattering geometry and the interaction potential are not fully known. Multiple scattering is more pronounced for high ion masses ($Ne^+$ and $Ar^+$) and small scattering angles. It will cause high energy shoulders to the single scattering peaks. This makes mass identification difficult, especially if there is a single scattering peak from a further target species close to the original peak. However, as the neutralisation probability is high for single scattering, collisions involving multiple scattering are even more likely to involve neutralisation. Therefore, the contribution of multiple scattering in the reflected ion yield is generally low.

Other factors which will affect the half width of the ISS peak are inelastic scattering and thermal vibrations. It appears that the primary ions experience inelastic losses, as well as elastic losses in the collision with the surface. These losses are caused by interaction with the electronic structure of the surface (7). This can be seen most clearly in the variation of the reflected ion yield in relation to the primary energy (8). For certain combinations of incident ion and target atom, oscillations are obtained in the yield curve. This will be dealt with in more detail in section 2.4 on Ion Neutralisation.

Temperature effects are most noticeable with high mass incident ions ($Ne^+$ and $Ar^+$) under conditions where multiple scattering is evident (9). In multiple scattering, the actual path

the incident ion follows along the surface is critical. Therefore, thermal vibrations, which will effect the positions of the target atoms along this path, will effect the relative contributions of single, double and multiple scattering. If single scattering events predominate, temperature effects are small.

The difference between experimental data and the peak energy of single scattering predicted by the binary collision model is usually less than 3% (10). Assuming that the possible number of different target species is limited and can be established by other methods (for example by using AES), it is possible to identify the target masses of the energy peaks obtained. In this work, the problem was simplified by using a known substrate and a known adsorbate of greatly differing masses.

## 2.3. Differential Scattering Cross-section.

Although the identification of the target mass is relatively straight forward, the quantitative determination of the number of target atoms is very difficult. The measured scattered intensity will be dependent on the incident ion intensity $I_o$, the number of scattering centres N ($cm^{-2}$), the differential scattering cross-section $\frac{d\sigma}{d\Omega}$, the neutralisation probability P and the solid angle of the detection system $\Delta\Omega$.

$$\text{i.e.} \quad I \sim I_o N P \frac{d\sigma}{d\Omega} \cdot \Delta\Omega$$

The role of neutralisation will be dealt with in the next section. In calculating the number of scattering centres, only those atoms which contribute to the scattering process should be taken into account. As ISS is extremely surface sensitive, the number of scattering centres must be limited to those in the first one or two atomic layers. The number of centres 'seen' by the incident ions is also effected by the shadowing of the other surface atoms. This will be dealt with in section 2.5. The value of $\Delta\Omega$ will be

dependent upon the particular experimental arrangement.

The scattering cross-section is a function of the interaction potential V(r) between the ion and the target atom. For the high energy range, in the MeV region, a simple Coulomb potential can be used. However, the interaction potential required for the energy range between 0.1 keV and 2.0 keV is not well known. The choice of interaction potential is important in determining the scattering cross-section. Hence, a brief description of the various interaction potentials used in ISS will be given here.

The potential due to a point charge ($Z_1.e$) at a distance r is given by

$$V(r) = \frac{Z_1.e^2}{r}$$

However, when considering the interaction of a low energy ion with an atom core, it is necessary to take into account the screening effect of the electrons of the atom. This screening reduces the strength of the potential. A number of different functions are available for the effective potential. These have a general form

$$V(r) = f(r/a).\frac{Z_1.e^2}{r}$$

where f(r/a) is a screening function and a is a screening length. The different forms of the interaction potential used in ISS are shown in Figure 2.5.

The Bohr potential (11) uses an exponential form of the screening function,

$$V(r) = \exp(-r/a).\frac{Z_1.e^2}{r}$$

where $Z_1.e$ is the nuclear charge. Here, the screening length (a) can be calculated from the radius of the first Bohr orbit ($a_o$) for an electron in the hydrogen atom,

$$\text{i.e.} \quad a = a_o Z_1^{-\frac{1}{2}}$$

Where the separation between the ion and atom core is small, this potential closely approximates to the Coulomb potential. Thus, for energetic collisions and for small impact parameters, the

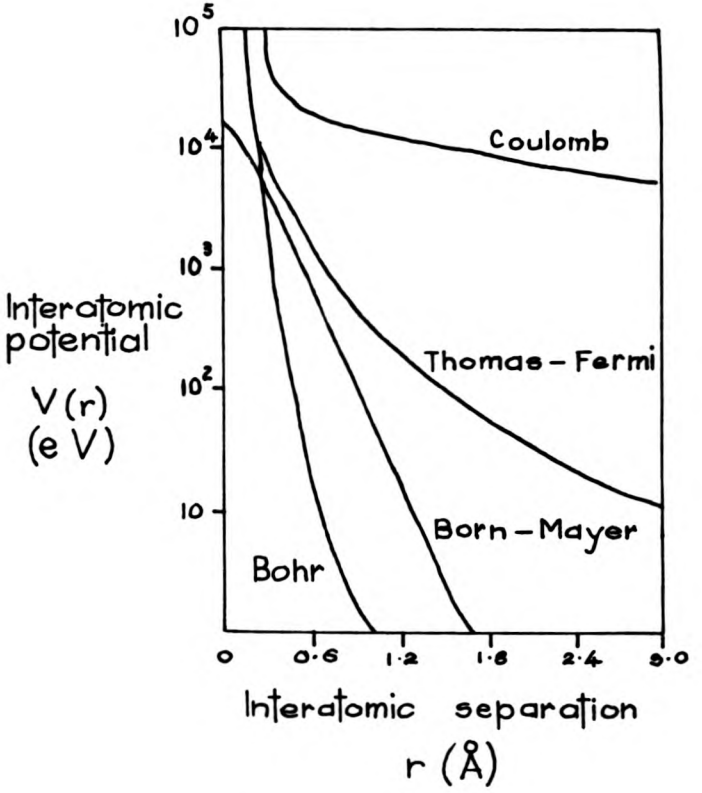
$10^5$
$10^4$
$10^3$
$10^2$
10
Interatomic potential
V(r)
(e V)
Coulomb
Thomas – Fermi
Born – Mayer
Bohr
0
0·6
1·2
1·8
2·4
3·0
Interatomic separation
r (Å)

Figure 2.5.

screening effect of the electrons is small. The impact parameter is the perpendicular distance between the incident trajectory of the ion and the initial position of the target atom (see Figure 2.6). When r is large compared with a, the effect of the screening is also large. This rapid decrease in the interaction potential means that the value obtained for the cross-section is low compared with the Born-Mayer and Thomas-Fermi potentials.

The Thomas-Fermi potential in the Moliere approximation uses a screening function (F(r)) which is the sum of three exponentials.

i.e. $F(r) = 0.35y + 0.55y^{4} + 0.10y^{20}$

where $y = \exp(0.3r)$

This function represents the Thomas-Fermi screening function quite well for small values of r. For small distances of approach, the Thomas-Fermi potential closely follows the Bohr potential. Hence, the screening by the electrons is weak for small values of r.

The Born-Mayer potential does not involve a screened version of the Coulomb potential. For the Born-Mayer potential,

$$V(r) = A \exp(-B.r)$$

where A and B are parameters which have been tabulated for all elements by Abrahamson (12). Since this potential does not contain the Coulomb function, it is not repulsive enough for collisions where r is small and is valid only for collisions with large impact parameters and small scattering angles (13).

The relationship between the scattering angle and the differential scattering cross-section is

$$\frac{d\sigma}{d\Omega} = \frac{p}{\sin \theta_{com}} \cdot \frac{dp}{d\theta_{com}}$$

where p is the impact parameter and $\theta_{com}$ is the scattering angle in the centre of mass frame. The scattering angle is related to the impact parameter and the interaction potential by

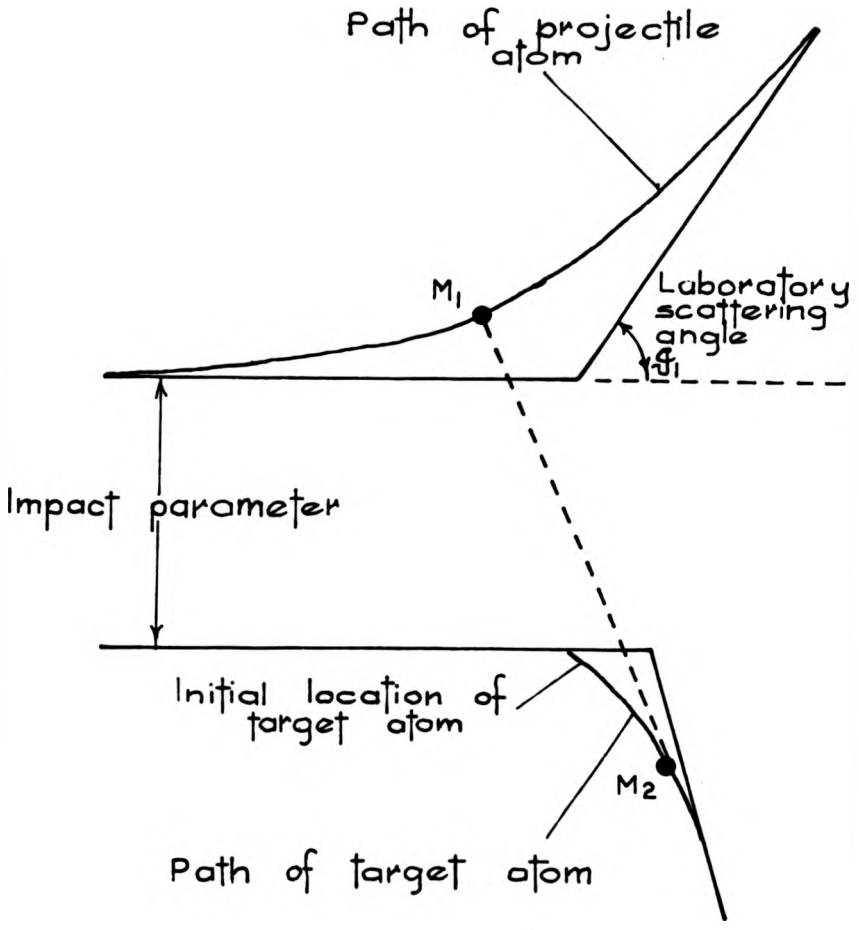
Path of projectile atom
M1
Laboratory scattering angle
Impact parameter
Initial location of target atom
M2
Path of target atom

Figure 2.6.

$$\theta_{com} = \pi - 2\int_{r_{min}}^{\infty} \frac{p\,dr}{r^2\left(1 - [p/r]^2 - V(r)/E\right)^{1/2}} \qquad (3)$$

where $r_{min}$ is the distance of closest approach between the ion and the atom and E is the relative kinetic energy. For the potentials used in ISS, the integral in Eqtn. (3) does not have an analytic solution. Hence, for evaluating impact parameters, distances of closest approach and scattering cross-sections, it is necessary to refer to numerically computed tables such as those provided by Robinson (14).

The Bohr potential has been used by Ball et al (15). The differential scattering cross-section derived from this potential was obtained from curves based on the tables of Everhart et al (16). It was found that at low energies (1.0 keV to 5.0 keV), the scattering cross-sections were most reliable for collisions between ions and atoms of low mass number (e.g. helium on silicon) and least reliable for high mass number combinations (e.g. argon on gold). They found that the energy dependence of the scattering cross-section approaches 1/E for helium on silicon at 1.0 keV for a scattering angle of 120°.

The Born-Mayer and Thomas-Fermi potentials have been used by Heiland and Taglauer (17). For collisions between high mass number ions and atoms, the differences between the potentials are not large. However, for low mass number collisions, the resulting cross-sections may differ by an order of magnitude. The scattering cross-section for collisions between 1.0 keV helium ions on oxygen and nickel over a scattering angle of 90° and 0.6 keV helium ions on oxygen and silver over a scattering angle of 60° are given in Table 2.2.

It can be seen that the scattering cross-section increases with decreasing scattering angle. The difference between the values obtained for the scattering cross-section with the different interaction potentials is shown in Figure 2.7. Below a mass number

Calculated differential scattering cross-sections for differing interaction potentials

| 1 keV $He^+$ $\psi_1 = 90°$ | Thomas-Fermi | Born-Mayer |
|---|---|---|
| $\left(\frac{d\sigma}{d\Omega}\right)_{He \to O}$ | $7.5 \times 10^{-3}$ Å$^2$/sr | $2.9 \times 10^{-4}$ Å$^2$/sr |
| $\left(\frac{d\sigma}{d\Omega}\right)_{He \to Ni}$ | $2.2 \times 10^{-2}$ Å$^2$/sr | $7.5 \times 10^{-3}$ Å$^2$/sr |
| ratio $\frac{d\sigma_O}{d\sigma_{Ni}}$ | 0.34 | 0.039 |

| 0.6 keV $He^+$ $\psi_1 = 60°$ | | |
|---|---|---|
| $\left(\frac{d\sigma}{d\Omega}\right)_{He \to O}$ | $2.2 \times 10^{-2}$ Å$^2$/sr | $1.1 \times 10^{-2}$ Å$^2$/sr |
| $\left(\frac{d\sigma}{d\Omega}\right)_{He \to Ag}$ | $9.5 \times 10^{-2}$ Å$^2$/sr | $1.4 \times 10^{-1}$ Å$^2$/sr |
| ratio $\frac{d\sigma_O}{d\sigma_{Ag}}$ | 0.23 | 0.079 |

Table 2.2.

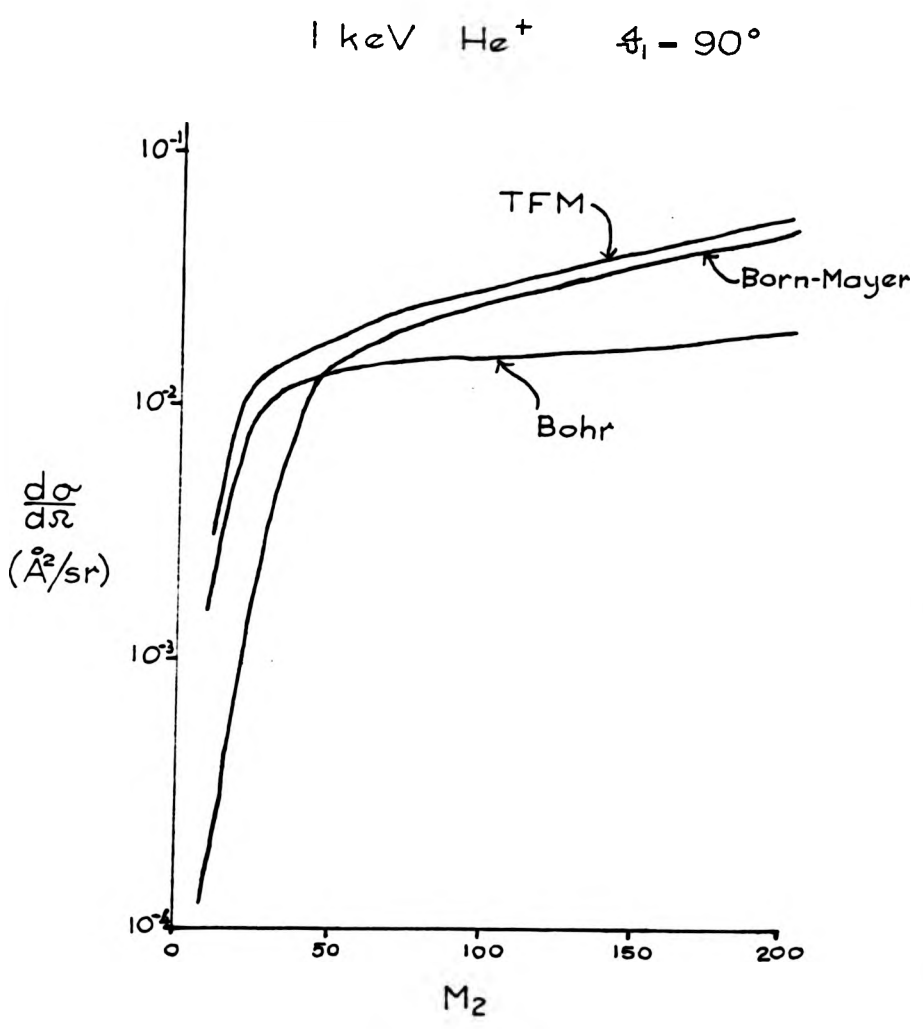
1 keV He+ ϑ1 = 90°
10-1
10-2
10-3
10-4
TFM
Born-Mayer
Bohr
dσ/dΩ
(Å2/sr)
0
50
100
150
200
M2

Figure 2.7.

of 100, the differences in the scattering cross-section obtained become large.

At present, the choice of interaction potential for a given ion-atom core collision is somewhat arbitrary. It is clearly an area where more work, both experimental and theoretical, is required. Thus, it is best if at least two potentials are used in the interpretation of experimental data. This will allow insight into the reliability of the values for the impact parameters and the differential scattering cross-sections which are obtained. From the values of the cross-sections obtained for helium on oxygen and nickel by Heiland and Taglauer (17), it can be seen that quantitative statements based on these cross-sections are uncertain to one order of magnitude. This is of particular importance when ion yields and absolute coverages are to be measured. It is possible to overcome some of this difficulty by using other surface sensitive techniques for calibration. The most appropriate choice for the interaction potential in this work is the Thomas-Fermi potential in the Moliere approximation.

## 2.4. Ion Neutralisation.

The second major factor influencing the scattered ion yield is the probability that the ion will remain charged. For the energy range and the type of ions used in ISS, only a small fraction of the incident ions remain ionised after impact. As shown in Figure 2.2, it is this high neutralisation probability which causes single scattering events to predominate in ISS spectra. Also, the high surface sensitivity of ISS is partly explained in terms of the large neutralisation probability. This is because ions which penetrate beyond the first one or two atomic layers of the surface are much more likely to be neutralised than those scattered from the surface.

However, this dependence on the high neutralisation probability

makes quantitative analysis difficult. A number of factors might be seen to effect the efficiency of neutralisation. Such probable factors are the incident ion species and energy, the substrate material and the type and position of the adsorbate atoms. Thus, a knowledge of the neutralisation probability is crucial in the quantitative interpretation of ISS data.

There are two basic ways of considering the neutralisation of an incident ion by a surface. The ion can be thought of as interacting with the overall surface or it can be seen as being neutralised by an individual atom on the surface. These two types of neutralisation will be dealt with in turn.

### 2.4.1. Ion-Surface Neutralisation.

Details of the neutralisation processes are not well known. The charge exchange mechanism has been studied principally by Hagstrum (18). Neutralisation is most likely to occur when the incident ion is near to the surface. Hence, the longer the ion is close to the surface, the higher the probability that it will be neutralised. Thus, the distance of closest approach and the perpendicular velocity of the ion to the surface will effect the neutralisation probability. It is assumed in ion-surface neutralisation that the electron density outside the surface is smooth and decreases with the perpendicular distance from the surface. The processes of neutralisation which have been suggested by Hagstrum are Auger neutralisation, resonance neutralisation and quasi-resonance charge exchange. A brief description of these processes is given in Figure 2.8.

These mechanisms were developed for the interpretation of secondary electron emission by slow ions (less than 10 eV). From these mechanisms, the transition rate (R(r)) of an electron being transferred from a metal surface to an ion is considered to decrease exponentially with the distance of the ion from the surface (r).

## Auger Neutralisation

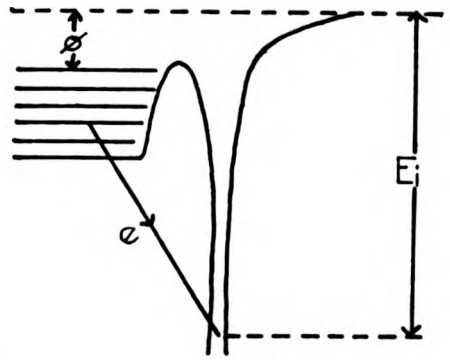


An electron from the valence band of the metal tunnels into the deep potential well of the incident ion. The excess energy is taken up in the ejection of a second electron from the valence band

## Resonance Neutralisation

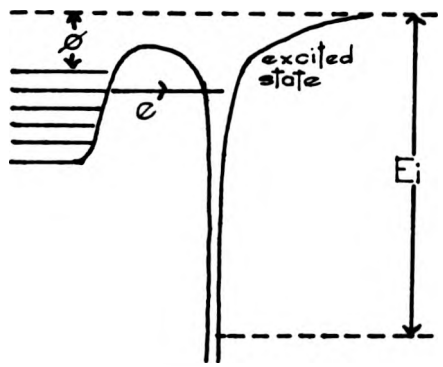


An electron from the valence band fills an excited state in the ion

## Quasi-resonance Charge Exchange

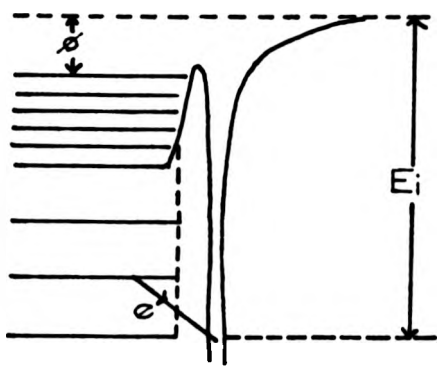


An electron from one of the core levels of the metal fills the hole in the ion

**Figure 2.8.**

i.e. $R(r) = A \exp(-ar)$

where A and a are constants for a particular ion-surface combination. The probability of undergoing this transition in a distance interval dr at a distance r from the surface is

$$\frac{R(r)\,dr}{V_\perp}$$

where $V_\perp$ is the velocity perpendicular to the surface. Therefore, the probability of the ion not being neutralised in dr is given by

$$(1 - \frac{R(r)\,dr}{V_\perp}) \simeq \exp(-\frac{R(r)\,dr}{V_\perp})$$

Hence, the probability of escaping neutralisation along this path is given by

$$P = \exp(-\int_s^\infty \frac{R(r)\,dr}{V_\perp})$$

where s is the distance of closest approach. We can put

$$V_r = \int_s^\infty R(r)\,dr$$

We already have

$$R(r) = A \exp(-ar)$$

and so

$$V_r = \int_s^\infty R(r)\,dr = A/a \exp(-as)$$

At the surface, s = 0, thereby giving

$$V_o = A/a \qquad \text{where } \exp(-as) = 1$$

Hence, the probability for escaping neutralisation near the surface can be written as

$$P = \exp(-V_o/V_\perp) = \exp(-\frac{A}{aV_\perp})$$

We see that $V_o$ is a characteristic constant for a particular ion-surface combination. Its value can be obtained from the neutralisation mechanisms. However, the value taken for this constant will affect the calculated value of P by a large amount. Smith (3) quotes a value for $V_o$ of $1.3 \times 10^5$ m/sec for helium on copper. Brongersma and Buck (19) use a value of between 4 and $7 \times 10^5$ m/sec for $V_o$ to investigate the neutralisation of neon ions on gold.

The value taken by Smith for $V_o$ has been used in Figure 2.9 to show how the probability of escape for helium ions on a copper

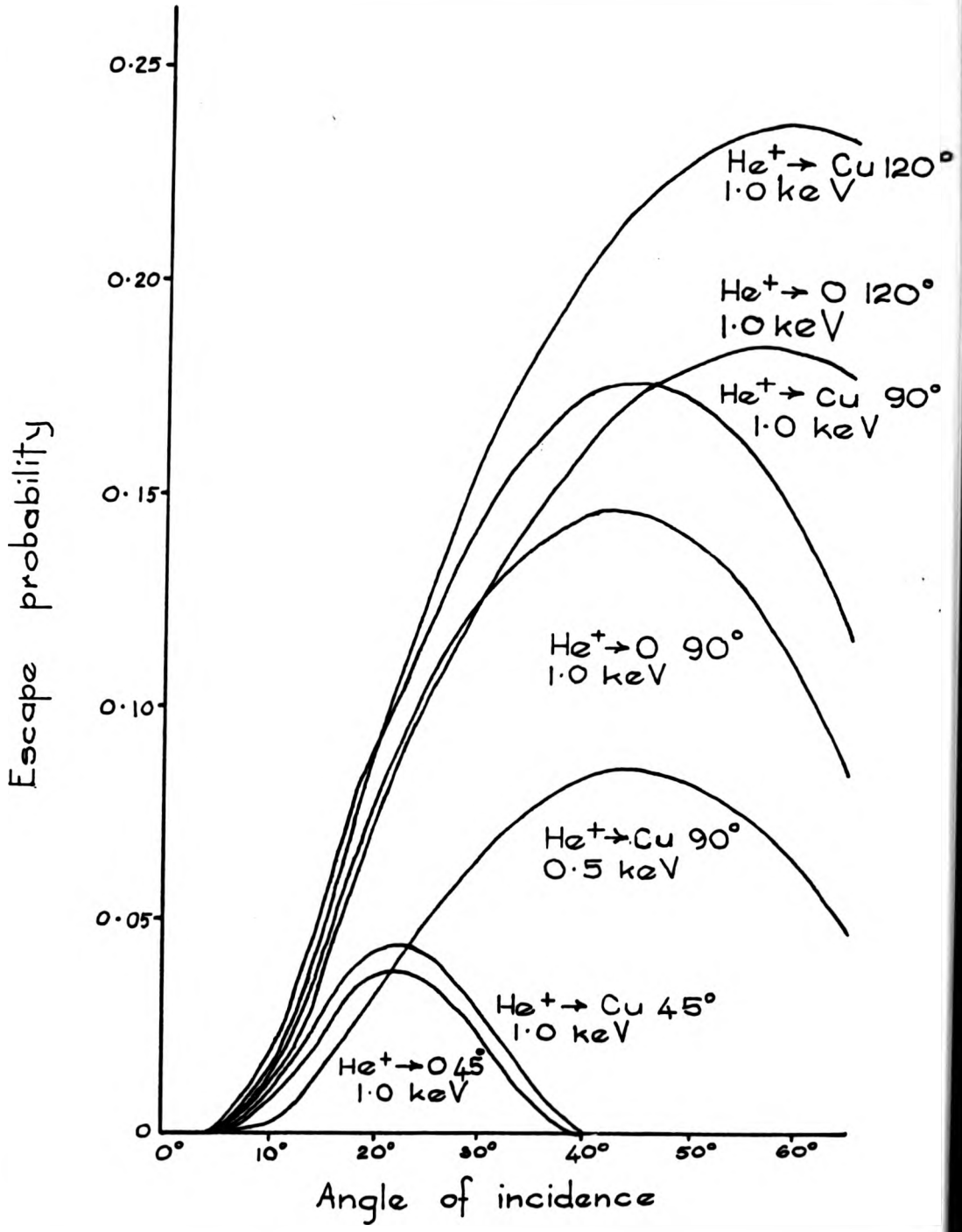
0·25
0·20
0·15
0·10
0·05
0
Escape probability
He+→ Cu 120°
1·0 keV
He+→ O 120°
1·0 keV
He+→ Cu 90°
1·0 keV
He+→ O 90°
1·0 keV
He+→ Cu 90°
0·5 keV
He+→ Cu 45°
1·0 keV
He+→ O 45°
1·0 keV
0°
10°
20°
30°
40°
50°
60°
Angle of incidence

Figure 2.9.

surface and an oxygen covered surface varies with the angle of incidence for different scattering angles and for different energies. It can be seen that reducing the primary energy of the incident ion will decrease the probability that the ion will escape neutralisation. A small scattering angle and glancing incidence will also decrease the escape probability, because the perpendicular velocity has been reduced. It should be noted that the maximum value for the escape probability does not occur at specular reflection. This is because the ion loses energy in the surface collision and so the value of $V_\perp$ is reduced. This simple treatment of the neutralisation probability is able to achieve good agreement with the overall polar variation of the ISS data. This can be seen in Figures 4.12 and 4.13 where the predicted ion escape probability is compared with the ion yield obtained from helium scattering on copper.

However, this simple exponential dependence for P is not always found experimentally. For example, Taglauer and Heiland (20) found that the neutralisation probability for helium and neon ions of energies of 0.3 keV and 2.0 keV on oxygen, sulphur and nickel did not give a good fit to the exponential function.

## 2.4.2. Ion-Atom Neutralisation.

As was stated in the introduction to this chapter, the role of ion neutralisation in ISS has been investigated in order to interpret the particular ISS data obtained in this work. Within this study of neutralisation, the emphasis has been placed upon the importance of ion-atom neutralisation. In this section, other experimental evidence is presented which indicates the need for the consideration of ion-atom effects. The extension of ion-atom neutralisation to surface structure analysis is included in Chapter 5.

As previously mentioned, for certain ion-atom combinations, oscillations have been observed in the relationship between the

reflected ion yield and the varying incident ion energy (for example the work of Erickson and Smith (8) and Brongersma and Buck (19)). This variation is attributed to oscillations in the neutralisation probability. The peaks obtained are quite evenly spaced when the yield is plotted against the reciprocal of the incident ion velocity. This velocity is proportional to the interaction time. Although there is no complete theoretical treatment of this effect, an understanding can be obtained by considering the mechanism of quasi-resonant charge exchange. As can be seen from Figure 2.8, an electron is transferred from a core level in the metal to the incident ion. There will be a transition rate for this process and for the reverse process. During the collision, the electrons which initially have been orbiting their respective nucleus, then orbit both nuclei. With these electrons being shared, it is possible for the ion to capture an electron from the surface atom. For high incident ion velocities, the interaction time will be short (about $10^{-16}$ seconds). A sufficiently large ion velocity will allow only one transfer to occur. As the ion velocity is lowered, a number of electron exchanges between the ion and the surface atom will be able to take place. This will cause a variation in the number of ions which are neutralised.

It is likely that all three mechanisms of charge exchange will operate to varying degrees for a given ion-atom combination. Thus, it is difficult to obtain accurate theoretical calculations of the ion yield. In this present work, ion-atom combinations have been chosen which do not exhibit oscillations. This is in an attempt to lessen the complexity of the interpretation of the experimental data. Oscillations in the ion yield have been used to distinguish between elements where the mass difference is too small to allow energy resolution (8). Also, information concerning the chemical state of the surface atom can be obtained from oscillatory ion yields. However, in terms of surface structure analysis, its

application is at present limited.

A further complication caused by ion-atom neutralisation is the interpretation of ion yields caused by the effect of coverage dependent neutralisation. Niehus and Bauer (10) found that although the AES signal from oxygen increased linearly from 0 to 1 monolayer for the adsorption on W(110), neither the ISS signal from tungsten nor that from oxygen was linear in this range. The variation of the oxygen signal in relation to the coverage has been interpreted as being due to an increase in the neutralisation probability which occurs as coverage increases. When oxygen covers more of the surface, the surface becomes more electronegative in nature. A more electronegative surface will give rise to a higher neutralisation probability.

It is clear that the experimental and theoretical situation in the area of ion-atom neutralisation on surfaces is not fully explained. It is not possible, at present, to determine accurately the number of target atoms involved in the scattered ion intensity. Calibration can be attempted using other surface techniques. However, the sampling volume is unlikely to be identical to ISS and so calibration may not be straight forward.

## 2.5. Surface Structure Analysis with ISS.

The aim of the present work was to use ISS for structural analysis. There are basically two ways in which ISS has been used to determine the positions of adsorbate atoms on single crystal surfaces. The first involves multiple scattering, where the variation of the relative contributions of the single and double scattering events can be used to infer structural information. The second method makes use of the fact that a surface atom has an elastic shadowing effect with respect to underlying neighbouring atoms. These two methods of obtaining structural determination will

be dealt with in turn.

The work of de Wit et al (21) on oxygen adsorption on Cu(110) will be taken as an example of multiple scattering for structural analysis. Here, small angles of incidence ($\phi$ = 20°), small scattering angles ($\vartheta_1$ = 45°) and neon ions were used. This is to ensure that multiple scattering events are evident in the recorded spectra. A difficulty with these experimental conditions is the damage caused to the target surface. For example, de Wit et al report three major peaks in the energy spectrum of 3.0 keV neon ions on an oxygen adsorbed surface. Two of these peaks are due to neon ions reflected from oxygen atoms and copper atoms. However, the third is due to oxygen sputtered from the surface. In an attempt to maintain a dynamic equilibrium, experiments were performed in a background pressure of $1 \times 10^{-6}$ torr of oxygen and at a target temperature of 250 °C.

Multiple scattering is sensitive to the path taken by the incident ion along the surface. As a single crystal is rotated azimuthally, the positions of the surface atoms relative to the incident ion beam will vary. Thus, the relative contributions of singly, doubly and multiply scattered ions will vary as the crystal is rotated. From this variation, it is possible to estimate the positions of the atoms involved in the scattering process. Hence, by studying this variation, surface structure analysis can be performed. Such variations obtained by de Wit et al from Cu(110) were explained in terms of the shadowing effect of neighbouring atoms.

The quantitative effect of this shadowing can be estimated by using a 'shadow cone' model (22). As previously mentioned, the scattering angle for a collision is dependent upon the impact parameter and the interaction potential. Figure 2.10 shows the possible trajectories from an incident ion $M_1$ scattered by a target

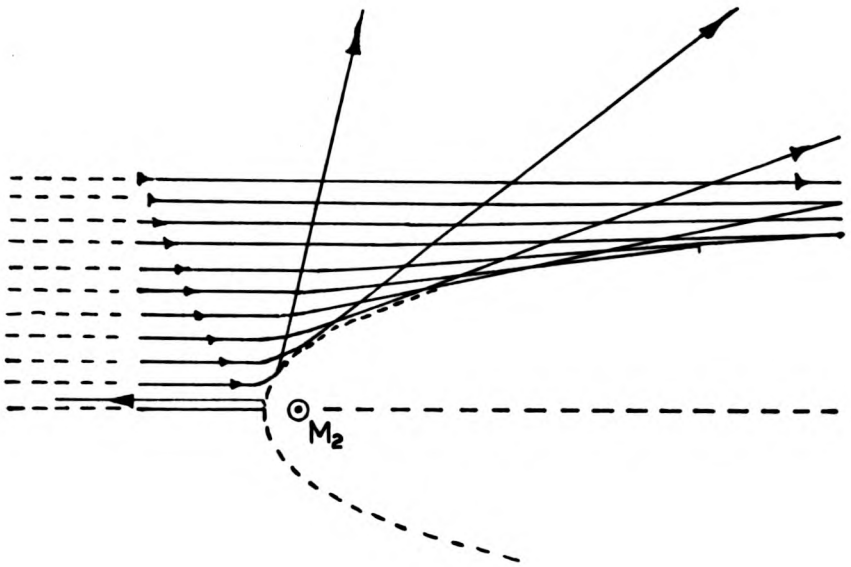


Figure 2.10.

atom $M_2$, with a varying impact parameter. Clearly, the resultant energy E, will be dependent upon the scattering angle. It can be seen that there is an area behind the target atom where there are no scattered particles. Also, there is an increase in the intensity of the scattered ions outside the edge of the shadow cone.

When a second target atom is situated in the edge of the shadow cone, it will receive an increased flux of particles. However, when it is within the shadow cone, a second collision is not possible. By varying the angle of incidence of the beam, it is possible to change the volume of the crystal within the shadow cone. This can greatly effect the proportion of incident ions which undergo single scattering events. Thus, by studying the variation of the intensity of the scattered neon ions from oxygen adsorbed Cu(110), it was possible to deduce the positions of the adsorbate and substrate atoms.

de Wit et al found that at incidence angles above 3°, little single scattering from oxygen could be detected along the ⟨100⟩ azimuth of the crystal. Thus, the oxygen was effectively shadowed by the copper atoms along this direction. From calculations using the shadow cone model, the authors conclude that the adsorbed oxygen lies about 0.6 Å below the midpoint between the neighbouring copper atoms in the ⟨100⟩ row (which is equivalent to structure (iii) in Figure 2.11).

This approach to surface structure analysis has been applied to oxygen on Ni(110) (23) and GaP(110) (24). The shadow cone model has been used in this work to study the elastic scattering effects for oxygen adsorbed on Ni(100). The results of this are presented in Chapter 5.

One of the major difficulties of applying ISS to surface structure analysis of adsorbate layers on single crystals is the damage caused by the ion beam. In many surface physics experiments,

a) Ag (110) (2 × 1) – O structure

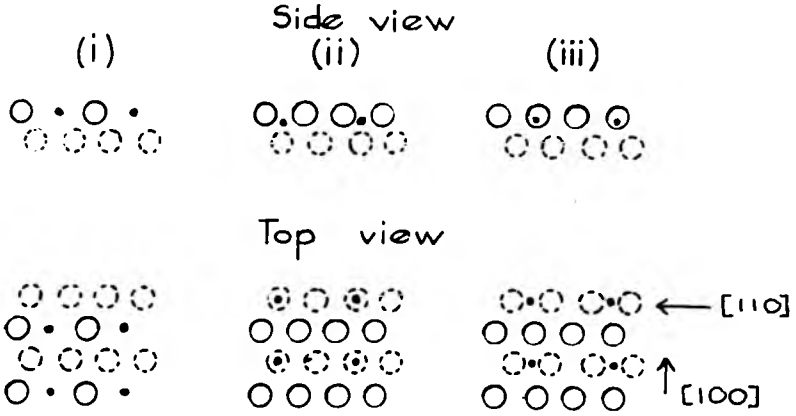


O top Ag atoms ○ second layer Ag atoms
• oxygen atoms

b) $He^+ \rightarrow Ag\,(110) - O$
$E_0 = 600\ eV$
$\chi = 30°$
$\vartheta_1 = 60°$

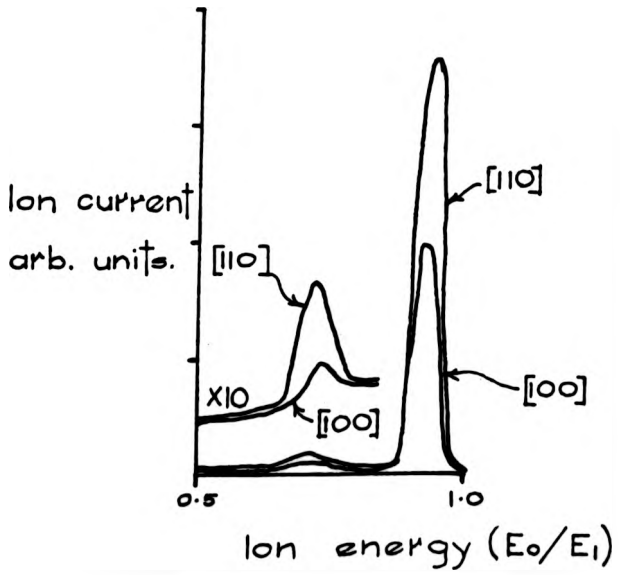


Figure 2.11.

inert gas ion beams of argon are used to sputter clean the sample. Sputtering may change the surface order of a single crystal such that annealing is required before further investigation of the surface is possible. As ISS is extremely surface sensitive, any surface roughness caused by the sputtering is likely to affect the ISS signal. This will be particularly evident where multiple scattering conditions are used. From a few systematic studies, it has been concluded that the sputtering yield is quite large for the type of ions and energies used in ISS. For example, a value of 0.07 atoms/ion for helium scattering and 0.48 atoms/ion for argon scattering have been quoted (25). de Wit et al used a current density of 6 $\mu A/cm^2$ for 100 seconds in order to record an energy spectrum. This corresponds to approximately $3.75 \times 10^{15}$ ions/$cm^2$ . Thus, a sputtering yield of 0.27 atoms/ion will produce the removal of a monolayer (approximately $10^{15}$ atoms) in this time. In order to increase the amount of time available for experiments, the ion beam current density must be reduced so that the ion dose is much less than $1 \times 10^{15}$ ions/$cm^2$. Due to the low yield of scattered ions, this limit is difficult to achieve with reasonable signal to noise ratios. Thus, the use of heavy noble gas ions for surface structure analysis is particularly difficult (26).

The second method for obtaining surface structural analysis from ISS involves experimental conditions where single scattering events predominate. It has been shown that ISS is extremely surface sensitive, thus the presence of an adsorbate atom will severely attenuate the single scattering signal from a substrate atom. An adsorbate atom above the top layer of a single crystal may shadow a number of nearby atoms. The degree of shadowing will be dependent upon the angle of incidence of the beam and the position of the adsorbate atom relative to the crystal lattice. In order to illustrate the use of shadowing for structural analysis, the work

of Heiland et al (27) on the adsorption of oxygen on silver will be used. Here, Heiland et al used a combination of ISS, LEED and AES to study oxygen adsorbed on Ag(110). Using LEED, a (2x1) oxygen structure was prepared. From the symmetry of the LEED pattern, three overlayer sites are possible (see Figure 2.11a). The ISS spectra for 0.6 keV He ions on Ag(110)(2x1)-O are shown in Figure 2.11b. The silver peak in the ⟨100⟩ direction is approximately half the height of the peak obtained in the ⟨110⟩ direction. The oxygen peak is almost undetected in the ⟨100⟩ direction. This suggests that there is mutual shadowing by the oxygen and silver atoms along the ⟨100⟩ direction.

The fraction of ions ($I_i/I_o$) elastically backscattered from the surface species i is given by

$$I = I_o N_i P_i \frac{d\sigma_i}{d\Omega}$$

where $N_i$ is the number of scattering centres seen by the ion beam, $P_i$ is the ion escape probability for the collision with the surface species and $\frac{d\sigma_i}{d\Omega}$ is the differential scattering cross-section. As previously stated, the differential scattering cross-section can be calculated from the interaction potential. The value of $N_i$ can be estimated from the surface structure which is being studied. Thus, if the ratio, for example, of the ISS oxygen and silver peaks is measured, the ratio of the ion escape probabilities can be found

$$\text{i.e.} \quad \frac{P_o}{P_{Ag}} = \frac{I_o}{I_{Ag}} \frac{\frac{d\sigma_{Ag}}{d\Omega}}{\frac{d\sigma_o}{d\Omega}} \frac{N_{Ag}}{N_o}$$

For the Ag(110)(2x1)-O system, the value of $N_{Ag}/N_o$ varies between 3 and 1, depending upon the structural model assumed. The measured intensities for $I_o/I_{Ag}$ is 1/29 in the ⟨110⟩ direction (see Figure 2.11b). Thus, Heiland et al obtain for the (2x1) structure a value for $P_o/P_{Ag}$ of between 1/18 and 5/4, depending on the

interaction potential used. This shows that the ratio of $P_o/P_{Ag}$ is not well known. However, it does show clearly that the level of neutralisation which is present is dependent upon the type of atom involved in the surface collision.

The exact number of scattering centres involved in the ISS scattering process will be dependent upon the degree of elastic shadowing. Heiland et al did not use the shadow cone arguement to estimate the shadowing caused by the adsorbed oxygen atoms. Instead they considered the relative sizes of the impact parameters of the oxygen and silver atoms. This was achieved by considering the amount of scattering required from the silver atom before affecting the scattering caused by the oxygen atoms. Figure 2.12a shows the ion trajectory which is involved in the collision. Heiland et al argue that the angular resolution of the energy analyser will affect the amount of scattering which will be possible before the resultant ion is not included within the scattered peak. This is because the total scattering angle of the 'double' collision which can be detected is $\Phi_1 + \Delta\Theta$ where $\Delta\Theta$ is the angular resolution of the analyser.

However, this arguement appears to be false. This is because scattering events which involve small changes in the major collision, for example $\Delta\Theta = 1^\circ$ (see Figure 2.12b), and a corresponding increase in the other collision would still allow the reflected ion to be detected by the analyser. Depending on the energy value obtained, such a collision would still be included within the ISS peak. For energy resolutions which are found experimentally, the smaller scattering angle may be much larger than $1^\circ$ before the energy value of the scattered ion is sufficiently different to prevent the ion from being included in the peak. The important point to note is that the size of the impact parameter for $1^\circ$ scattering is much larger than for $2^\circ$ scattering, whereas the change in the large scattering angle impact parameter is very small. Thus, from such arguements

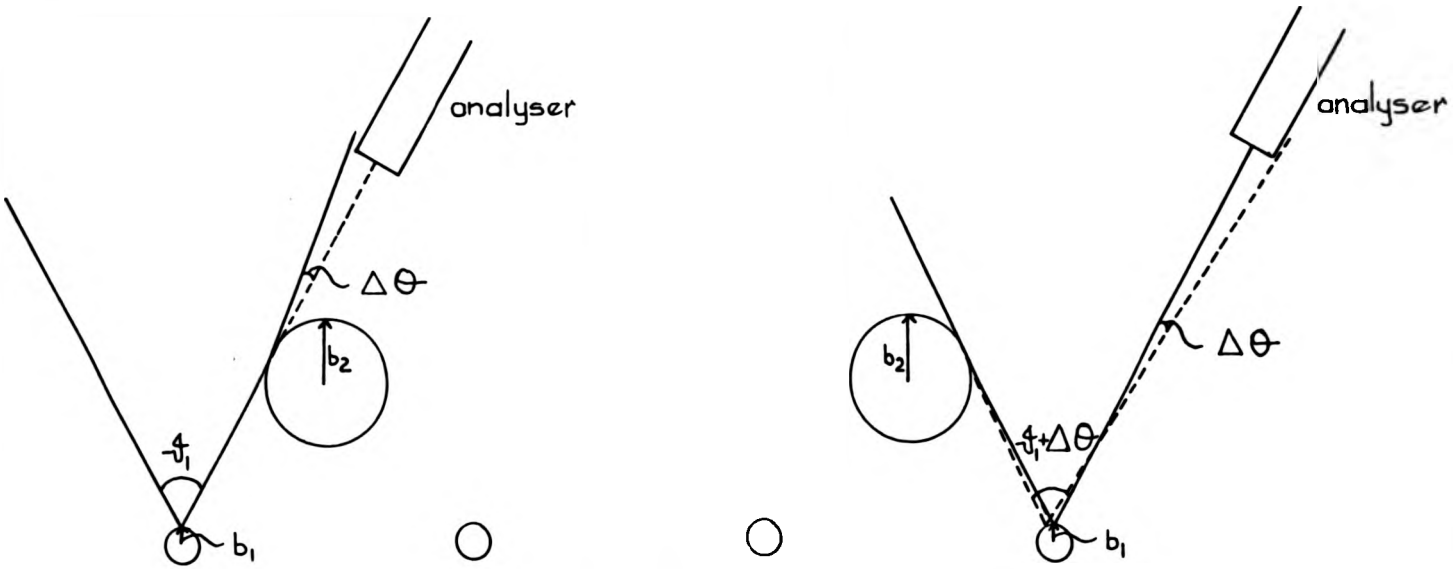


$\Delta\theta$ is the angular resolution of the analyser

a) $b_1$ is the impact parameter for scattering angle $-\theta_1$.

$b_2$ is the impact parameter for scattering angle $\Delta\theta$.

b) $b_1$ is the impact parameter for scattering angle $\theta_1+\Delta\theta$.

$b_2$ is the impact parameter for scattering angle $\Delta\theta$.

**Figure 2.12.**

it is not possible to make qualitative judgements upon the degree of shadowing obtained from adsorbate atoms on single crystal substrates. Also, the 'effective' impact parameter obtained from the shadow cone model is smaller (equivalent to a scattering angle $\simeq 6^{\circ}$) than the value obtained for $1^{\circ}$ scattering. However, using this method for surface structure determination, the probable adsorbate site is obtained from atom diagrams where the radii of the atoms are equal to the calculated impact parameters for $1^{\circ}$ scattering and for scattering over the total angle. Heiland et al used the Bohr potential to calculate the impact parameters used in Figure 2.11a, but other potentials have been used (17).

Structure (i) in Figure 2.11a is a reconstructed model where every second silver atom has been replaced by an oxygen atom. This structure would not give the ISS data which has been obtained. The oxygen signal for this structure would be roughly independent of azimuthal angle. If the oxygen is located in the top of the second plane of silver atoms, as in structure (ii), the oxygen atoms would only be shadowed to a small extent by the silver atoms. If,however, the oxygen is located between the silver atoms, as in structure (iii), then strong shadowing would be expected along the $\langle 100 \rangle$ direction. This is in agreement with the observed experimental variation, and so Heiland et al propose this as the structure for oxygen adsorbed on Ag(110).

The height of the oxygen atoms with respect to the silver lattice is more difficult to obtain. As has already been stated, the choice of interaction potential can greatly effect the impact parameter and the scattering cross-section obtained. The position of the oxygen atom is estimated by calculating its impact parameter using the different interaction potentials. By this means, the limiting positions of the oxygen atoms can be found. Heiland et al chose the limits for the oxygen atoms position by the following

criteria. The lower limit was given by the position where the oxygen atom can no longer contribute to the scattering in the <110> direction. The upper limit was where the oxygen atom started to contribute to the scattering in the <100> direction. From this, they were able to show that the oxygen atom is at the same height as the silver layer, within +1 Å and -2 Å. From a consideration of the atomic radii, a position where the centres are at the same height is favoured. Thus, it can be seen that the final position of the adsorbate atom is difficult to measure with precision.

This type of surface structure analysis has been applied to a number of systems. Some of the systems which have been studied are O on Ni(110) (26), CO on W(100), Ni(100) and Ni(111) (28) and O on W(100) (29). In general, the results obtained are in agreement with the structure proposed by LEED I(V) analysis. However, on the Ni(110) oxygen adsorbed surface, further LEED I(V) modelling has been carried out which suggests a different structure from that previously suggested (30). It has been proposed that the ISS data can be interpreted in terms of this more recent structure (31). This shows that at present the understanding of the processes involved in ISS is not sufficient to allow unambiguous surface structure analysis.

In the present work, the experimental approach to structural analysis used by Heiland et al has been followed, rather than that of de Wit et al. There were three major reasons for this choice. Firstly, it was hoped that the interpretation of the experimental data would be more straight forward. This is because the interpretation of this data is not based on the calculation of scattering yields. Secondly, the amount of surface damage caused by the beam of helium ions is smaller than for the neon ions used in the multiple scattering approach. Thirdly, the approach of Heiland et al has been more widely used for surface structure

analysis. Thus, it was hoped that with quite simple instrumentation it would be possible to achieve useful structural analysis of a number of different single crystal surfaces. In fact, it has not been possible to gain a satisfactory interpretation of the present work using this simple approach. However, it has been possible to interpret the results by extending the role of neutralisation in ISS.

# Chapter 3.

# The Experimental Arrangement.

## 3.1. The Ultra High Vacuum System.

The aim of this work was to study solid surfaces with LEED, AES and ISS. This is most conveniently achieved when all three techniques are available within the same experimental chamber. For this purpose a complete Ultra High Vacuum (U.H.V.) system was required. The target chamber and the overall pumping configuration were designed by Woodruff. The remainder of the experimental set-up was developed by the author. The construction of the equipment was carried out in the mechanical and electronic workshops of the Department of Physics at the University of Warwick.

### 3.1.1. The Experimental System.

The complete experimental system is shown in Figure 3.1. It consists of a target chamber mounted on a service well. The system is pumped via an ion pump, which is situated below the service well, and a trapped oil diffusion pump on the side of the service well. The target chamber has two levels. The top level is for LEED, using a retarding field analyser (R.F.A.) and the lower level for AES and ISS, using a cylindrical mirror analyser (C.M.A.). A schematic diagram of the system is shown in Figure 3.2. The system was leak tested using a mass spectrometer and helium as a probe gas. After this initial leak testing procedure, a pressure of $2 \times 10^{-10}$ torr was obtained after a bake out of 48 hours at a temperature of 150 $^{\circ}$C.

The method used for achieving an ultra high vacuum was as follows:

(i) The system was 'roughed down' from atmospheric pressure to 0.01 torr using a single stage rotary pump (Edwards ES200)

The Complete Experimental System

**Figure 3.1.**

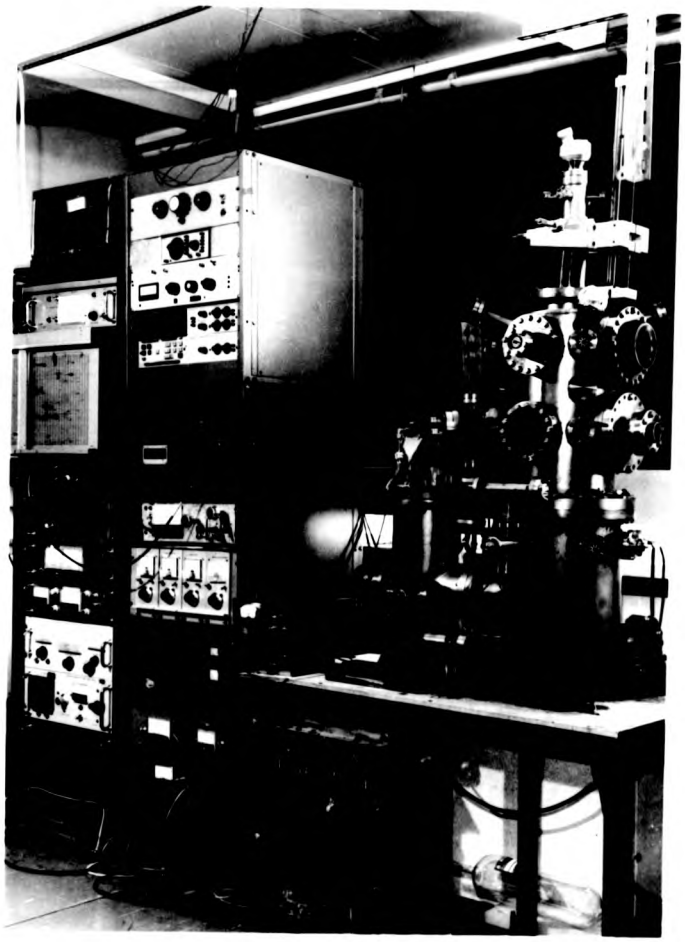

The Complete Experimental System

Figure 3.1.

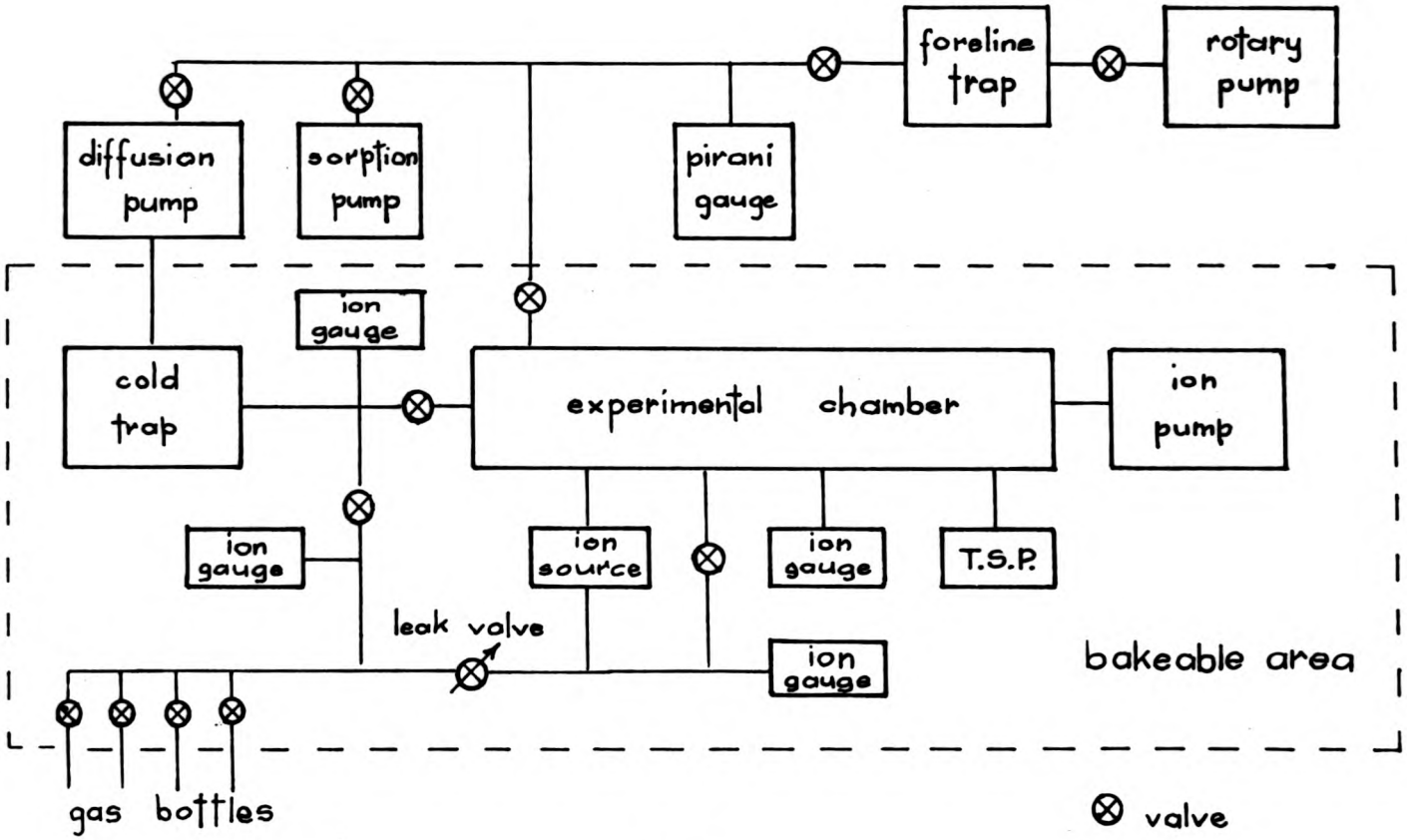
foreline trap
rotary pump
diffusion pump
sorption pump
pirani gauge
ion gauge
cold trap
experimental chamber
ion pump
ion gauge
ion source
ion gauge
T.S.P.
leak valve
ion gauge
bakeable area
gas bottles
valve

Figure 3.2.

with a pumping speed of 200 litres/minute. A trap filled with zeolite was placed between the experimental system and the rotary pump to lessen the contamination of the experimental chamber with rotary pump oil.

(ii) The diffusion pump was used to reduce the pressure to $10^{-6}$ torr. This pump (Edwards E04) was charged with 150 $cm^3$ of Santovac 5, a polyphenylethyl oil with a vapour pressure of less than $10^{-9}$ torr. The diffusion pump was backed with a rotary pump. The possibility of 'backstreaming' from the diffusion pump into the experimental chamber was lessened by the use of a trap. The trap was of similar design to the Vacuum Generators (V.G.) CCT cold trap. The trap had a vessel which could be filled with liquid nitrogen. Copper chevrons were located on the vessel which tended to condense both water vapour and oil vapour, thus reducing backstreaming.

(iii) Once a pressure of $1x10^{-6}$ torr was achieved, the diode ion pump was used to reduce the pressure to $1x10^{-7}$ torr. The ion pump was particularly useful for 'clean' pumping at low pressures. It could not be used during ISS experiments since an ion pump will not pump large gas loads, especially where inert gases are involved. Thus, the ion pump was used in this work for holding the experimental chamber at U.H.V. pressures whilst experiments were not being performed.

(iv) The system was 'baked' at a temperature of 150 °C for 48 hours. During this time the ion pump was not operating. The diffusion pump was used to remove the large gas loads experienced during the bakeout. After 48 hours the system was allowed to cool. When the temperature of the system was approximately 100 °C, the ion pump was restarted. Also at this point, all the filaments in the system were outgassed thoroughly. A titanium sublimation pump (T.S.P.), which was included in the service well, was also

outgassed at this stage.

(v) The T.S.P. was fired once every 30 minutes while the system cooled to room temperature. At room temperature, a pressure of $2 \times 10^{-10}$ torr was obtained. The T.S.P. was fired infrequently once U.H.V. conditions had been attained.

(vi) It was possible to valve off the diffusion pump and maintain U.H.V. using the ion pump and the T.S.P.. For experiments with ISS, large amounts of inert gas were necessary for the operation of the ion gun. This required that the diffusion pump, rather than the ion pump, be used to remove the gas. The diffusion pump was also required when gases were being adsorbed onto surfaces and for inert gas ion bombardment, which was used for cleaning samples. The diffusion pump could be backed with sorption pumps to lessen the level of vibration in the system.

### 3.1.2. Residual Gas Analysis.

The experimental system included two mass spectrometers - a V.G. Micromass magnetic mass spectrometer and a V.G. Q4 quadrupole mass spectrometer. The Micromass had a mass range of 0-200 a.m.u.. Thus, the Micromass could be used for studying the contamination of the experimental chamber by pump oils. The Micromass was used in the initial leak testing mentioned above. For routine work, the Micromass was superseded by the Q4. The quadrupole mass spectrometer was easier to use and removed the problems of strong magnetic fields. Thus, the Q4 provided a convenient method of residual gas analysis. A typical U.H.V. residual gas spectrum from the Q4 is shown in Figure 3.3. The mass numbers of the residual gas ions are also shown in this figure. The Q4 was used to monitor the purity of the gases involved in this work. The Micromass was retained for high mass number gas analysis.

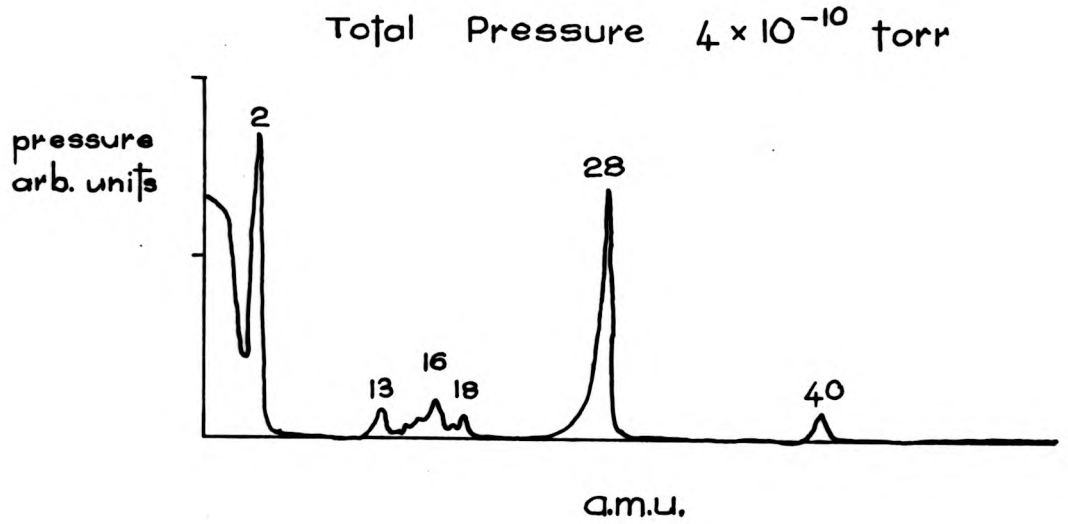
Total Pressure $4 \times 10^{-10}$ torr
pressure
arb. units
2
28
16
13
18
40
a.m.u.

Figure 3.3.

### 3.1.3. Gas Handling Line.

For this work, it was important that high purity gases could be admitted into the experimental chamber at a controlled rate. This was achieved by using a stainless steel line connected to the main chamber by a V.G. MD7 leak valve. The leak rate was controlled by the leak valve and by adjusting the effective pumping speed in the chamber. The latter was achieved by varying the position of the valve between the diffusion pump and the main chamber. It was possible to pump down the gas handling line via a separate valve to the diffusion pump. A Pirani gauge (pressure range 760 torr to 0.01 torr) and an ion gauge (pressure range $10^{-3}$ torr to $10^{-9}$ torr) were included so that a wide range of pressures could be measured. The gas handling line could be baked separately from the main chamber. The base pressure obtained in the gas handling line was $2 \times 10^{-9}$ torr. The line was backfilled with the required gas to a pressure of approximately 1 torr. All the gases used in this work were of B.O.C. research grade.

### 3.1.4. The Specimen Manipulator and Specimen Holder.

For the experiments which were performed, the specimen mounting had to fulfil a number of different functions. It had to allow rotation of the crystal about a polar angle ($0^{\circ}$ to $360^{\circ}$) and an azimuthal angle ($0^{\circ}$ to $120^{\circ}$)(see Figure 3.4). To ensure that the crystal be accurately placed at the center of the experimental system, a lateral motion of the crystal of approximately $\pm$ 1 cm in two perpendicular directions was included in the manipulator. This movement was controlled by two micrometers. It was necessary to include approximately 25 cm of vertical movement to allow the sample to be moved from one experimental level to the other. This adjustment could be used to position the sample accurately at either of the experimental levels. The bellows and the micrometer arrangement

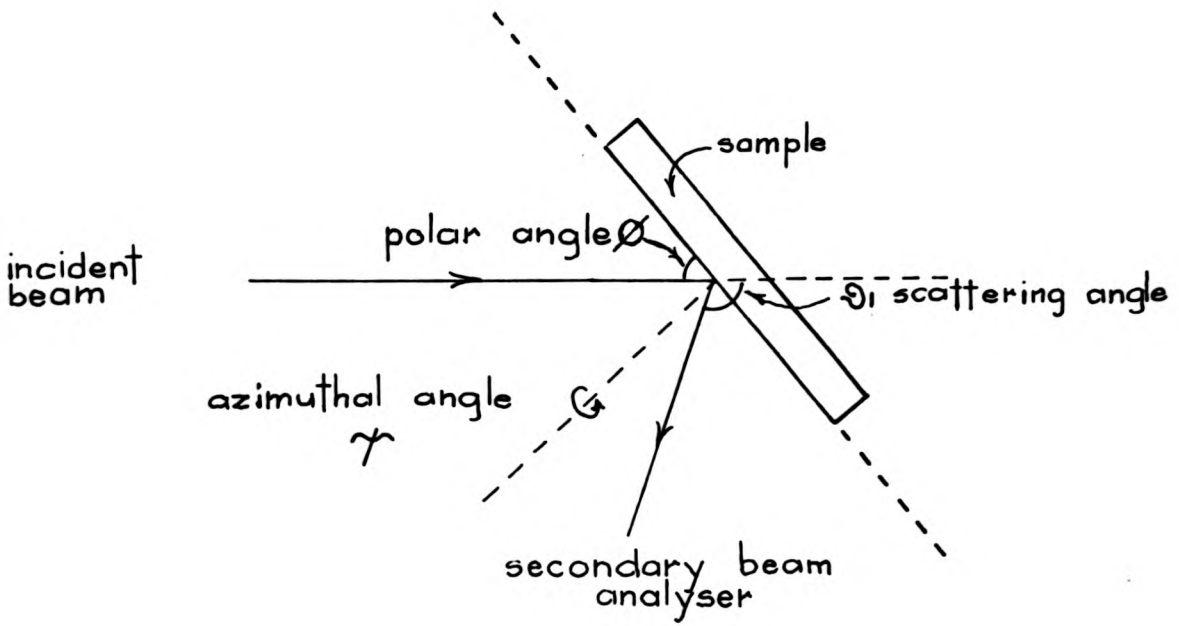
sample
polar angle ∅
incident beam
ϑi scattering angle
azimuthal angle
γ
secondary beam analyser

Figure 3.4.

can be seen in Figure 3.1.

The sample holder itself is shown in Figure 3.5. The azimuthal rotation was achieved by means of a moving wire. The wire, which was tensioned by a non-magnetic spring, turned on a pulley. The polar and azimuthal variations were obtained using a V.G. RD2. The experimental requirements for the holder were that it should be isolated from earth and be heated to a temperature of between 600 °C and 800 °C. The isolation was required so that the specimen current could be measured during ISS and AES. The isolation was produced using ceramic spacers and the resistance to earth was generally between 50 kΩ and 100 kΩ. The heating was required for specimen cleaning and annealing. Cleaning was effected by inert gas ion bombardment. The damage caused to the crystal by the bombardment was removed by annealing the crystal at a high temperature. In this design, the sample was heated by electron bombardment. A tungsten filament behind the sample was used to emit electrons. The sample was raised to a potential of +1kV to attract these electrons. An emitted electron current of approximately 10 mA was sufficient to produce the required temperature rise. Evaporation of tungsten from the filament could coat insulators and hence lower the resistance of the sample to earth. It was necessary to arrange the sample holder as shown in Figure 3.6 to reduce this problem. A chromel-alumel thermocouple was used to determine the sample temperature.

### 3.1.5. Retarding Field Analyser (R.F.A.) and LEED Gun.

It was decided to construct a 3 grid retarding field analyser (R.F.A.) for LEED similar to the standard V.G. LEED optics. This allowed the LEED patterns obtained to be compared directly with those of other experimenters. A second advantage was that it gave the possibility of performing AES at this level. Initially, the grids

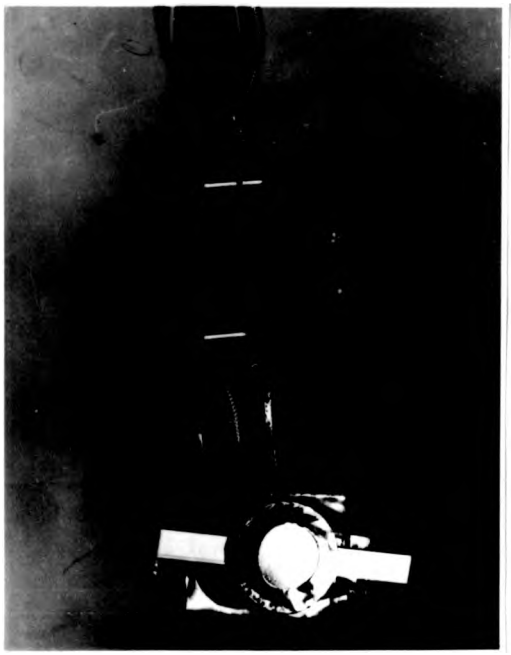

The Sample Holder

Figure 3.5.

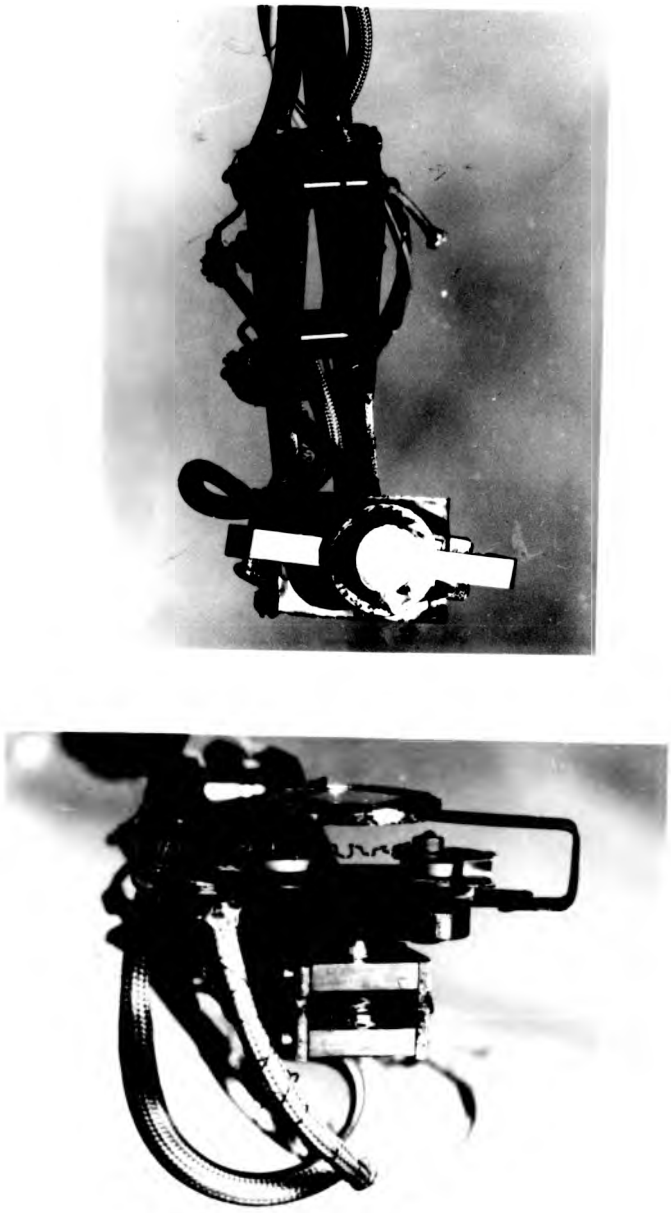

The Sample Holder

Figure 3.5.

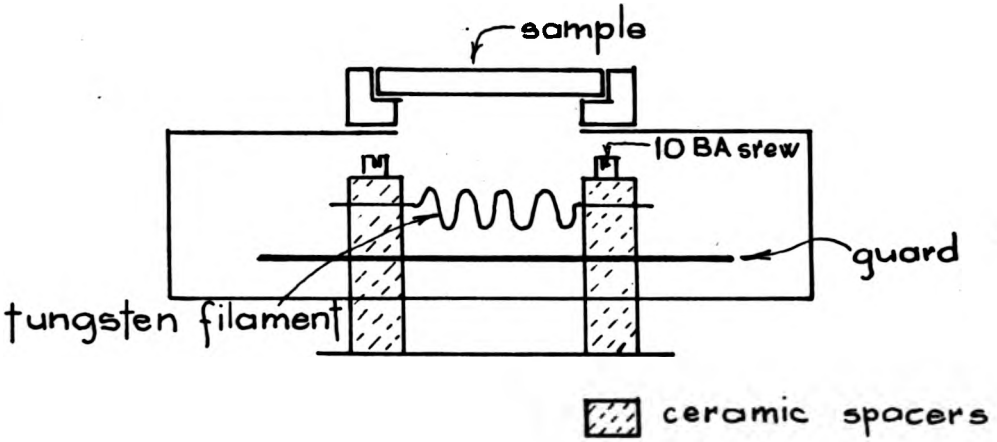
sample
10 BA screw
guard
tungsten filament
ceramic spacers

Figure 3.6.

were made from 90% transparent tungsten mesh. However, these grids did not prove sufficiently rigid. Electroplating with chromium was attempted to reduce the flexibility. Unfortunately, it was found impossible to produce successfully plated grids. The grids were finally fabricated from 75% transparent stainless steel mesh, which did not require plating to increase its rigidity. The radius of curvature required for the grids was produced by stretching the stainless steel mesh over accurately machined formers, which were made of perspex. A central hole was required to give clearance for the LEED electron gun. This hole was stamped out and flattened gold wire was used to give a smooth circumference to the hole. The phosphor screen was prepared by V.G.

The LEED gun was designed by McDonnell and consisted of a $LaB_6$ cathode, a three element lens and a set of X-Y deflection plates. These were all mounted inside a stainless steel tube, which allowed flexibility in the dimensions of the lens system. The deflection plates could be used to scan the electron beam. Three sets of perpendicular rectangular Helmholtz coils were constructed to neutralise any magnetic field in the chamber. The residual magnetic field could be detected by scanning the deflection plates to produce a crude scanning electron micrograph. The fields from the coils were adjusted until a variation in the energy of the electron beam did not effect the position of the scanning picture. From the scanning picture, it was found that the electron gun would not produce a focused beam below 30 eV. As LEED was to be used only to monitor surface order and surface structures, this was not seen as critical. A photograph of the completed R.F.A. and LEED gun can be seen in Figure 3.7.

### 3.1.6. The Cylindrical Mirror Analyser (C.M.A).

A number of different electrostatic energy analysers have been

The LEED Optics and LEED Gun.

Figure 3.7.

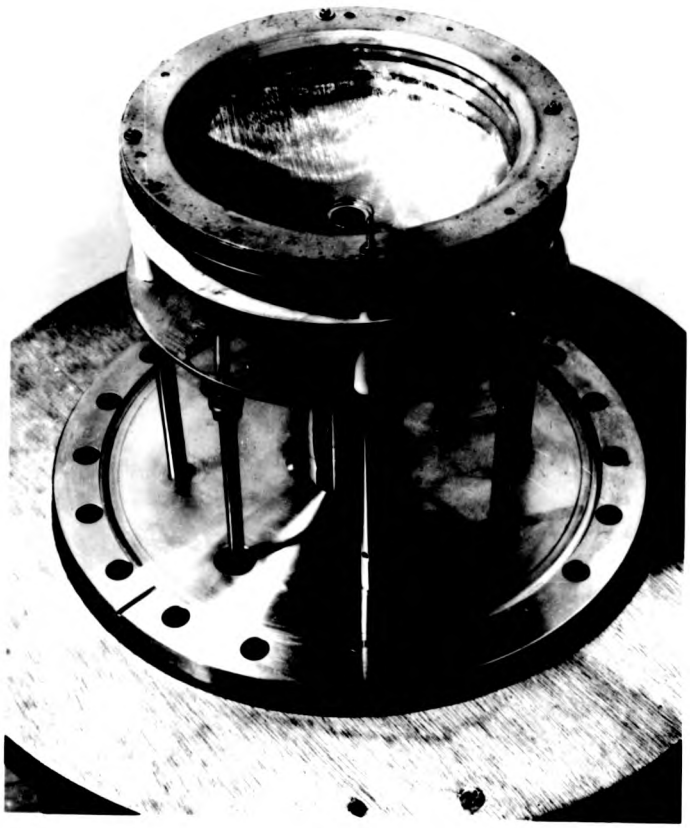

The LEED Optics and LEED Gun.

Figure 3.7.

used to study AES. Of these, the C.M.A. has become widely used for routine AES analysis and has been incorporated into a number of standard commercial Auger spectrometers. The major advantages of the C.M.A. are that it has a relatively simple and robust construction, the energy resolution ($E/\Delta E$) is typically greater than 100 and it has a high value of transmission. A full C.M.A. is able to detect electrons from a complete circular cone. The C.M.A. manufactured by V.G. has only a 120° azimuthal sector for analysis. Although this reduces the signal level by a factor of 3, it has the advantage that an electron gun can be mounted on the same 8" flange. The C.M.A. constructed for this work was similar to the V.G. C.M.A.. This type of C.M.A. was chosen because of its suitability for use with ISS in addition to AES. It was suitable for ISS as it defined the scattering angle unambiguously. Using this C.M.A., it was also possible to mount the ion source on the same 8" flange, giving a scattering angle of 120°. However, a major limitation of using a C.M.A. for an essentially angle-resolved technique was the inability to change the scattering angle without physically moving the ion source. A possible drawback of the C.M.A. is the large acceptance angle through which ions can be detected. The influence of this and other features of the experimental set-up for ISS were discussed in Chapter 2.

The major aim in choosing a C.M.A. was that both AES and ISS could be performed using the same analyser. Changing from analysing electrons to ions could be achieved by changing the sign of the voltage applied to the plates of the C.M.A.. A photograph of the completed C.M.A. is shown in Figure 3.8. The detection stage was designed to use channel plate multipliers.

Channel plate multipliers consist of a matrix of fused glass tubes. The internal diameter of the tubes is approximately 12.5 microns and their length approximately 0.5 mm. The inside of the

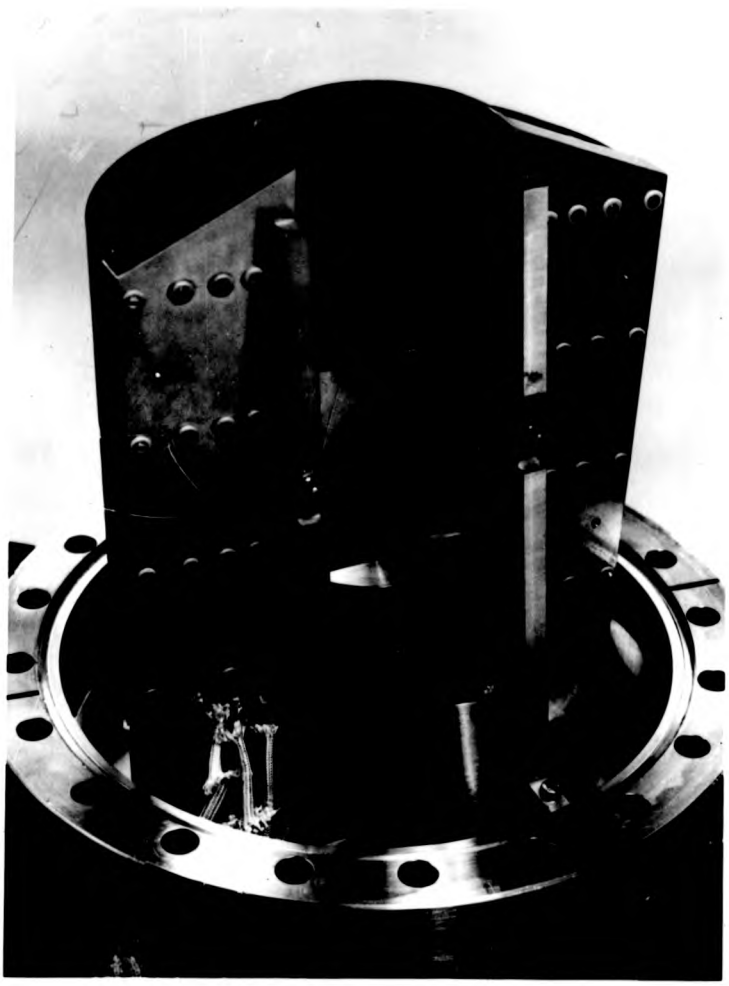

The Cylindrical Mirror Analyser (C. M. A.)

Figure 3.8.

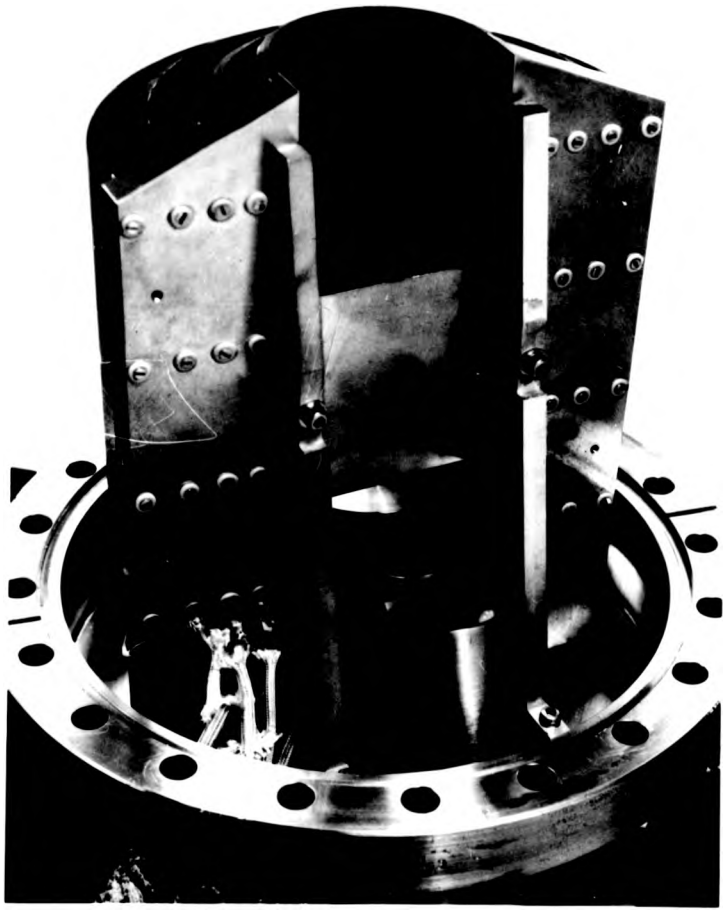

The Cylindrical Mirror Analyser (C. M. A.)

Figure 3 8.

tube is coated with high resistivity, high secondary electron emission material. A large accelerating potential is placed across the plate, such that an electric field of 3 kV/mm is present. An electron or ion of sufficient energy will cause secondary electron emission near the mouth of the tube. When the accelerating voltage gradient is sufficient to allow these electrons to cause further electron emission, a cascade is set up. As the tubes are coated throughout their length, the amplification of the device can be pictured as a continuum photomultiplier.

The gain of the device is limited by ionic feedback. This is where a secondary electron causes an ion to be formed in the tube. A positive ion is accelerated in the opposite direction to the electron. When this ion strikes the wall of the tube, further electrons may be emitted and the device becomes unstable. The maximum operating gain will clearly be dependent upon the ambient pressure in the region of the device. The gains of the channel plates used in this work were between $10^4$ and $10^6$.

In order to estimate the possible working conditions of the detection system, it can be assumed that on average a minimum number of tubes or channels involved in the operation of the plate would be one hundred and that the active area would be approximately 1 $cm^2$. The maximum output current per channel was approximately $10^{-9}$ amps, giving a maximum output current density of $10^{-6}$ amps/$cm^2$. For AES operations, the input signal was of the order of $10^{-10}$ amps/$cm^2$, hence a maximum gain of $10^4$ was found. Thus, in this work, only one channel plate was required for AES operation. The output from this channel plate was fed into a phase sensitive detector (P.S.D.) which required an analogue signal. This limited the useful gain of the channel plate to approximately $10^8$.

For ISS, the signal level was such that pulse counting techniques were required. Using the values for the experimental

parameters involved in this particular set up, it was calculated that the maximum counting rate would be $10^6$ cps. Again, this would be detected over an area of approximately 1 $cm^2$. Thus, the net current density arriving at the detection system was estimated to be $10^{-6}$ amps/cm . A gain of $10^6$ was possible before the saturation current density of $10^{-6}$ amps/$cm^2$ was reached. In order to achieve this gain, two channel plates are required. Hence, for ISS, the channel plates were operated in the saturated mode. The individual incident ions can be counted as pulses of electrons generated by the channel plates. The change from AES to ISS was achieved by biasing the channel plates with two separate external resistance chains.

A number of different mounting arrangements for the channel plates were tested and the final design is shown in Figure 3.9. It was found that the background noise level was strongly influenced by the mounting of the plates. A major problem had been the electric sparking on the plates caused by poor contacts at particular points of the channel plates. This not only caused signal noise, but also damaged the surface of the channel plates where sparking occured. Good electrical contact was achieved by using rings of annealed gold wire which were pressed on to the channel plates by spring tension. The channel plates were located by rings of machineable glass ceramic (M.G.C.). The collector used was a stainless steel disc coated with colloidal graphite which lessens the secondary electron emission. The whole assembly was mounted inside a stainless steel tube. This had the advantages of aiding easy assembly and of screening the channel plate multipliers from stray electrons or ions. Using this holder, it was possible to operate the C.M.A. for AES and ISS on a regular basis. It was found that the gain of the channel plates decreased with continued operation in a U.H.V. environment over a period of weeks. The original gain

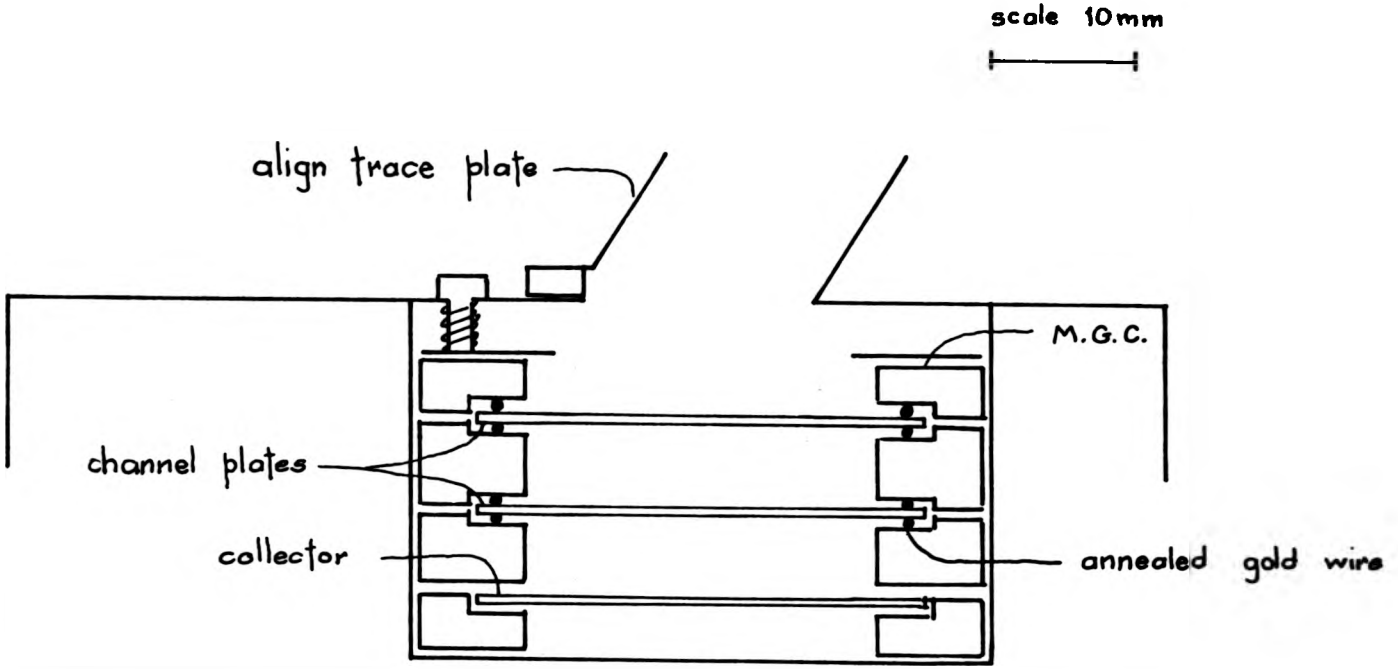


Figure 3.9. Detection System

was restored by letting the system up to atmospheric pressure.

### 3.1.7. The Mass Analysed Ion Gun.

An aim of this work was to construct a relatively straight forward ISS experimental set up. The validity of the ISS data would be largely dependent on the quality of the ion source. Thus a compromise was required between the overall complexity of the system and the need for reliable data. For simplicity, it was decided to design an ion source which would not require differential pumping. This meant that the pressure in the target chamber would be high during the operation of the gun. A maximum value for the pressure was taken as $1 \times 10^{-6}$ torr. Thus, it was important that the supply of inert gas to the ion gun was of high purity. This was ensured by using a bakeable gas handling line as has been previously mentioned (see section 3.1.3). The purity of research grade B.O.C. gases is better than 99.99%. Thus, a pressure of $1 \times 10^{-6}$ torr of inert gas gives a level of approximately $1 \times 10^{-10}$ torr for the contaminate gases.

One of the simplest types of ion source which can operate in this pressure region is an inverted Bayard-Alpert gauge. This source has a filament to emit electrons. These electrons are attracted to a grid and ionise gas atoms in this region. The energy of these electrons is usually much higher than the first ionisation potentials of gas atoms (e.g. 24.5 eV for He). The electron energy used in this work was approximately 60 eV. At this value, the ratio between the ionisation cross-sections for helium and carbon monoxide is approximately 1:10 (1). Thus, the percentage contamination in the ion beam is greater than the percentage contamination in the gases. In order to reduce this level of contamination, mass analysis of the beam must be used.

An ion gun based on the Bayard-Alpert gauge, as designed by Pittaway (2), was constructed. However, this source did not prove

satisfactory as the ion current at the target was unstable and the level of the current was unacceptably low. It was therefore decided that the problems of designing an efficient ion source and mass analyser would best be overcome by modifying a commercial mass spectrometer. Large magnetic fields would have been undesireabe and so a quadrupole mass spectrometer was chosen. A further consideration was that to vary the scattering angle, it was necessary to move the ion gun. Thus, the complete assembly was designed to mount on a $2\frac{3}{4}$" flange. A V.G. Q4 quadrupole mass spectrometer was used as the size of the rods was compatible with the clearance given by a $2\frac{3}{4}$" flange. The mass range available was 0-60 amu, which is adequate for the type of ions used in ISS. The mass filter was able to reject about $1:10^3$ gas ions, which would improve the purity of the beam significantly.

The mass spectrometer was inverted and the ion collector replaced by a three element lens and deflection plates. The energy of the ion beam was achieved by 'floating' the source region and quadrupole rods negatively with respect to earth. The ions which passed through the mass spectrometer were accelerated towards the first element of the lens, which was held at earth potential.

The spot size of the beam was estimated by deflecting the beam along a rectangular target. The beam was tracked along the sides of the rectangle to calibrate the deflection plates. The amount of deflection required to reduce the target current to zero from maximum was then measured and the spot size estimated. The value for the spot size obtained was 5mm. This value was confirmed by using the scanning electronics on the deflection plates. From the resolution obtained in the scanning picture, it was possible to estimate the beam size.

The energy spread of the ion gun was measured by placing a stainless steel mesh in front of the target and ramping the mesh

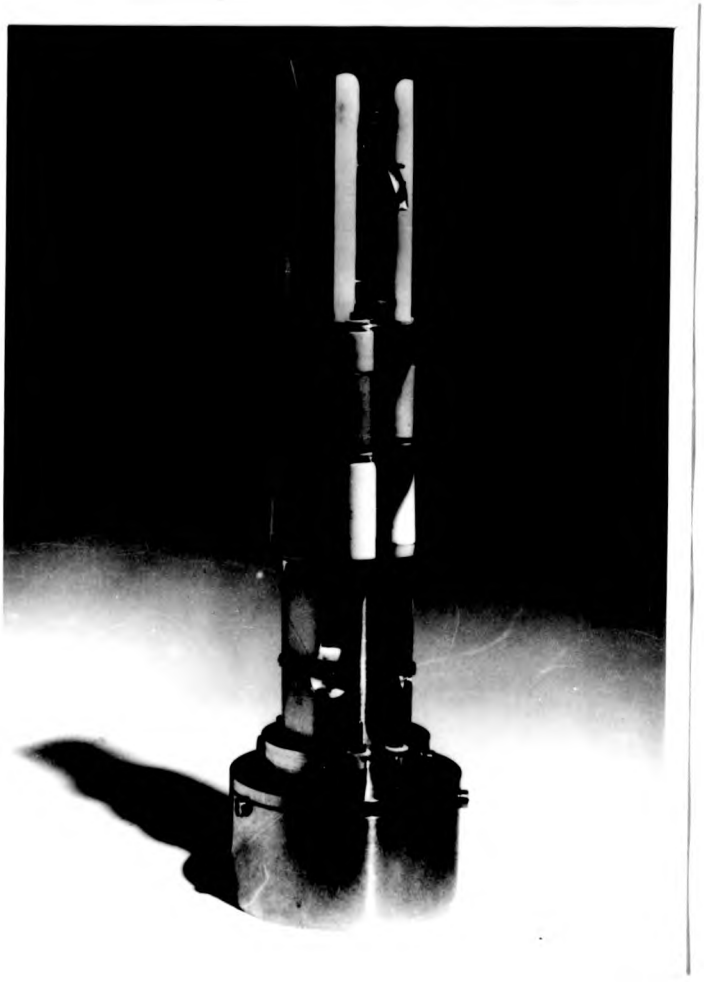

The Mass Analysed Ion Gun

Figure 3.10.

The Mass Analysed Ion Gun

Figure 3.10.

with a positive voltage in order to repel the incident ions. The current arriving at the target was detected. The value obtained for the energy spread was approximately 5 eV for a 1.0 keV beam of helium ions. The dependence of the beam current on the background pressure was also investigated. It was not possible to measure the pressure in the source region of the ion gun directly, so an ion gauge was placed in the gas line leading to the gun. There was also an ion gauge in the main target chamber. The calculated conductance between the source region and these ion gauges showed that the ion gauge in the target chamber gave a better measure of the source pressure and that the value of the pressure in the source region was likely to be a factor of ten greater than the target pressure. A beam current of between $1x10^{-9}$ amps and $2.5x10^{-9}$ amps was achieved with a target chamber pressure of $2x10^{-7}$ torr between ion energies of 0.5 keV and 1.5 keV. The beam current increased in an approximately linear manner between pressures of $7x10^{-8}$ torr and $5x10^{-7}$ torr. The insulation of the ion source electronics was insufficient to allow beam energies of greater than 1.5 keV. A photograph of the completed ion gun is shown in Figure 3.10.

## 3.2. The Electronic Configuration.

A major aim of this project was to allow for rapid analysis of surfaces using the three techniques available. Hence, an important feature of the apparatus was the ability to change quickly from one technique to another. This was achieved by using a number of common power supplies for the different modes of operation. The electronics required for each technique will be dealt with in turn.

### 3.2.1. LEED.

A schematic diagram of the arrangement used for LEED is shown

in Figure 3.11. For LEED, an electron beam of an energy between 0 eV and 300 eV, with a beam current of approximately 1 $\mu$A and a spot size of less than 1 mm are required. As previously stated, the LEED gun used here was designed by McDonnell. The first element of the lens system was used to extract electrons from the source region to give an acceptable beam current at low energies. The focusing conditions of the lens system were dependent on the energy of the beam. Thus, it was necessary to allow for a variation in the beam energy and focusing conditions whilst viewing the LEED pattern. The filament supply (Coutant LB100) was a fully floating variable 0-10 volt and 0-10 amp d.c. output supply. The lens potentials were derived from two 0-300 volt d.c. supplies in series (A.P.T. Ltd.). The remote variation of the lens supplies was produced using two 100 k$\Omega$ potentiometers. The accelerating potential for the beam energy was derived from a 0-1.5 keV supply (NM120: J&P Ltd.). The output voltage of the NM120 could be programmed. The input voltage required was obtained from a 1.5 V battery ramp.

The position of the electron beam on the target could be controlled by the use of the scanning electronics as previously mentioned. A d.c. shift voltage and a variable level sawtooth voltage were applied to the deflection plates of the electron gun. This had the effect of scanning the electron beam across the target. The current arriving at the target was used to drive the Z-mod of an oscilloscope with the scanning voltages applied to the X and Y axes. The picture produced was used to determine the focusing conditions of the gun. The picture was also used to ensure that the centre of the sample was located at the optimum position with respect to the LEED optics.

The electrons scattered from the target travelled towards the analyser in a field free space as the first grid (G4) was held at earth potential. The electrons were then retarded by two grids (G2/G3).

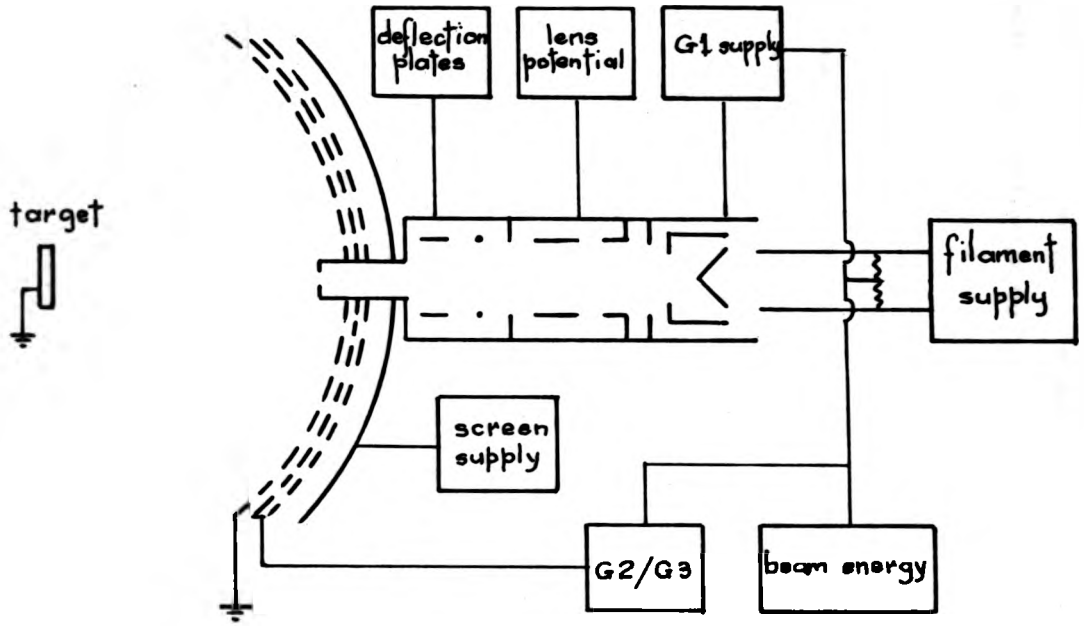
target
deflection plates
lens potential
G1 supply
filament supply
screen supply
G2/G3
beam energy

Figure 3.11.

The voltage of these grids was set a small variable amount (approximately 7 V) below the beam energy. This allowed only the elastic and quasi-elastic electrons to be accelerated towards the phosphor screen. The contrast of the LEED pattern could be adjusted by the bias set on the G2/G3 grids.

The residual magnetic fields were neutralised by using Helmholtz coils. These consisted of three sets of coils (0.75 m square) of 60 turns of copper wire wound on to aluminium formers. Three separately variable d.c. supplies (0-15 V, 0-3 A) were constructed for use with the coils. When no magnetic field was present, a variation in the energy of the LEED gun would have no effect on the position of the specular reflection of the electron beam. This criterion was used to neutralise the residual magnetic field in the chamber.

Using this experimental arrangement for LEED, it was possible to produce LEED patterns from clean and adsorbate surfaces down to a beam energy of 60 eV.

### 3.2.2. AES.

A schematic diagram of the arrangement used in this work for AES is shown in Figure 3.12. For AES, an electron beam of 1.0 keV to 3.0 keV with a beam current of 1 $\mu$A and a spot size of less than one millimetre can be used. The electron gun used here was a Superior Electronics SE/3K/5U with a tungsten filament. The filament supply used was the same as for the LEED gun. The beam energy and the focusing potential were obtained from a 0-10 kV power supply (V.G. 180 series). The effective source size could be varied by the use of the Wehneldt cylinder (G1). The potential on this electrode could be varied and this had the effect of changing the size of the hole through which electrons could be transmitted. This potential was produced by a 90 V battery floated by the beam

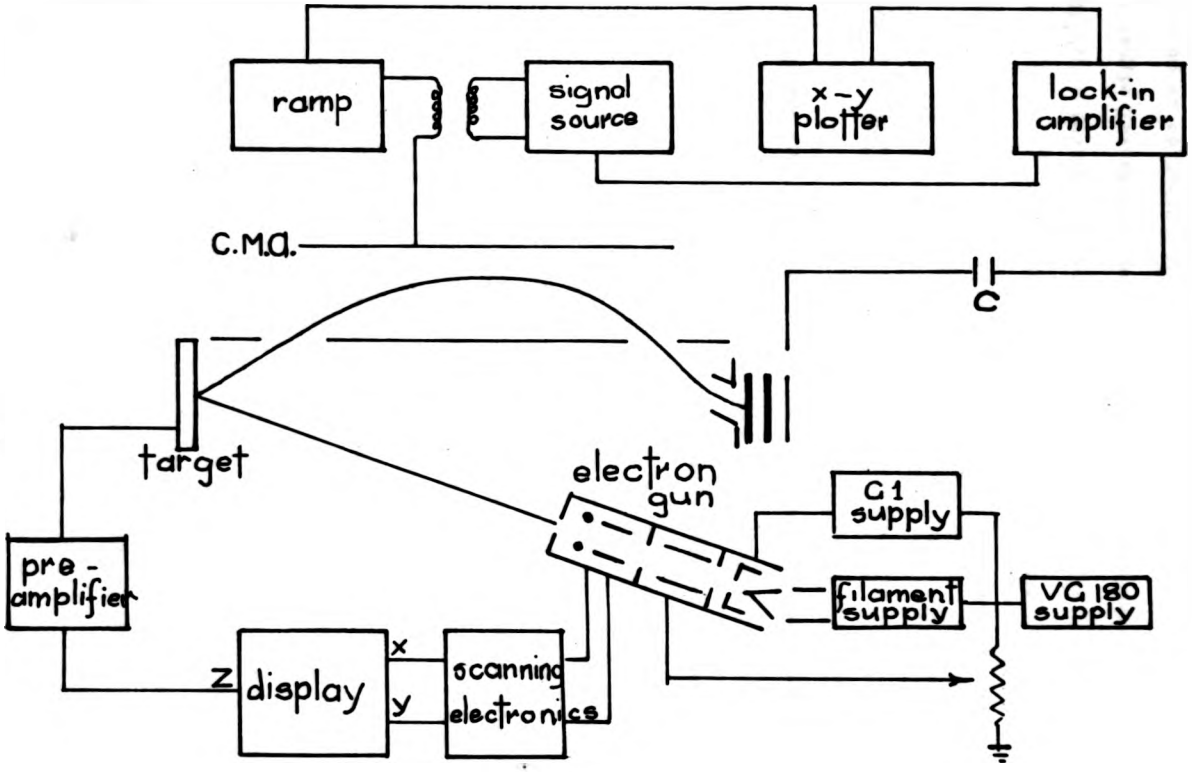
ramp
signal source
x-y plotter
lock-in amplifier
C.M.A.
C
target
electron gun
G1 supply
pre-amplifier
filament supply
VG 180 supply
z
display
x
y
scanning electronics

Figure 3.12.

energy. The position of the beam on the target was controlled by the scanning electronics used for the LEED gun.

For AES, the electrons emitted from the target were analysed using the C.M.A. An energy scan was produced by ramping the voltages on the plates of the C.M.A.. The supply used for this was the J&P:NM 120 used for the LEED gun beam energy. The ramp speed was variable between 1 kV/sec and less than 1 V/sec. The design of the J&P:NM 120 did not allow faster ramp speeds. The voltages for the plates were provided by a resistor chain. The C.M.A. included an 'align trace' electrostatic deflection plate. This was used to adjust the position of the analysed beam with respect to the detection system. The J&P:NM 120 was used to ramp the align trace plate together with the C.M.A. plates. The align trace potential was completely variable within the range of the ramp.

A modulation of 2 kHz with an amplitude of up to 5 V peak to peak (Brookdeal Signal Source) was superimposed on the outer plate of the C.M.A. via an isolating transformer.

Taylor's theorem states that

$$f(x + \Delta x) = f(x) + \Delta x f'(x) + \frac{\Delta x^2 f''(x)}{2!} + \ldots\ldots\ldots$$

In this case, we have a small voltage variation of $\Delta x = k\sin wt$, and so terms with $\Delta x^3$ and above can be ignored. Thus,

$$f(x + k\sin wt) = f(x) + k\sin wt.f'(x) + \frac{k^2\sin^2 wt}{2}.f''(x)$$

but, $\sin^2 wt = \frac{1}{2} - \frac{1}{2}\cos 2wt$. Thus,

$$f(x + k\sin wt) = f(x) + k\sin wt.f'(x) - \frac{k^2 f''(x)}{4}(\cos 2wt - 1)$$

For the C.M.A., where N(E) is equivalent to f(x)

$$N(E + \Delta E) = N(E) + k\sin wt.N'(E) - \frac{k^2}{4}(\cos 2wt - 1)N''(E)$$

Thus, if the amplitude of the in-phase fundamental signal is measured for such a modulation, the $N'(E)$ distribution is obtained. A lock-in amplifier (Brookdeal Lock-In 9501) was used for this purpose. In AES, where there is a large slowly varying background level, this differentiation helps to resolve the extra features

caused by Auger emission. The voltages required for the detection system were obtained from a 0-10 kV (V.G. 180 series).

### 3.2.3. ISS.

A schematic diagram of the arrangement used for ISS in this work is shown in Figure 3.13. The ion source used for ISS was described in section 3.1.7. The electronics supplied with the Q4 used as a mass spectrometer were modified to operate the ion gun. The accelerating potential and focussing potential for the gun were obtained from a 0-10 kV supply (V.G. 180 series). As the beam current was much lower for the ion gun compared with the electron guns, the scanning electronics could only be used at a much slower scanning rate. The required speed was such that one complete scan of the ion gun took approximately 10 seconds. Thus, a scanning 'picture' could only be obtained by using a long exposure photograph. However, for routine use, simple d.c. voltages were applied to the deflection plates of the ion source.

The C.M.A. was used to analyse the signal in the ISS mode. The J&P:NM 120 was modified so that its polarity could be changed easily. Thus, the same supply was used for AES and ISS. The voltages required for the detection system were derived from a 0-10 kV supply (V.G. 180 series). The pulses produced from the channel plates were amplified (Brookdeal Fast Preamplifier) before being fed into the counting electronics (Brookdeal Photon Counting System). In order to produce a workable signal to noise ratio, the ramp speed used was approximately 1 V/sec. A complete energy scan required approximately 1000 seconds. However, it was generally only necessary to scan a small part of the spectrum in order to measure the ISS peaks. Any variation in the beam current arriving at the specimen would effect the value of the signal obtained. Thus, it was important to normalise the ISS signal. This was achieved

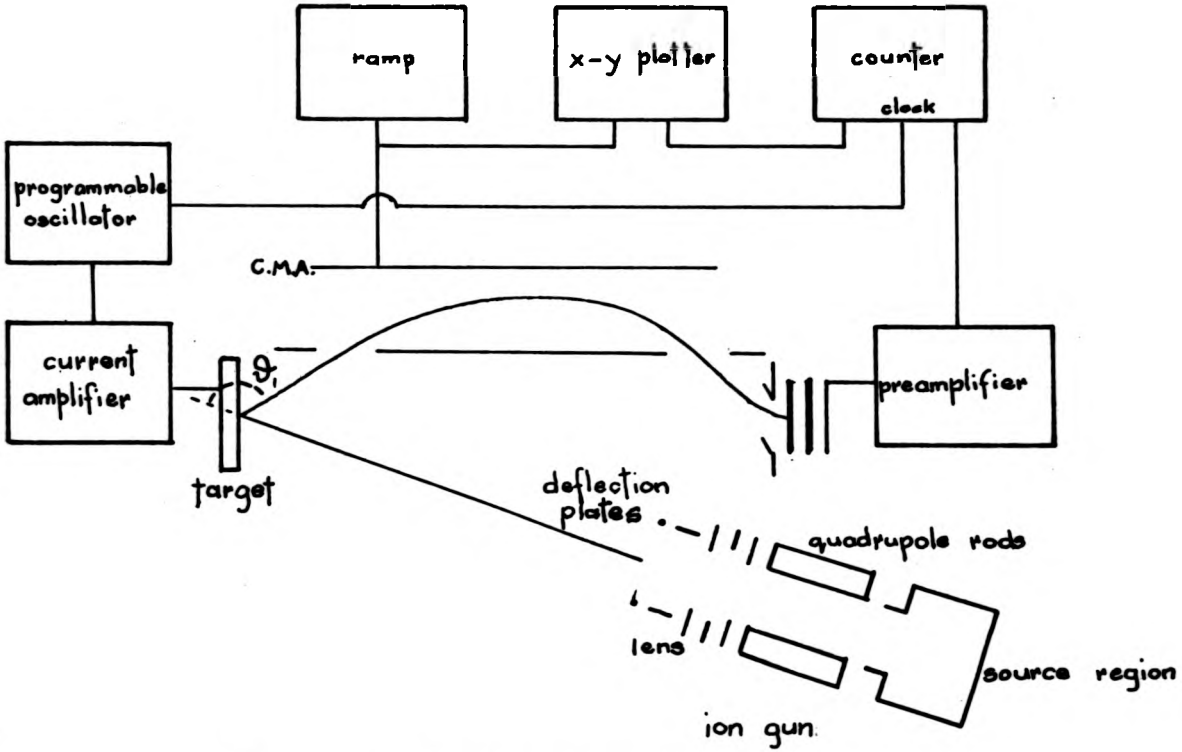


Figure 3.13. Arrangement for ISS.

by converting the specimen current into a voltage. This voltage was fed into a voltage controlled signal source. The frequency of the signal source was used as a clock pulse for the Photon Counting System. Thus, the output used for the ISS results was proportional to the number of counts produced per incident ion.

# Chapter 4.

## An ISS Study of Clean and Oxygen Adsorbed Cu(100).

### Introduction.

Once the experimental system had been successfully completed, a study of clean Cu(100) and the oxygen adsorbed Cu(100) surfaces was undertaken. There were two major reasons for this. Firstly, it allowed the experimental set-up to be tested and, secondly, it was hoped that further understanding of the adsorption of oxygen on Cu(100) would be gained. It was found that the ISS yield was low on heavily contaminated surfaces. In fact, single scattering events from 1.0 keV $He^+$ were not detected until a partially clean surface was obtained. Further, in order to test the experimental arrangement, a well-characterised surface was essential. Thus, before any ISS experiments could be attempted, the production of a clean, well-ordered surface was necessary.

### 4.1. Cleaning Cu(100).

The Cu(100) specimen was prepared from a single crystal rod (99.999% purity - Metals Research Ltd.) of random orientation. The rod was oriented by X-ray Laue back-reflection to within $1^\circ$ of the desired crystal plane. A slice was cut from the rod using spark erosion. The sample was then mechanically polished using diamond paste of progressively smaller particle size ($\frac{1}{4}\mu m$ being the finest paste). After this, the specimen was electropolished in a solution of orthophosphoric acid and sulphuric acid. Once a satisfactory finish had been obtained, the specimen was mounted in the sample holder and degreased using trichloroethylene before being placed in the experimental system.

An AES spectrum of an 'as loaded' Cu(100) specimen that had been baked and outgassed, but not subjected to any other treatment,

is shown in Figure 4.1. The major surface contaminants which can be seen in the spectrum are carbon, oxygen and sulphur. The carbon and oxygen are due mainly to the presence of carbon monoxide and carbon dioxide in the residual gases of the chamber. The sulphur concentration was increased by the outgassing procedure. Hence, the sulphur was assumed to have segregated from the bulk of the copper crystal.

A clean, well-ordered surface was obtained using a combination of argon ion bombardment and high temperature annealing. The argon ion gun was based on a conventional ion gauge. The main chamber was filled with argon up to a pressure of approximately $2 \times 10^{-4}$ torr. The gun produced a variable energy beam with a current density of approximately 1 $\mu A/cm^2$. For this work, an energy of between 350 eV and 450 eV for the ion beam was used. It was necessary to outgas the ion gun thoroughly before use in order to minimise the possibility of contamination by residual gas ions in the beam. High purity argon (BOC Ltd. - Grade X) was used and a typical mass spectrum of the gases in the system during bombardment isshown in Figure 4.2. A dynamic flow of gas was achieved by partially valving off the diffusion pump and continuously leaking argon into the system. The diffusion pump was used to pump away the argon after a bombardment. The ion pump was not restarted until the pressure in the main chamber was in the $10^{-9}$ torr region. It was usually possible to achieve a pressure of about $5 \times 10^{-10}$ torr within two minutes of the end of a bombardment.

In order to obtain a sharp LEED pattern, the 'as bombarded' surfaces were annealed. Two procedures were used for this purpose. Firstly, the method used by McDonnell and Woodruff (1) was used. Here, the sample is heated to 450 $^{o}$C. This low temperature annealing is to lessen the amount of sulphur segregation. However, it was found that after a number of cycles, it was possible to

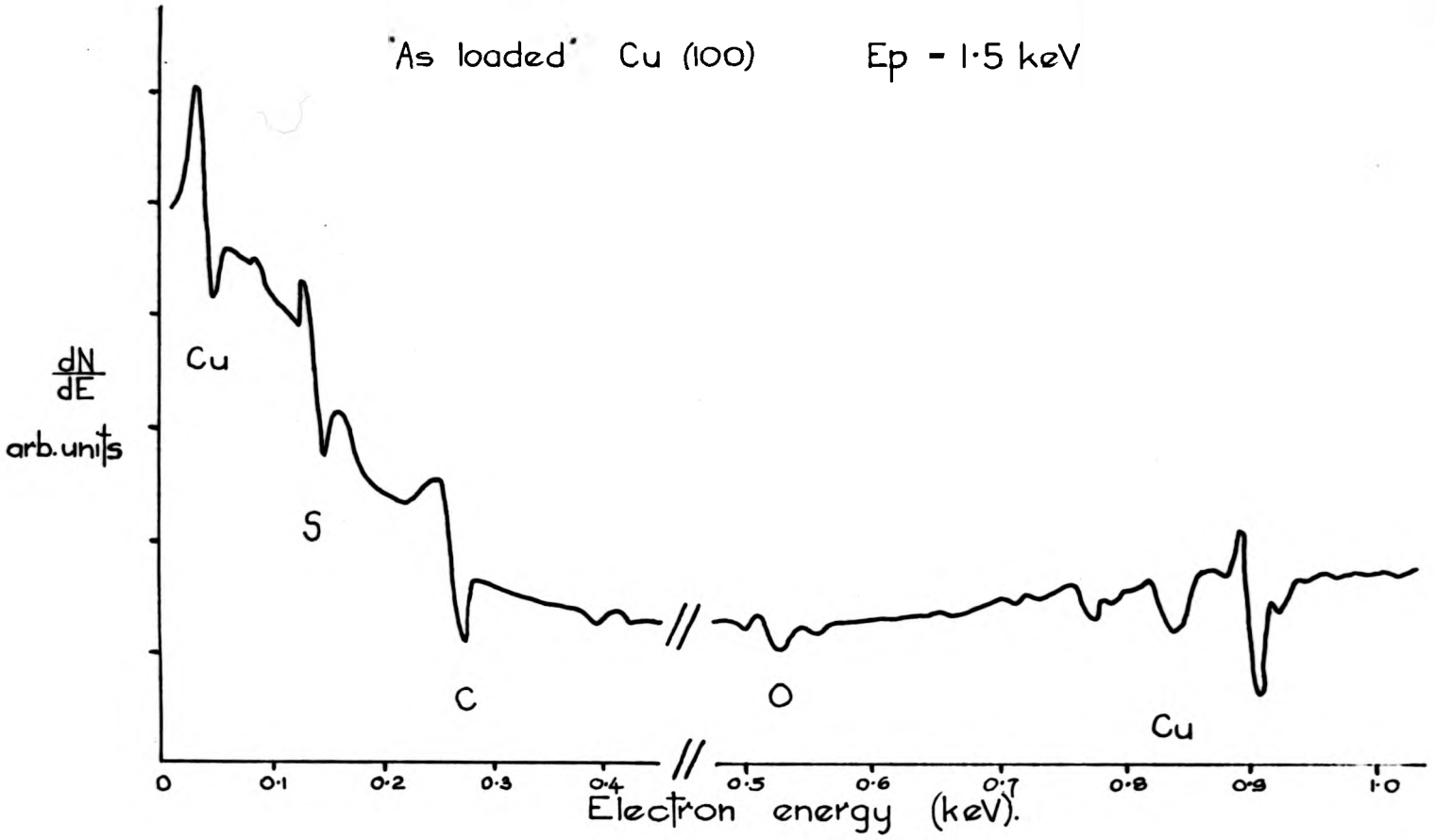
'As loaded' Cu (100) Ep - 1·5 keV
dN/dE
arb. units
Cu
S
C
O
Cu
0
0·1
0·2
0·3
0·4
0·5
0·6
0·7
0·8
0·9
1·0
Electron energy (keV).

Figure 4.1.

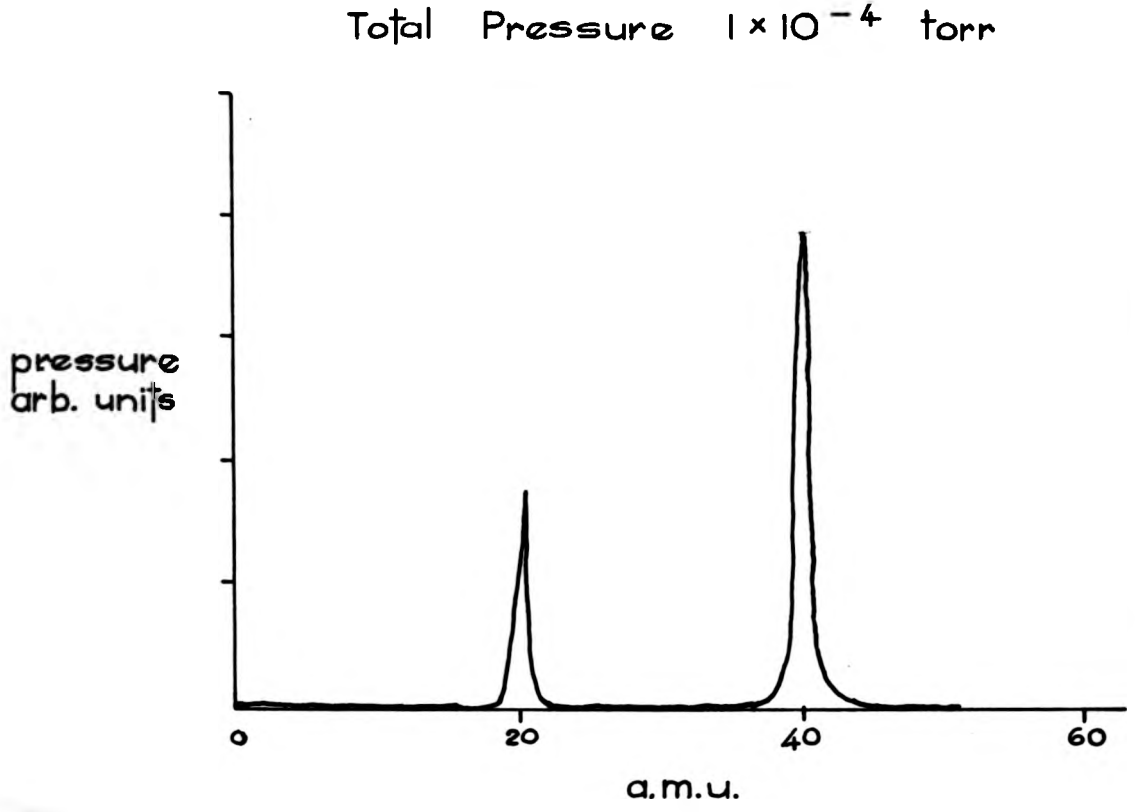


Figure 4.2.

anneal the specimen to a temperature of 800 °C without detectable sulphur contamination. Thus, a second method, involving higher temperature annealing,was used. This technique produced LEED patterns with a lower background intensity than the first method. However, it was not possible to produce LEED patterns which were as distinct as those obtained from Ni(100). This may be due to residual damage in the Cu(100) which has not been removed by the annealing. It is this second method which has been used throughout the work reported in this chapter.

A clean, well-ordered Cu(100) surface was produced by using cycles of one hour bombardment followed by annealing for five minutes. It was necessary to cycle the crystal approximately 10-15 times before a clean, well-ordered surface was produced from an 'as loaded' sample. However, once the specimen had been initially cleaned, subsequent contamination and adsorbed oxygen could be removed by one or two cleaning cycles. A LEED pattern of clean Cu(100) is shown in Figure 4.3. The nomenclature used for the beams is shown in this figure, as is the azimuthal angle.

An AES spectrum of clean Cu(100) is shown in Figure 4.4. It was possible to detect carbon contamination up to a level where the ratio of the 60 eV copper peak height to the 272 eV carbon peak height was 200:1. This corresponds to a coverage of carbon of less than 0.01 monolayers (2). It was not possible to detect sulphur contamination after the first few cleaning cycles. Hence, its coverage was likely to be less than the coverage of carbon as the sensitivity of AES to these two elements is similar.

## 4.2. Characterisation Experiments for ISS using Helium Ions.

Having obtained a clean, well-ordered Cu(100) surface, the study of the instrumental effects of this particular ISS arrangement was begun. The experiments were carried out with a

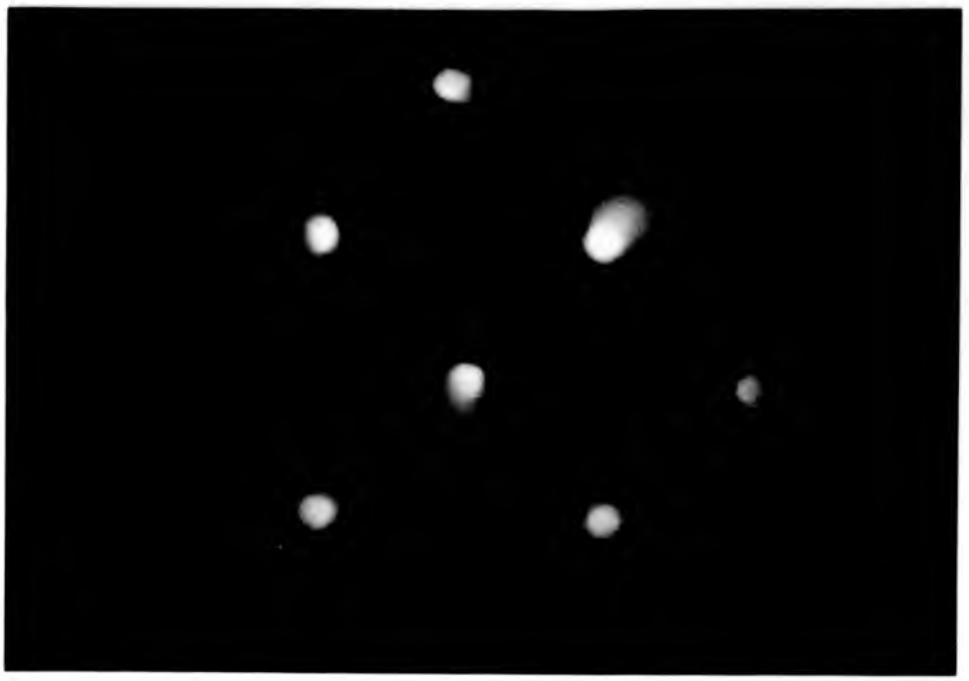

Clean Cu (100)

Electron energy ≃ 100 eV

$\bar{1}1$

$\bar{1}0$ $0\bar{1}$

$\bar{1}\bar{1}$ $00$ $11$ $\rightarrow \chi = 45°$

$0\bar{1}$ $10$

Figure 4.3.

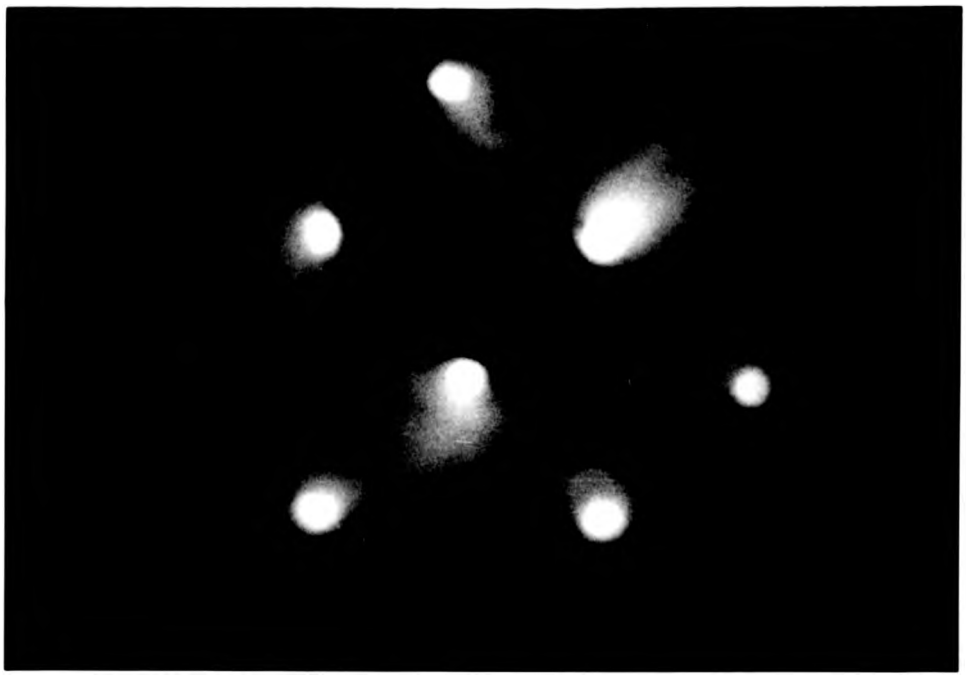

Clean Cu (100)

Electron energy ≃ 100 eV

$\bar{1}\dot{1}$

$\bar{1}\dot{0}$ $0\dot{1}$

$\bar{1}\dot{1}$ $0\dot{0}$ $1\dot{1}$ $\rightarrow \chi = 45°$

$0\dot{\bar{1}}$ $1\dot{0}$

Figure 4.3.

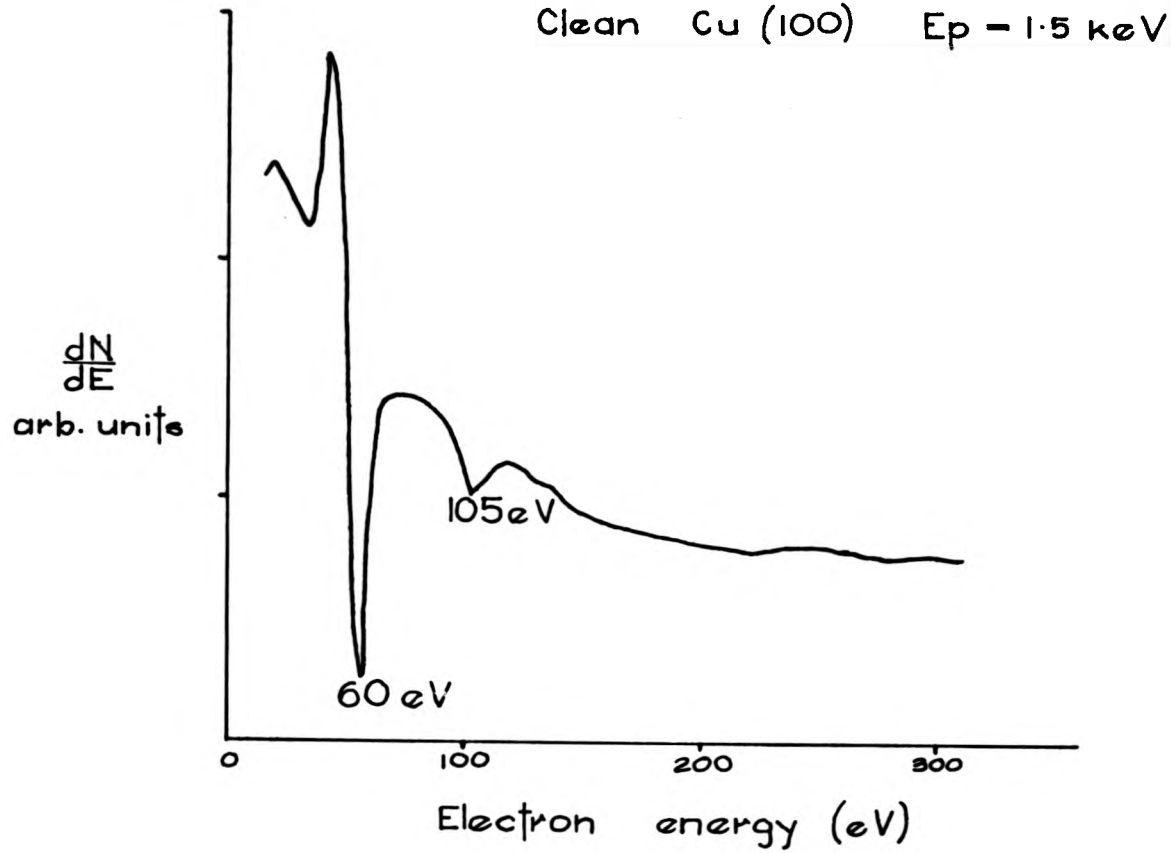
Clean Cu (100) Ep = 1·5 keV
dN/dE
arb. units
105eV
60 eV
0
100
200
300
Electron energy (eV)

Figure 4.4.

fixed scattering angle of 90°. A clean Cu(100) ISS spectrum for 1.0 keV helium ions scattered over 90° is shown in Figure 4.5. The major feature is caused by helium ions singly scattered from copper atoms. There is also a small peak at low energies which is caused by ions sputtered from the surface.

A number of the experimental parameters can be varied in order to investigate the effects of the set-up. For example, the width and intensity of the singly scattered helium peak at various incident energies were measured. Figure 4.6 shows the variation of the half width of the copper peak with energy. It can be seen that the relationship between the half width and the energy is approximately linear. For 90° scattering of a 1.0 keV $He^+$ beam, the half width is approximately 24 volts. This effectively corresponds to scattering from a mass number between 57 and 70. This shows that the mass resolution of the system is quite low. As was shown in Table 2.1, the angle of acceptance of the C.M.A. ( $\pm$ 6°) causes a maximum possible variation approximately equal to the experimentally measured half width. Hence, the half width caused by the acceptance angle of the analyser will be less than the total experimental half width. Thus, the experimental half width must be increased by other factors. One of these will be the energy spread of the incident ion beam, which was measured as 5 eV. This value can also be inferred from Figure 4.6, where the extrapolated half width at zero beam energy is approximately 5 eV. As a high mass resolution was not of particular interest in this work, this overall level of half width was acceptable.

An important measurement in ISS is the scattered ion yield. In order to obtain an accurate value for this, a measurement of the area under the peak is needed. However, as already noted, the output signal of the C.M.A. is proportional to E.N(E) rather than N(E). Thus, the sensitivity of the analyser is proportional to the energy

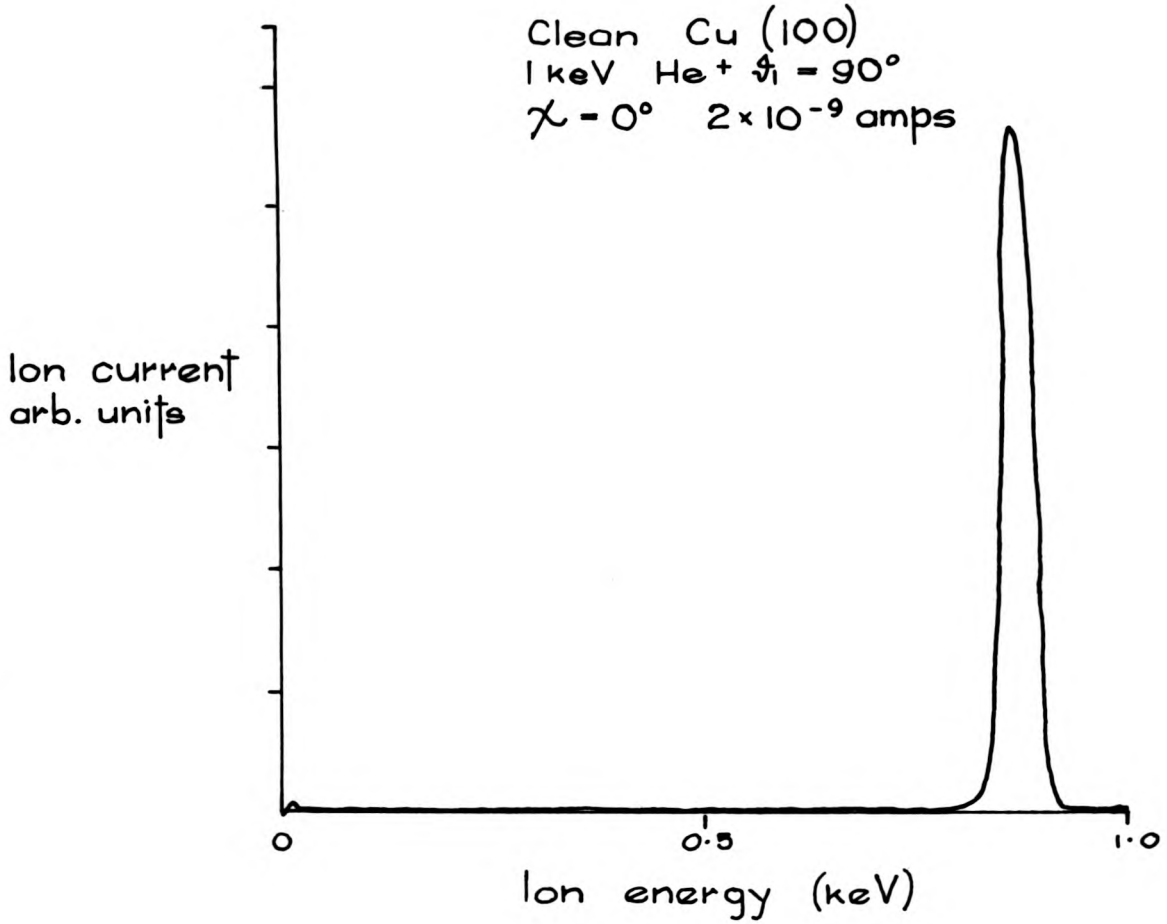
Clean Cu (100)
1 keV He+ $\vartheta_i = 90°$
$\chi = 0°$ $2 \times 10^{-9}$ amps
Ion current
arb. units
0
0·5
1·0
Ion energy (keV)

Figure 4.5.

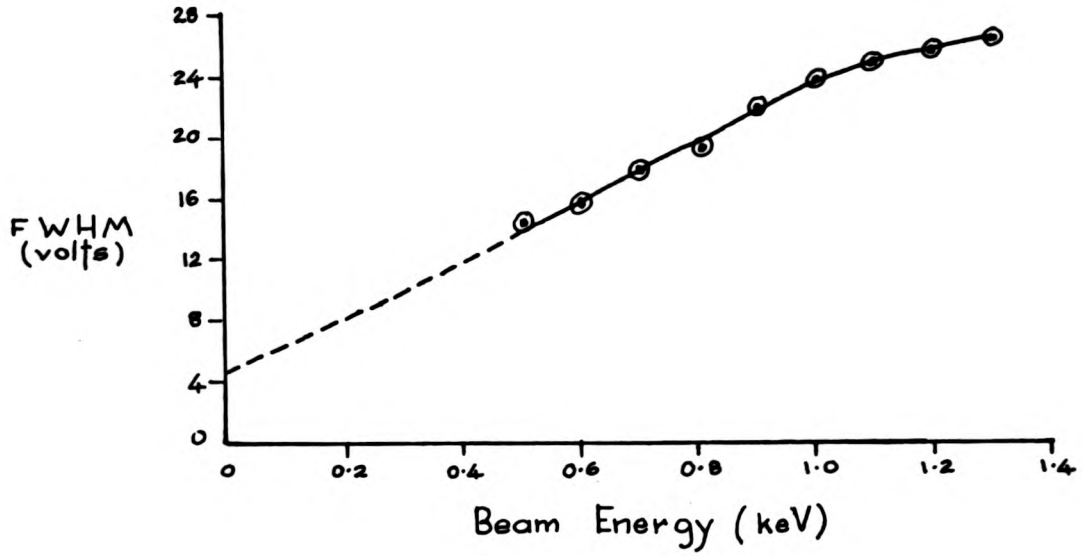
FWHM
(volts)
28
24
20
16
12
8
4
0
0
0·2
0·4
0·6
0·8
1·0
1·2
1·4
Beam Energy (keV)

Figure 4.6.

analysed. However, from Figure 4.6, the half width of the peak is also approximately proportional to the energy. Thus, as the analyser becomes more sensitive, the peaks become wider. Therefore, the total scattered yield is proportional to the height of the peak. Throughout this work, the scattered yield has been measured using peak heights.

The form of the yield curve found for helium ions is shown in Figure 4.7. The shape of the curve is similar to that obtained by Smith (3). A maximum is found at approximately 700 eV. The maximum is caused by the fact that although the cross-section is found to be inversely proportional to the energy (4), the probability of neutralisation decreases with increasing energy. Hence, a maximum will occur at a particular energy where these two effects are balanced. A number of experiments were performed with varying beam energy to determine whether there were any important energy effects. In general, the experimental data were found to be quite insensitive to the beam energy. In fact, although the maximum ion yield is obtained at 700 eV, the beam current produced by the ion gun is proportionately higher at 1.0 keV. Thus, most experiments were performed at a beam energy of 1.0 keV.

One of the possible sources of error in the experimental arrangement was in the wide acceptance angle out of the plane of scattering of the analyser. This angle was approximately $\pm 60^{o}$. The effect of this was studied by using a removeable aperture between the sample and the C.M.A. which would effectively lower the acceptance angle of the analyser to $\pm 5^{o}$. A diagram of the experimental arrangement is shown in Figure 4.8a. The electron gun used for AES was used to produce a scanning picture of the sample with the slit positioned in front of the target. As the size of the slit arrangement was known, the scanning picture could be calibrated. It was possible to move the slit vertically in front of the sample and also to move it away from the sample. The maximum peak height with the slit in position

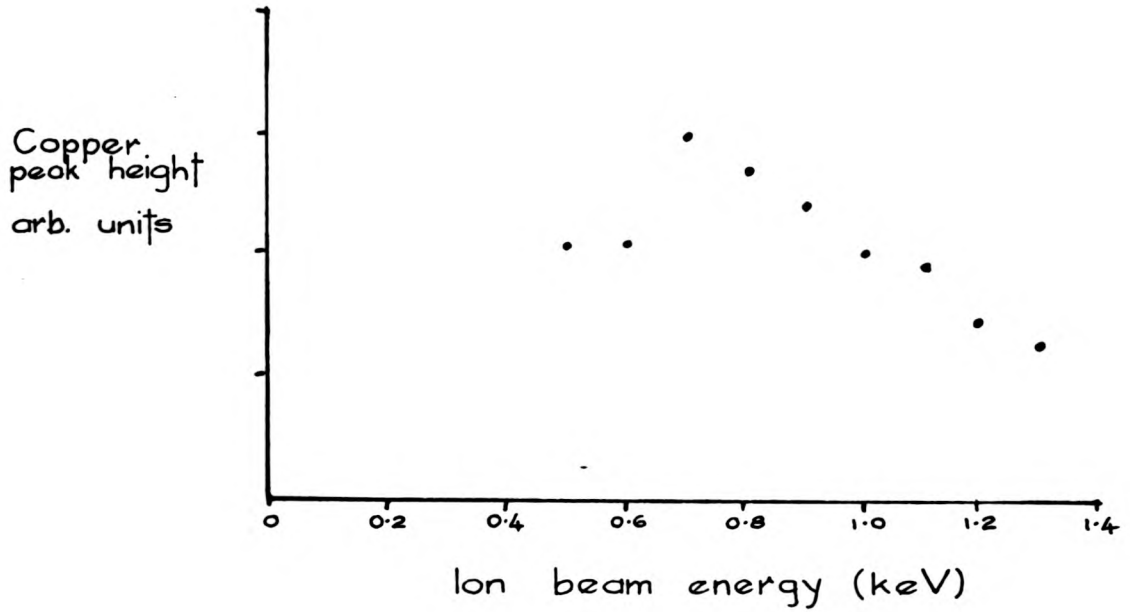
Copper
peak height
arb. units
0
0·2
0·4
0·6
0·8
1·0
1·2
1·4
Ion beam energy (keV)

Figure 4.7.

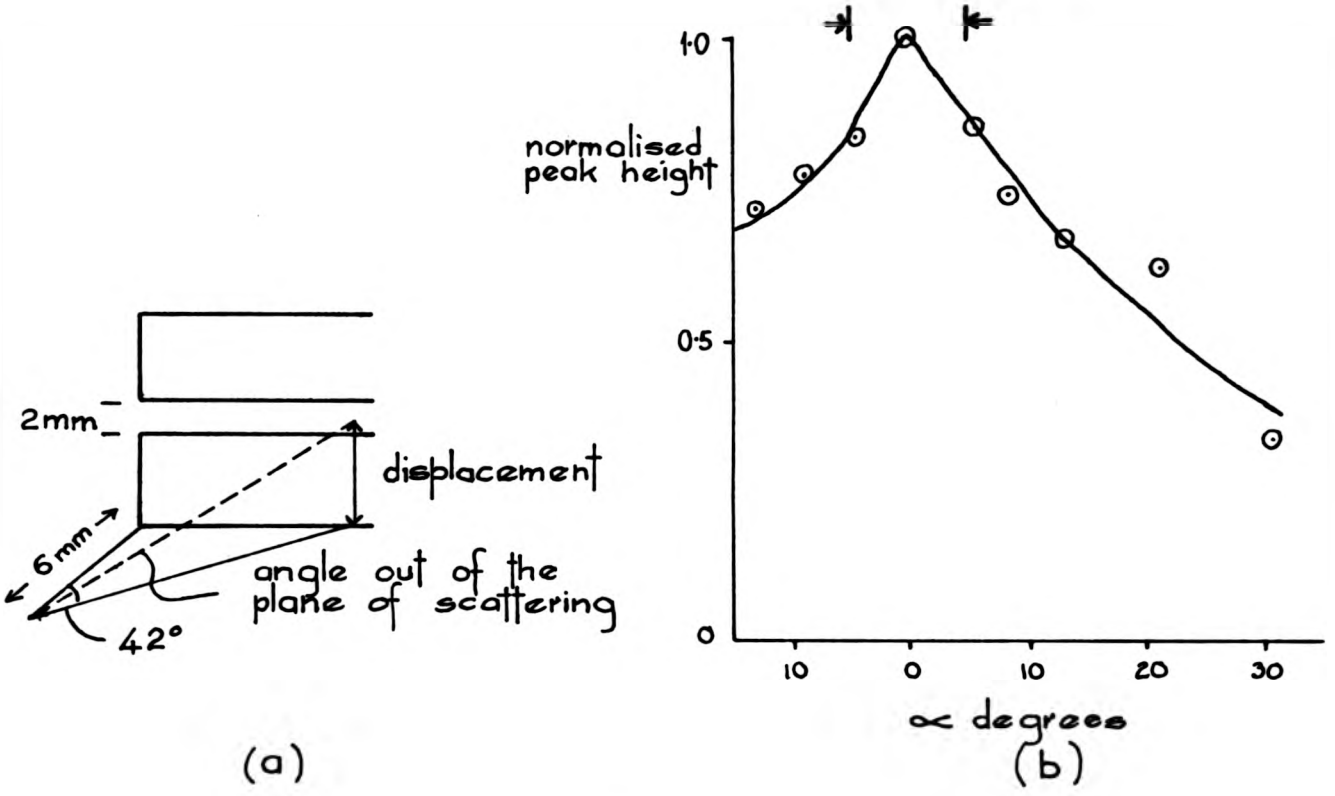
2mm
displacement
6mm
angle out of the plane of scattering
42°
(a)
1·0
0·5
0
normalised peak height
10
0
10
20
30
∝ degrees
(b)

Figure 4.8.

was approximately 20% of the peak height without it. Figure 4.8b shows the normalised peak height plotted against the angle out of the plane of scattering. It was found that the slit did not affect the form of the results obtained. This is in agreement with Niehus and Bauer (5), who found that for routine surface analysis, the presence of the slit in front of the C.M.A. was not required. Hence, in the following work, unless explicitly stated, all the data was collected without a slit in front of the C.M.A.

## 4.3. Oxygen Adsorption on Cu(100).

The oxygen adsorption on Cu(100) has been previously studied by McDonnell and Woodruff (1). They found that a dose of $1x10^{-6}$ torr-minutes of oxygen at room temperature produced a $(\sqrt{2}x\sqrt{2})R45^{\circ}$-O LEED structure. Further oxygen exposure to a level of $1x10^{-4}$ torr-minutes gave a (2x2)-O LEED structure. This sequence of adsorbate structures has not been found by other workers (for example, Hofmann et al (6)). In the present work, a dose of $1x10^{-6}$ torr- minutes gave a $(\sqrt{2}x\sqrt{2})R45^{\circ}$-O LEED pattern, but weak extra spots were also present. Further adsorption to $1x10^{-4}$ torr-minutes increased the intensity of these extra spots. The structure of the complete LEED pattern corresponds to a $(\sqrt{2}x2\sqrt{2})R45^{\circ}$-O structure. The oxygen dose was varied, but it was found to be difficult to stop the adsorption at the $(\sqrt{2}x\sqrt{2})R45^{\circ}$-O LEED pattern. Figure 4.9 shows the LEED pattern obtained after a dose of $1x10^{-6}$ torr-minutes. Some of the extra spots for the $(\sqrt{2}x2\sqrt{2})R45^{\circ}$-O LEED pattern are visible. This series of adsorption structures is the same as that found by Hofmann et al (6).

A dynamic exposure of oxygen was used. The oxygen was of high purity (BOC Ltd. - Grade X). A mass spectrum taken during adsorption is shown in Figure 4.10. The diffusion pump was used to reduce the pressure to the low $10^{-7}$ torr region after adsorption. The T.S.P.

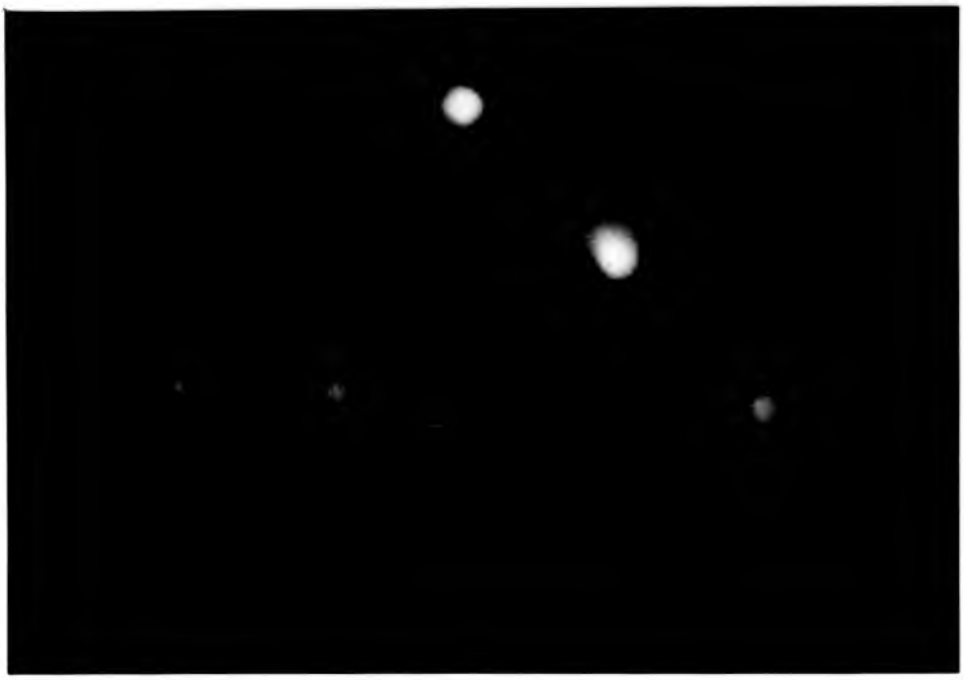

Cu (100) $(\sqrt{2} \times 2\sqrt{2})$ R 45° – O

Electron energy ≃ 100 eV

$\bar{1}0$ o × o 01

o o o

× o 00 o ×

o o o

01 o × o 10

· clean surface

× $(\sqrt{2} \times \sqrt{2})$ R 45°

o $(\sqrt{2} \times 2\sqrt{2})$ R 45°

Figure 4.9.

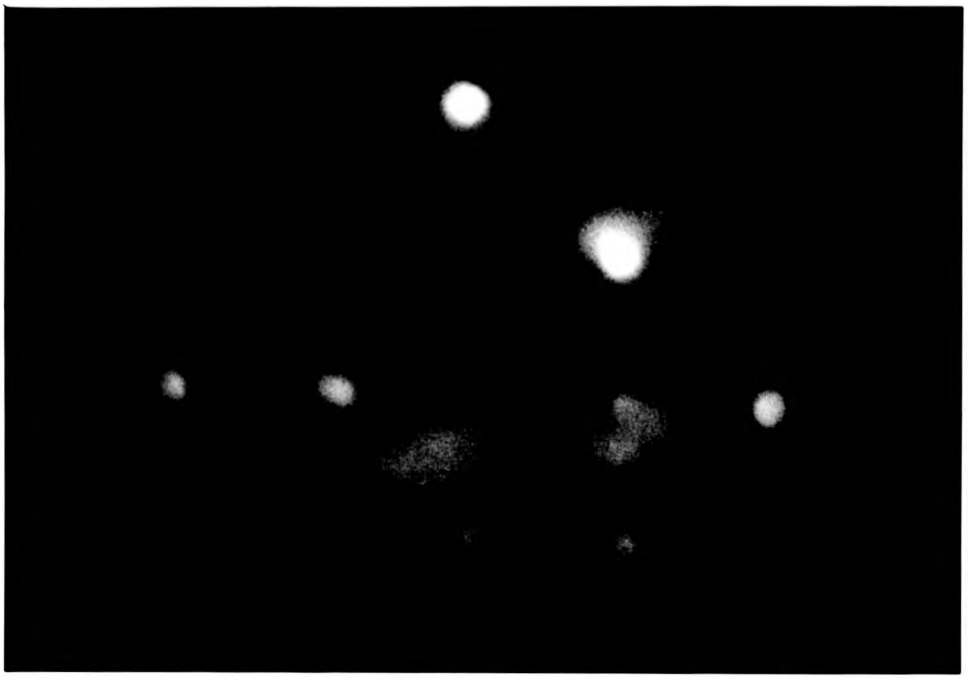

Cu (100) $(\sqrt{2} \times 2\sqrt{2})$ R 45° – O

Electron energy ≃ 100 eV

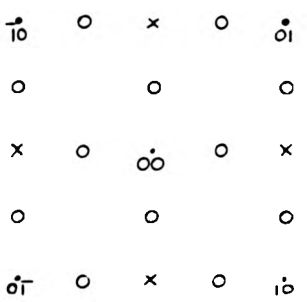


· clean surface

× $(\sqrt{2} \times \sqrt{2})$ R 45°

o $(\sqrt{2} \times 2\sqrt{2})$ R 45°

Figure 4.9.

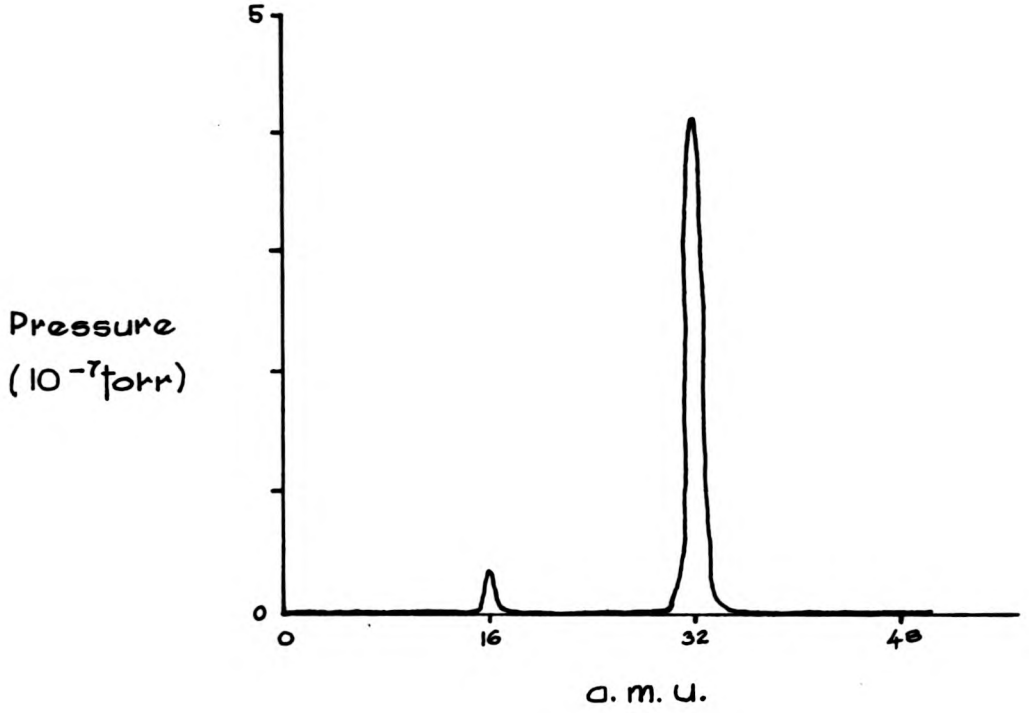


Figure 4.10.

and the ion pump were required to re-establish a pressure of $5 \times 10^{-10}$ torr. It was possible to pump away the oxygen within two minutes. An AES spectrum taken after adsorption is shown in Figure 4.11. The oxygen coverage can be estimated by using the calibration of Argile and Rhead (2). Here, a ratio of approximately $10^{-2}$ between the 512 eV oxygen peak and the 62 eV copper peak was found to correspond to a coverage of one monolayer. Using the values obtained from Figure 4.11, and correcting for the varying energy sensitivity of the C.M.A., the coverage of oxygen in this work is approximately 0.5 monolayers.

It was found that the same LEED structures could be obtained at lower oxygen doses if the crystal was heated to approximately 350 °C before adsorption. This is in agreement with the work of Hofmann et al (6). However, the difficulty in stopping at the $(\sqrt{2}x\sqrt{2})R45^{\circ}$-O structure was still found. Clearly, this lack of control on the structure obtained presents experimental difficulties. It was found that the ISS data from the two structures, which had been previously checked with LEED, was similar. LEED was not used to check the structure after each adsorption and so it was necessary to assume that the $(\sqrt{2}x2\sqrt{2})R45^{\circ}$-O structure is present to some degree in the work reported here.

The LEED study of the oxygen adsorption on Cu(100) shows that this system is not as straight-forward as the oxygen on Ni(100) system, which was studied later (see Chapter 5). This lack of ideal behaviour was found by Onuferko et al (7) and other workers (for example (6)). This will clearly complicate the interpretation of the experimental data. A more detailed account of the adsorption of oxygen on Cu(100) is given in Chapter 6.

## 4.4. ISS with $He^{+}$ on clean and oxygen adsorbed Cu(100).

Having studied the instrumental effects of the apparatus, a

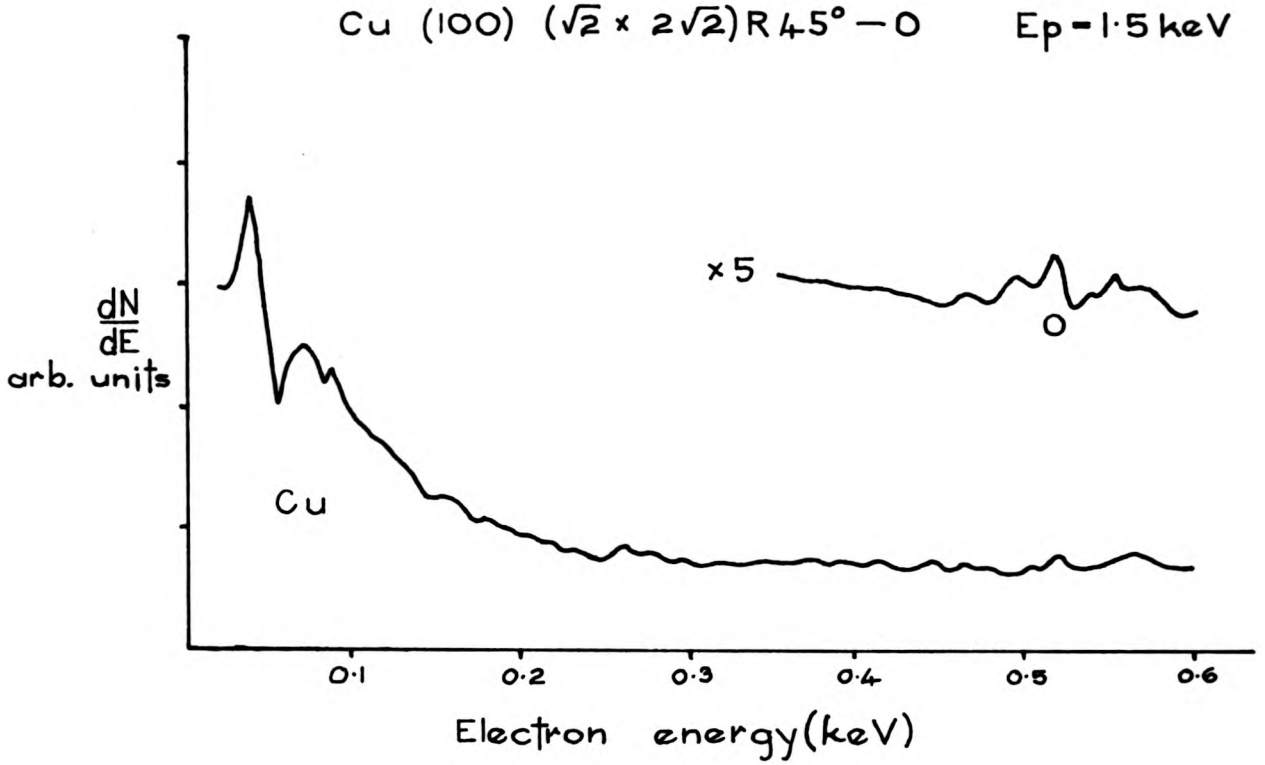
Cu (100) (√2 × 2√2)R45° – O
Ep = 1·5 keV
dN/dE
arb. units
×5
O
Cu
0·1
0·2
0·3
0·4
0·5
0·6
Electron energy(keV)

Figure 4.11.

detailed investigation of the Cu(100)-oxygen system was begun. The majority of the experiments were performed with helium ions. There were two major reasons for this. The first was that most previous surface structure determination using ISS has been performed with helium ions. The second reason was that the degree of surface damage caused by helium ions is much less than for other inert gas ions. The interpretation of the data collected using helium ions is quite complex, and so this is dealt with separately in Chapter 6. In the present section, the experimental results will be reported. Some experiments were carried out using neon and argon ions and these are given in the next section.

The results obtained from clean Cu(100) will be dealt with first. The majority of the experiments were performed with a beam energy of 1.0 keV, whilst a small number were carried out at other energies in the 0.5 keV to 1.5 keV energy range. However, these showed little qualitative difference from the results of the 1.0 keV incident energy experiments.

The effect of the angle of incidence on the scattered yield was measured for different incident energies and different scattering angles. Figure 4.12 shows the variation obtained from $90^{\circ}$ scattering using incident energies of 0.5 keV, 0.7 keV and 1.0 keV. It can be seen that the form of the variations is similar. The ion escape probability, as calculated in Chapter 2, is shown in the same figure. A close agreement between the two sets of curves can be observed.

The variation of the ion yield for different angles of incidence at different scattering angles is shown in Figure 4.13. Both the experimental data and the calculated escape probabilities have been normalised. This means that the different values of the differential scattering cross-section for the various scattering angles are not included. Again, the agreement between the two sets of curves is

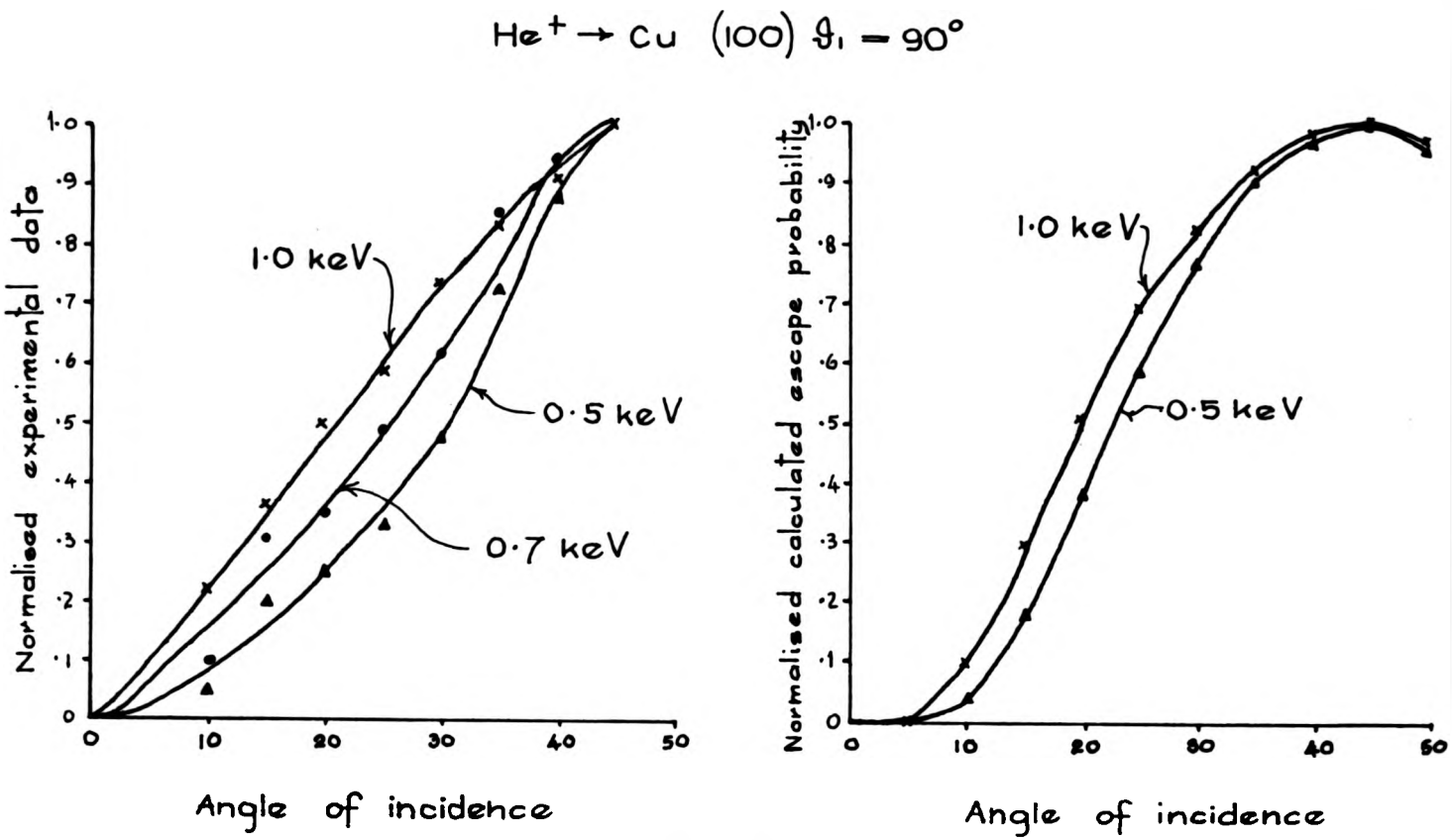
He+ → Cu (100) ϑ1 = 90°
Normalised experimental data
1·0 keV
0·5 keV
0·7 keV
Angle of incidence
Normalised calculated escape probability
1·0 keV
0·5 keV
Angle of incidence

Figure 4.12.

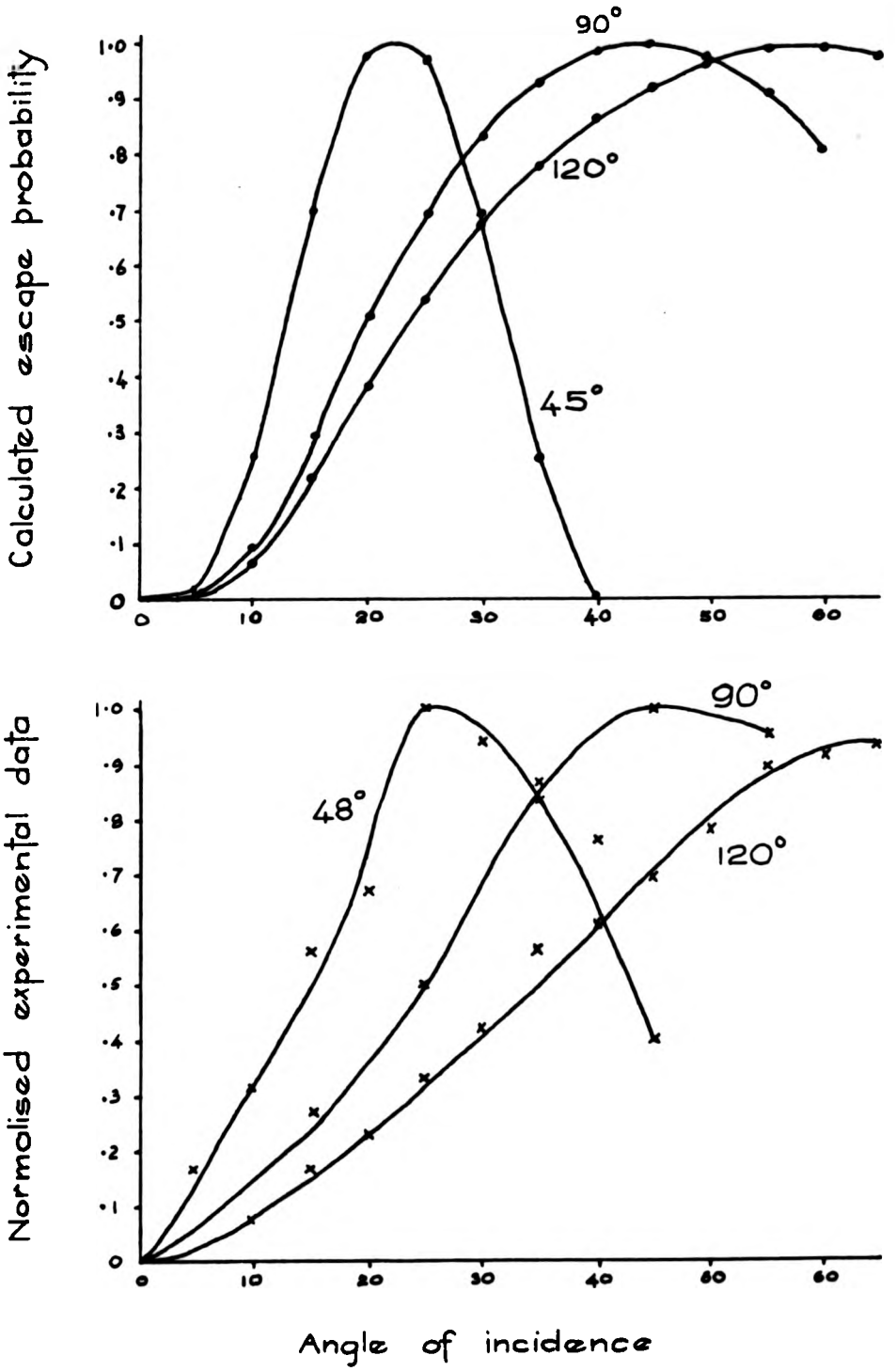
Calculated escape probability
90°
120°
45°
Normalised experimental data
90°
48°
120°
Angle of incidence

Figure 4.13.

quite good. Broadening due to the angular acceptance of the analyser can be seen, particularly for the scattering angle of $48^\circ$. It is difficult to carry out qualitative interpretation of experiments where the angle of incidence is varied. This is because as the polar angle changes, the rate of neutralisation changes to a large extent. This makes it more difficult to separate the variation in the signal due to elastic shadowing.

Figure 4.14 shows the variation of the ion intensity as a function of the azimuthal angle for the scattering angles of $90^\circ$ and $48^\circ$. Both sets of results were taken at specular reflection. For $90^\circ$ scattering, there is no marked variation in the ion yield. In the $90^\circ$ scattering case for $\gamma = 45^\circ$, the second layer of copper atoms should be shadowed by the top layer of copper atoms. However, in the $\gamma = 0^\circ$ direction, alternate layers of atoms are displaced laterally. This will lower the possibility of the second layer of atoms being shadowed by the top layer. This should lead to an increase in the scattered intensity from the $\gamma = 0^\circ$ direction. However, this variation was not found. This indicates that neutralisation effectively removes all ions which penetrate below the top layer. This result is in agreement with Niehus and Bauer (5), who found that for 0.6 keV helium ions, scattering was only due to the first atomic layer. This shows clearly the importance of neutralisation in ISS with these experimental conditions.

There is a marked variation in the yield obtained for $48^\circ$ scattering. This cannot be explained in terms of simple elastic scattering, as this predicts a maximum in the $\gamma = 0^\circ$ direction (see above). In order to understand the experimental results, it has been necessary to consider the role of neutralisation in detail. A fuller treatment of the arguements involved in elastic shadowing are given in Chapter 5 where a known structure, Ni(100)($\sqrt{2}$x$\sqrt{2}$)R45°-O, was chosen so that the effects of elastic shadowing could be

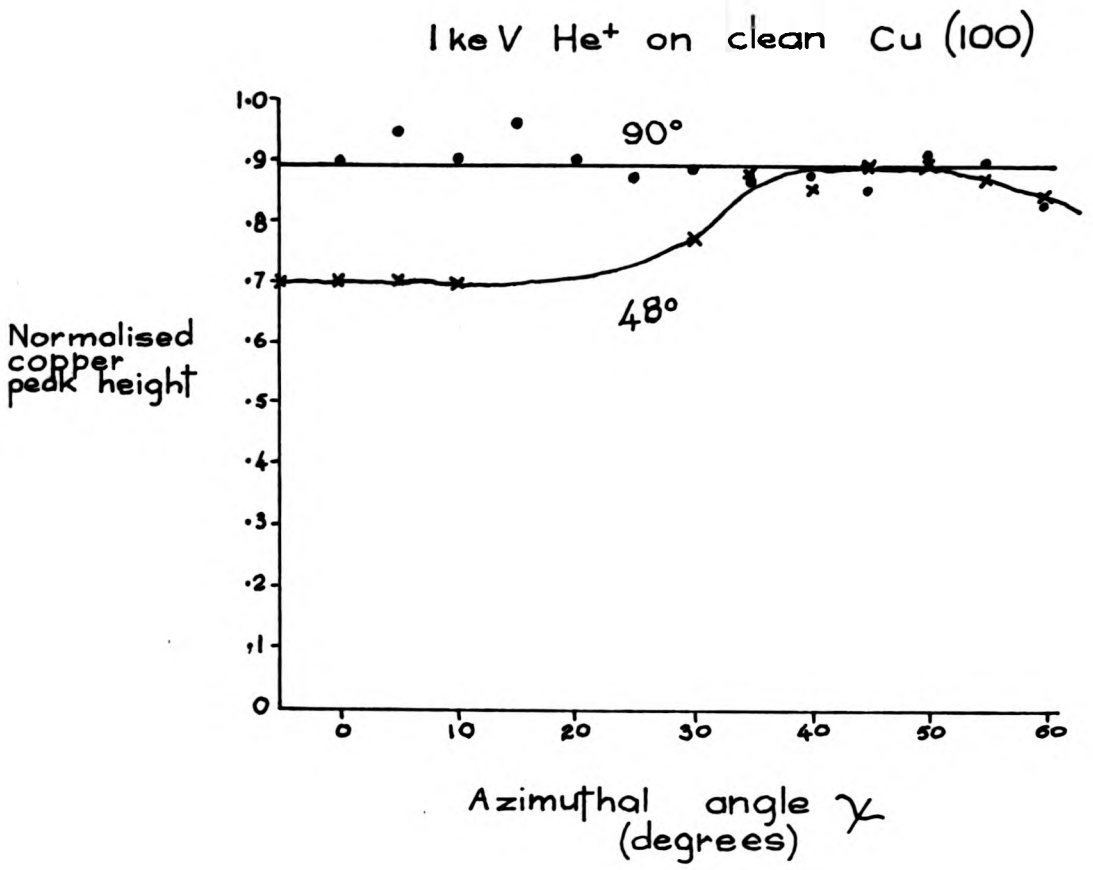
1 keV He+ on clean Cu (100)
90°
48°
Normalised copper peak height
1·0
·9
·8
·7
·6
·5
·4
·3
·2
·1
0
0
10
20
30
40
50
60
Azimuthal angle χ (degrees)

Figure 4.14.

calculated from a well understood model structure.

The surface sensitivity of ISS to contamination is dependent on the scattering geometry. It was found that with a scattering angle of 48°, ISS with $He^+$ proved more sensitive than AES to carbon contamination. For 90° scattering, the relative sensitivity of the two techniques was reversed. The high sensitivity of ISS with a 48° scattering angle is due to the large value of the differential scattering cross-section.

The sputtering caused by the helium ions is low. There is, however, experimental evidence that helium became embedded in the sample. For example, after 90 minutes of bombardment of 1.0 keV helium ions at a current of $5 \times 10^{-9}$ amps, subsequent heating of the crystal to 400 °C gave a rate of pressure rise of helium of $3 \times 10^{-11}$ torr/sec. Thus, heating could be used to remove this helium if necessary. However, experiments were usually performed for approximately 45 minutes and dose dependent effects were not evident.

Contamination of the sample occured in some experiments. This was caused by impure inert gas being leaked into the experimental chamber. The ion beam itself remained pure, due to the mass analysis, but reactive gases in the background pressure caused contamination. Thus, it was necessary to take particular care in the use of the gas handling line. Both contamination and crystal damage will affect the ISS data obtained. In order to lessen the possibility of this having an effect on the interpretation of the data, each experiment was performed a number of times until a consistent result was evident.

The experiments performed on the adsorbate surface were similar to those used on the clean surface. The two major types of experiments performed were the variation of the azimuthal angle at constant polar angle and the variation of the polar angle at constant azimuthal angle. These experiments were carried out with various

incident energies, scattering angles and ion species. In this section, only the results obtained from helium scattering are included.

Figure 4.15 shows a typical azimuthal variation obtained for constant polar angle using 1.0 keV helium ions scattered over a $90^{\circ}$ scattering angle. The effect of different incident energies was investigated. It was found that the general form of the curve remained constant. The level of anisotropy, that is, the ratio between the maximum and minimum copper signal, varied with different incident energies. The amount of anisotropy was smallest for 500 eV ions. The level of the oxygen signal remained constant with the variation of the azimuthal angle. Figure 4.16 shows a complete energy spectrum for 1.0 keV $He^{+}$ scattered through $90^{\circ}$ from an oxygen adsorbed surface. The attenuation of the copper signal for an azimuthal angle of $45^{\circ}$ between the clean surface and the adsorbed surface is approximately a factor of three. The result is similar to the work of Heiland and Taglauer (8) on oxygen adsorbed on Ni(111) using 1.0 keV $He^{+}$. In that work, an attenuation by a factor of three was found to correspond to a surface coverage of $^{2}/_{3}$ of a monolayer.

Figure 4.17 shows a polar variation for 1.0 keV $He^{+}$ scattered over $90^{\circ}$. It can be seen that the copper signal is still present at very grazing angles of incidence. This shows that the oxygen atoms do not completely shadow the copper atoms even at these grazing angles. Also, the azimuthal variation can still be detected. Similar results were obtained for 0.7, 0.8 and 1.3 keV helium ions.

The results obtained for a scattering angle of $120^{\circ}$ were similar to those obtained from $90^{\circ}$ scattering. A major difference in the azimuthal variation was that the degree of shadowing anisotropy between the $0^{\circ}$ and $45^{\circ}$ azimuths was less than for the $90^{\circ}$ case. The polar variation obtained for a 1.0 keV helium beam is shown in Figure 4.18. It can be seen that between a polar angle

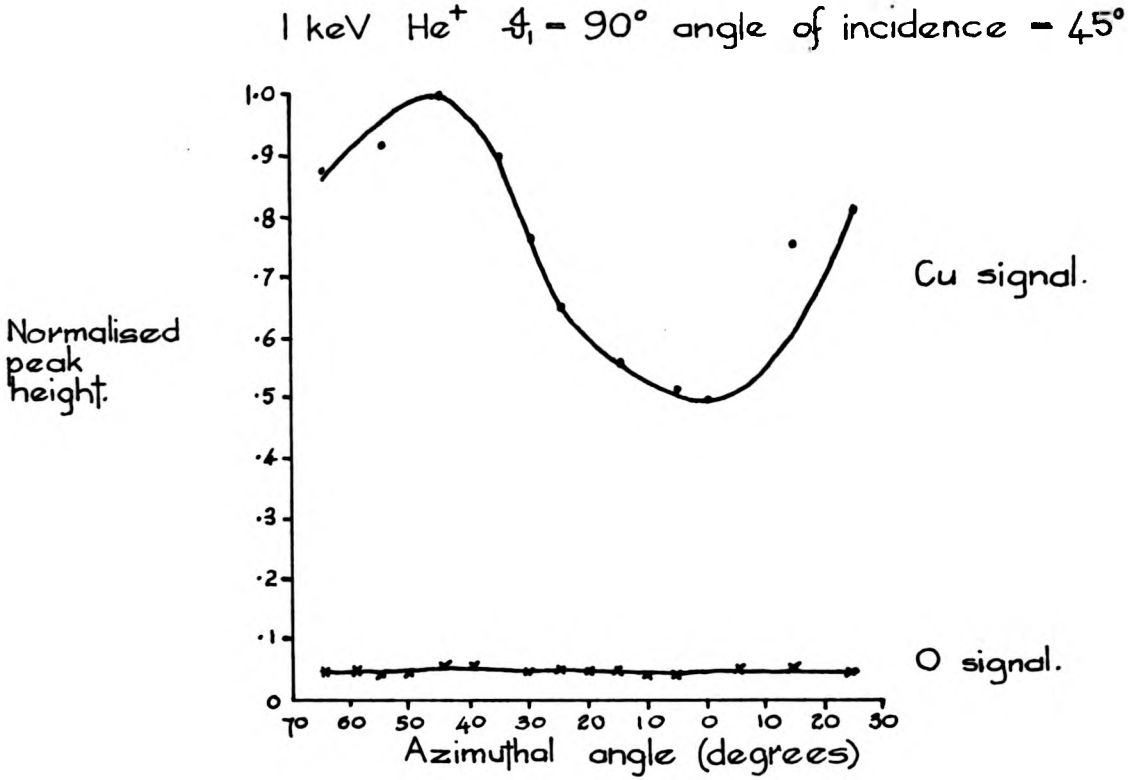
1 keV He+ $\phi_1$ = 90° angle of incidence = 45°
Normalised peak height.
1·0
·9
·8
·7
·6
·5
·4
·3
·2
·1
0
70 60 50 40 30 20 10 0 10 20 30
Azimuthal angle (degrees)
Cu signal.
O signal.

Figure 4.15.

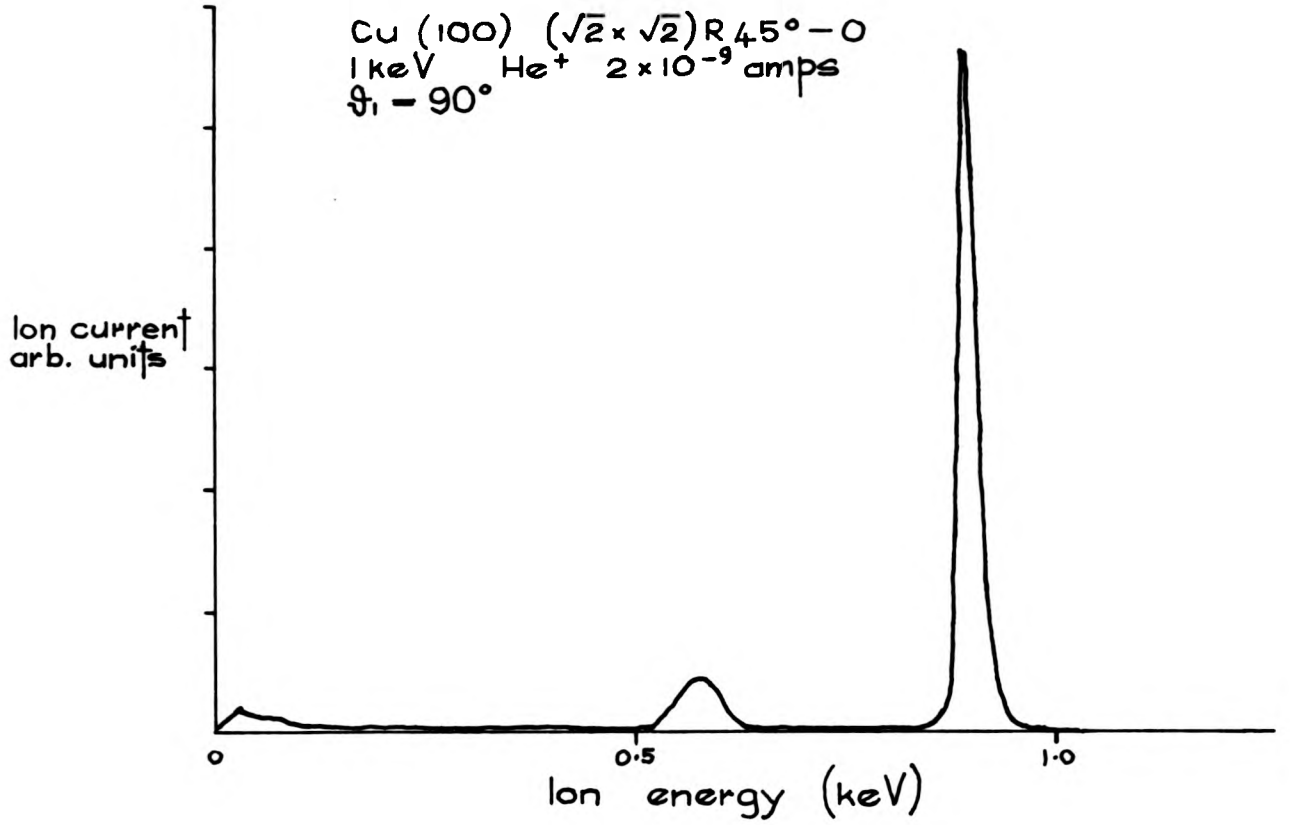
Cu (100) (√2 × √2) R 45° – O
1 keV He+ 2 × 10⁻⁹ amps
ϑ1 = 90°
Ion current
arb. units
0
0·5
1·0
Ion energy (keV)

Figure 4.16.

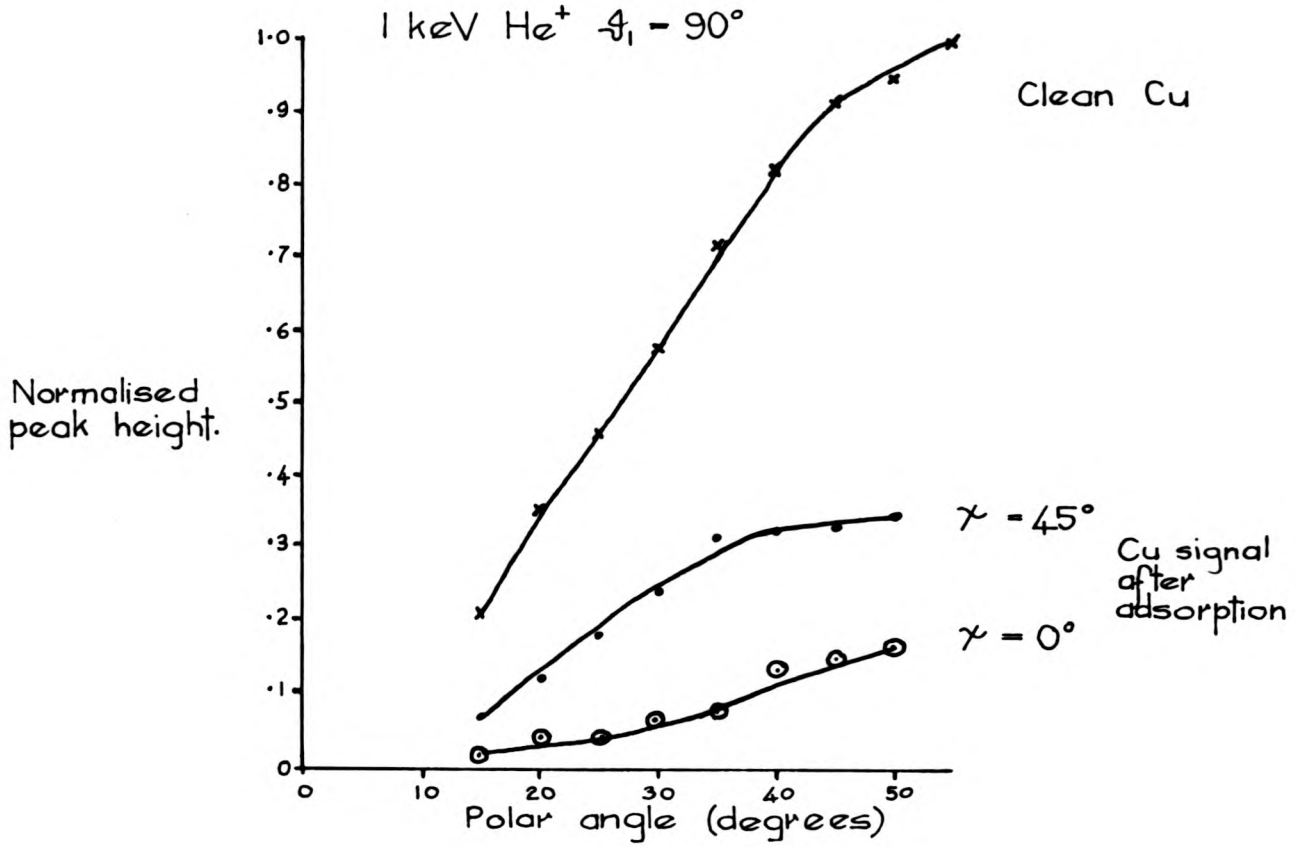
1 keV $He^+$ $\phi_1 = 90°$
Clean Cu
Normalised peak height.
$\chi = 45°$
$\chi = 0°$
Cu signal after adsorption
1·0
·9
·8
·7
·6
·5
·4
·3
·2
·1
0
0
10
20
30
40
50
Polar angle (degrees)

Figure 4.17.

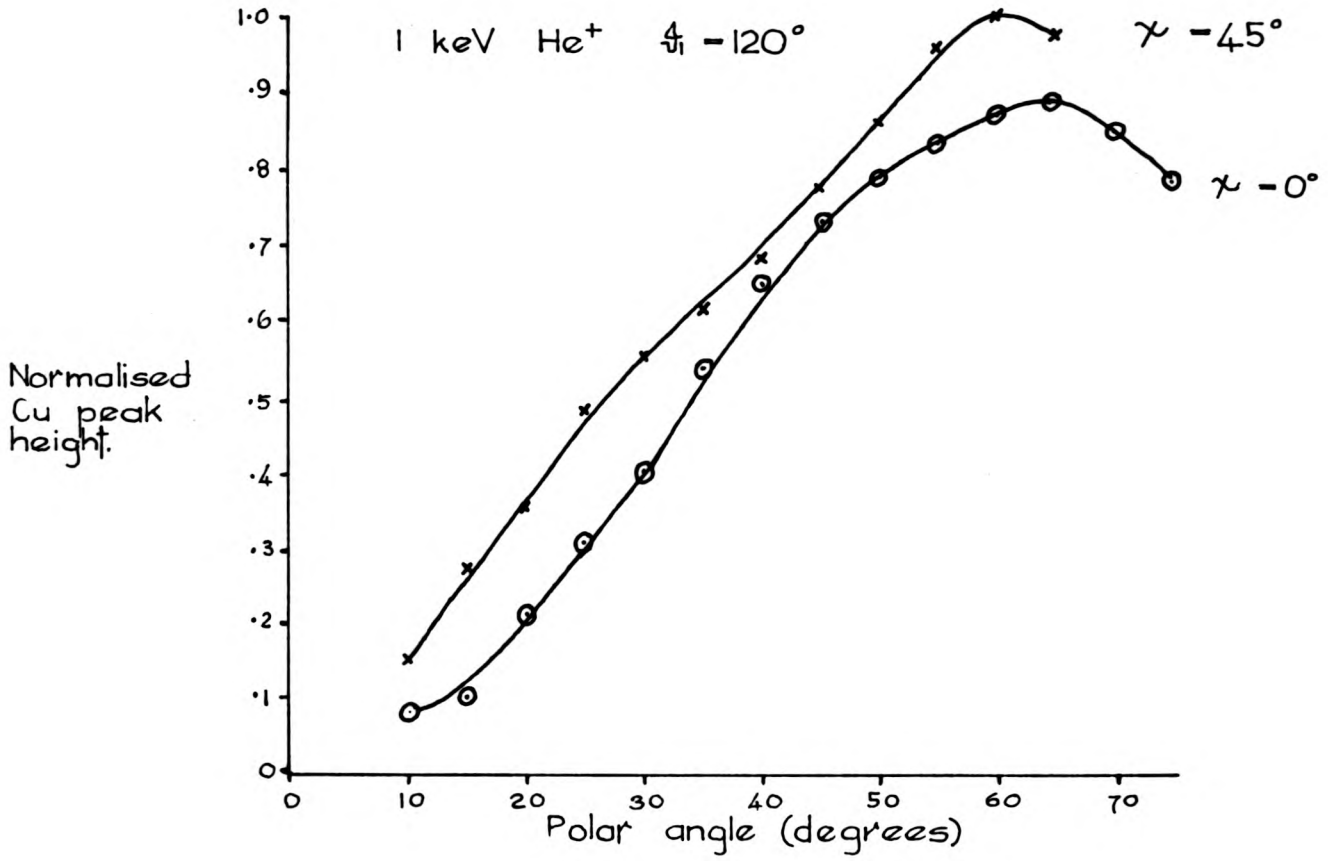
1 keV He+ φ1 -120°
χ -45°
χ -0°
Normalised Cu peak height.
1·0
·9
·8
·7
·6
·5
·4
·3
·2
·1
0
0
10
20
30
40
50
60
70
Polar angle (degrees)

Figure 4.18.

of 35° and 50°, the curve for the 45° azimuth approaches the curve for the 0° azimuth. Azimuthal variations were taken in this range of polar angles. The azimuthal variation was still present, but at a reduced magnitude.

Experiments were performed at a scattering angle of 48° with 1.0 keV helium ions. Figure 4.19 shows the energy spectrum obtained from 1.0 keV helium ions scattered from the adsorbed surface in the azimuths of 0° and 45°. The copper signal in the $\gamma$ = 45° azimuth has been attenuated by a factor of approximately five from the clean surface value. A typical azimuthal variation obtained at a constant polar angle of 24° is shown in Figure 4.20. The signal from helium ions scattered by oxygen atoms is independent of the azimuthal angle. This was also found in the cases of $\vartheta_1$ = 90° and $\vartheta_1$ = 120°. However, by comparing the relative size of the oxygen peak for the $\vartheta_1$ = 90° and $\vartheta_1$ = 48° (see Figure 4.15), it can be seen that the oxygen signal is approximately twice as large in the 90° case as in the 48° case. The form of the shadowing of the copper peak is the same in these two scattering angles. However, the copper peak is attenuated more strongly in the 48° scattering case. It should be added that there is an azimuthal dependence in the clean surface data for this scattering angle. Figure 4.21 shows the polar variations found for the scattering of 1.0 keV helium ions along the two major azimuths. The level of the relative shadowing between the two major azimuths decreases as the angle of incidence is decreased, whereas the oxygen signal remains independent of the azimuth.

Summary.

It is clear that the particular ISS experimental conditions which have been reported are sensitive to surface structure. This can be seen in both the clean copper data for 48° scattering and

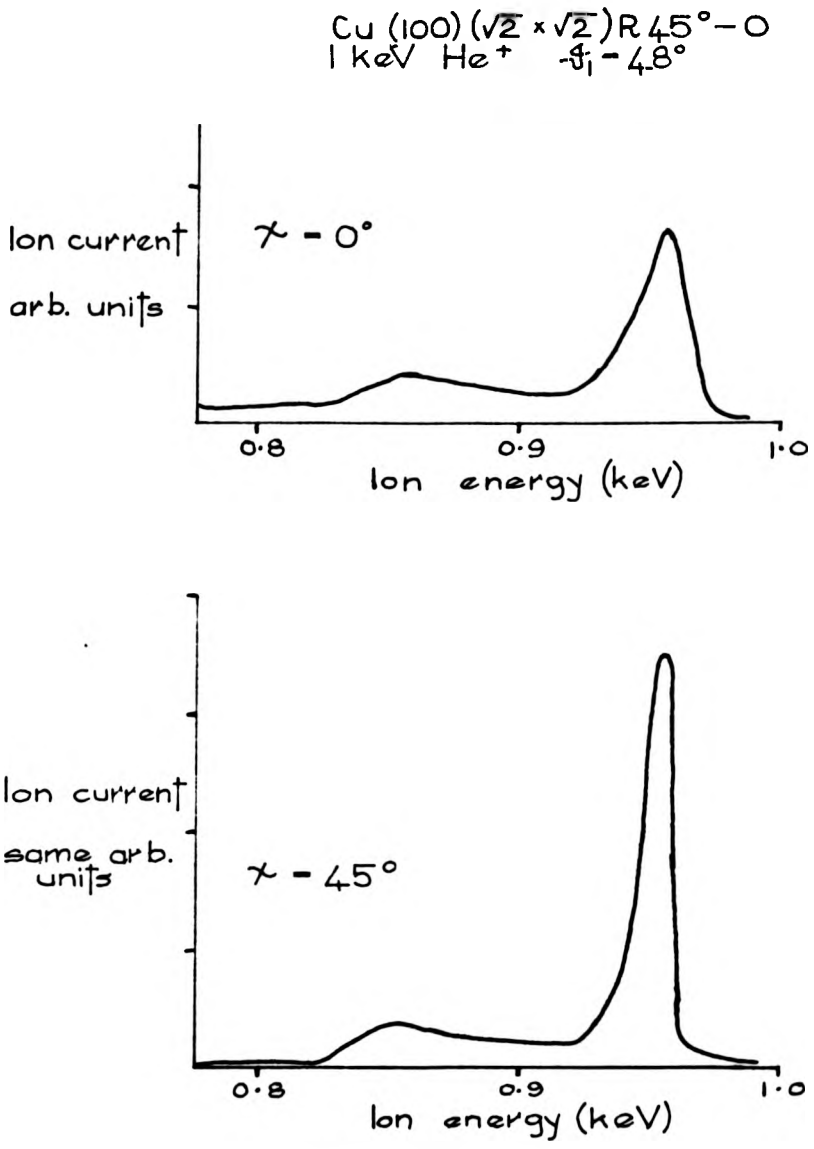
Cu (100) (√2 × √2) R 45° – O
1 keV He+ -ϑi = 4.8°
Ion current
arb. units
χ = 0°
0·8
0·9
1·0
Ion energy (keV)
Ion current
same arb. units
χ = 45°
0·8
0·9
1·0
Ion energy (keV)

Figure 4.19.

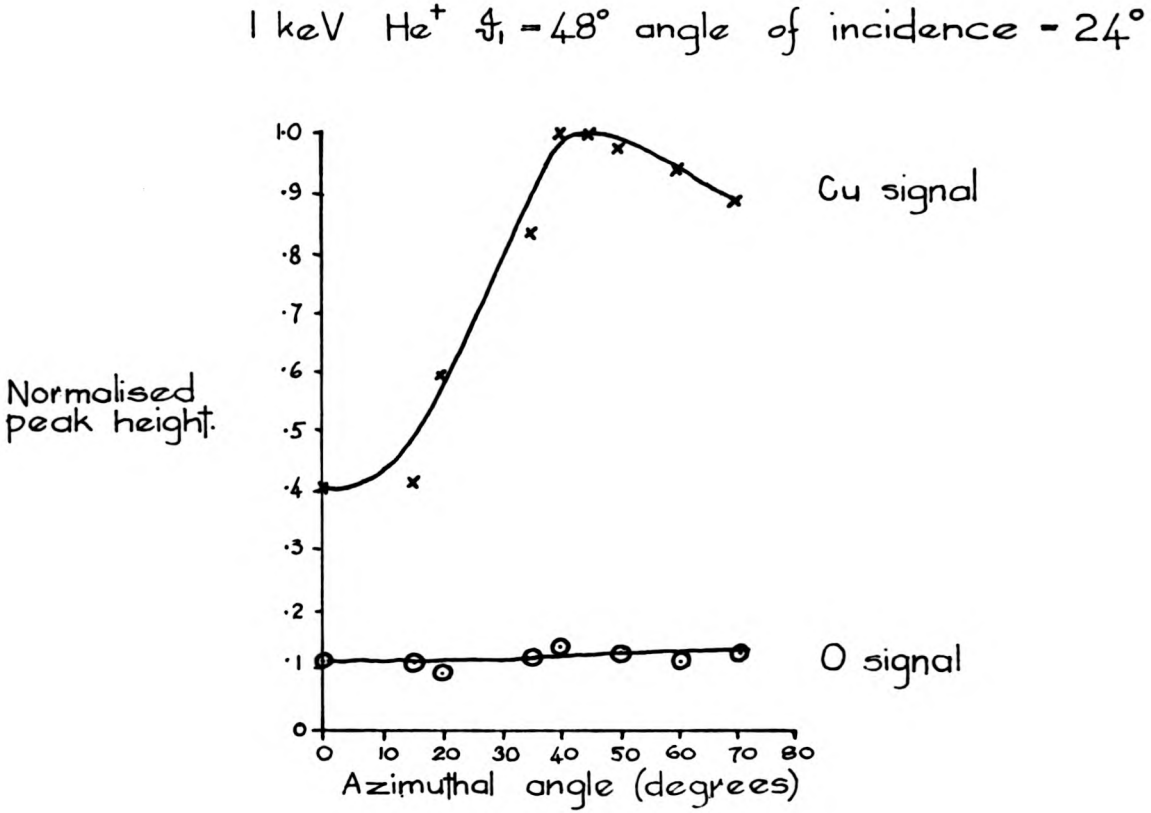
1 keV He+ ψ1 = 48° angle of incidence = 24°
Normalised peak height.
1·0
·9
·8
·7
·6
·5
·4
·3
·2
·1
0
0 10 20 30 40 50 60 70 80
Azimuthal angle (degrees)
Cu signal
O signal

Figure 4.20.

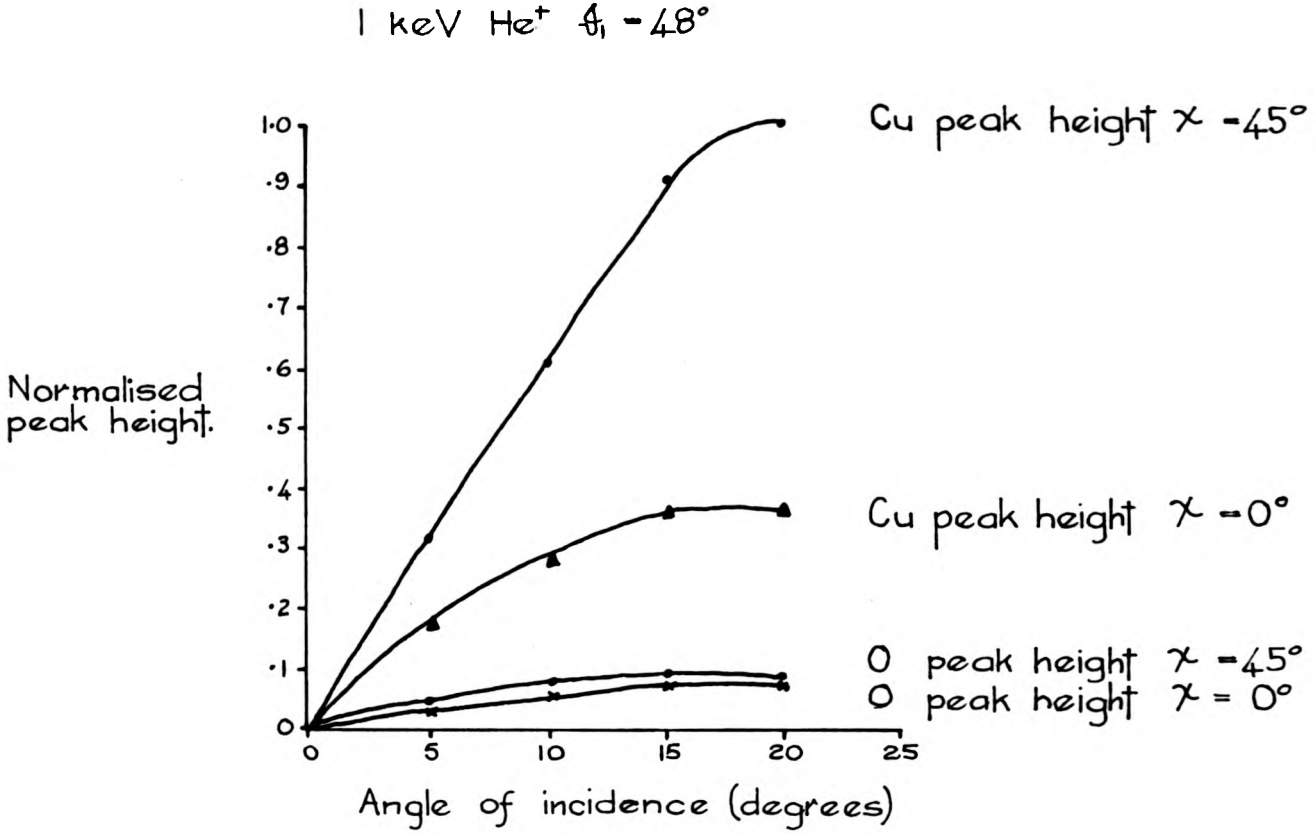
1 keV He+ θ1 = 48°
Normalised peak height.
1·0
·9
·8
·7
·6
·5
·4
·3
·2
·1
0
0
5
10
15
20
25
Angle of incidence (degrees)
Cu peak height χ = -45°
Cu peak height χ = 0°
O peak height χ = -45°
O peak height χ = 0°

Figure 4.21.

in the oxygen adsorbed data for all three scattering angles. However, the form of the variations obtained cannot be explained by simple elastic shadowing arguements. A more detailed investigation of elastic shadowing has been performed for the nickel surface. Again, it was not possible to understand the equivalent experimental results for the nickel surface in terms of elastic scattering. It has been necessary to study in detail the role of ion-atom neutralisation to obtain a satisfactory understanding of the processes involved in ISS under these particular experimental conditions. This is dealt with in Chapter 6 for the oxygen adsorbed copper surface.

## 4.5. ISS with $Ne^+$ and $Ar^+$ on clean and adsorbed Cu(100).

A number of experiments were performed using neon ions and a few spectra were recorded with argon ions. The experiments carried out with neon ions will be presented first. A spectrum of 1.0 keV $Ne^+$ ions on clean copper is shown in Figure 4.22. It can be seen from this figure that the yield of sputtered ions is greater than for helium ions. Thus, neon scattering will damage the crystal surface more quickly than helium scattering. It was necessary, therefore, to perform experiments with neon ions using smaller ion doses. This was achieved by allowing the ion beam to be incident on the target only while data was being collected. The ion gun was 'switched off' by using the mass filter on the gun. As ISS is extremely surface sensitive, surface damage caused by the incident ions will affect the scattered yield. It was found that a dose of approximately $10^{15}$ ions/cm$^2$ of 1.0 keV neon ions was sufficient to produce enough damage to affect the experimental results obtained.

The ion yield produced by 1.0 keV neon ions scattered over 90° from a clean copper surface whilst varying the azimuthal angle, is shown in Figure 4.23. It can be seen that the yield remains

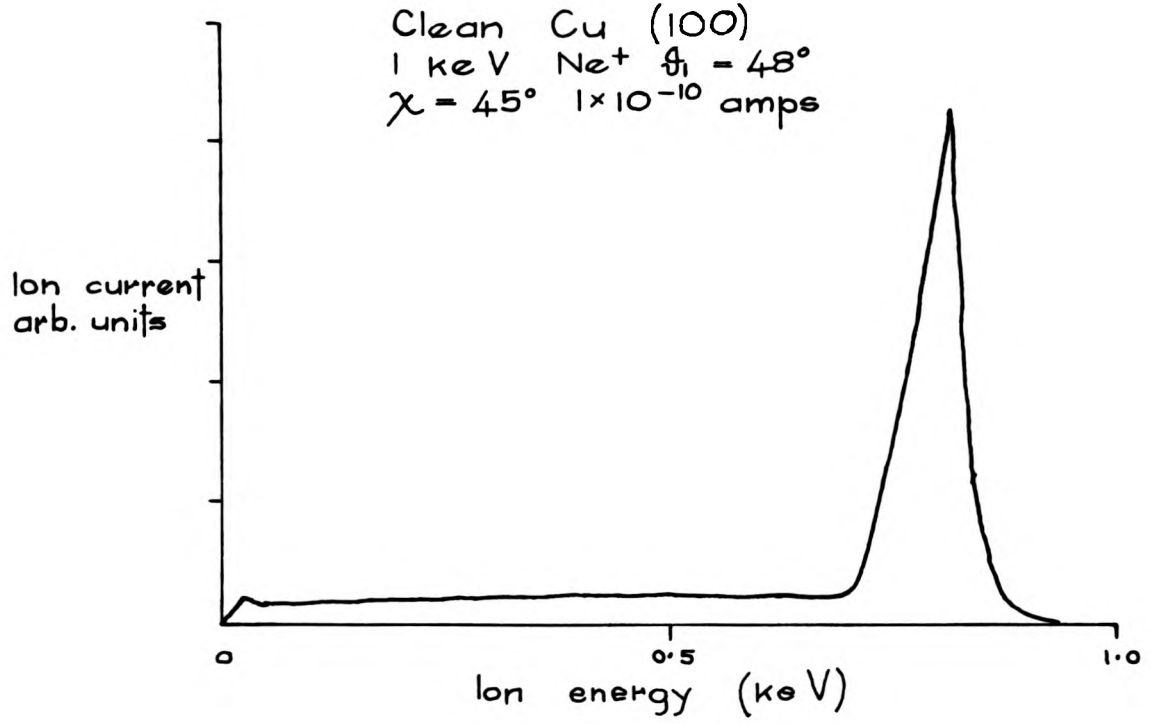
Clean Cu (100)
1 keV Ne+ $\theta_1 = 48°$
$\chi = 45°$ $1 \times 10^{-10}$ amps
Ion current
arb. units
0
0·5
1·0
Ion energy (keV)

Figure 4.22.

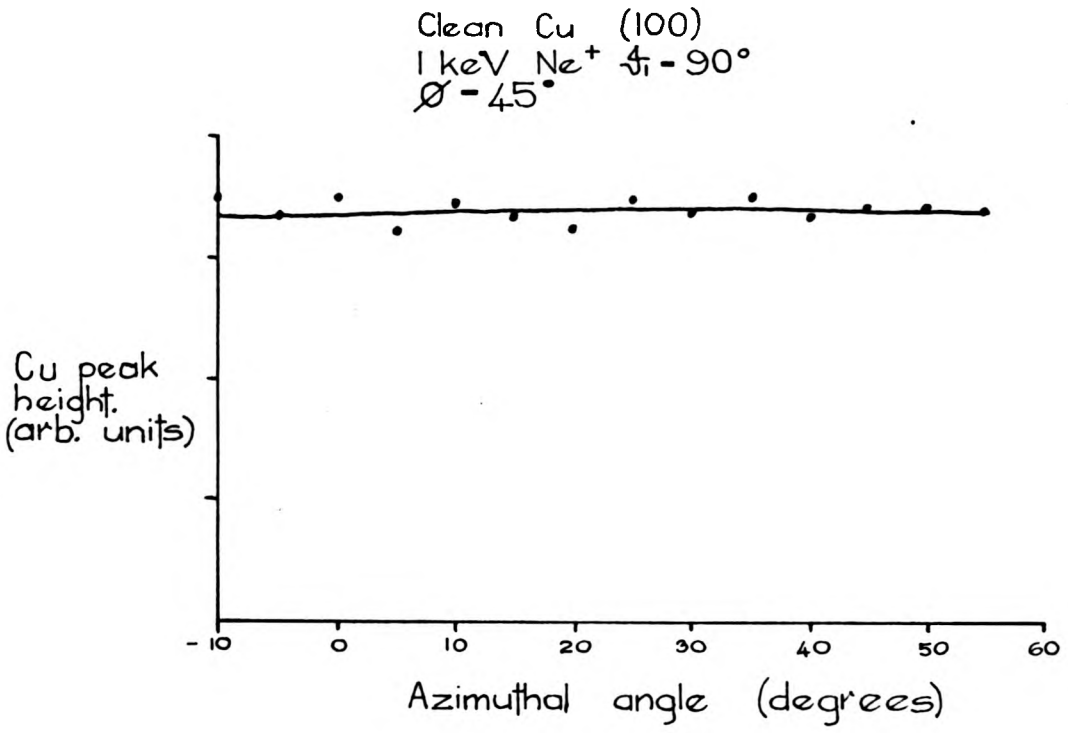
Clean Cu (100)
1 keV Ne+ ψi = 90°
Ø = 45°
Cu peak height. (arb. units)
-10
0
10
20
30
40
50
60
Azimuthal angle (degrees)

Figure 4.23.

constant to within 10%. The polar variation was also obtained for 1.0 keV and 0.5 keV neon ions and is shown in Figure 4.24. In general, the results obtained for neon scattering are similar to those found for helium scattering.

Experiments were performed on the oxygen adsorbed surface using neon ions of 0.5 keV and 1.0 keV. For 90° scattering, it is not possible to detect oxygen atoms with ISS and so only the copper peak height could be studied. Figure 4.25 shows an energy spectrum obtained from 0.5 keV neon ions. It can be seen that the level of sputtering was high. This is a problem particularly in adsorption studies where the desorption cross-section is appreciable. This led to a difficulty in obtaining consistent experimental results. A major problem was the compromise between limiting the ion dose and taking sufficient data to allow reliability in the results.

Figure 4.26 shows an azimuthal variation for 0.5 keV and 1.0 keV neon ions for a scattering angle of 90°. The level of shadowing of the copper signal remains constant within the experimental accuracy obtained for 1.0 keV ions. Whereas, there is a slight minimum at $\gamma = 45°$ for the 0.5 keV case. The polar variations found for 0.5 keV and 1.0 keV are similar to those found for helium scattering, except that the azimuthal variation is greater in the helium case. Similar results were obtained for neon scattering over an angle of 120°.

An energy spectrum for 1.0 keV neon ions scattered over 48° for the two major azimuths from the absorbed surface is shown in Figure 4.27. The spectra indicate the level of noise present in the results, which is much greater than that for helium scattering where the incident ion current was higher. It can be seen that the level of the peak due to scattering from copper atoms is not strongly dependent upon the azimuthal angle. The attenuation of this peak with respect to the clean surface is approximately a factor of three. A broad peak occurs at lower energies due to scattering events involving oxygen.

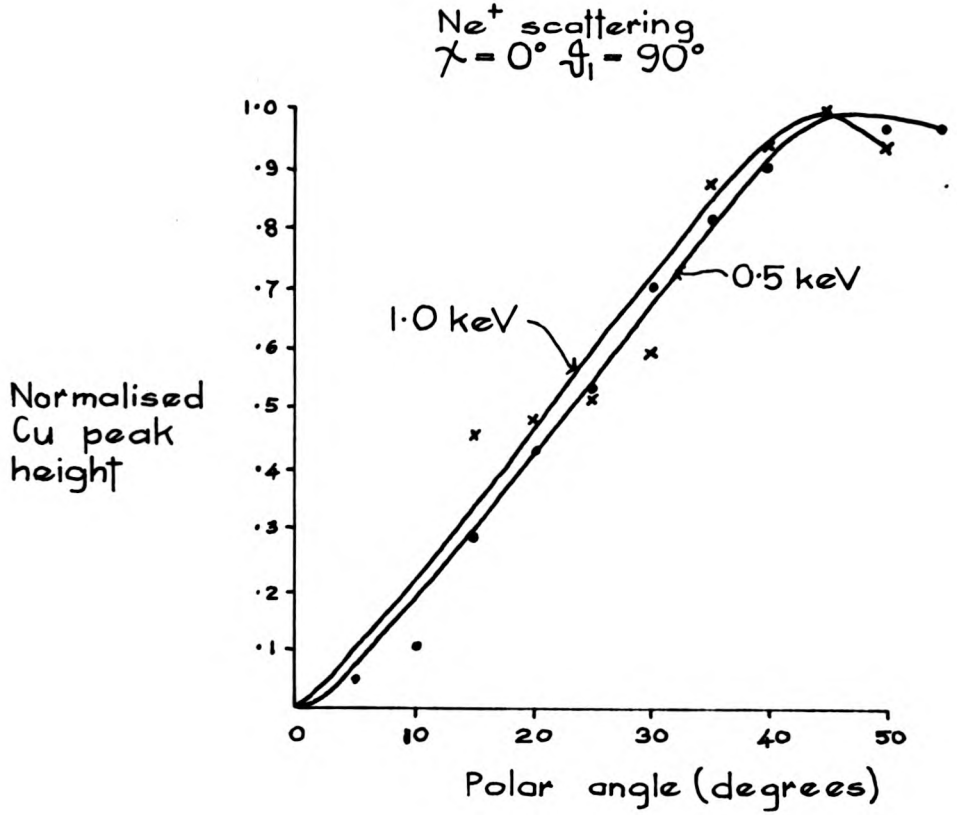
Ne+ scattering
χ = 0° ϕ1 = 90°
Normalised Cu peak height
1·0
·9
·8
·7
·6
·5
·4
·3
·2
·1
0
10
20
30
40
50
Polar angle (degrees)
1·0 keV
0·5 keV

Figure 4.24.

Cu (100) $(\sqrt{2} \times \sqrt{2})$ R 45° – O

$\phi_1 = 90°$ $\chi = 0°$

0·5 keV $Ne^+$ $2 \times 10^{-10}$ amps

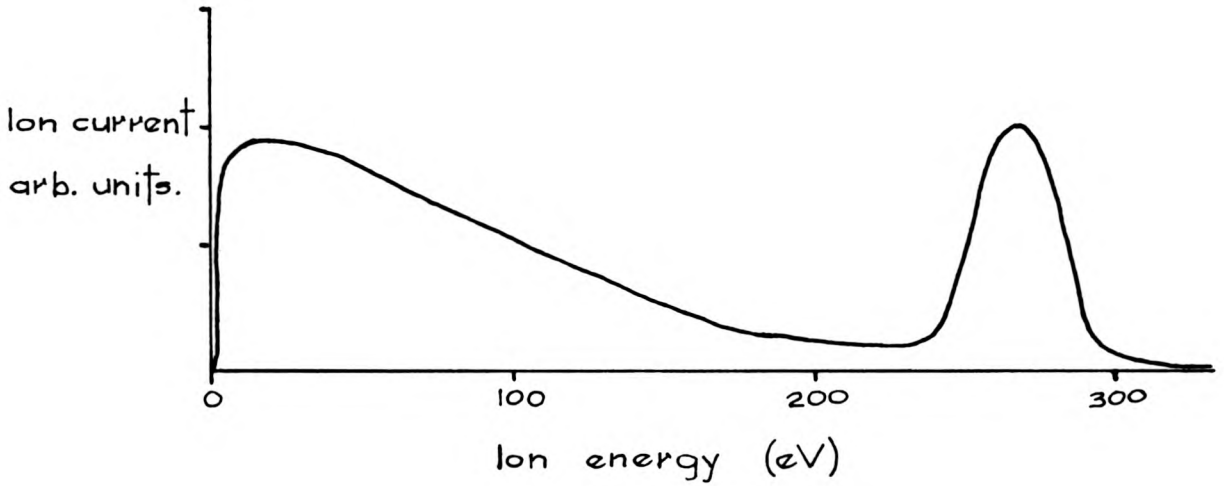


Figure 4.25.

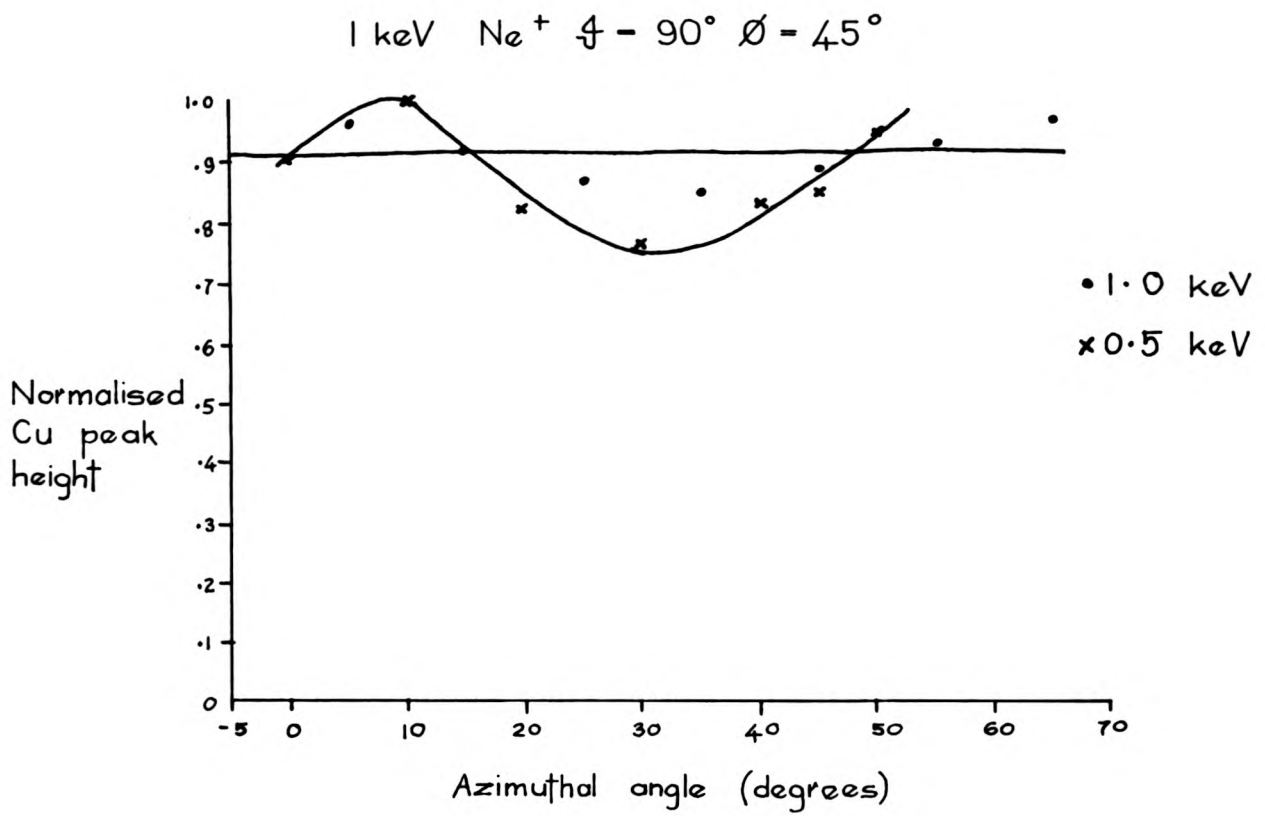
1 keV Ne+ ϕ = 90° Ø = 45°
1·0
·9
·8
·7
·6
·5
·4
·3
·2
·1
0
-5
0
10
20
30
40
50
60
70
Normalised Cu peak height
Azimuthal angle (degrees)
• 1·0 keV
× 0·5 keV

Figure 4.26.

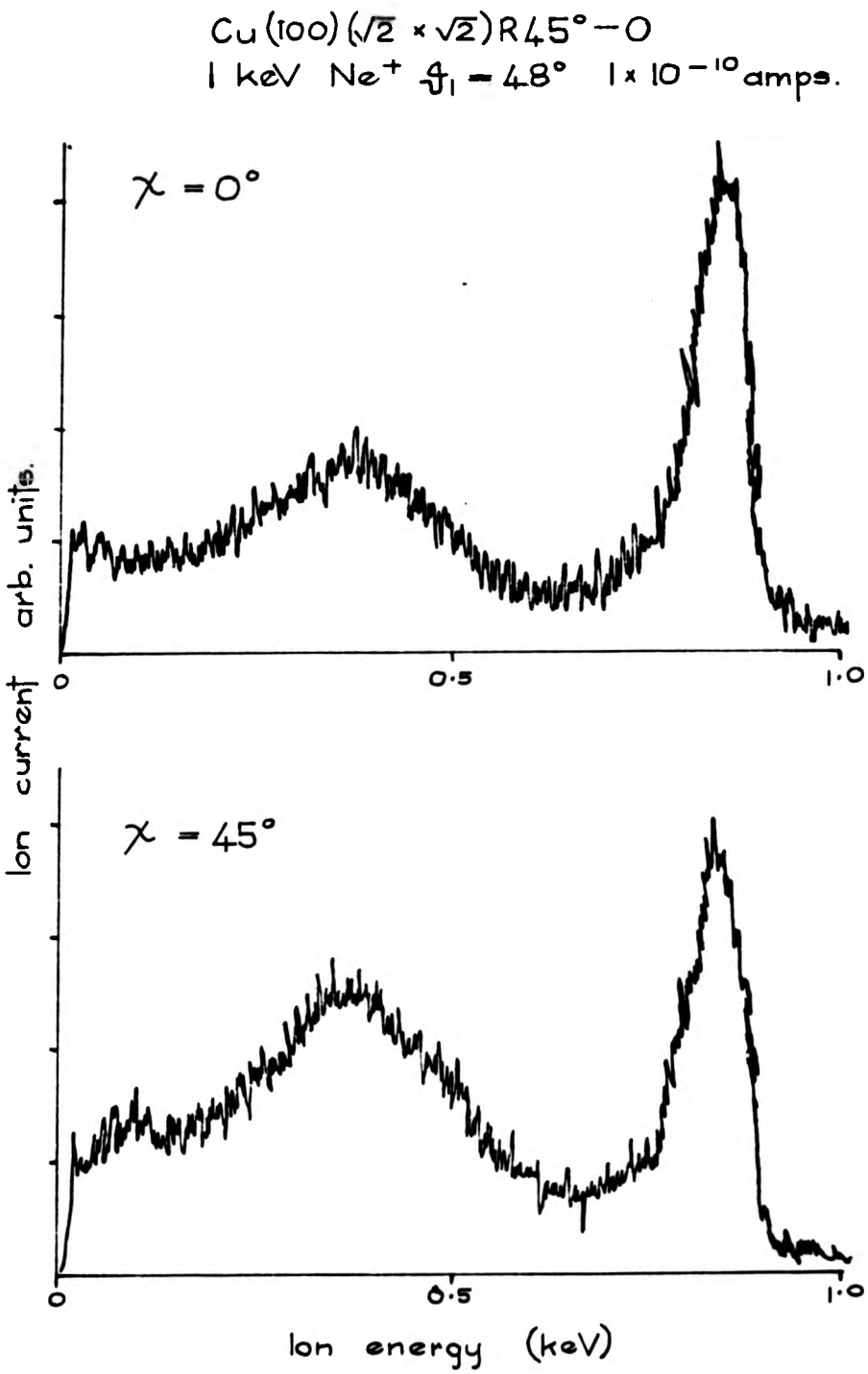
Cu (100) (√2 × √2) R45° – O
1 keV Ne+ ϑ1 = 48° 1 × 10⁻¹⁰ amps.
χ = 0°
χ = 45°
Ion current arb. units.
0
0.5
1.0
Ion energy (keV)

Figure 4.27.

The large width of this peak is caused both by the effects of multiple scattering and by the large acceptance angle of the analyser. The height of this peak is noticeably greater in the $\gamma = 45^{\circ}$ azimuth. Polar variations were taken to determine whether there was any anisotropy in the copper peak at more glancing angles of incidence. There was no evidence of different levels of shadowing between the two azimuths.

A spectrum obtained from 1.0 keV argon ions scattered over $48^{\circ}$ from clean Cu(100) is shown in Figure 4.28. The major peak is due to argon ions singly scattered from copper atoms. However, there is a large degree of background signal in the spectrum. This is caused by sputtering of the surface and by multiple scattering of the argon ions. The form of this spectrum is too complex to allow additional adsorbate features to be understood. Therefore, no further experiments were performed with argon ions.

Summary.

The results obtained from neon scattering are in many respects equivalent to those found for helium scattering. The only clear difference for $90^{\circ}$ scattering is found from the oxygen adsorbed surface with 0.5 keV neon ions. Here, the peak due to scattering from copper atoms is greater in the $\gamma = 0^{\circ}$ azimuth. This may be due to elastic effects dominating the ion yield. For the $48^{\circ}$ scattering angle using 1.0 keV neon ions there appears to be a difference in the level of shadowing of the oxygen peak between the two major azimuths. This may be due to self-shadowong by the oxygen atoms or by shadowing by the copper atoms. The shadowing by copper atoms is only likely to be significant if the oxygen atoms are nearly coplanar with the copper surface. For the reasons stated previously, the data collected from helium scattering are more reliable than the neon data. Hence, the majority of the surface structure analysis has been carried out using the results of helium scattering.

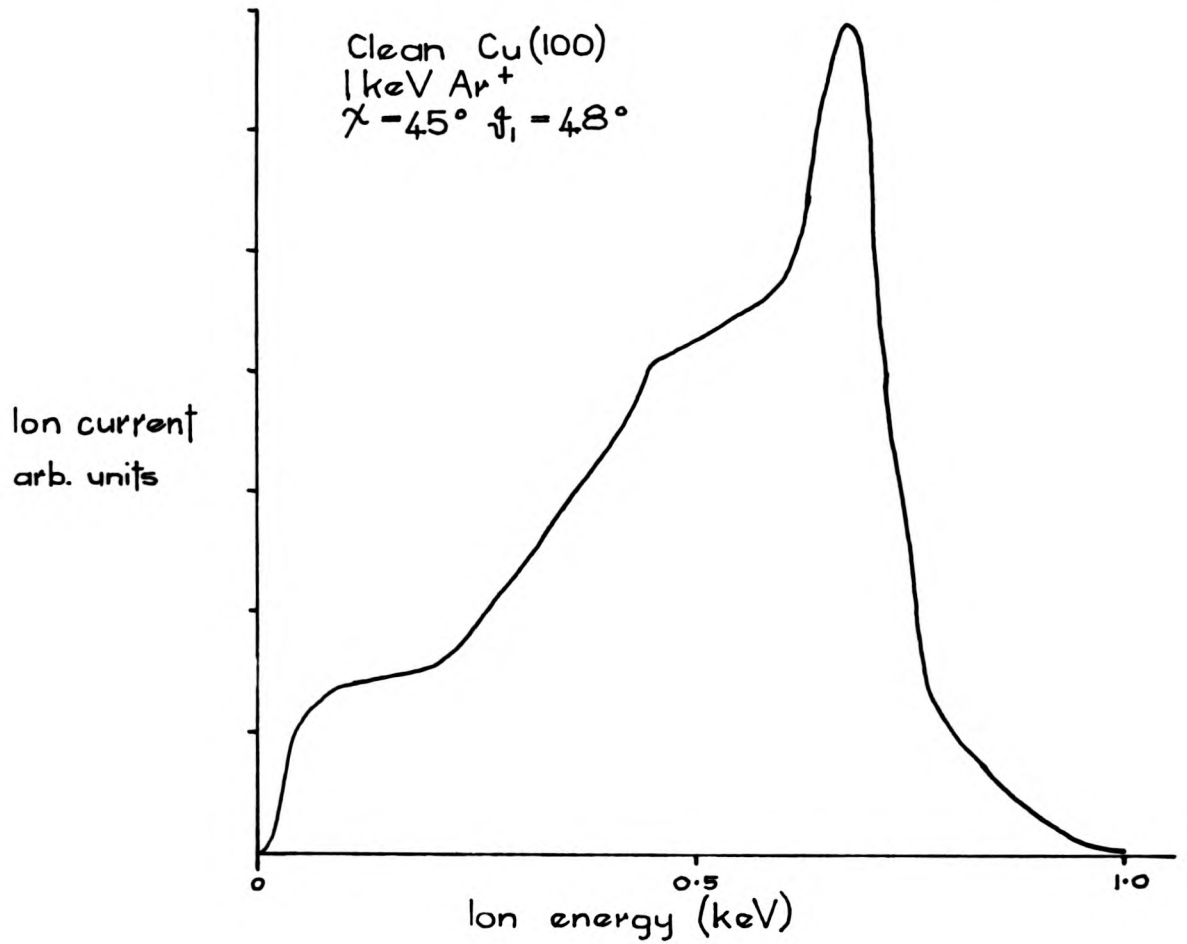
Clean Cu(100)
1keV Ar+
χ -45° ϕ1 -4.8°
Ion current
arb. units
0
0·5
1·0
Ion energy (keV)

Figure 4.28.

## Chapter 5.

## An ISS study of the Ni(100)($\sqrt{2}$x$\sqrt{2}$)R45°-O and (2x2)-C surfaces.

### Introduction.

The results of ISS on the oxygen adsorbed Ni(100) surface are presented in this chapter. This work was performed in order to obtain further understanding of the processes involved in ISS by using a known surface structure. The clean surfaces of nickel and the oxygen adsorbed surfaces were among the first to be studied using LEED I(V) data analysis. The agreement obtained between the experimental I(V) data and the theoretical I(V) curves for one particular model structure of the Ni(100)($\sqrt{2}$x$\sqrt{2}$)R45°-O system was good (1). From this analysis, the preferred site for this adsorbate is found to be a 4-fold site with the oxygen atom at a height of 0.9 Å above the nickel surface plane. A sectional view along the ⟨100⟩ ($\gamma$ = 45°) azimuth and a plan view of this structure are shown in Figure 5.1.

The ISS experiments performed on the nickel surface were similar to those reported for the copper surface. It was hoped that this information would give further insight into the surface structure of the Cu(100)($\sqrt{2}$x$\sqrt{2}$)R45°-O system. In this chapter, the effects of elastic scattering and neutralisation will be dealt with for the known Ni(100)($\sqrt{2}$x$\sqrt{2}$)R45°-O system. It will be shown that the role of neutralisation is important in the interpretation of the surface structure using ISS.

Some experiments were performed on the Ni(100)(2x2)-C structure. LEED I(V) data had already been taken with an experimental system within the Surface Physics group at Warwick (2). The aim of performing the ISS experiments on this system was to limit the number of model structures which needed to be considered for the LEED I(V) data analysis. The final structure chosen from the LEED

Structural model for the Ni (100) $(\sqrt{2} \times \sqrt{2})R45°-O$ surface

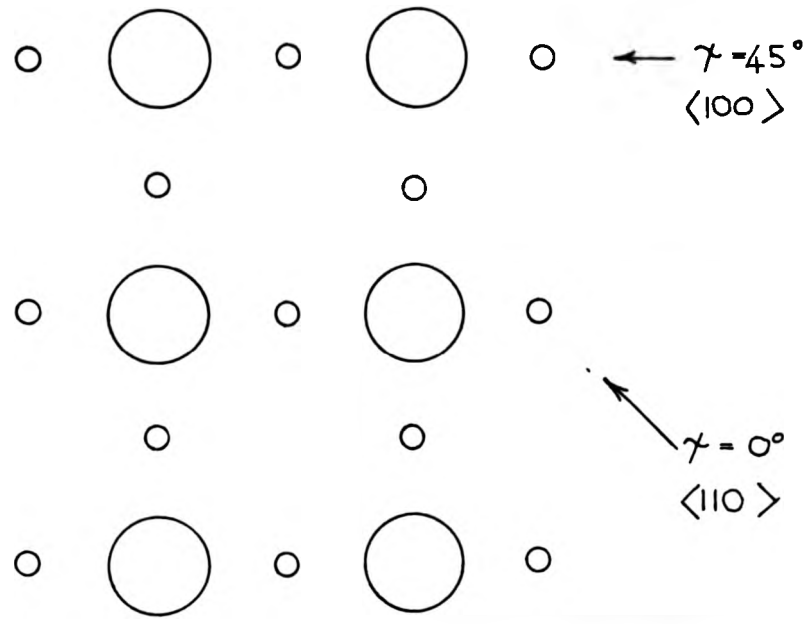


Plan view of the surface

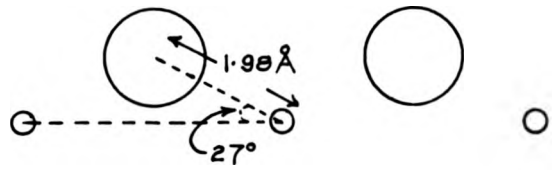


Side view of the (100) surface along the ⟨100⟩ azimuth

Figure 5.1.

studies has been used to test further the theory developed to interpret the Ni(100)($\sqrt{2}$x$\sqrt{2}$)R45°-O ISS data.

## 5.1. Cleaning Ni(100).

The initial preparation of the Ni(100) surface was identical to the procedure adopted for the Cu(100) specimen. However, nickel is chemically more reactive than copper and so more cycles of argon ion bombardment and annealing were required to produce a clean, well-ordered surface. The sample was annealed at a temperature of approximately 800 °C. An AES spectrum of the 'as loaded' sample is shown in Figure 5.2. The sample had previously been out gassed. The major contamination is caused by sulphur and carbon. As for the Cu(100) specimen, the sulphur is caused by sulphur segregating from the bulk. The carbon contamination is likely to be due both to segregation and to contamination by the residual gases in the chamber.

After approximately 15 to 20 cleaning cycles, the AES spectrum shown in Figure 5.3 was produced. This shows no peaks due to surface contamination. The LEED pattern obtained from this surface is given in Figure 5.4. It can be seen that the background intensity in the LEED pattern is much lower than for the Cu(100) case. This suggests that the quality of the crystallinity is higher for the Ni(100) surface. However, as was noted in the previous chapter, the surface sensitivity of the ISS with a scattering angle of 48° and 1.0 keV helium ions was greater than the sensitivity obtained with AES for this particular experimental arrangement. In fact, the presence of carbon was detected on this surface with ISS. A further two cleaning cycles were required to remove this carbon. It was found that a detectable level of carbon would build up on the surface within 45 minutes in a vacuum of $5 \times 10^{-10}$ torr. This limited the amount of time available for experimental measurements. The level of carbon on the surface could be reduced by heating the sample up to 800 °C.

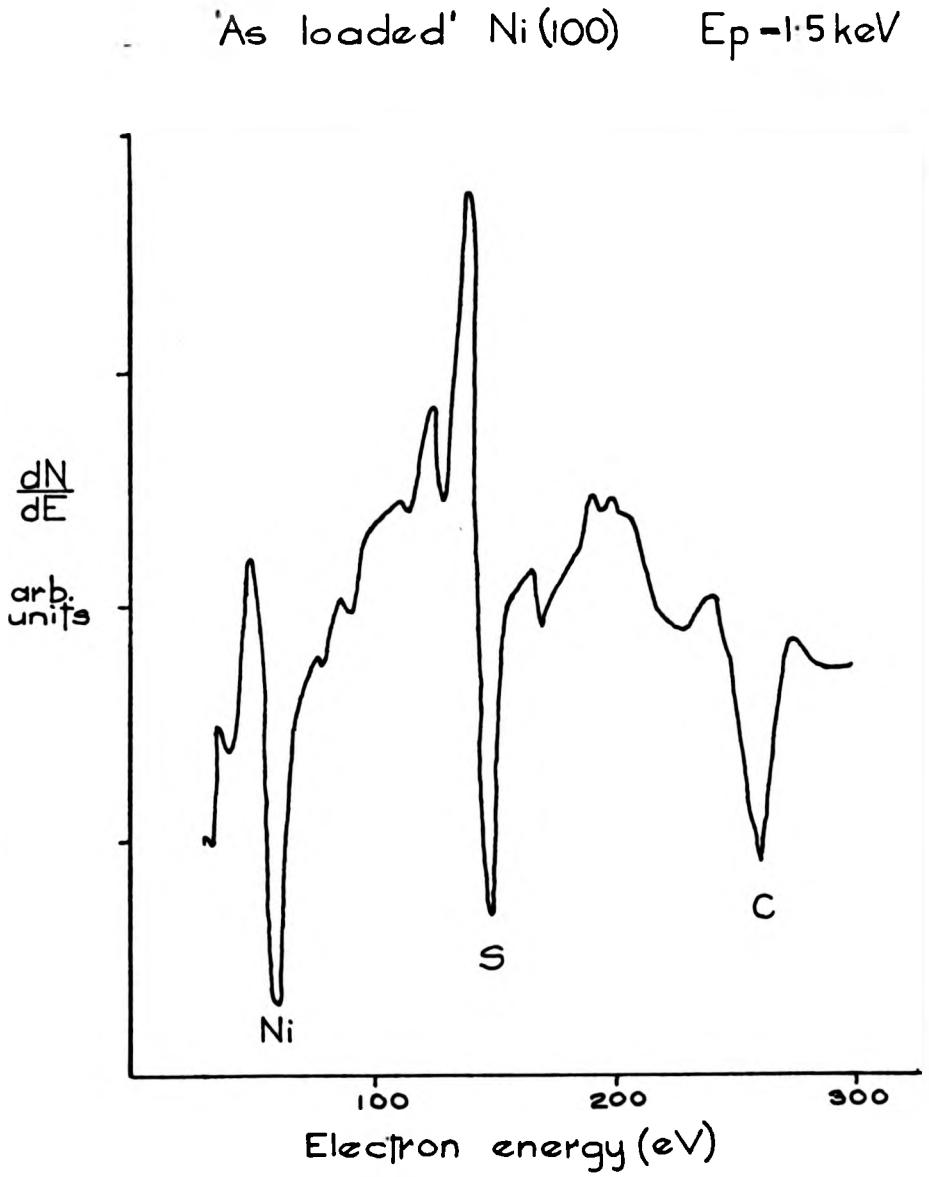
'As loaded' Ni(100) Ep=1·5keV
dN/dE
arb. units
Ni
S
C
100
200
300
Electron energy (eV)

Figure 5.2.

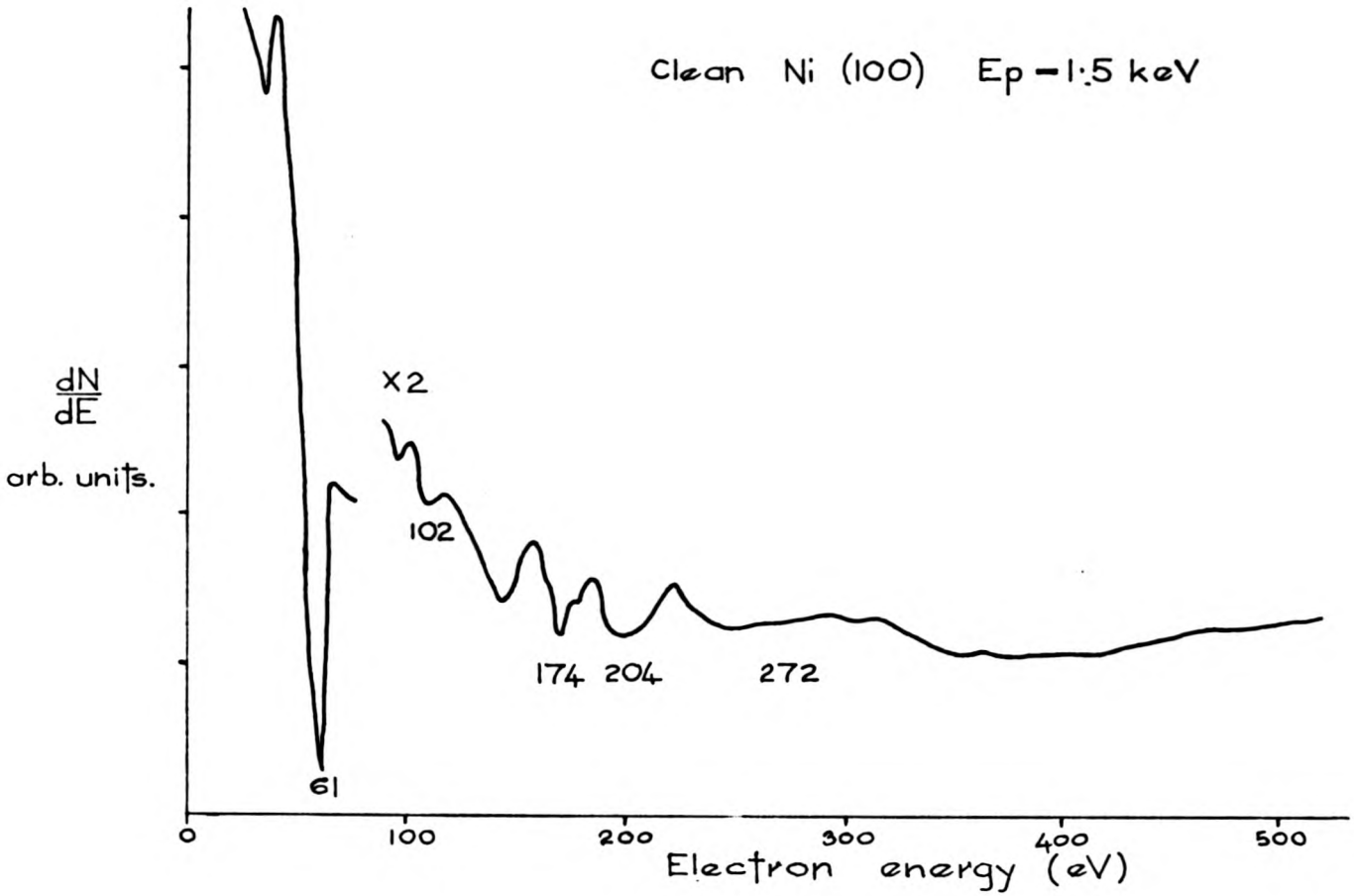
Clean Ni (100) Ep = 1.5 keV
dN/dE
arb. units.
x2
102
174
204
272
61
0
100
200
300
400
500
Electron energy (eV)

Figure 5.3.

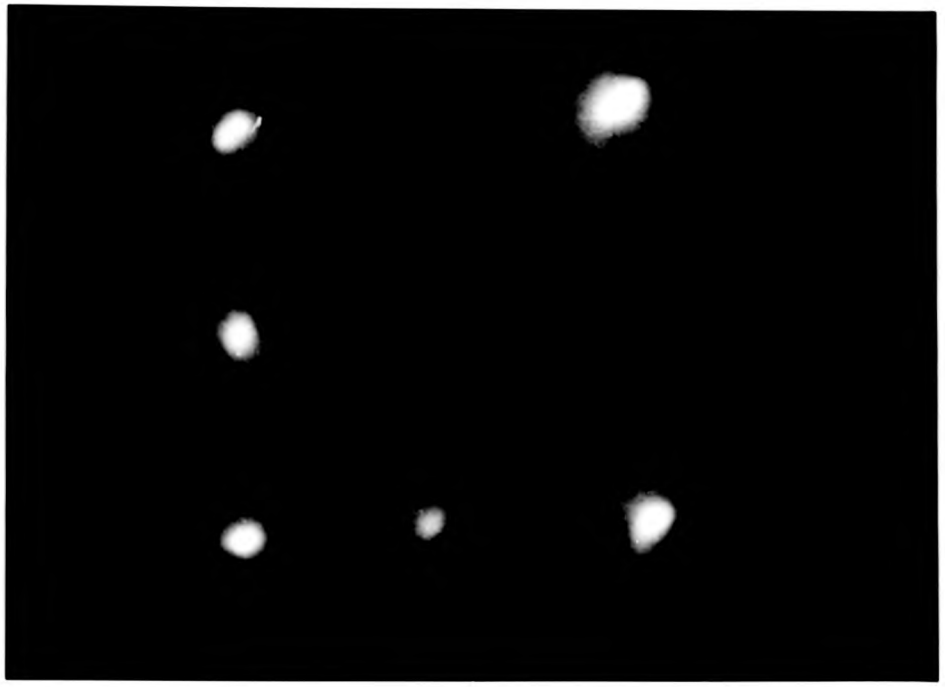

Clean Ni (100) Electron energy ≃ 100 eV

**Figure 5.4.**

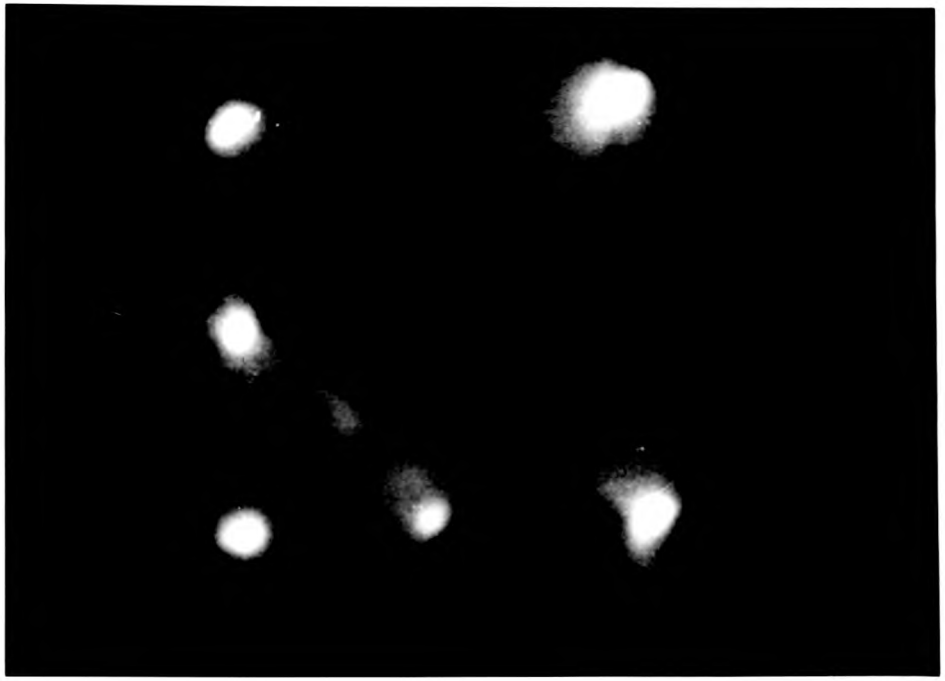

Clean Ni (100) Electron energy ≏ 100 eV

Figure 5.4.

It is likely that the carbon diffuses into the surface. The presence of residual carbon was of particular importance for the work on the Ni(100)(2x2)-C surface.

## 5.2. Oxygen adsorption on Ni(100).

Having prepared a clean, well-ordered Ni(100) surface, it was possible to study the adsorption of oxygen on that surface. In order to obtain a Ni(100)($\sqrt{2}$x$\sqrt{2}$)R45°-O structure, the sample was exposed to $5\times10^{-7}$ torr-minutes of oxygen gas at a pressure of $1\times10^{-7}$ torr at room temperature. This is less than the oxygen dose required to produce the equivalent structure on the Cu(100) surface at room temperature. A brief heating to approximately 300 °C improved the surface order as monitored by LEED. A LEED pattern obtained from this surface is shown in Figure 5.5. Again, the level of the background intensity is much less than for the oxygen adsorbed Cu(100) surface. An AES spectrum from the adsorbed surface is shown in Figure 5.6. Using the calibration of Argile and Rhead (3), the coverage of oxygen on this surface is approximately 0.3 monolayers, which is in reasonable agreement with the expected value of 0.5 monolayers.

## 5.3. ISS on clean and oxygen adsorbed Ni(100).

The majority of the experiments with ISS were performed with 1.0 keV helium ions, whilst a few experiments were carried out with neon ions. An energy spectrum obtained from 1.0 keV helium ions incident on a clean nickel surface for a scattering angle of 90° is shown in Figure 5.7. As for the copper surface, there is a large peak due to helium ions scattered elastically from the nickel atoms and a small sputtered peak at low energies. The azimuthal variation was measured for the scattering angles of 90° and 48°. The results obtained are shown in Figure 5.8. The 90° scattering geometry gives

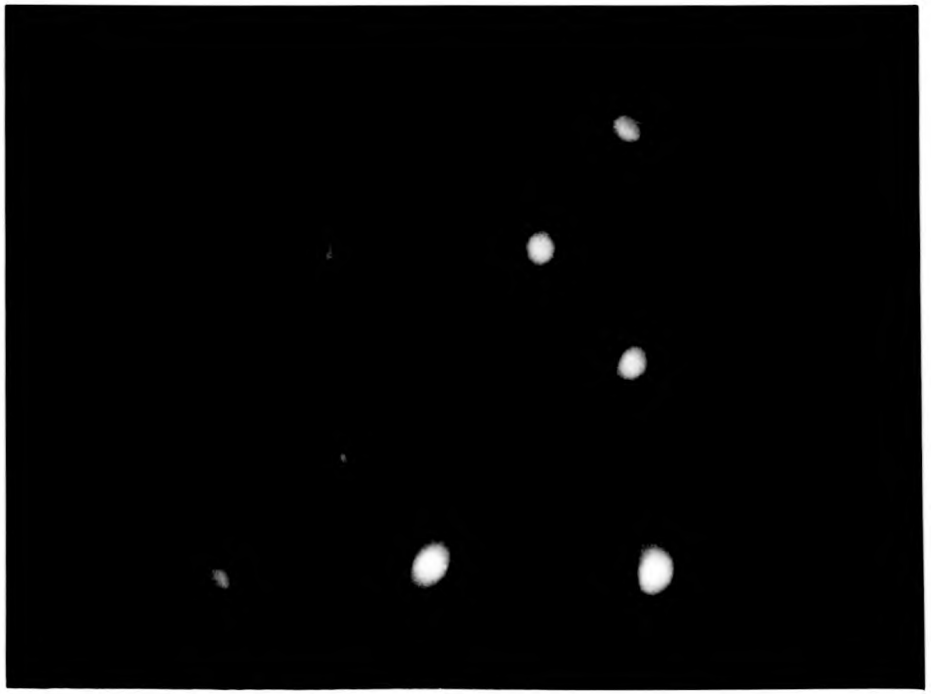

Ni (100) $(\sqrt{2} \times \sqrt{2})$ R 45° – O

Electron energy ≃ 100 eV

Figure 5.5.

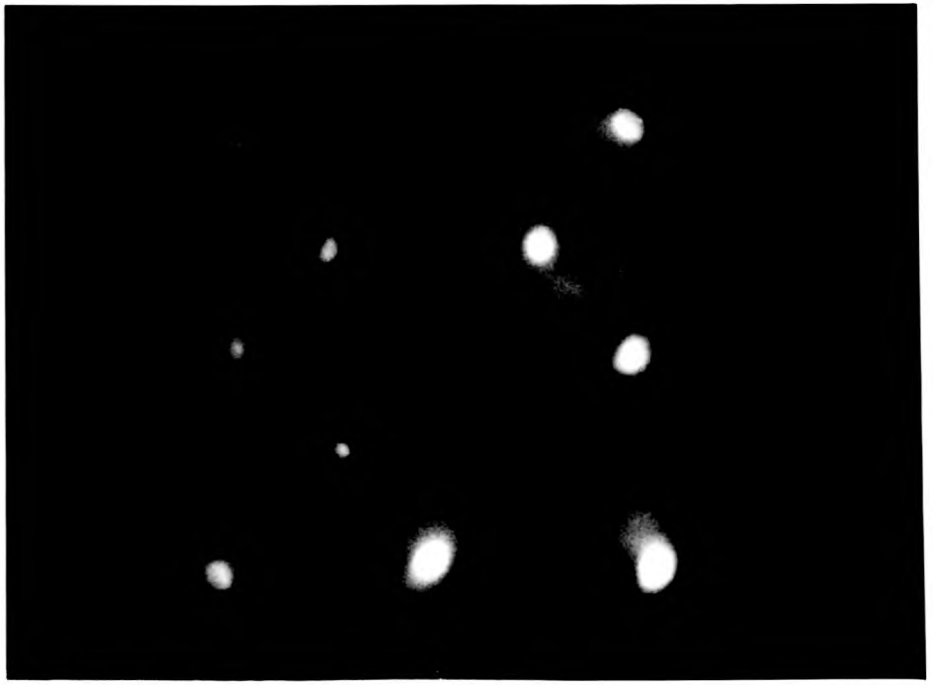

Ni (100) $(\sqrt{2} \times \sqrt{2})$ R 45° – O

Electron energy ≏ 100 eV

Figure 5.5.

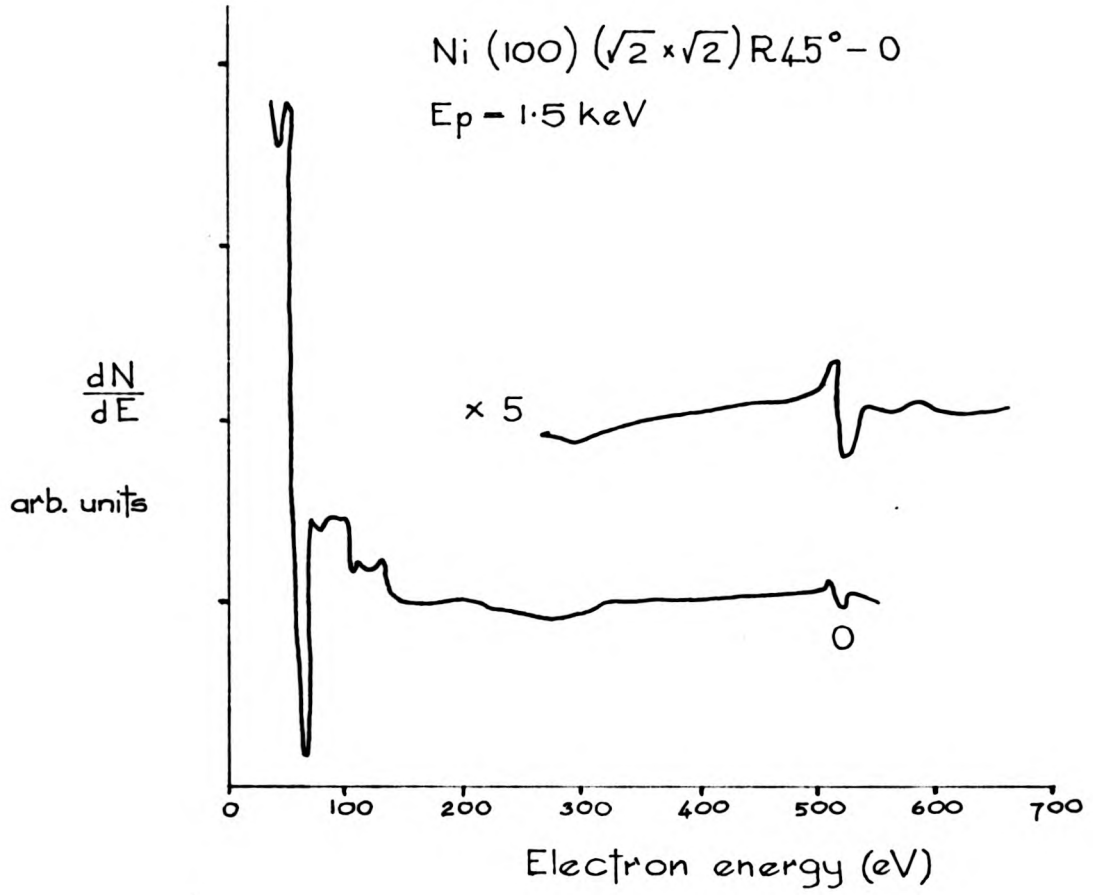
Ni (100) (√2 × √2) R45° – O
Ep – 1·5 keV
dN/dE
arb. units
× 5
O
0
100
200
300
400
500
600
700
Electron energy (eV)

Figure 5.6.

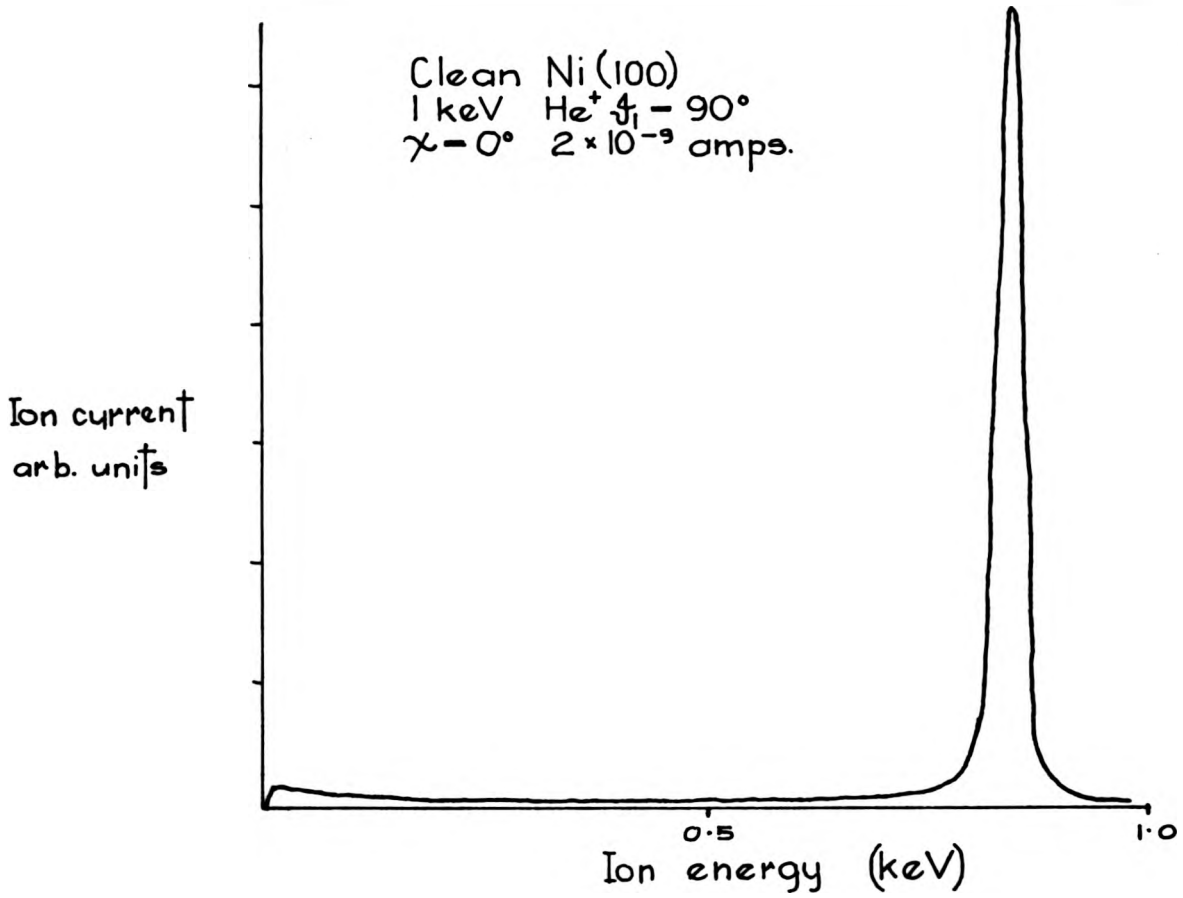
Clean Ni (100)
1 keV He+ ϕ1 = 90°
χ = 0° 2 × 10⁻⁹ amps.
Ion current
arb. units
0·5
1·0
Ion energy (keV)

Figure 5.7.

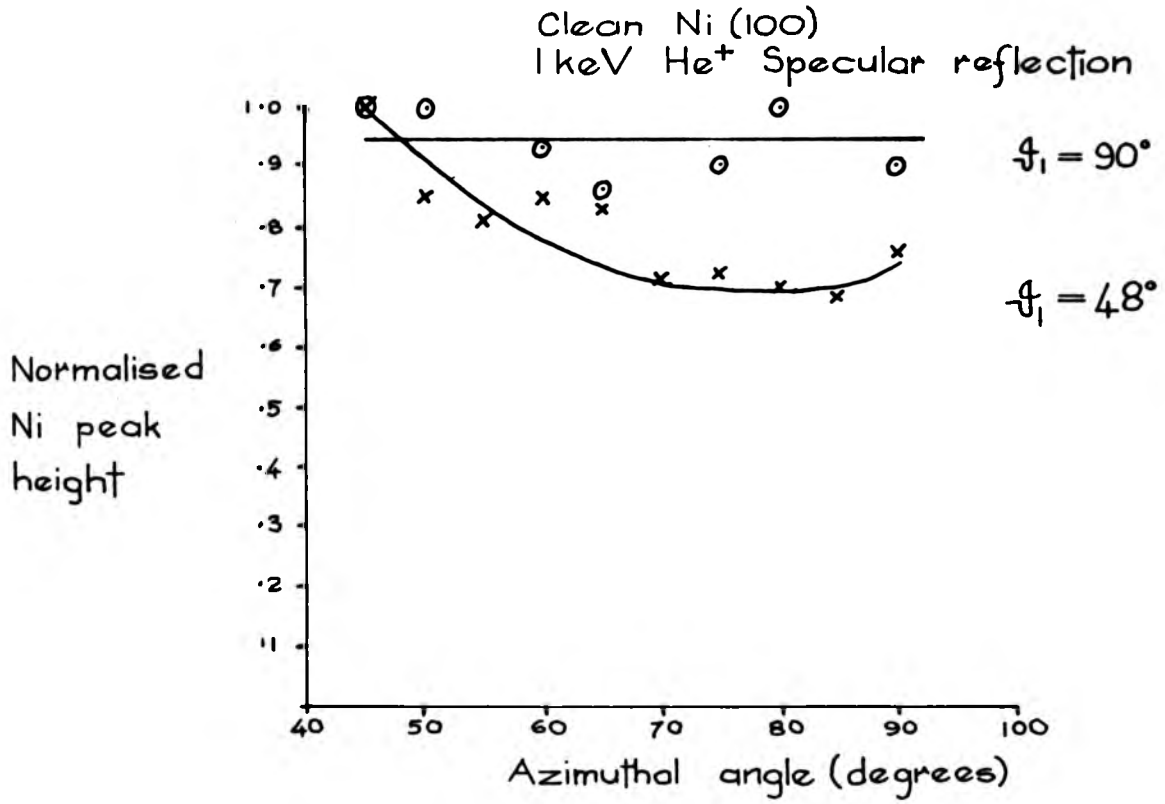
Clean Ni (100)
1keV He+ Specular reflection
Normalised
Ni peak
height
1·0
·9
·8
·7
·6
·5
·4
·3
·2
·1
40
50
60
70
80
90
100
Azimuthal angle (degrees)
ϑ1 = 90°
ϑ1 = 48°

Figure 5.8.

a straight line to within the experimental accuracy, whereas for 48° scattering there is a marked variation in the peak heights. The maximum peak height for the 48° case has been normalised to the 90° value. The polar variation at constant azimuth for these two scattering angles was also measured. The results obtained were very similar to those found for the copper surface.

ISS measurements from the adsorbed surface were taken with scattering angles of 90° and 48°. A spectrum obtained in the 45° azimuth for 90° scattering is shown in Figure 5.9. In comparison with the same spectrum for the oxygen on Cu(100) surface, it can be seen that the oxygen signal is proportionately larger on the nickel surface. Typical values for the ratio of the oxygen peak to the substrate peak for 90° scattering were

$$\left[\frac{O}{Ni}\right]_{\gamma=45^\circ} = 0.1 \qquad \left[\frac{O}{Ni}\right]_{\gamma=0^\circ} = 0.2$$

$$\left[\frac{O}{Cu}\right]_{\gamma=45^\circ} = 0.06 \qquad \left[\frac{O}{Cu}\right]_{\gamma=0^\circ} = 0.13$$

The azimuthal variation obtained from helium scattering over 90° from the nickel adsorbed surface is shown in Figure 5.10. In the figure, three different angles of incidence are included. It can be seen that as the angle of incidence is reduced, the ratio between the maximum and minimum nickel signal remains approximately constant.

A difference between the copper and nickel systems can be seen if the azimuthal variation is measured at more grazing angles of incidence. This is shown in Figure 5.11, where the polar variation for $\gamma = 0^\circ$ and $\gamma = 45^\circ$ are given for both the nickel and copper systems. The oxygen signal shadows the nickel atoms to a larger extent than for the copper atoms. In fact, the nickel peak has nearly vanished below angles of incidence of 15°. This can be seen more clearly in Figure 5.12, where the ratio of the oxygen peak to the substrate peak is given.

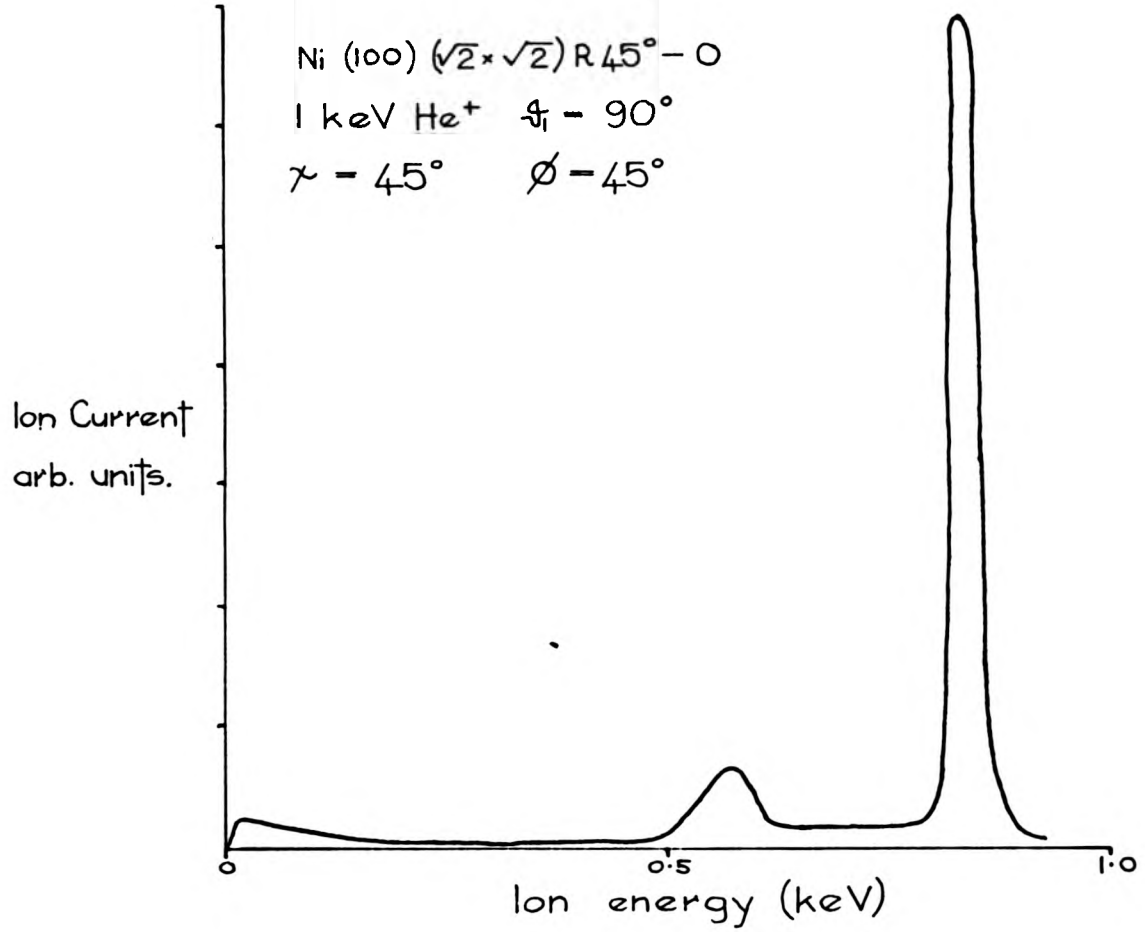
Ni (100) (√2 × √2) R 45° – O
1 keV He+ ϕi = 90°
χ = 45° ϕ = 45°
Ion Current
arb. units.
0
0·5
1·0
Ion energy (keV)

Figure 5.9.

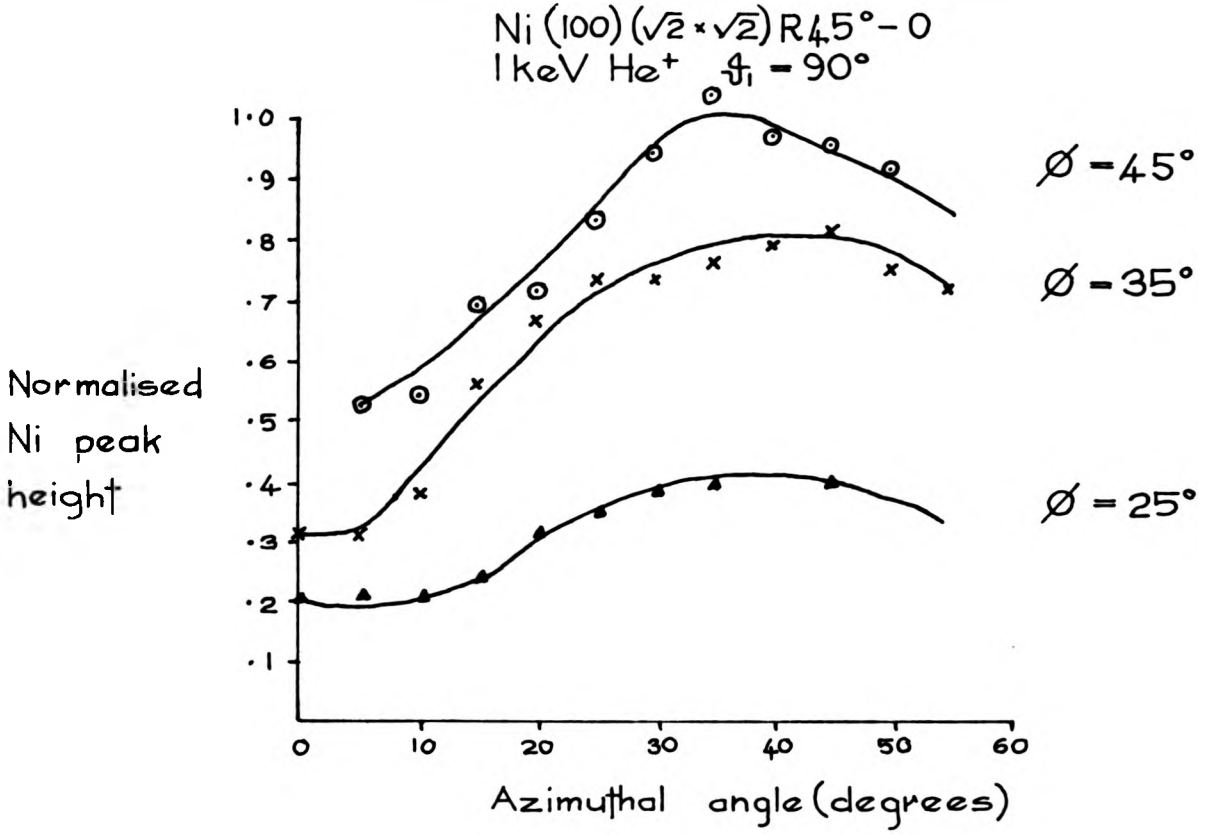
Ni (100) (√2 × √2) R45° - O
1 keV He+ ϑi = 90°
Normalised
Ni peak
height
1·0
·9
·8
·7
·6
·5
·4
·3
·2
·1
0
10
20
30
40
50
60
Azimuthal angle (degrees)
Ø = 45°
Ø = 35°
Ø = 25°

Figure 5.10.

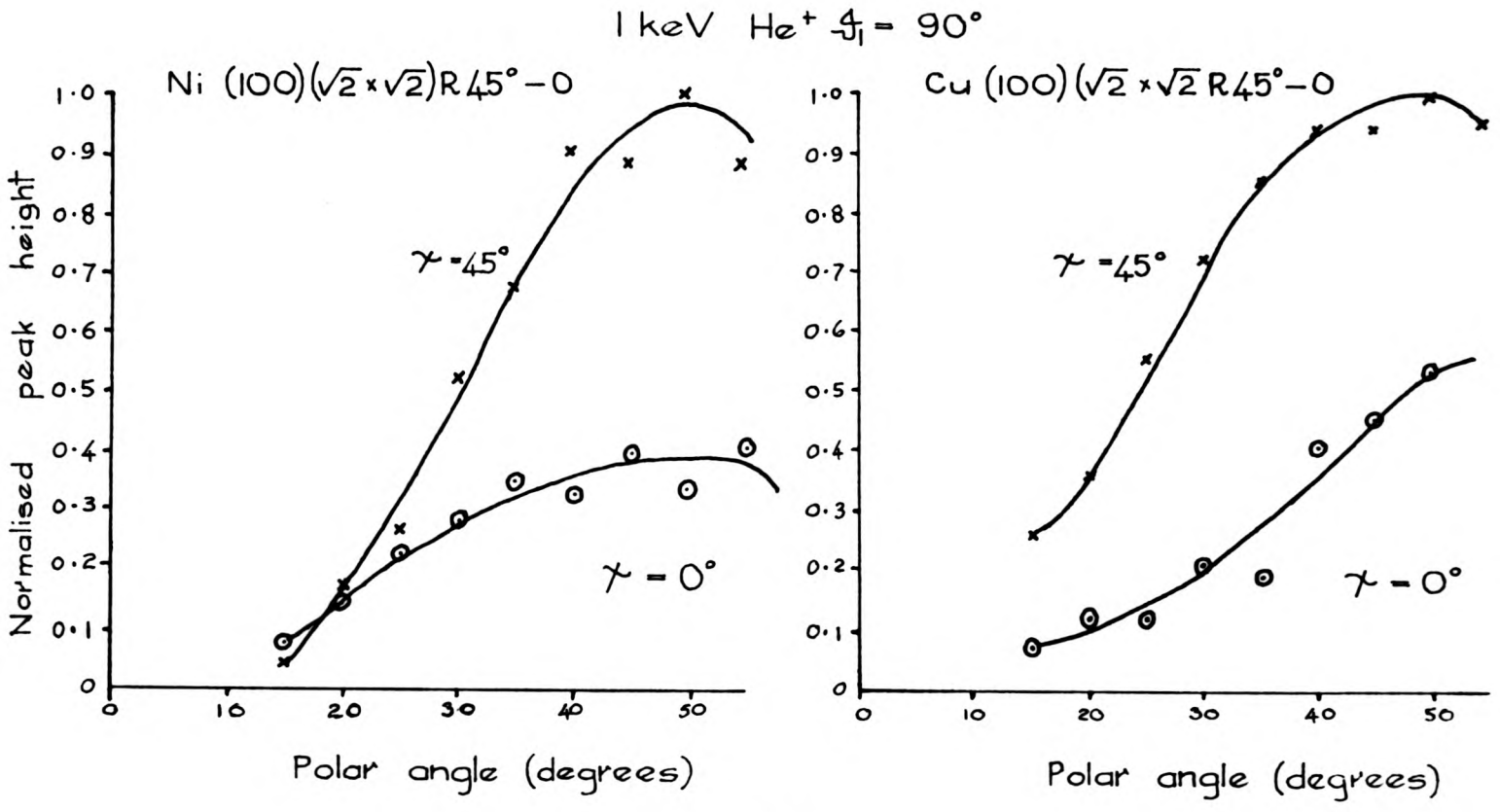
1 keV He+ φ1 = 90°
Ni (100)(√2 × √2)R45°–O
Cu (100)(√2 × √2 R45°–O
Normalised peak height
χ = 45°
χ = 0°
Polar angle (degrees)
0
0·1
0·2
0·3
0·4
0·5
0·6
0·7
0·8
0·9
1·0
10
20
30
40
50

Figure 5.11.

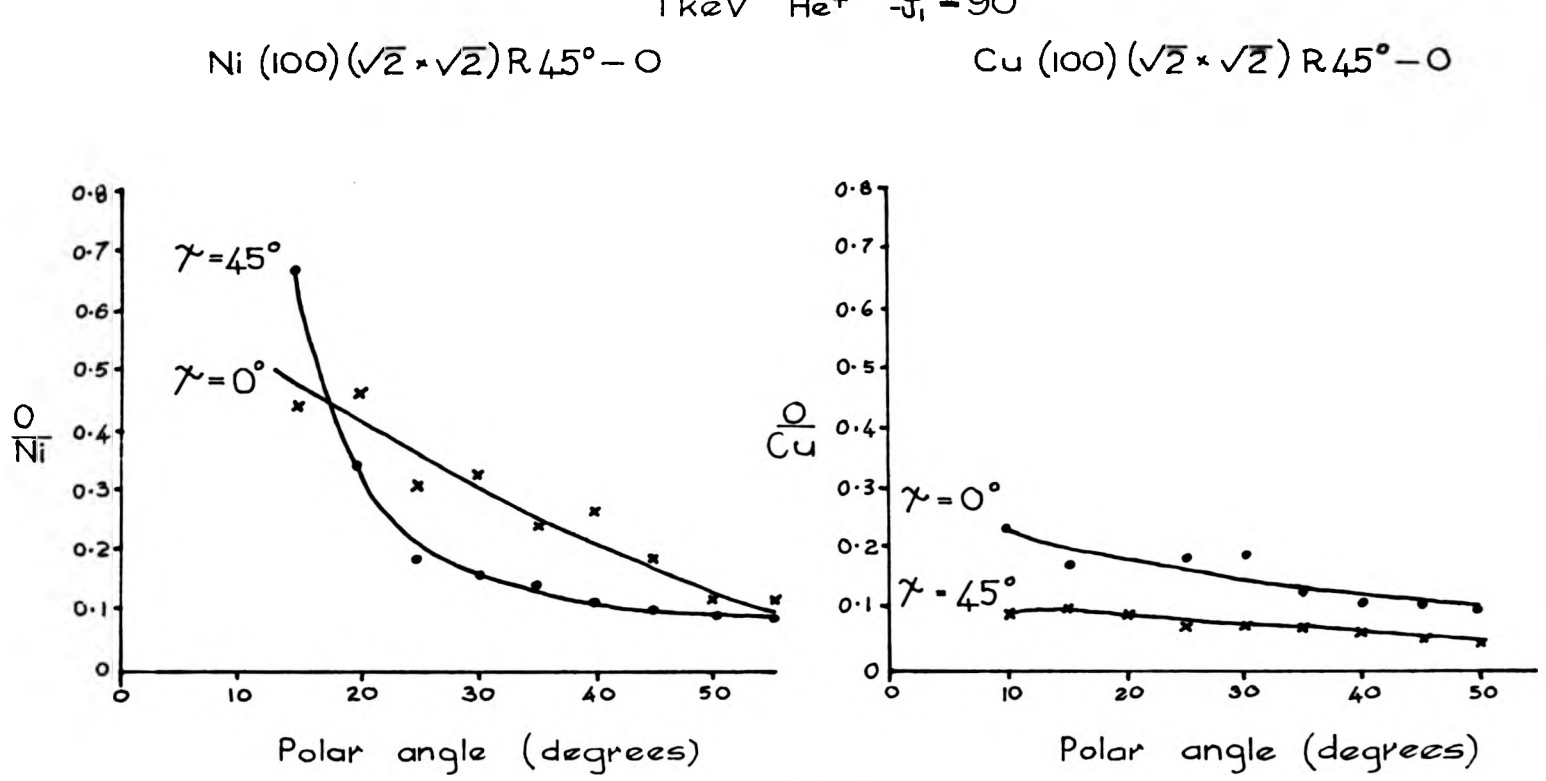
1 keV He+ -ϑ1 = 90°
Ni (100) (√2 × √2) R 45° – O
Cu (100) (√2 × √2) R 45° – O
O/Ni
O/Cu
χ = 45°
χ = 0°
χ = 0°
χ = 45°
0·8
0·7
0·6
0·5
0·4
0·3
0·2
0·1
0
0
10
20
30
40
50
Polar angle (degrees)
Polar angle (degrees)

Figure 5.12.

ISS measurements were also performed for a scattering angle of $48^\circ$. Figure 5.13 shows energy spectra obtained from 1.0 keV $He^+$ ions at azimuthal angles of $0^\circ$ and $45^\circ$. It can be seen that the oxygen signal is increased by changing from the $45^\circ$ to the $0^\circ$ azimuth, whilst the nickel peak is severely attenuated. The values of the oxygen and nickel peak heights for the two major azimuths were measured at different angles of incidence. It was found that the ratio of the oxygen peak to the nickel peak remained constant as the angle of incidence was made more glancing. Thus, there was no evidence of the oxygen peak 'cutting off' the nickel peak more quickly in one particular azimuth. A complete azimuthal variation for $\vartheta_1 = 48^\circ$ is shown in Figure 5.27.

Figure 5.14 shows a complete azimuthal variation for the Ni(100) $(\sqrt{2}x\sqrt{2})R45^\circ$-O surface with $\vartheta_1 = 90^\circ$. The level of attenuation of the oxygen signal is not as large as that shown in Figure 5.12. This illustrates the variation in ISS results obtained from different experimental runs. This may be due to a variation in the absolute oxygen coverage present after separate adsorption cycles.

Figure 5.15 shows a complete energy spectrum from clean Ni(100) with 1.0 keV neon ions scattered over $90^\circ$. The level of sputtered ions is much larger than for helium ions. The azimuthal variation obtained for 1.0 keV neon ions for this scattering angle was a straight line to within $\pm$ 10%. Polar variations for the $\gamma = 0^\circ$ and $\gamma = 45^\circ$ were measured. The results obtained for both the azimuthal and polar variations were similar to those found for neon scattering from clean Cu(100).

## 5.4. Discussion of the ISS results.

In this section, model calculations have been used in order to estimate the degree of shadowing on the clean nickel surface and the oxygen adsorbed surface. The azimuthal variations obtained at constant polar angle will be considered in most detail. This is

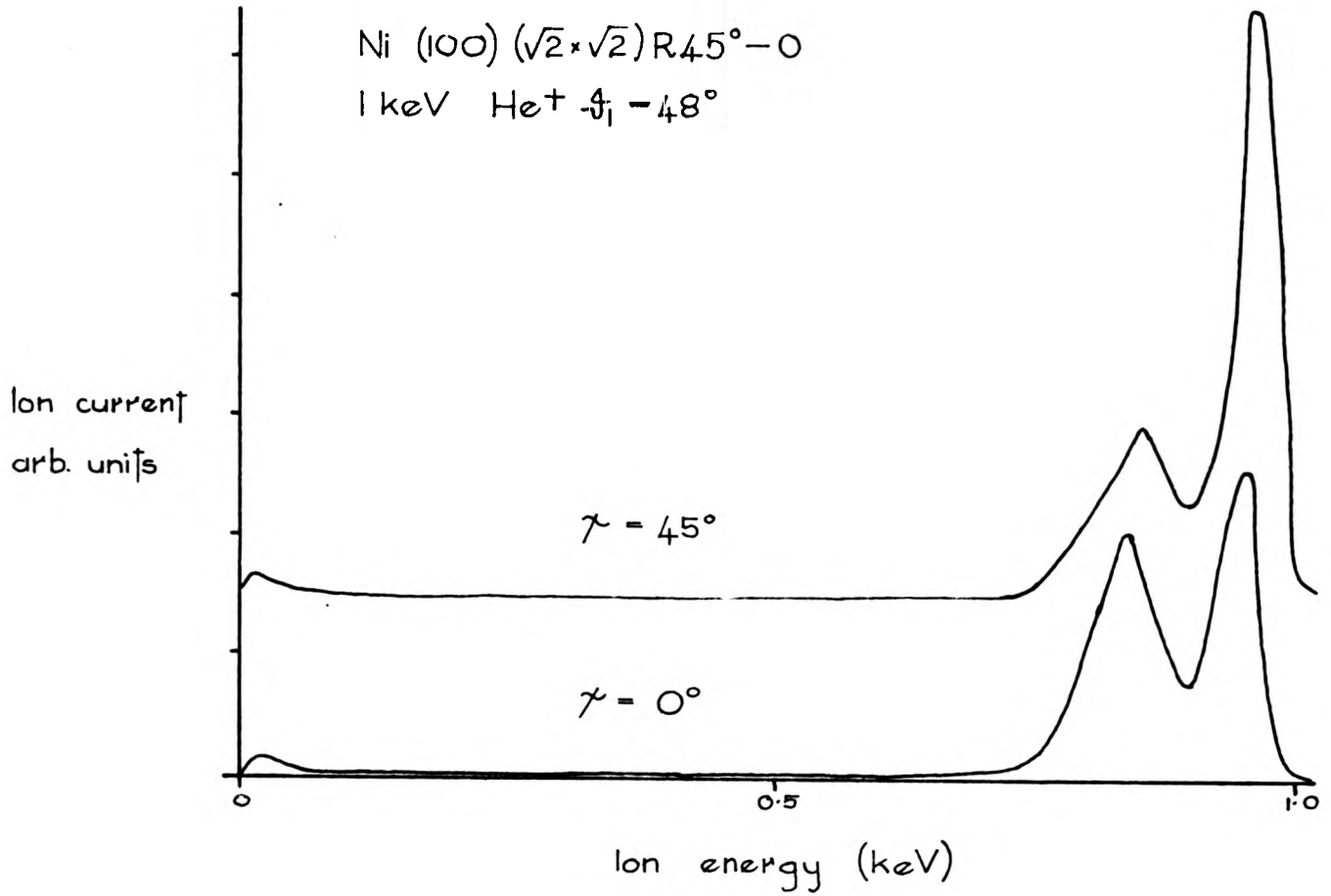
Ni (100) (√2 × √2) R45° – O
1 keV He+ ϑ1 = 48°
Ion current
arb. units
γ = 45°
γ = 0°
0
0·5
1·0
Ion energy (keV)

Figure 5.13.

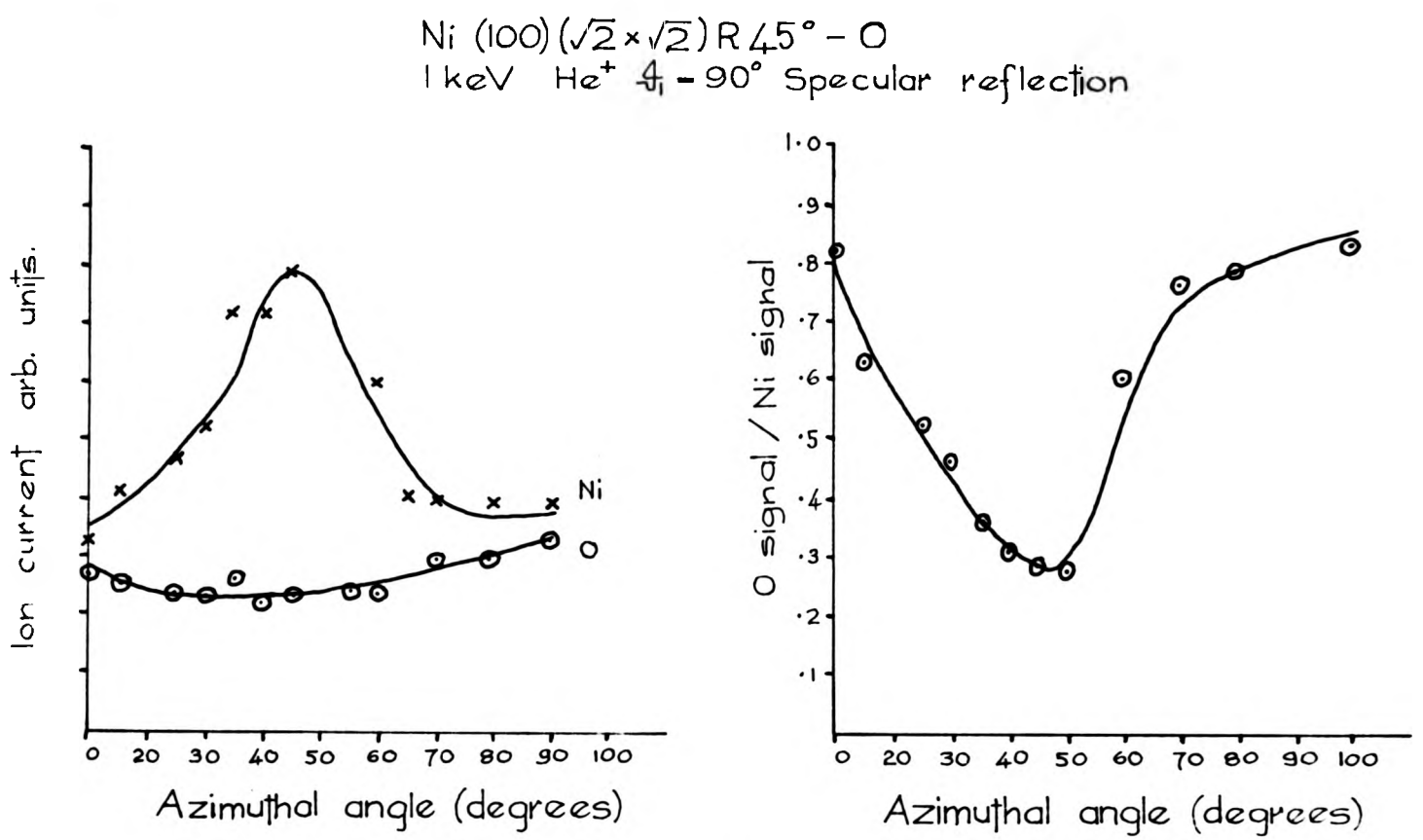
Ni (100) (√2 × √2) R 45° – O
1 keV He+ ϕi = 90° Specular reflection
Ion current arb. units.
Ni
O
0 20 30 40 50 60 70 80 90 100
Azimuthal angle (degrees)
O signal / Ni signal
1·0
·9
·8
·7
·6
·5
·4
·3
·2
·1
0 20 30 40 50 60 70 80 90 100
Azimuthal angle (degrees)

**Figure 5.14.**

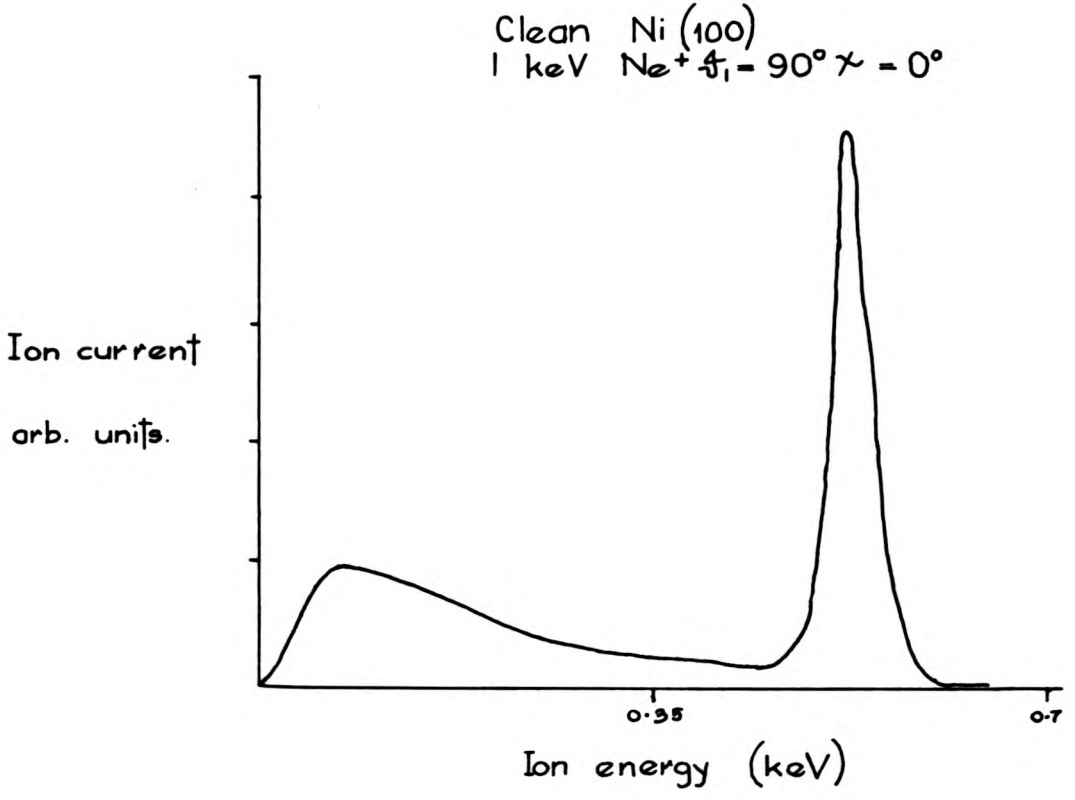
Clean Ni (100)
1 keV Ne+ $\phi_1 = 90°$ $\chi = 0°$
Ion current
arb. units.
0·35
0·7
Ion energy (keV)

Figure 5.15.

because qualitative interpretation of the polar angle variation is difficult due to the effect of the changing neutralisation probabilities. The two major factors which affect the ISS yield are elastic scattering and ion neutralisation. These two influences will be dealt with in turn.

5.4.1. Elastic Scattering.

As was shown in Chapter 2, the major effects of elastic scattering can be understood by considering the shadow cone. Figure 5.16 shows the trajectories of 1.0 keV helium ions approaching an oxygen atom. The scattering of the incident ions has been calculated using the Thomas-Fermi potential in the Moliere approximation. The trajectories have been simplified as two straight lines, rather than straight lines a long distance from the oxygen atom which join smoothly near the atom. Any atoms which are included within the shadow cone will not be able to contribute to the scattering. The shadowing effect for 90° scattering from a clean Ni(100) surface is illustrated in Figure 5.17. Here, a section in the $\gamma = 45°$ ( $\langle 100 \rangle$ ) azimuth through a clean Ni(100) surface is shown. The shadow cone for 1.0 keV helium ions scattered by nickel atoms drawn from the top nickel layer at an angle of incidence of 45° can be seen. The nickel atoms below the top layer are represented in this diagram by circles with a radius equal to the impact parameter for 90° scattering. This shows that only the top layer of nickel atoms can contribute to the ISS signal. In contrast, in the $\gamma = 0°$ ( $\langle 110 \rangle$ ) azimuth, alternate layers of nickel atoms are displaced laterally. Thus, the second layer of atoms will not be included within the shadow cones. This increase in the number of scattering centres should lead to an increased yield in this azimuth. However, the experimental result (see Figure 5.8) shows no azimuthal variation under these conditions. This suggests that any helium ions

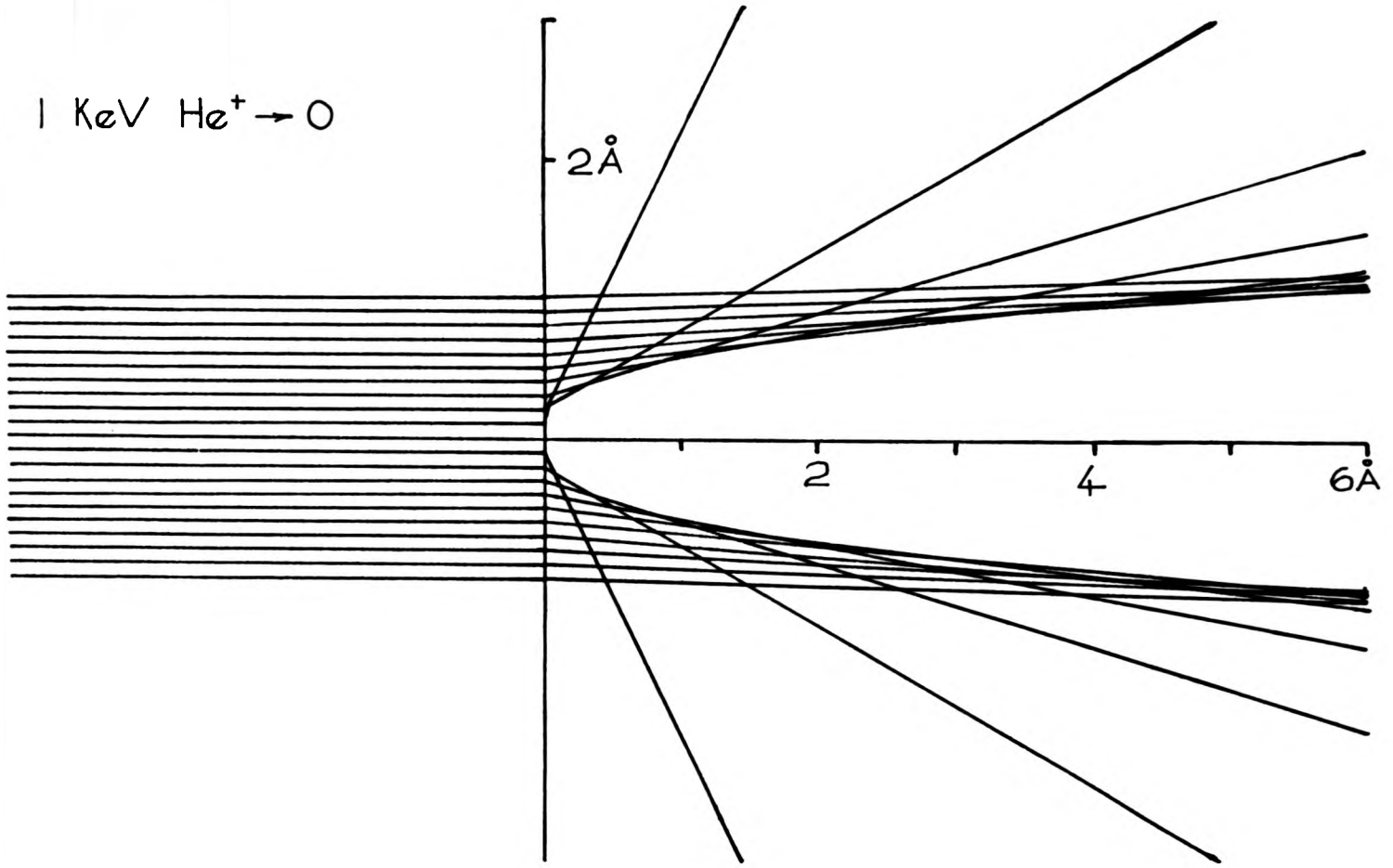


Figure 5.16.

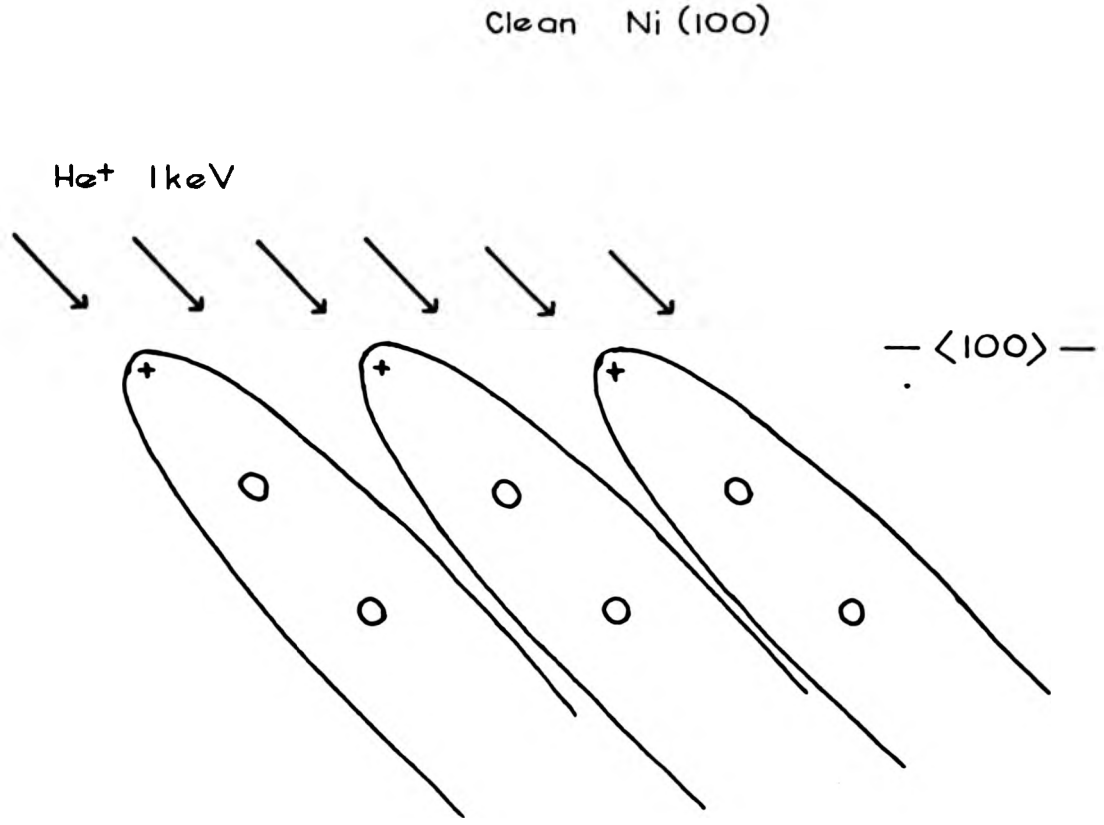


Figure 5.17.

which penetrate the first nickel layer will be neutralised.

At grazing incidence, the shadow cone model shows that single scattering is not possible. This is because each atom lies in the shadow cone of the previous atom. Thus, a second way of investigating elastic shadowing is required for these conditions. The type of collisions which are most likely at grazing incidence along low index azimuths of a crystal are double and multiple scattering events. In order to estimate the effect of such collisions, a calculation must be made which takes account of the scattering by successive atoms in a chain. Calculations of this kind have been performed previously for very grazing angles and for heavier incident ions and higher energies.

Figures 5.18 and 5.19 show the results of chain scattering from a clean Cu(100) surface for an angle of incidence of $24^{\circ}$, which is specular reflection for $\vartheta_1 = 48^{\circ}$. The spacing of the atom in the low index azimuths of the Cu(100) surface has been used for the spacing of the atoms in the chain. Calculations such as these would yield similar results if performed on the Ni(100) surface. The calculations assume that each scattering event is separate and the trajectories can be approximated as for the shadow cone. The helium on nickel scattering was treated using the Thomas-Fermi potential and the scattering angles were calculated as shown in Chapter 2. In the computer simulation, ions are 'fired' along trajectories regularly spaced along the chain. Hence, the density of the points in Figures 5.18 and 5.19 indicates the relative probability of scattering or the intensity of the ISS signal. The calculations show the characteristic scattering loops with maximum and minimum possible scattering angles. The upper part of the loop is dominated by double scattering and the lower part dominated by single scattering. The shorter atom spacing in the $\langle 110 \rangle$ direction leads to a larger minimum scattering angle. Thus, the specular

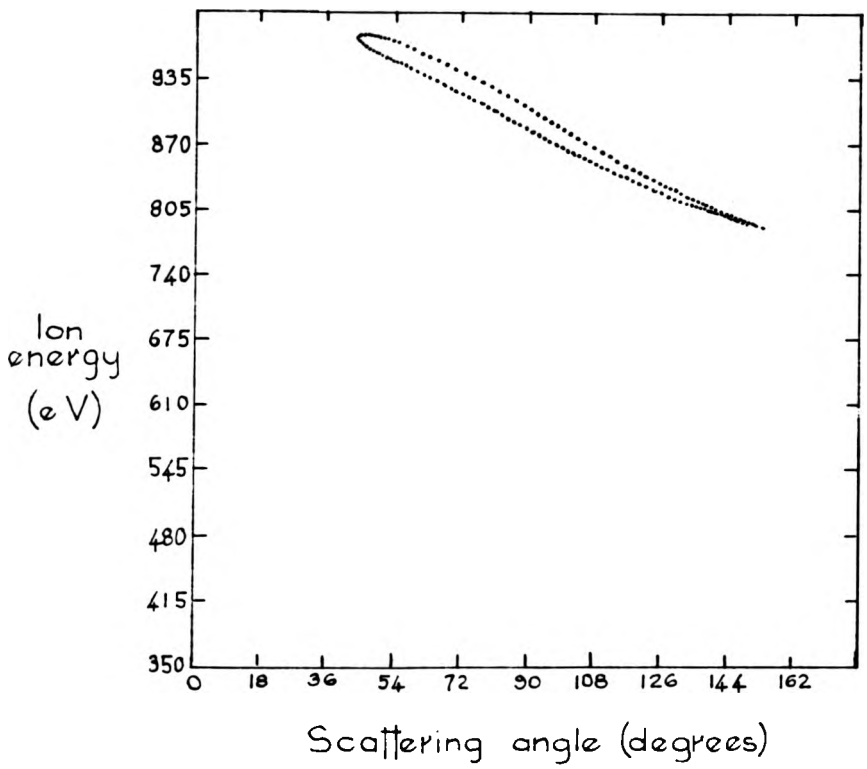


1 keV $He^+$ on Cu (100)

$\gamma = 0°$ (<110>) $\phi = 24°$

8 atoms in the chain

Space between atoms 2·55 Å

**Figure 5.18.**

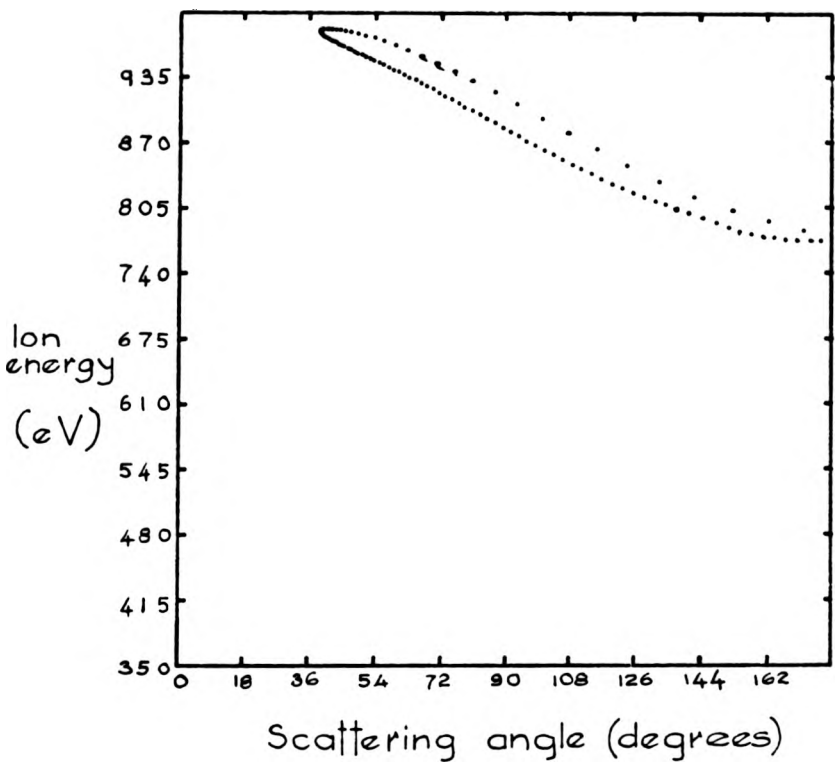


1 keV $He^+$ on Cu (100)

$\chi$ - 45° (<100>) $\phi$ = 24°

8 atoms in the chain

Space between atoms 3·61 Å

Figure 5.19.

reflection ( $\phi = 24^\circ$ ) for $48^\circ$ scattering is closer to the end of the loop in this azimuth. It follows that a higher intensity would be expected which contains more double scattering events. Therefore, this type of calculation suggests, considering only elastic scattering, that the maximum ISS signal is along the $\langle 110 \rangle$ , $\gamma = 0^\circ$ direction, which is the opposite of the experimental result obtained in Figure 5.8. Thus, the clean surface azimuthal anisotropy cannot be attributed to elastic scattering effects.

Similar problems in the interpretation occur in attempting to understand the experimental results obtained from the Ni(100)-$(\sqrt{2}x\sqrt{2})R45^\circ$-O surface shown in Figure 5.14. A schematic diagram of the accepted adsorbate structure was given in Figure 5.1. The oxygen atoms are shown as circles with a radius equal to the shadow cone in Figure 5.16 at a distance 1.98 Å behind the atoms. This corresponds to the shadow size for these atoms relative to the top nickel layer in the $\langle 100 \rangle$ azimuth at $\phi = 27^\circ$. However, the effective size of the oxygen atom is similar for all neighbouring nickel atoms. From Figure 5.1, it can be seen that for an angle of incidence of $24^\circ$ the oxygen atoms will totally shadow alternate nickel atom rows along the $\langle 100 \rangle$ direction, whilst no shadowing should occur along the $\langle 110 \rangle$ direction. Thus, approximately twice the signal from nickel would be expected in the $\gamma = 0^\circ$ direction to the $\gamma = 45^\circ$ direction. This conclusion is supported by more sophisticated 'chain' and layer calculations, where two dimensional surface atoms are included. Again, this conclusion is in direct contradiction to the experimental result shown in Figure 5.14.

These elastic scattering arguements can also be applied to the $90^\circ$ scattering case from the adsorbed surface. With $\gamma = 45^\circ$, the nickel atoms in the $\langle 100 \rangle$ row lie just outside the oxygen shadow cone. These atoms will experience an increased ion flux as can be seen from the shadow cone. This 'ion focusing' can lead

to an increased ion yield and so could account for the lower nickel signal in the $\gamma = 0^{\circ}$ direction relative to the $\gamma = 45^{\circ}$ direction. However, as the consideration of the elastic effects has not allowed the interpretation of the other major features of the ISS data, it is clearly necessary to assess the possible reasons for this problem, rather than considering more subtle elastic scattering effects.

5.4.2. Ion-Atom Neutralisation.

The second factor which affects the scattered ion yield is ion neutralisation. In previous studies using ISS for surface structure analysis (for example, see ref. (5)) a simple ion-surface neutralisation model has been used to interpret ISS data from clean and adsorbate covered surfaces. This type of neutralisation, as was shown in Chapter 2, predicts that the rate of neutralisation is independent of the azimuth of the crystal or the position of an adsorbate atom. However, there is evidence that the neutralisation processes in ISS require the consideration of the interaction of the incident ion with individual target atoms. A particular example of this is where ion yields oscillate with ion energy for certain ion-atom combinations (6).

A general consequence of an ion-atom neutralisation process is that the closer the trajectory of the ion passes to an atom, the greater the neutralisation probability. Hence, it is likely that the rate of neutralisation will be dependent upon the crystallography of the surface. It is this second type of neutralisation which appears to dominate the experimental results reported here.

An attempt to quantify ion-atom neutralisation can be made by analogy with the ion-surface neutralisation model developed by Hagstrum (7) which is described in Chapter 2. Thus, it is assumed that the neutralisation rate for an ion, a distance r from a surface

atom, is given by A exp(-ar), where A and a are constants. The experimental results show no evidence of multiple scattering due to the high neutralisation rate. Thus, it is only necessary to consider ions which pass close to only one atom. As these ions suffer only weak elastic scattering from all other atoms, their trajectories can be considered as straight lines of constant velocity v, characterised by the impact parameter b. Figure 5.20 shows a diagram of this trajectory. If x is the distance along this path relative to the distance of closest approach, then

$$r = (x^2 + b^2)^{1/2}$$

The rate of neutralisation is thus given by

$$R(r) = A \exp - a(x^2 + b^2)^{1/2}$$

The probability of the ion not being neutralised is

$$P_{ion} = \exp - \int R(r)dt$$

In this case, the integral must be evaluated from $r = -\infty$ to $r = b$. If the scattering is weak, the probability of being neutralised on the incoming and outgoing paths will be equal. Hence, the total probability of the ion not being neutralised is given by

$$P_{ion} = \exp -2\int_{r=-\infty}^{r=b} A \exp -ar.dt = \exp -2R_{tot}$$

As shown above

$$r^2 = x^2 + b^2 \quad \text{and } x = vt \text{ if } t = 0 \text{ when } x = 0$$

Hence,

$$dx = vdt \quad \text{and} \quad r = b \text{ for } x = 0 \text{ and } r = \infty \text{ for } x = \infty$$

Therefore,

$$R_{tot} = \int_{r=-\infty}^{r=b} A \exp -ar.dt = \int_{-\infty}^{0} \frac{A}{v} \exp -a(x^2 + b^2)^{1/2}.dx$$

Thus,

$$P_{ion} = \exp - \frac{2A}{v} \int_{-\infty}^{0} \exp -a(x^2 + b^2)^{1/2}.dx = \exp - \frac{2A}{av}.ab.K_1(ab) \qquad (1)$$

where $K_1$ is a modified Bessel function.

This simple model for ion-atom neutralisation shows that $P_{ion}$ is a function of the impact parameter b and the constants A and a. A number of values for the constants A and a have been used, based

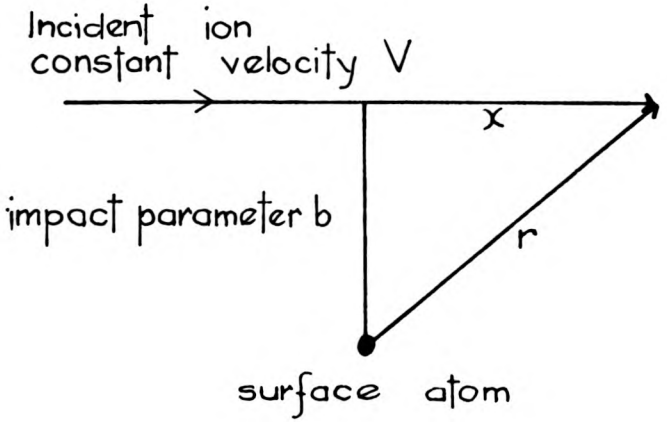


The trajectory of the incident ion over atoms which are not the principle scatterer

Figure 5.20.

on the values which have been successful in describing ion-surface neutralisation (8). Table 5.1 shows the effect of varying the values of the parameters A and a for clean Ni(100) with a scattering angle of 48°. As the overall neutralisation was assumed to be dependent upon the value of A exp-ar, the probability of an ion escaping neutralisation would be expected to increase as A decreases and a increases. This overall trend can be seen in the table. The ratio of the peak in $\gamma = 0°$ and $\gamma = 45°$ directions is also shown in the table. This shows that as the overall degree of ion-atom neutralisation becomes greater, the variation between the predicted peak heights for the two azimuths increases.

The calculations were performed assuming that the elastic scattering could be described by a single scattering event from a target atom which was one of a cluster of 25 nickel top layer atoms and (for the adsorbate structure) 9 oxygen overlayer atoms. The neutralisation due to all these atoms was calculated using the model developed above. However, the trajectory was separated into an inward and outward part and the integral in equation (1) was evaluated over finite limits for both parts.

$$\text{i.e.} \quad P_{ion} = \exp\left(-\frac{A}{v}\int_{-\infty}^{c} \exp(-a(x^2 + b^2)^{1/2})dx\right)$$

where c is the distance beyond the point of closest approach where the major change in direction caused by the elastic scattering takes place. This integral was solved numerically using the Gauss-Legendre quadrature method.

Using this numerical approach, it has been possible to model the surface structures which have been studied in this work. The calculations have been performed only for the two principal azimuths as the experimental results show no intermediate structure. Table 5.2 shows the theoretical and experimental azimuthal variations obtained using the values of A and a which give the most consistent experimental agreement. As was noted earlier, the reproducibility of the relative

Clean Ni (100) $\phi_i = 48°$

| a | A/v | $\chi = 0°$ | $\chi = 45°$ | $\chi = 0°/\chi = 45°$ |
|---|---|---|---|---|
| 1·3 | 0·46 | 0·032 | 0·036 | 0·889 |
| 1·3 | 0·62 | 0·010 | 0·0121 | 0·826 |
| 1·3 | 0·77 | 0·0033 | 0·0040 | 0·825 |
| 1·6 | 0·63 | 0·014 | 0·019 | 0·737 |
| 1·75 | 0·57 | 0·023 | 0·031 | 0·719 |
| 1·9 | 0·53 | 0·0331 | 0·045 | 0·733 |
| 1·9 | 0·79 | 0·0061 | 0·0094 | 0·649 |
| 2·0 | 0·35 | 0·107 | 0·130 | 0·823 |
| 2·0 | 0·40 | 0·077 | 0·097 | 0·794 |
| 2·0 | 0·60 | 0·021 | 0·030 | 0·700 |
| 2·5 | 0·40 | 0·078 | 0·100 | 0·780 |
| 2·5 | 1·00 | 0·0017 | 0·0032 | 0·531 |
| 3·0 | 0·17 | 0·331 | 0·363 | 0·912 |
| 3·0 | 1·00 | 0·0013 | 0·0023 | 0·565 |

Table 5.1.

| Scattering angle | | | 48° | | 90° | |
|---|---|---|---|---|---|---|
| Azimuth | | | ⟨110⟩ | ⟨100⟩ | ⟨110⟩ | ⟨100⟩ |
| Clean surface Ni peak | expt. | | 0·82 | 1·00 | 1·00 | 1·00 |
| | theory | | 0·82 | 1·00 | 0·97 | 1·00 |
| $(\sqrt{2}\times\sqrt{2})R45°$–O structure | Ni peak | expt. | 0·12 | 0·25 | 0·12 | 0·30 |
| | | theory | 0·15 | 0·17 | 0·31 | 0·29 |
| | O peak | expt. | 1·5 | 1·0 | 1·0 | 1·0 |
| | | theory | 1·2 | 1·0 | 1·0 | 1·0 |

For the model calculations the parameters used were —
Ni $(A/av) = 0·7$, $a = 2·0$ Å$^{-1}$ ; O $(A/av) = 0·7$, $a = 1·5$ Å$^{-1}$

Table 5.2.

peak heights from the adsorbed surface to the clean surface was not good. In fact, a variation of between 10-20% was found for this measurement. The level of error between the individual peaks for the two major azimuths was less than 10%. It has been assumed that the values of A and a may be different for nickel and oxygen atoms, but that the adsorption does not affect the values used for nickel. The values taken for the parameters in the table are a = 2.0 $Å^{-1}$ and A/av = 0.7 for nickel peaks and a = 1.5 $Å^{-1}$ and A/av = 0.7 for the oxygen peaks. These values are in reasonable agreement with those used by Tolk et al (9) for the ion-surface interaction of 1.0 keV helium ions on a copper surface (a = 1.3 $Å^{-1}$ , A/av = 1.0).

There are clearly a number of simplifications in the model which must be overcome if greater agreement is to be obtained between the experimental values and the theoretical values. The first simplification is that elastic shadowing has not been included in the calculations. The role of elastic shadowing can be included by using the shadow cone concept and the chain model developed in Chapter 2. However, the calculations involving both elastic shadowing and ion-atom neutralisation would require substantial amounts of computing time.

The second simplification which is inherent in the ion-atom model developed above is that no change in the neutralisation of the nickel atoms has been assumed between the clean and adsorbed surfaces. This is unlikely to be the case for the Ni(100)($\sqrt{2}$x$\sqrt{2}$)R45°-O surface and other chemisorbed surfaces. The ion-atom neutralisation mechanisms involve the valence electrons from the surface atom (see Figure 2.8). For the case of nickel atoms, the electrons involved are from the 3d and s-p bands. There are a large number of electrons in the 3d band and these are highly localised, whereas, the s-p band is more delocalised. The anisotropy in the clean surface neutralisation will be caused by the 3d electrons, whereas, the s-p band gives an

isotropic 'ion-surface' neutralisation level. Thus, for the clean surface, the ion-atom model can be used to gain agreement for the relative yield between the two major azimuths. The adsorption of the oxygen, being highly electronegative, will tend to displace the s-p electrons from their delocalised distribution causing them to become localised near to the oxygen atoms. Hence, the level of ion-atom neutralisation caused by nickel atoms for the adsorbed surface would be expected to be greater than for the clean surface. However, in the simple model calculations quoted in Table 5.2, the parameters a and A/av which have been chosen for the oxygen may include a contribution which was in the nickel s-p band on the clean surface. Hence, using this simple model, it is not possible to estimate the reduction of the nickel peak due to the oxygen adsorption.

It is difficult to quantify these changes in the neutralisation parameters as they have not been measured experimentally. However, the values used for the anisotropic ion-atom neutralisation used in Table 5.2 does not give a large level of neutralisation (for example, $P_{ion} \simeq 0.14$ for $\vartheta_1 = 48^\circ$). The isotropic neutralisation caused by the s-p band on the clean nickel surface could be estimated using the value for A/av found experimentally for the ion-surface neutralisation (for example, A/av = 0.7 (8)). Hence, a simple approximation for the oxygen adsorption could be made which involved removing the isotropic neutralisation caused by the nickel s-p band. This leads to more effective neutralisation processes for the oxygen atoms. These assumptions are clearly simplistic. However, they allow relatively straight-forward calculations to be made which can be used to show whether these effects lead to an improvement between the theoretical calculations and the experimental results.

Calculations using these approximations for the oxygen adsorption are shown in Table 5.3. It can be seen that the overall agreement is improved. The only defficiency is for the $\vartheta_1 = 90^\circ$ nickel

| Ni (100)$(\sqrt{2} \times \sqrt{2})$ R 45 – O structure | | | | | | |
|---|---|---|---|---|---|---|
| Scattering angle | | | 48° | | 90° | |
| Azimuth | | | ⟨110⟩ | ⟨100⟩ | ⟨110⟩ | ⟨100⟩ |
| $(\sqrt{2} \times \sqrt{2})$R45°–O | Ni peak | expt. | 0·12 | 0·25 | 0·12 | 0·30 |
| | | theory | 0·12 | 0·26 | 0·18 | 0·20 |
| | O peak | expt. | 1·5 | 1·0 | 1·0 | 1·0 |
| | | theory | 1·5 | 1·0 | 1·1 | 1·0 |

As Table 5·2 but assuming that the clean Ni surface has an ion-surface neutralisation with (A/av – 0·7) which is lost on adsorption. The oxygen parameters used were A/av – 1·7 and a – 1·3 Å$^{-1}$

Table 5.3.

scattering peak. However, it was shown in the previous section that 'ion focusing' is present under these experimental conditions. Thus, if elastic scattering was included within these calculations, the agreement might be more satisfactory.

In summary, therefore, it has been shown that the elastic shadowing model is unable to account for the observed azimuthal anisotropies, whereas a simple ion-atom neutralisation model is able to predict the general features of the experimental data. Moreover, simple approximations used for the changes in the neutralisation caused by adsorption enable the agreement between experiment and theory to be substantially improved.

## 5.5. Ethylene adsorption on Ni(100).

The adsorption of ethylene was studied with ISS in parallel with studies using LEED I(V) analysis which were performed within the Surface Physics group at the University of Warwick. The results of the LEED I(V) data on this surface structure are reported by Onuferko et al (2). ISS experiments were carried out on this surface in order to limit the number of model structures which needed to be considered for the LEED I(V) analysis. It is also useful in giving a further structure for testing the ion-atom neutralisation model developed in the previous section.

The adsorption was performed at a sample temperature of approximately 400 °C and with an ethylene dose of $1 \times 10^{-6}$ torr-minutes. An AES spectrum of the surface is shown in Figure 5.21. The LEED pattern obtained from the sample is given in Figure 5.22. The sample was reheated briefly to approximately 150 °C after adsorption to improve the intensity of the extra spots. These spots were only visible when the crystal had cooled to room temperature. The pattern corresponds to a Ni(100)(2x2)-C overlayer structure. However, the pattern has a number of spots missing for the complete symmetry.

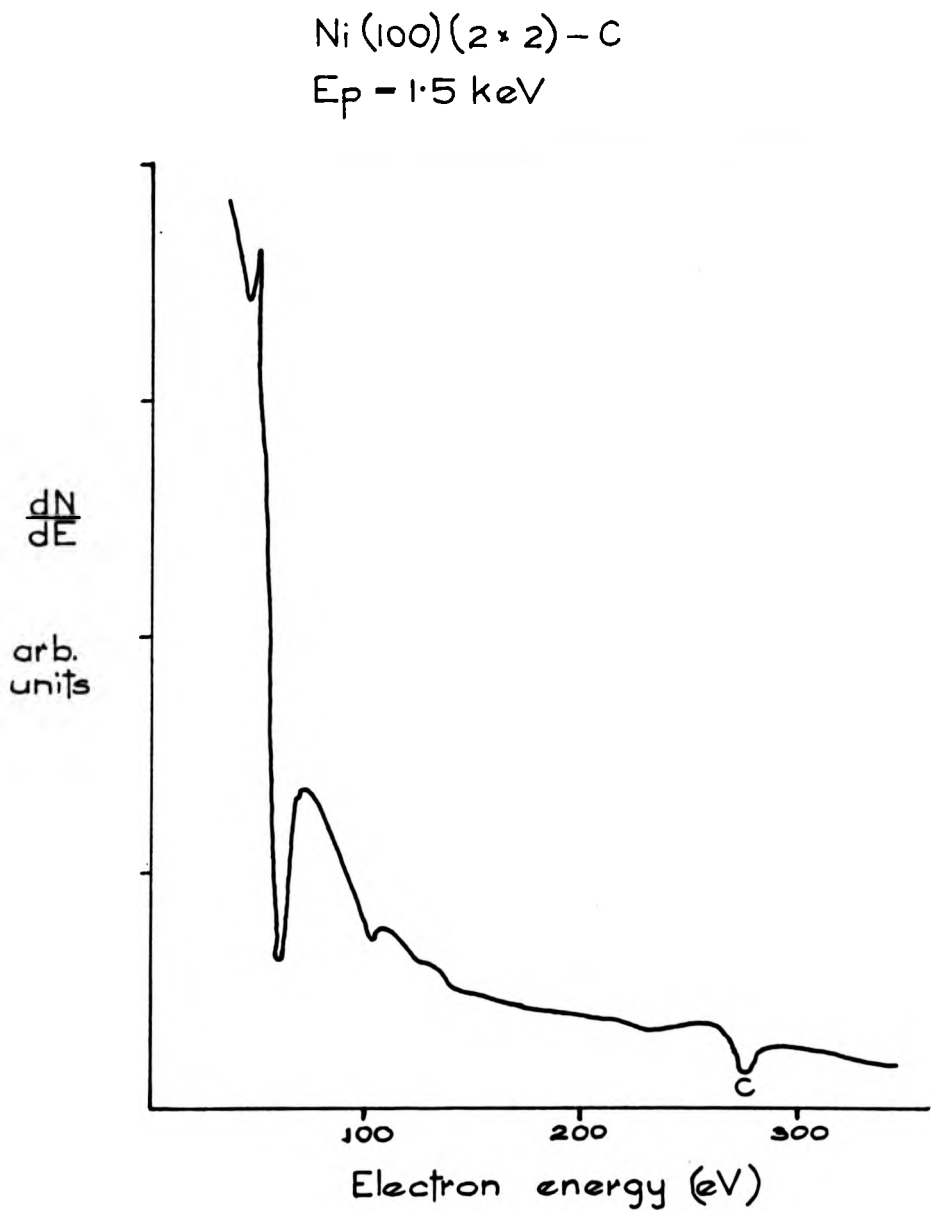
Ni (100) (2 × 2) – C
Ep = 1·5 keV
dN/dE
arb. units
C
100
200
300
Electron energy (eV)

Figure 5.21.

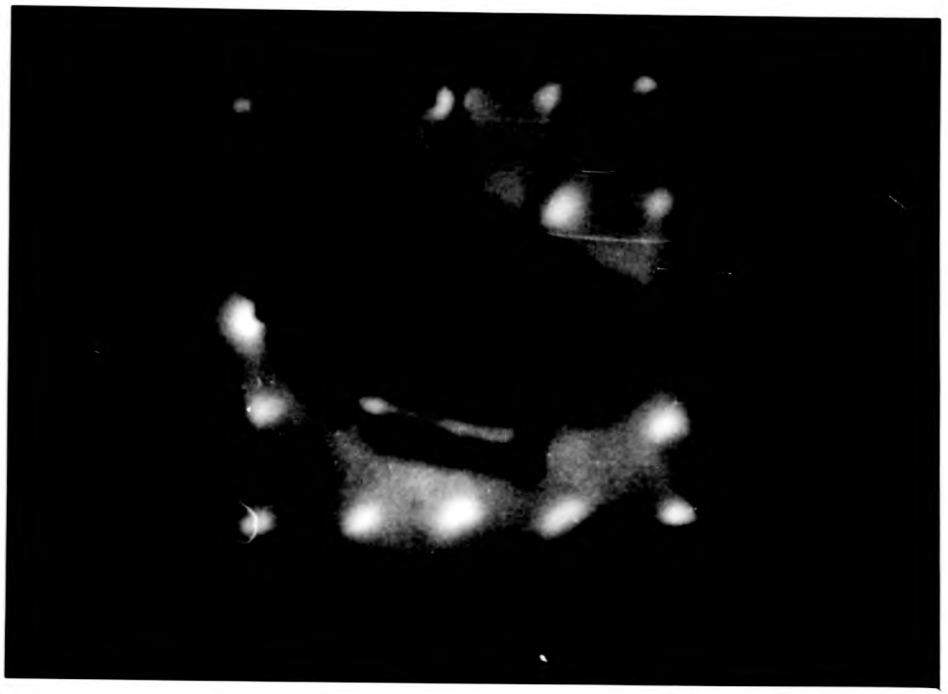

Ni (100) (2 × 2) – C

Electron energy ≃ 100 eV

**Figure 5.22.**

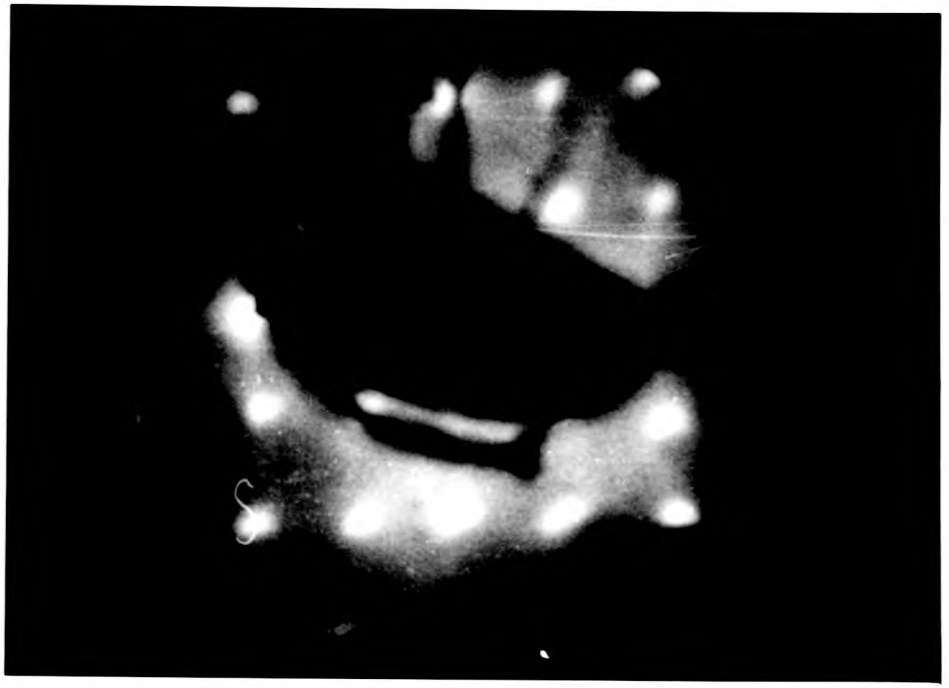

Ni (100) (2 × 2) – C

Electron energy ≃ 100 eV

Figure 5.22.

In fact, the LEED pattern implies the presence of glide symmetry lines which suggest distortion of the nickel surface layer (2).

This structure was studied with ISS using scattering angles of 90° and 48° with 1.0 keV helium ions. With a scattering angle of 90°, the sensitivity of the arrangement was not sufficient to discern a peak due to helium ions elastically scattered by carbon atoms. This is because the neutralisation probability for carbon is higher than for oxygen and the differential scattering cross-section falls rapidly for target masses below 20 a.m.u. for helium ions (see Figure 2.6). However, the intensity of the nickel peak was reduced substantially from the clean surface value. An azimuthal variation of the nickel peak at specular reflection is shown in Figure 5.23. There is a small variation between the $\gamma = 0°$ and $\gamma = 45°$ azimuths. The amplitude of the variation is less than for the Ni(100)($\sqrt{2}$x$\sqrt{2}$)R45°-O surface. A polar variation for the two major azimuths is shown in Figure 5.24. As the angle of incidence is reduced, the asymmetry falls below the level of sensitivity of the experimental system. Figure 5.25 shows a comparison between the azimuthal variations found for the Ni(100)($\sqrt{2}$x$\sqrt{2}$)R45°-O and the Ni(100)(2x2)-C surfaces for 90° scattering. In general, the results obtained for the carbon overlayer follow the same trends as for the oxygen overlayer. The major difference is the smaller variation obtained for the carbon structure.

At a scattering angle of 48°, a peak due to helium scattering from carbon atoms becomes visible. Figure 5.26 shows the energy spectra for the $\gamma = 0°$ and $\gamma = 45°$ azimuths for the 1.0 keV helium beam. The carbon peak is barely visible in the $\gamma = 45°$ direction, whereas the nickel peak is largest in this direction. Again, the major trends are similar to those of the oxygen structure. The level of attenuation of the nickel peak is less than for the oxygen structure. Figure 5.27 shows complete azimuthal variations

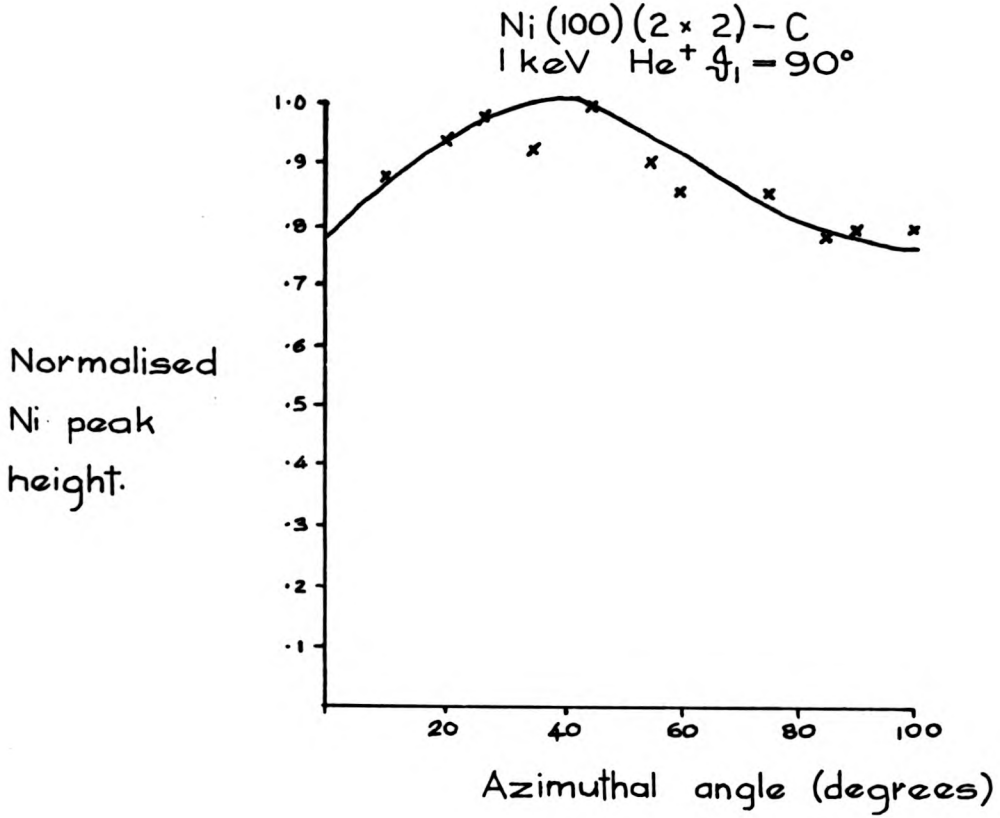
Ni (100) (2 × 2) – C
1 keV He+ ϕ1 = 90°
Normalised
Ni peak
height.
1·0
·9
·8
·7
·6
·5
·4
·3
·2
·1
20
40
60
80
100
Azimuthal angle (degrees)

Figure 5.23.

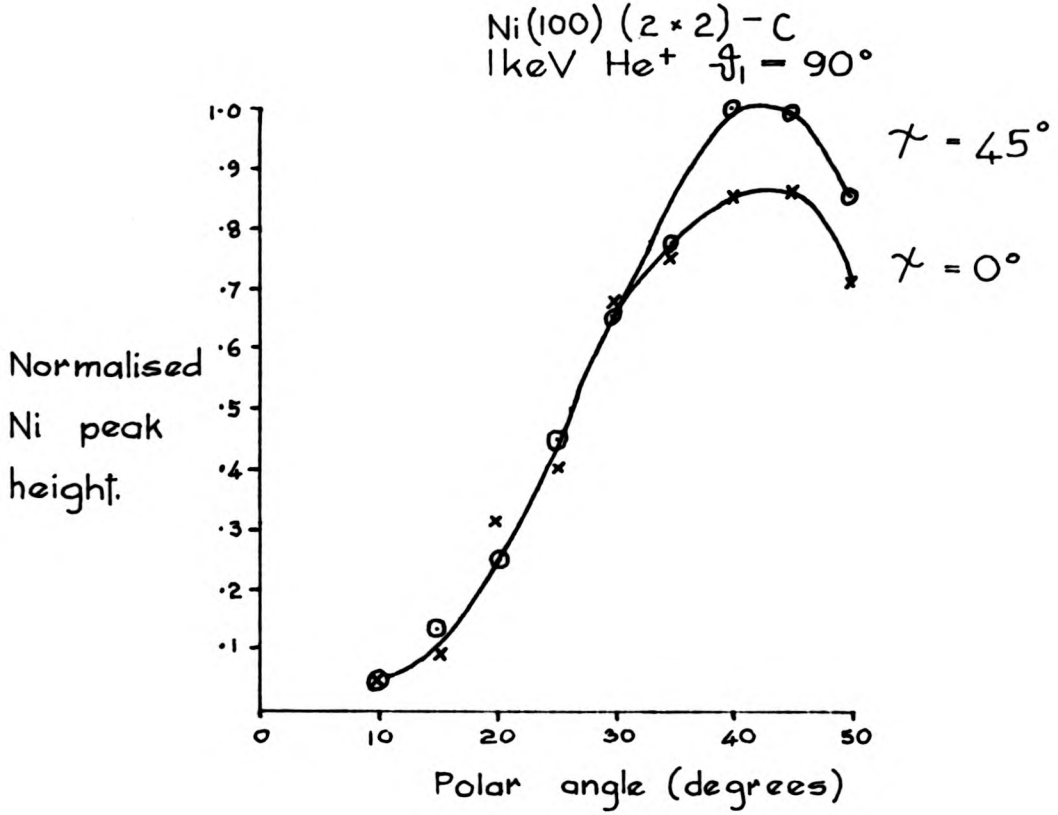
Ni(100) (2 × 2) – C
1keV He+ ϑ1 = 90°
χ = 45°
χ = 0°
Normalised
Ni peak
height.
1·0
·9
·8
·7
·6
·5
·4
·3
·2
·1
0
10
20
30
40
50
Polar angle (degrees)

Figure 5.24.

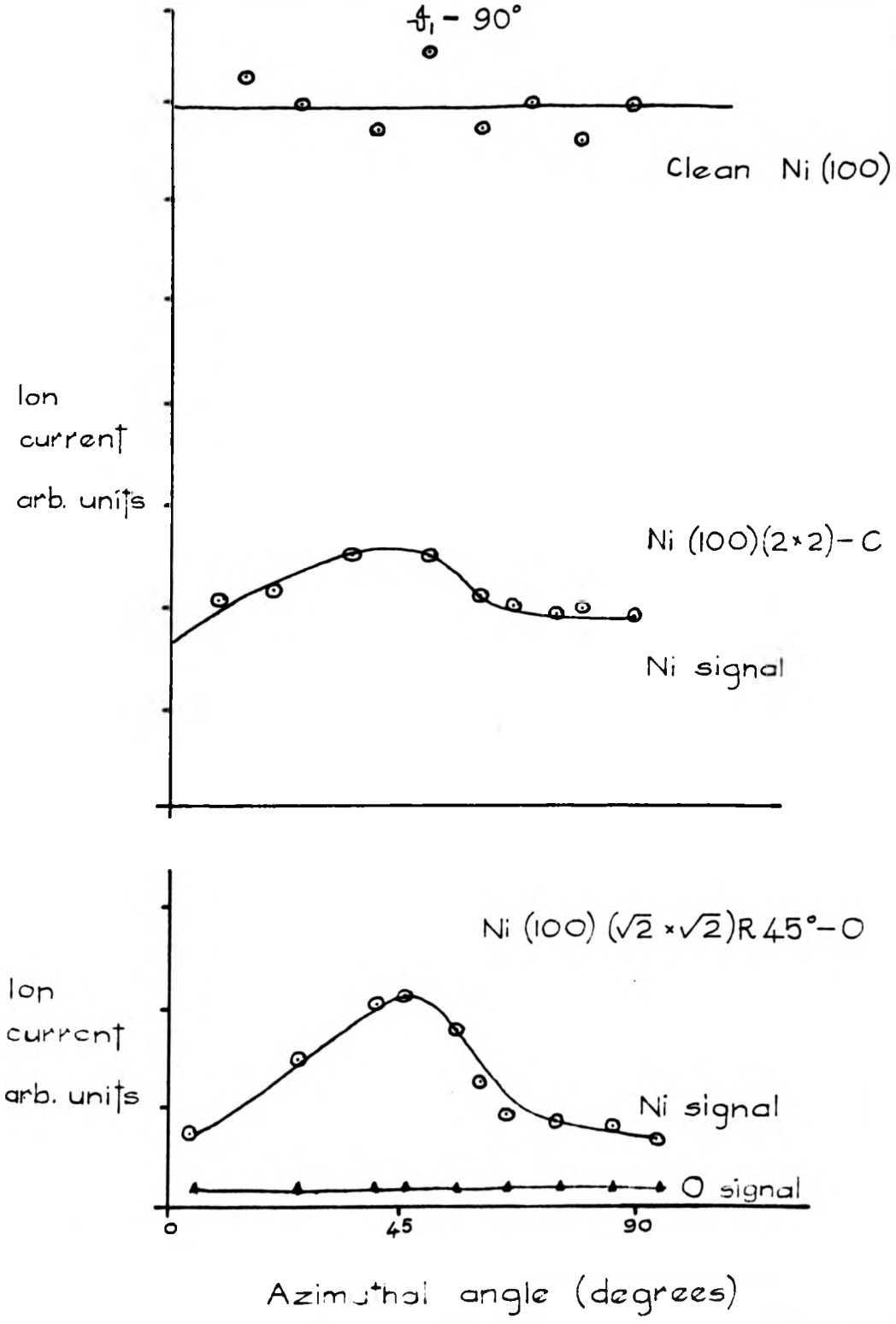
$\phi_1 - 90°$
Clean Ni (100)
Ion current arb. units
Ni (100)(2×2)-C
Ni signal
Ni (100) (√2 ×√2)R 45°-O
Ion current arb. units
Ni signal
O signal
0
45
90
Azimuthal angle (degrees)

Figure 5.25.

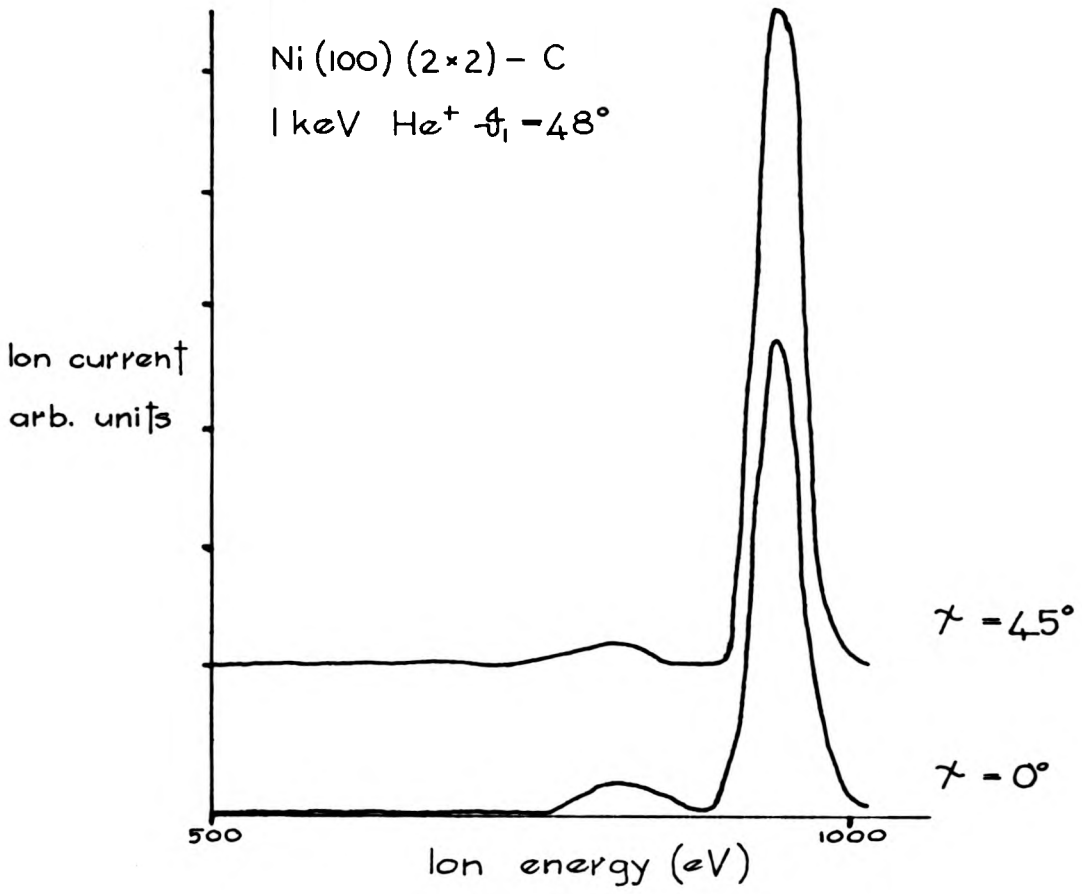
Ni (100) (2×2) – C
1 keV He+ ϑ1 = 48°
Ion current
arb. units
χ = 45°
χ = 0°
500
1000
Ion energy (eV)

Figure 5.26.

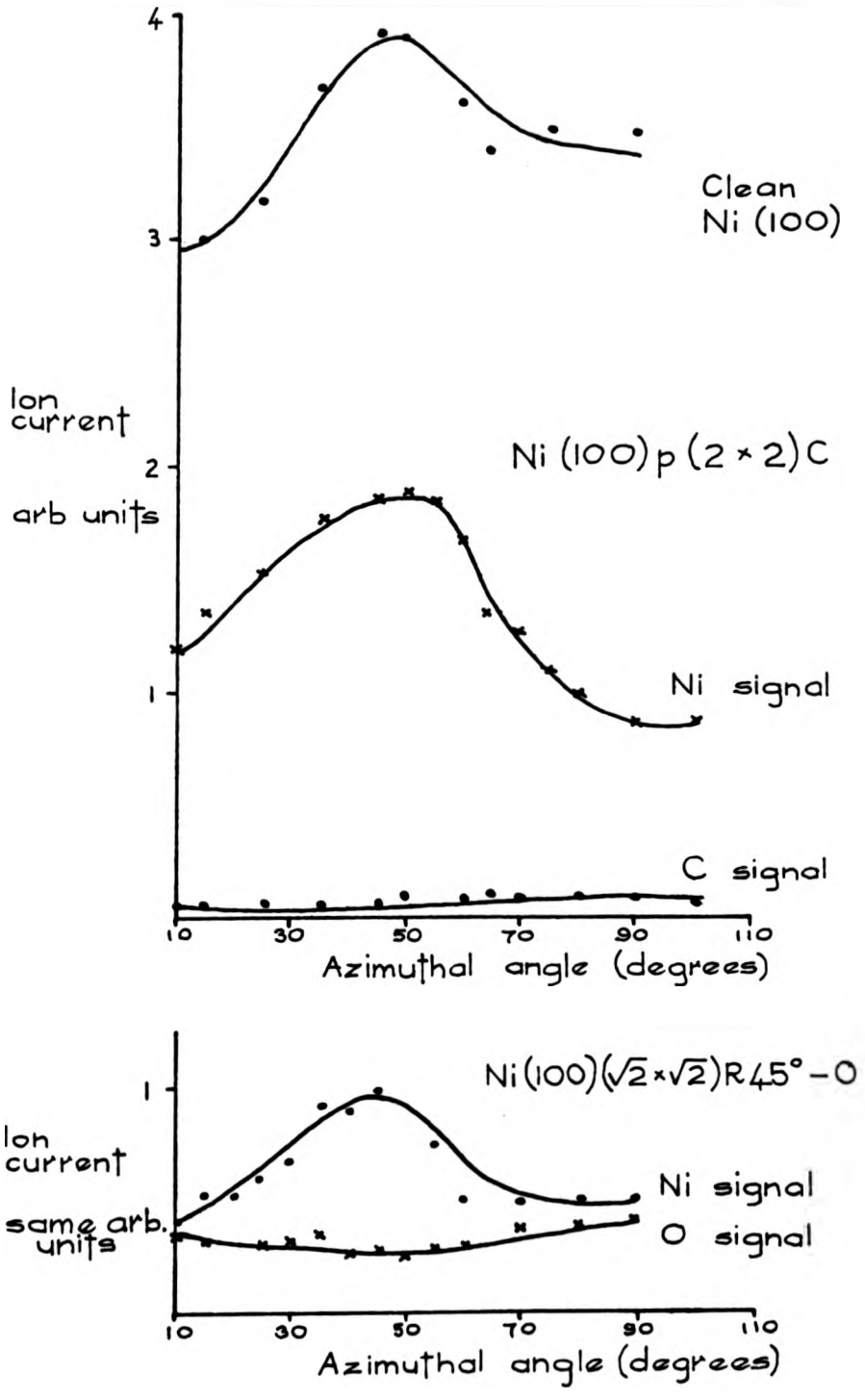
4
3
2
1
Clean
Ni (100)
Ion
current
arb units
Ni (100) p (2 × 2) C
Ni signal
C signal
10
30
50
70
90
110
Azimuthal angle (degrees)
Ni (100) (√2 × √2) R45° – O
Ion
current
same arb.
units
Ni signal
O signal
10
30
50
70
90
110
Azimuthal angle (degrees)

Figure 5.27.

for the Ni(100)($\sqrt{2}$x$\sqrt{2}$)R45°-O and the Ni(100)(2x2)-C structures.

The results obtained for the Ni(100)(2x2)-C system follow similar trends to those reported from the Ni(100)($\sqrt{2}$x$\sqrt{2}$)R45°-O surface. The structural model for the carbon adsorption proposed by Onuferko et al (2) places the carbon atoms approximately coplanar with the nickel surface in the four-fold hollows in the lattice. This causes the top layer of nickel atoms to be distorted by a small amount. Thus, the major difference between the positions of these two adsorbates is their height above the nickel surface layer. It is clear that the degree of elastic shadowing will be much less for the carbon case, but that any features due to elastic shadowing will be of a similar nature for both the oxygen and carbon adsorbates. Thus, consideration of elastic shadowing is not able to predict the experimental observations obtained from the Ni(100)(2x2)-C surface for 1.0 keV helium ion scattering. Therefore, as for the oxygen adsorption, the role of ion-atom neutralisation must be investigated.

Table 5.4 shows the ion yields predicted by the ion-atom neutralisation model. The surface structure used for the calculations is that proposed by Onuferko et al (2). The results obtained by Theory 1 in the table use the same parameters for carbon as those used for oxygen in Table 5.2. Theory 2 has a slightly increased value for A in order to optimise the agreement for the absolute yields. Both these theoretical calculations show qualitative agreement with the experimental results. The major discrepancy is that the anisotropy predicted in the nickel peak is smaller than that found experimentally for both scattering angles. For this near coplanar site, strong 'ion focusing' for the $\vartheta_1 = 90°$ scattering case would not be expected and so this cannot increase the level of anisotropy. However, the effect on the neutralisation due to nickel atoms by

| Ni (100) (2×2)–C structure | | | | | | |
|---|---|---|---|---|---|---|
| Scattering angle | | | 48° | | 90° | |
| Azimuth | | | ⟨110⟩ | ⟨100⟩ | ⟨110⟩ | ⟨100⟩ |
| (2×2)–C | Ni peak | expt | 0·22 | 0·47 | 0·27 | 0·35 |
| | | Theory1 | 0·25 | 0·28 | 0·45 | 0·47 |
| | | Theory2 | 0·18 | 0·20 | 0·37 | 0·38 |
| | | Theory3 | 0·20 | 0·32 | 0·31 | 0·34 |
| | C peak | expt. | 2·0 | 1·0 | — | — |
| | | Theory1 | 1·5 | 1·0 | 1·1 | 1·0 |
| | | Theory2 | 1·6 | 1·0 | 1·1 | 1·0 |
| | | Theory3 | 1·9 | 1·0 | 1·1 | 1·0 |

The theoretical values for the model parameters for the neutralisation are – for Theory 1 $(A/av)_c = 0.7$ $a_c = 1.5$ Å$^{-1}$
for Theory 2 $(A/av)_c = 0.9$ $a_c = 1.5$ Å$^{-1}$
for Theory 3 $(A/av)_c = 2.1$ $a_c = 1.3$ Å$^{-1}$

For Theory 3, the Ni ion-surface interaction was removed as in Table 5·3

Table 5.4.

adsorbing carbon on to the nickel surface has not been considered. Theory 3 includes this effect in the same manner as for the oxygen adsorption. This may be a more extreme approximation as the carbon atoms are not as electronegative as the oxygen atoms. However, this simple approach allows the effect of the carbon adsorption to be estimated. As for the oxygen adsorption, a substantial improvement in the qualitative agreement between the experimental data and the theoretical calculations is observed.

A further important point to note is that from purely elastic shadowing arguements, little anisotropy would be predicted for the essentially coplanar carbon site. One of the advantages predicted for ISS, on the basis of elastic shadowing arguements, was that coplanar adsorbate sites would be readily distinguishable from sites well above the crystal surface. This feature is not observed for the Ni(100) surface using 1.0 keV helium ions. This is of particular importance in the use of ISS on the Cu(100)($\sqrt{2}$x$\sqrt{2}$)R45°-O surface where a reconstructed surface has been proposed by McDonnell and Woodruff (10).

Conclusion.

It has been shown that the experimental data from two 'known' surface structures can only be interpreted if the role of ion-atom neutralisation is taken into consideration. This increases the difficulty of using 1.0 keV helium ions for surface structure analysis on the (100) crystal face in comparison with a situation where elastic shadowing effects dominate. The success of the ion-atom neutralisation model can be seen by considering Tables 5.3 and 5.4 where the neutralisation for the Ni(100)($\sqrt{2}$x$\sqrt{2}$)R45°-O and the Ni(100)(2x2)-C surfaces has been studied. The major difference between the two sites is the height of the adsorbate atoms above the nickel surface. For both sites, the general trend of the anisotropy predicted is similar. Although the overall level of anisotropy does vary, with the present

level of understanding, it is unlikely that quantitative surface structure analysis will be possible for the (100) surface using 1.0 keV helium ions. This is due to the simplifications inherent in the model for neutralisation and because other effects (for example, elastic shadowing) have been excluded. However, it is possible to make qualitative statements concerning the surface sites which are indicated from the ISS data.

# Chapter 6.

## Structural Analysis of Oxygen Adsorbed on Cu(100).

### Introduction.

The major stimulus for the present ISS study of the oxygen adsorption on Cu(100) was the work of McDonnell and Woodruff (1). In that work, the Cu(100)($\sqrt{2}$x$\sqrt{2}$)R45°-O structure was studied in detail using LEED I(V) analysis. The use of LEED I(V) data for surface structure determination was dealt with briefly in Chapter 1. As was noted, in this type of analysis it is necessary to propose structural models which can be used to calculate theoretical I(V) curves. These predicted I(V) curves are then compared with the experimental data. The model which gives the 'best fit' is assumed to be the surface structure.

The four model structures proposed by McDonnell and Woodruff for a half monolayer coverage are shown in Figure 6.1. Three of these models have respectively one fold, two fold and four fold coordinated oxygen atoms above the surface layer of the copper atoms (Models A1, A2 and A4). The fourth model consists of oxygen atoms in a reconstructed copper surface (Model R1). The best agreement between the theoretical I(V) curves and the experimental data was found for the reconstructed surface model. However, the level of agreement was not as good as that achieved by other workers on the Ni(100)($\sqrt{2}$x$\sqrt{2}$)R45°-O surface (2). For the nickel structure, the position of the oxygen atoms was found to be a four fold site with the oxygen atoms 0.9 Å above the surface layer. More recent studies have generally concluded that the oxygen adsorbed Cu(100) surface is not reconstructed ((3), (4) and (5)). Thus, the initial aim of the present work was that the ISS data obtained would give a clear indication as to the surface structure of this system.

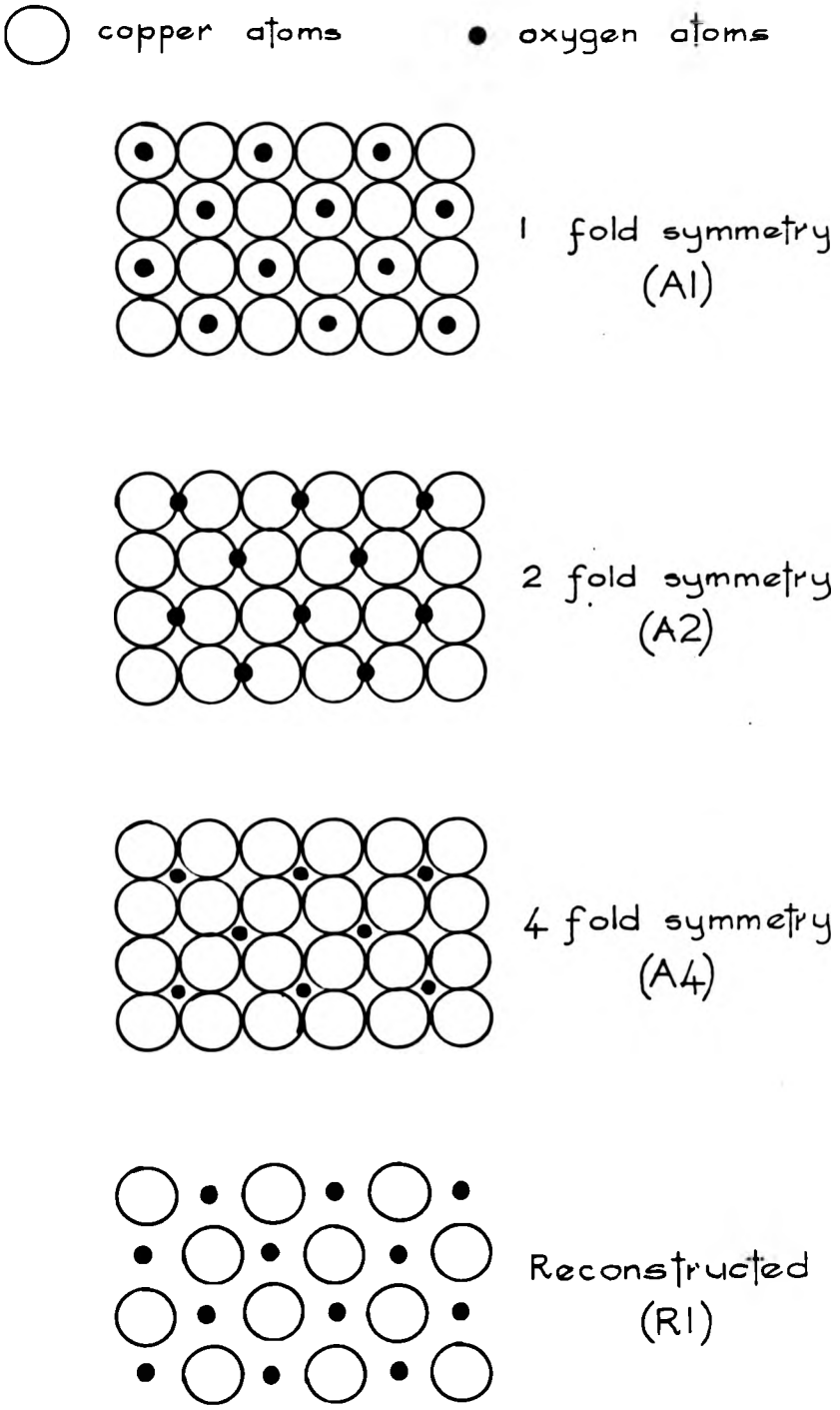
copper atoms
oxygen atoms
1 fold symmetry
(A1)
2 fold symmetry
(A2)
4 fold symmetry
(A4)
Reconstructed
(R1)

Figure 6.1.

In view of this discrepancy between the conclusion of the study by McDonnell and Woodruff (1) and these more recent studies, further experimental work on the Cu(100)($\sqrt{2}$x$\sqrt{2}$)R45°-O surface was carried out with LEED I(V) analysis in the Surface Physics Group at the University of Warwick. The results of this study are reported elsewhere (6). However, the major conclusions will be reported later in this chapter.

Interpretation of previous work using ISS for surface structure analysis has relied upon elastic shadowing effects which are dependent on the crystallography of the surface structure (7). For example, if the adsorbate atoms are above the surface layer, then the level of elastic scattering will be dependent upon the azimuthal angle of the crystal for given scattering conditions. However, if the adsorbate atom is coplanar with the surface, then little elastic shadowing is possible. Thus, ISS should be capable of distinguishing between the two major types of surface structure proposed for the Cu(100)($\sqrt{2}$x$\sqrt{2}$)R45°-O surface. As was shown in Chapter 5, the role of ion-atom neutralisation is crucial in the interpretation of the data collected under the experimental conditions used in this work. This has the result that even for near coplanar sites, as for the Ni(100)(2x2)-C system, there is a marked anisotropy in the ISS data. Thus, it is not possible to differentiate between the two major types of surface site with the level of certainty which was initially expected.

As previously mentioned, oxygen adsorption on the Cu(100) surface has been studied with a number of surface sensitive techniques. The more recent of these studies will be reviewed in the next section. Not all these studies include 'in situ' LEED, and so it is not always possible to be certain of the overlayer symmetry which is present. Not all of these studies have concentrated on surface structure analysis. The conclusions of these studies do

not allow the position of the adsorbed oxygen atoms to be found with certainty. The final section of this chapter will attempt to combine the conclusions of these studies, the more recent LEED study and the ISS study. A different structural model will be proposed which allows a number of the results of these different studies to be interpreted.

## 6.1. Recent studies of the oxygen adsorbed Cu(100) surface.

Studies of the oxygen adsorption on Cu(100) under well characterised experimental conditions have included the use of angle resolved photoemission (3), angle resolved deep core level X-ray photoemission (4), work function measurements (5), angle resolved Auger electron emission (8) and angle resolved secondary ion mass spectroscopy (9), as well as the LEED analysis already mentioned. Not all of these studies concentrated on surface structure determination and so only those parts which are relevant to this problem will be dealt with.

Angle resolved Ultra-violet Photoemission Spectroscopy (U.P.S.) involves the study of electrons emitted from the less tightly bound levels of the surface atoms (for example, the copper 3d band). The information gained from this technique can give an indication of the bonding involved in a surface structure. Lloyd et al (3) used angle resolved U.P.S. to study the oxidation of Cu(100). Their apparatus did not include LEED, and so it was not possible to completely characterise the surface order of the adsorbed oxygen. However, from the U.P.S. data, the changes in the chemical state of the copper atoms could be inferred. These changes were correlated with the development of the LEED pattern as the adsorption progressed. For low oxygen exposures ( up to $2 \times 10^{-5}$ torr-minutes at room temperature), there was little change in the U.P.S. spectra compared with the clean surface results. At the upper end of this

region, the LEED pattern is expected to be the $(\sqrt{2}x\sqrt{2})R45°$-O structure. The authors conclude that this state of adsorption " does not involve the chemisorption of the oxygen atoms". The adsorption was performed at room temperature and in the present ISS work such adsorption leads to a poorly ordered structure as monitored by LEED. At higher exposures, where the $(\sqrt{2}x2\sqrt{2})R45°$-O pattern is seen, changes in the U.P.S. spectra were obtained. The modification of the U.P.S. data was interpreted by the authors as being due to the chemisorption of the oxygen atoms and the reconstruction of the copper surface. These results indicate a possible reason for the difficulty found in stopping the adsorption at the $(\sqrt{2}x\sqrt{2})R45°$-O structure in the present work using ISS. This is because the $(\sqrt{2}x2\sqrt{2})R45°$-O structure is seen as the more stable structure.

The second technique applied to this system was X-ray Photoelectron Spectroscopy (X.P.S.) which uses X-rays with an energy of typically 1.5 keV. These X-rays are able to cause the emission of electrons from the core levels of the surface atoms. Kono et al (4) have studied the azimuthal variations of such emissions from copper and oxygen atoms on a Cu(100)$(\sqrt{2}x\sqrt{2})R45°$-O surface. These experiments were performed with a small angle between the sample surface and the acceptance aperture of the electron energy analyser (typically $10°$). This is to increase the probability of elastic scattering of the detected electrons by the ion cores of the surface atoms, a process strongly peaked in the forward directions for these electron energies. Strong anisotropy in the emission was found for electrons released from both copper and oxygen atoms under these conditions. The authors studied two of the possible surface structures illustrated in Figure 6.1. These were the reconstructed surface (R1) and the four fold adsorption site (A4). The best agreement with theoretical calculations for the reconstructed surface was with oxygen atoms at 0.2 Å below the copper surface

atoms. However, there are a number of discrepancies between the experimental data and the theoretical predictions. Closer agreement was found for the four fold site with the oxygen atoms coplanar with the copper surface. It is clear that this technique is most sensitive to the position of the adsorbate atom when it is low with respect to the surface. Indeed, little azimuthal anisotropy is predicted for the emission from an atom well above the surface.

The third technique which has been applied recently to the adsorption of oxygen on Cu(100) is the measurement of work function changes. This study was performed by Hofmann et al (5) for the $(\sqrt{2}x\sqrt{2})R45°$-O and the $(\sqrt{2}x2\sqrt{2})R45°$-O structures. These experiments were carried out in a system which included LEED. The sequence of adsorbate symmetries was similar to that found in the present ISS work. The oxygen adsorption was performed at several temperatures between room temperature and 720 °K. The initial LEED structure found for the room temperature adsorption was a pattern where four spots are placed in the positions occupied by the extra spots of the $(\sqrt{2}x\sqrt{2})R45°$-O structure. This diffuse 'four spot' pattern was only seen after adsorption carried out at and below 350 °K. The authors interpreted this pattern as being due to islands of molecular adsorbed oxygen atoms on four fold sites. Two different sites are possible for a four fold coordination (see Figure 6.2). If two domains of these different sites are included within the coherence area of the electron beam used for LEED, then interference effects can cause spots to split. A completely formed $(\sqrt{2}x\sqrt{2})R45°$-O structure can also include these two sites. If the resulting domains are regular in size and their boundaries run in preferred directions, then a sharp splitting will result. However, in general this is not the case, and so the splitting results in the broadening of the spots.

From the work function measurements, a maximum was found for

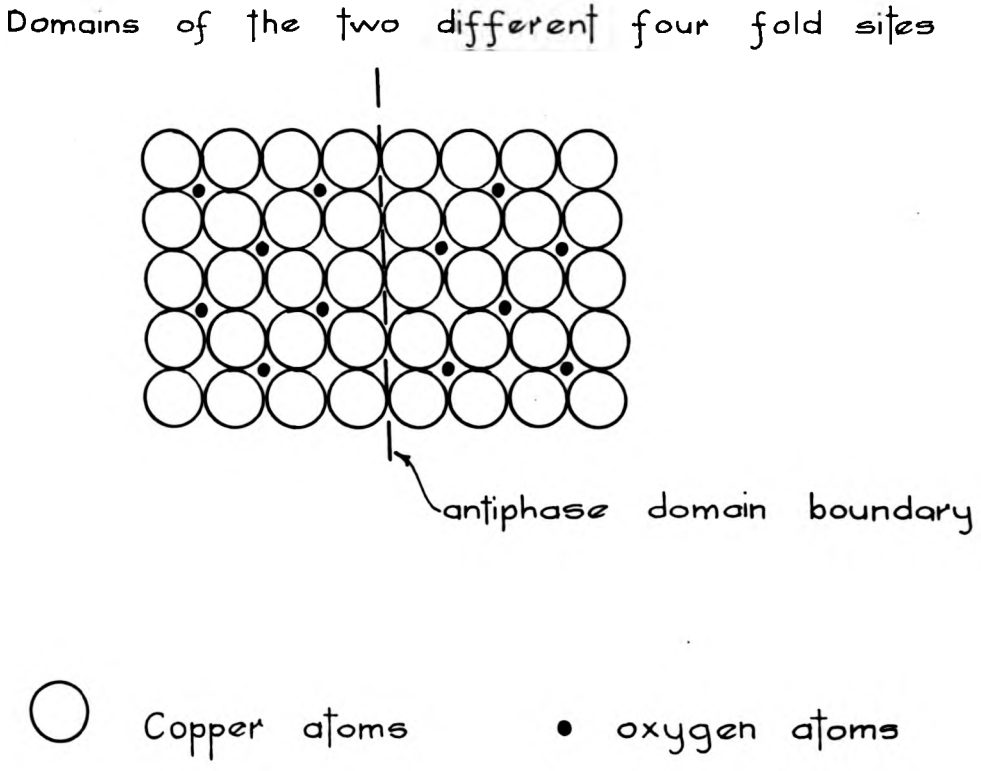
Domains of the two different four fold sites
antiphase domain boundary
Copper atoms
oxygen atoms

Figure 6.2.

the $(\sqrt{2}x\sqrt{2})R45^{\circ}$-O structure at all temperatures of adsorption. The work function falls to a minimum as the $(\sqrt{2}x2\sqrt{2})R45^{\circ}$-O structure is formed. The authors interpret this decrease as being due to the formation of a reconstructed surface layer or the incorporation of the oxygen atoms below the surface layer. This suggestion is supported by the fact that prolong ed heating of the $(\sqrt{2}x2\sqrt{2})R45^{\circ}$-O structure causes the $(\sqrt{2}x\sqrt{2})R45^{\circ}$-O surface to be formed. The authors suggest that the 'extra' oxygen atoms diffuse into the bulk of the crystal. Figure 6.3 shows the surface structure model proposed by Hofmann et al for the $(\sqrt{2}x2\sqrt{2})R45^{\circ}$-O structure. This is only a tentative suggestion which allows the experimental results to be readily interpreted.

The fourth technique which has been applied recently to this adsorbate system is angle resolved AES(8)Here, the $(\sqrt{2}x2\sqrt{2})R45^{\circ}$-O structure was studied. It was found that, compared with the clean surface result, the presence of oxygen caused little change in the azimuthal profile obtained for the 61 eV copper Auger transition taken at glancing emergence angles. This suggests that the top layer of the copper lattice is not rearranged by a significant amount. The reason for this conclusion is that the Auger electrons which are detected are emitted predominantly from the top atomic layers. Thus, any change in the positions of these atoms should effect the detected yield. As the adsorption of the oxygen did not effect the profile greatly, it was not possible to gain any further information as to the position of the adsorbed oxygen atoms.

The final technique which has been applied to the oxygen adsorption on Cu(100) is angle resolved secondary ion mass spectroscopy (S.I.M.S.) (9). Here, a Cu(100)$(\sqrt{2}x\sqrt{2})R45^{\circ}$-O surface was produced by room temperature adsorption using an oxygen dose of $2x10^{-5}$ torr-minutes. The surface was then bombarded with $Ar^{+}$ ions with energy of typically 1.5 keV. The azimuthal variations of the

Structural model proposed by Hofmann etal (5) for the Cu (100) $(\sqrt{2} \times 2\sqrt{2})$ R 45° – O surface

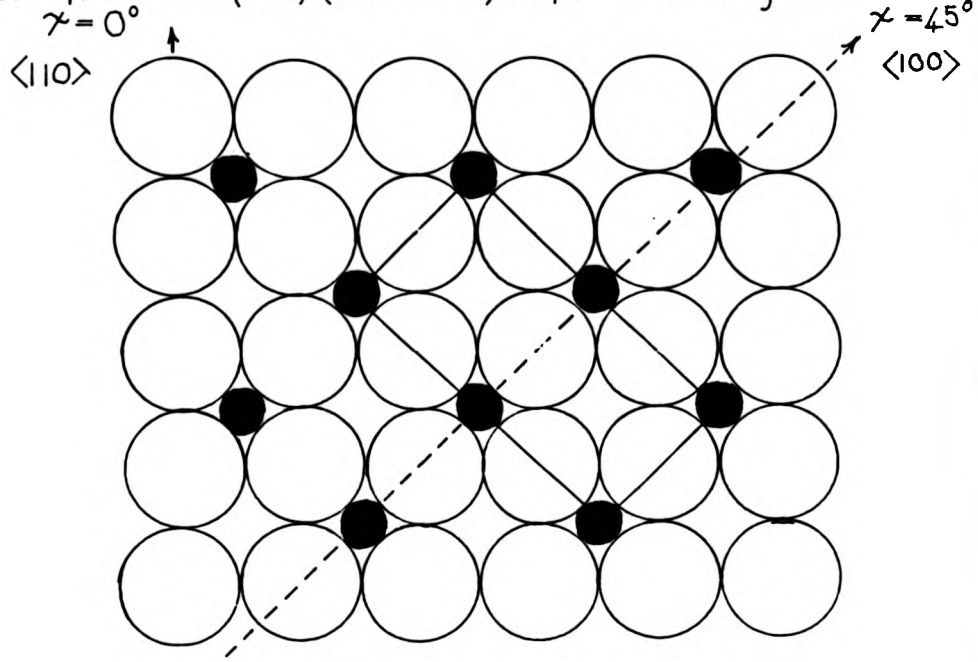


Plan view of the surface

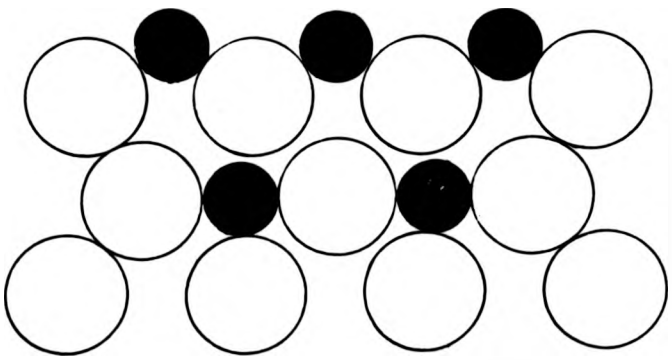

Side view of the (100) surface along the ⟨100⟩ azimuth

Figure 6.3.

sputtered copper and oxygen ions emitted at an angle of 45° with respect to the surface normal were measured. The authors performed model calculations for the four fold site (A4) and found that the best agreement between experiment and theory was for a distance of 1.2-1.5 Å between the oxygen atoms and the copper surface layer. However, this conclusion should be regarded as preliminary. The authors have not considered the other possible model structures shown in Figure 6.1 in their calculations. Furthermore, 'in situ' LEED was not available for these experiments and it is likely, from the present ISS study, that the Cu(100)($\sqrt{2}$x$\sqrt{2}$)R45°-O surface would be present to a large degree at these oxygen exposures. Finally, the four fold site suggested leads to a very large Cu-O bond length (2.17-2.35 Å) compared with the typical bulk oxide length (1.95 Å for CuO).

It can be seen that there are a number of suggestions as to the surface structure of the ($\sqrt{2}$x$\sqrt{2}$)R45°-O and ($\sqrt{2}$x2$\sqrt{2}$)R45°-O systems. Table 6.1 illustrates the results of the different techniques reported in this section. It is generally thought that the ($\sqrt{2}$x$\sqrt{2}$)R45°-O surface is not reconstructed as suggested by McDonnell and Woodruff (1). The most likely site appears to be a four fold site, as is found for the same symmetry on Ni(100). The ($\sqrt{2}$x2$\sqrt{2}$)R45°-O structure may include oxygen atoms which are either coplanar with or are below the copper surface layer. These conclusions will be kept under consideration in the next section where the LEED study of Onuferko and Woodruff (6) and the ISS results will be dealt with.

## 6.2. LEED and ISS structural studies of the adsorption of oxygen on Cu(100).

### 6.2.1. LEED.

It has been shown that the reconstructed model which was

| | $(\sqrt{2} \times \sqrt{2})R45° - O$ | | $(\sqrt{2} \times 2\sqrt{2})R45° - O$ | |
|---|---|---|---|---|
| | Bonding | Oxygen site | Bonding | Oxygen site |
| Angle Resolved U.P.S.(3) | not chemisorbed | — | chemisorbed | |
| Angle Resolved X.P.S. (4) | chemisorbed | 4 fold coplanar | not measured | not measured |
| Work Function (5) | chemisorbed | 4 fold above surface | chemisorbed | 4-fold coplaner + included oxygen (see fig. 63) |
| Angle Resolved A.E.S. (8) | not measured | not measured | not reconstructed | |
| Angle Resolved S.I.M.S.(9) | chemisorbed | 4 fold 1·2 – 1·5 Å above surface | not measured | not measured |

Table 6.1.

proposed by McDonnell and Woodruff (1) for the Cu(100)($\sqrt{2}$x$\sqrt{2}$)R45°-O surface has not been confirmed by the findings of other workers. Thus, further experimental and theoretical work on this system using LEED I(V) analysis has been performed in the Surface Physics group at the University of Warwick (6). The major results of this work will be reported in this section.

The oxygen adsorption in the LEED study was performed above room temperature, as in the present ISS study. This improves the surface order of the structure. However, it was found that after the ($\sqrt{2}$x$\sqrt{2}$)R45°-O structure had been observed, the ($\sqrt{2}$x2$\sqrt{2}$)R45°-O structure slowly appeared without further adsorption. This effect was noticed in the experiments performed for the ISS study. A second observation from the LEED work was that the ($\sqrt{2}$x$\sqrt{2}$)R45°-O pattern showed evidence of spot splitting. The LEED I(V) data collection was restricted to the ($\sqrt{2}$x$\sqrt{2}$)R45°-O pattern as the intensity of the extra spots of the ($\sqrt{2}$x2$\sqrt{2}$)R45°-O pattern was low.

The LEED I(V) data obtained was compared with dynamical theory calculations for one fold, two fold, four fold and reconstructed surfaces. Also, the four fold model proposed by Kono et al (4), where the oxygen atom is essentially coplanar with the copper surface layer, was studied. The site found by LEED for the Ni(100)($\sqrt{2}$x$\sqrt{2}$)R45°-O surface is a four fold site with the oxygen atoms 0.9 Å above the surface layer. However, the agreement between the theoretical calculations and the experimental data for this site on the copper surface is poor. The same four fold site, with the oxygen placed in a coplanar position, gives a more satisfactory agreement. However, rather better agreement is found for a two fold bridge site (A2). The two fold site is supported by the presence of the spot splitting. It can be seen that only fractional order beams will split for the one fold and four fold sites and that the two fold site allows splitting of the (10) beam as well as the fractional order beams.

This latter type of splitting was observed by Onuferko and Woodruff (6). Thus, this LEED study suggests that the site for the $(\sqrt{2}x\sqrt{2})R45^{\circ}$-O surface is a two fold one and that the spacing of the oxygen atoms above the top copper layer is approximately 1.4 Å.

This is in apparent contradiction to the angle resolved X.P.S. studies of Kono et al (4). However, as was noted earlier, this experimental technique is particularly sensitive to adsorbate atoms which are low lying relative to the surface layer. Also, this particular experimental arrangement did not include 'in situ' LEED. It has been noted that the $(\sqrt{2}x\sqrt{2})R45^{\circ}$-O structure readily evolves into the $(\sqrt{2}x2\sqrt{2})R45^{\circ}$-O surface. Thus, a possible explanation of this difficulty in interpretation between the two techniques is that the X.P.S. is monitoring the effect of the four fold coplanar oxygen atom in the $(\sqrt{2}x2\sqrt{2})R45^{\circ}$-O structure.

In view of this, LEED calculations were performed for a $(\sqrt{2}x2\sqrt{2})R45^{\circ}$-O surface involving mixed four fold and two fold sites (with overlayer spacings of 0.1 Å and 1.4 Å respectively). A diagram of this structure is shown in Figure 6.4. The level of correspondence between the experimental data and the theoretical calculations for this structure is somewhat improved relative to that obtained for the two fold site alone.

Thus, the overall agreement found for the LEED study of oxygen adsorption on Cu(100) is not as good as that found for the Ni(100) surface (2). This may be partially explained by the fact that it is unlikely that a surface structure such as that shown in Figure 6.4 would be completely formed and so a number of domains would be present on the surface. If these occur within the coherence area for LEED, then splitting of spots will occur. This type of structure will give poor long-range order and so may also account for the poor surface order as monitored by LEED.

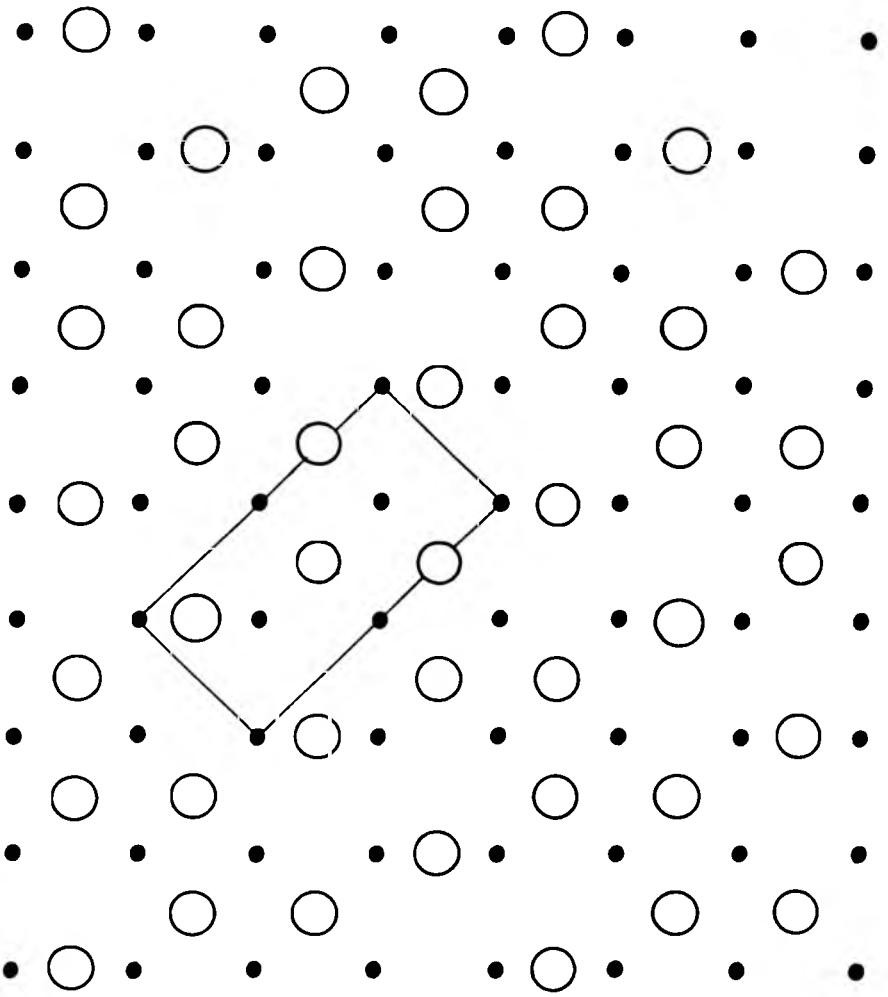

Surface structure for the Cu(100)$(\sqrt{2}\times 2\sqrt{2})R45°-O$ surface proposed by Onuferko and Woodruff

● copper surface layer atoms

○ adsorbed oxygen atoms

Figure 6.4.

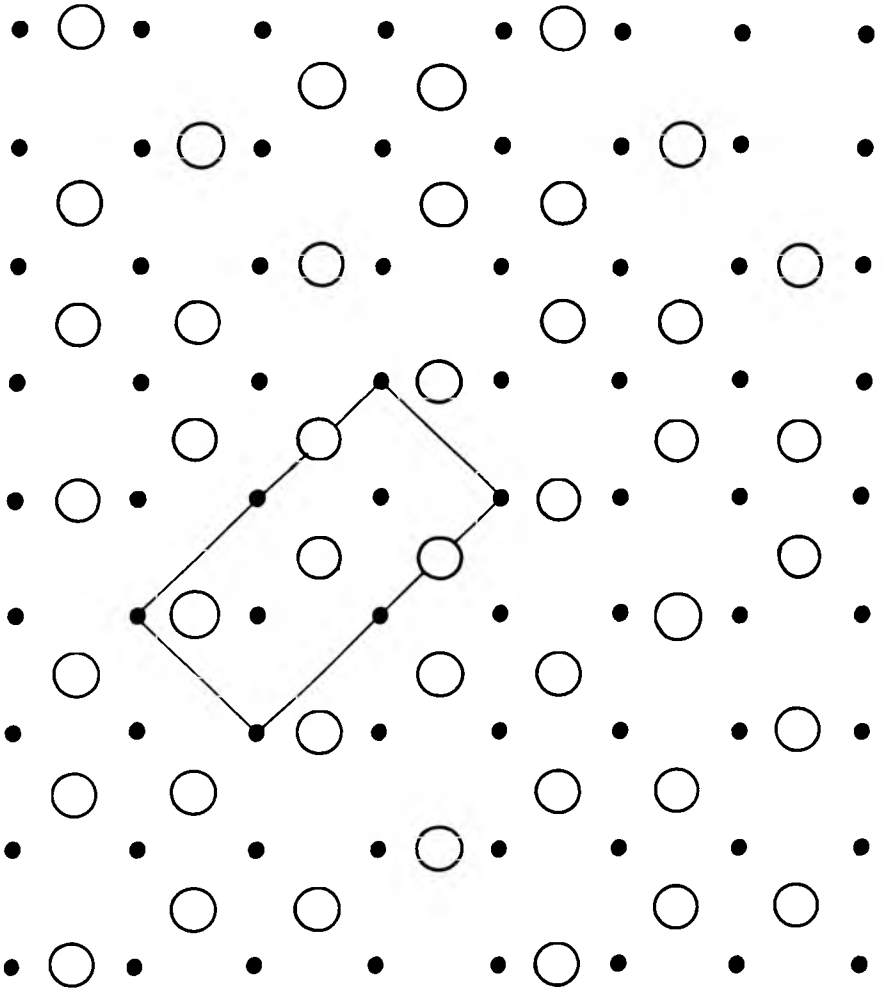

Surface structure for the Cu(100)($\sqrt{2}\times 2\sqrt{2}$)R45°–O surface proposed by Onuferko and Woodruff

● copper surface layer atoms

○ adsorbed oxygen atoms

Figure 6.4.

6.2.2. ISS.

It was shown in Chapter 5 that ion-atom neutralisation plays an important role in determining the ion yield obtained for the experimental conditions used in this work. This has the result that simple structural analysis, such as the work of Heiland and Taglauer (7), described in Chapter 2, is not applicable to the present case. Using the ion-atom model developed in Chapter 5, it has been possible to interpret the ISS results obtained from two known surface structures, namely the Ni(100)$(\sqrt{2}x\sqrt{2})R45^{\circ}$-O and the Ni(100)(2x2)-C systems. Although the model predicts differences between the two surfaces due to the position of the adsorbate atoms, it is unlikely that quantitative surface structure analysis will be possible with the present level of understanding of the processes involved in ISS.

This can be seen in Tables 6.2 and 6.3, where the ion-atom model has been applied to the Cu(100)$(\sqrt{2}x\sqrt{2})R45^{\circ}$-O surface. The model structures proposed by McDonnell and Woodruff (1) and the near coplanar four fold site suggested by Kono et al (4) are included. Table 6.2 does not include the effect on the neutralisation due to the copper atoms of adsorbing the oxygen atoms. Table 6.3 uses the simple approximation for adsorption adopted in Chapter 5. The major trend of the ISS data is that the maximum peak due to scattering from the substrate atoms is found in the $\gamma = 45^{\circ}$ azimuth. All the surface sites considered in Tables 6.2 and 6.3 show this overall feature. This is the case even for the reconstructed surface model. It can be seen that the different possible surface sites do lead to different predictions in the peak heights. For example, the one fold site gives an extremely large azimuthal anisotropy in the copper signal, particularly when the approximation for adsorption is taken into consideration. Also, the coplanar site gives an opposite anisotropy for the oxygen signal compared

| Cu (100) $(\sqrt{2} \times \sqrt{2})$ R 45° – O structure | | | | | | | | |
|---|---|---|---|---|---|---|---|---|
| | Cu signal | | | | | | O signal | |
| Scattering angle | 48° | | | 90° | | | 48° | 90° |
| Azimuth | ⟨110⟩ | ⟨100⟩ | ⟨110⟩/⟨100⟩ | ⟨110⟩ | ⟨100⟩ | ⟨110⟩/⟨100⟩ | ⟨110⟩/⟨100⟩ | ⟨110⟩/⟨100⟩ |
| Experimental value | 0·09 | 0·20 | 0·45 | 0·16 | 0·35 | 0·46 | 1·14 | 1·00 |
| 4 fold 0·9 Å | 0·161 | 0·180 | 0·89 | 0·328 | 0·308 | 1·06 | 1·23 | 1·04 |
| Coplanar reconstructed | 0·242 | 0·320 | 0·76 | 0·346 | 0·365 | 0·95 | 0·81 | 0·98 |
| 4 fold 0·1 Å | 0·259 | 0·300 | 0·86 | 0·477 | 0·481 | 0·99 | 1·62 | 1·08 |
| 1 fold 1·85 Å | 0·073 | 0·193 | 0·38 | 0·188 | 0·276 | 0·68 | 1·18 | 1·03 |
| 2 fold 1·4 Å | 0·098 | 0·158 | 0·62 | 0·212 | 0·256 | 0·83 | 1·18 | 1·03 |

The theoretical values for the model parameters for the neutralisation are A/av = 0·7, $a = 2{\cdot}0\ \text{Å}^{-1}$ for copper and A/av = 0·7 $a = 1{\cdot}5\ \text{Å}^{-1}$ for oxygen

Table 6.2.

| Cu(100) $(\sqrt{2} \times \sqrt{2})$ R 45° – O structure | | | | | | | | |
|---|---|---|---|---|---|---|---|---|
| | Cu signal | | | | | | O signal | |
| Scattering angle | 48° | | | 90° | | | 48° | 90° |
| Azimuth | ⟨110⟩ | ⟨100⟩ | ⟨110⟩//⟨100⟩ | ⟨110⟩ | ⟨100⟩ | ⟨110⟩//⟨100⟩ | ⟨110⟩//⟨100⟩ | ⟨110⟩//⟨100⟩ |
| Experimental value | 0·09 | 0·20 | 0·45 | 0·16 | 0·35 | 0·46 | 1·14 | 1·00 |
| 4 fold 0·9 Å | 0·153 | 0·319 | 0·48 | 0·212 | 0·237 | 0·89 | 1·48 | 1·09 |
| 4 fold 0·1 Å | 0·592 | 0·853 | 0·69 | 0·642 | 0·660 | 0·97 | 1·96 | 1·14 |
| Coplanar reconstructed | 0·569 | 1·400 | 0·41 | 0·596 | 0·707 | 0·84 | 0·98 | 1·03 |
| 1 fold 1·85 Å | 0·035 | 0·394 | 0·09 | 0·059 | 0·141 | 0·42 | 1·42 | 1·08 |
| 2 fold 1·4 Å | 0·056 | 0·120 | 0·47 | 0·082 | 0·102 | 0·81 | 1·42 | 1·08 |

As table 6·2 but assuming that the clean Cu surface has an ion–surface neutralisation with (A/av = 0·7) which is lost on adsorption. The oxygen parameters used were A/av = 1·7, a = 1·3 Å$^{-1}$.

Table 6.3.

with the experimental data. However, none of these sites give satisfactory agreement with the experimental data for the scattering conditions used in this work. Thus, it is not possible at present to use the ion-atom neutralisation model to perform surface structure analysis from unknown surfaces.

However, by comparing the results obtained from the Cu(100)($\sqrt{2}$x$\sqrt{2}$)R45°-O surface with those from the Ni(100)($\sqrt{2}$x$\sqrt{2}$)R45°-O and Ni(100)(2x2)-C surfaces, it is possible to make qualitative statements concerning the surface structures which have been studied in this work. The major results obtained from these surfaces with 1.0 keV helium ions are summarised in Table 6.4.

A number of factors can be noted from these results. Firstly, for $\vartheta_1 = 90°$, the Ni(100)($\sqrt{2}$x$\sqrt{2}$)R45°-O surface is the most heavily attenuated by the oxygen atoms. This can be seen most readily in the reduction of the nickel signal from the clean surface to the adsorbed surface. The carbon covered surface shows the least attenuation. This is due mainly to the oxygen atoms being higher than the carbon atoms relative to the nickel surface layer. The Cu(100)($\sqrt{2}$x$\sqrt{2}$)R45°-O case is similar to the Ni(100)($\sqrt{2}$x$\sqrt{2}$)R45°-O case. In fact, throughout the measurements given in Table 6.4, the effect of the presence of carbon atoms is generally less than the effect of the oxygen atoms. Similarly, the Cu(100)($\sqrt{2}$x$\sqrt{2}$)R45°-O variation is generally closer to the results obtained for the oxygen adsorbed nickel surface. The same overall trend can be seen in the $\vartheta_1 = 48°$ case. This overall result is not found for grazing incidence for $\vartheta_1 = 90°$. Here, the anisotropy in the copper substrate signal remains, whereas the nickel peaks are more severely attenuated so that no anisotropy is seen. A further difference between the oxygen adsorbed copper surface and nickel surface can be seen in the anisotropy of the oxygen peak. For both $\vartheta_1 = 90°$ and $\vartheta_1 = 48°$, there is a difference in the peak heights for the oxygen for the

| | Nickel | | Copper |
|---|---|---|---|
| | Oxygen | Carbon | Oxygen |
| $\phi_1 = 90°$ Specular reflection | | | |
| $\frac{\text{substrate peak } \gamma=45°}{\text{clean substrate peak } \gamma=45°}$ | 0·28 | 0·40 | 0·33 |
| $\frac{\text{substrate peak } \gamma=45°}{\text{substrate peak } \gamma=0°}$ | 2·5 | 1·3 | 2·0 |
| $\frac{\text{adsorbate peak } \gamma=0°}{\text{substrate peak } \gamma=0°}$ | 0·2 | not seen | 0·13 |
| $\frac{\text{adsorbate peak } \gamma=45°}{\text{substrate peak } \gamma=45°}$ | 0·1 | not seen | 0·06 |
| $\frac{\text{adsorbate peak } \gamma=45°}{\text{adsorbate peak } \gamma=0°}$ | 1·2 | not seen | 1·0 |
| $\phi_1 = 90°$ Glancing incidence | | | |
| $\frac{\text{substrate peak } \gamma=45°}{\text{substrate peak } \gamma=0°}$ | 1·0 | 1·0 | 3·0 |
| $\phi_1 = 48°$ Specular reflection | | | |
| $\frac{\text{substrate peak } \gamma=45°}{\text{substrate peak } \gamma=0°}$ | 2·0 | 1·4 | 2·2 |
| $\frac{\text{adsorbate peak } \gamma=0°}{\text{substrate peak } \gamma=0°}$ | 0·80 | 0·06 | 0·25 |
| $\frac{\text{adsorbate peak } \gamma=45°}{\text{substrate peak } \gamma=45°}$ | 0·29 | 0·04 | 0·11 |
| $\frac{\text{adsorbate peak } \gamma=45°}{\text{adsorbate peak } \gamma=0°}$ | 0·7 | 0·8 | 1·0 |

The experimental peak heights were all obtained for 1 keV helium ions

Table 6.4.

two major azimuths on the Ni(100)($\sqrt{2}$x$\sqrt{2}$)R45°-O surface. Only a small variation was detected for 48° and no variation for 90° on the oxygen adsorbed copper surface. It can be seen that there are small differences between the experimental results used in Tables 6.3 and 6.4. This illustrates the differences obtained from differing experimental runs.

These results can be understood qualitatively if the model suggested by Onuferko and Woodruff (6) for the Cu(100)($\sqrt{2}$x2$\sqrt{2}$)R45°-O surface is considered. As in their LEED study, we consider this appropriate because great difficulty was found in stopping the adsorption at the Cu(100)($\sqrt{2}$x$\sqrt{2}$)R45°-O stage and so it is likely that the ($\sqrt{2}$x2$\sqrt{2}$)R45°-O system is always present to some degree. Firstly, the similarity with the nickel-oxygen rather than the nickel-carbon system can be attributed to the relative height of the adsorbed oxygen atoms. A larger neutralisation effect would be expected for the oxygen in the two fold bridge site than in the coplanar reconstructed site. This can be seen in Tables 6.2 and 6.3 where the level of attenuation due to neutralisation for both scattering angles is larger for the two fold site than for the coplanar site.

Secondly, the persistance of the copper substrate signal at grazing incidence may be due to the incomplete formation of the adsorbed surface or to domain effects in this lower symmetry surface. It was noted earlier that a structure as complex as that shown in Figure 6.4 is unlikely to be perfectly formed. This will lead to poor long range order on the adsorbed surface. The area of the crystal which is sampled in the ISS measurements is quite large (and so it is likely that areas of incomplete adsorption will be included in the measured region). These areas will contribute a signal due to scattering from copper atoms even at grazing angles. Finally, it has been noted that no anisotropy was found in the oxygen signal for the

copper surface. This may be indicative of the lack of periodic rows of oxygen atoms along either the $\gamma = 0^{\circ}$ or the $\gamma = 45^{\circ}$ azimuths. It can be seen from Figure 6.4 that this is a feature of the complex adsorption structure suggested by Onuferko and Woodruff (6).

In conclusion, the surface structure of the oxygen adsorption on Cu(100) is still not known with the level of certainty which has been achieved for the Ni(100) surface. It is unlikely that a reconstructed surface is present for the Cu(100)$(\sqrt{2}x\sqrt{2})R45^{\circ}$-O case. The major difficulty appears to be in choosing between the two fold and the four fold sites. The work of Kono et al (4) suggests that a four fold near coplanar oxygen site is present. However, as LEED was not available for this work, the $(\sqrt{2}x2\sqrt{2})R45^{\circ}$-O surface may be present to some extent during these experiments. Thus, it may be assumed that this coplanar site is due to the $(\sqrt{2}x2\sqrt{2})R45^{\circ}$-O structure. The two fold oxygen atom is then taken as the preferred site for the $(\sqrt{2}x\sqrt{2})R45^{\circ}$-O surface. Hence, the most probable surface structure for the $(\sqrt{2}x\sqrt{2})R45^{\circ}$-O system is a two fold site, with the $(\sqrt{2}x2\sqrt{2})R45^{\circ}$-O surface being formed by a mix of two fold and four fold sites. These conclusions are supported to some extent by the ISS data collected in this work. However, a better understanding of the processes involved in ISS under the experimental conditions used in this work is required before surface structure determination is possible with a reasonable level of certainty. Also, the non-ideal behaviour of the oxygen adsorbed on Cu(100) makes surface structure analysis problematic.

## Chapter 7.

## Summary.

The major aim of the work reported here was to investigate the use of ISS for surface structural analysis. In order to achieve this, it was necessary to construct a new experimental system which would allow ISS, AES and LEED to be performed within the same experimental chamber. This arrangement was required to enable the reproduction of well-ordered adsorbate surfaces. The AES and LEED were required to monitor the surface structure present. The ISS could then be applied to these well-characterised surfaces.

The successful completion of this experimental system was reported in Chapter 3. This system was applied initially to the clean Cu(100) surface and the oxygen adsorbed surface. These surfaces were chosen because of the lack of agreement found concerning the site of the oxygen atoms for the Cu(100)$(\sqrt{2}x\sqrt{2})R45^{\circ}$-O surface. Thus, the preliminary work required to investigate the instrumental effects of the experimental apparatus was carried out on the clean Cu(100) surface. The major result of these studies, as were reported in Chapter 4, was that the instrument performs well and that the large acceptance angle of the C.M.A. introduces no spurious effects. Further, the mass resolution of the system was sufficient for the atom species which would be used in the surface structural analysis. Following these initial experiments, ISS data were collected with the aim of establishing the surface structure of the Cu(100)$(\sqrt{2}x\sqrt{2})R45^{\circ}$-O surface.

Previous surface structure analysis using ISS has relied upon predicting relative ion yields by considering the variations in elastic shadowing. This can be estimated by considering the impact parameters for the particular experimental conditions present. A second method is to use the shadow cone model noted in Chapter 2. Both these approaches assume that the critical parameters in

determining the relative ion yields are elastic shadowing effects. The neutralisation probability is assumed to be independent of the azimuth of the crystal, and so is not an important factor in producing relative ion yields. Such studies using ISS have been applied with a large degree of success to a number of adsorbates on the Ni(110) and Ag(110) surfaces (1).

The present ISS study was performed using 1.0 keV helium ions on Cu(100) and Ni(100) clean and adsorbed surfaces. The results obtained cannot be explained by considering only the variations due to elastic scattering effects, whilst assuming a constant level of neutralisation. However, it has been shown, in Chapter 5, that a reasonable level of understanding of the experimental data can be achieved by considering ion-atom neutralisation. In order to establish this fact, the Ni(100)($\sqrt{2}$x$\sqrt{2}$)R45°-O surface was studied. This system has been studied in detail with LEED I(V) analysis and a good agreement was found between the experimental data and the theoretical I(V) curves for a surface model with four fold coordinated oxygen atoms 0.9 Å above the surface layer (2). Thus, the theory developed for ion-atom neutralisation could be tested against this known surface structure.

The results obtained from the ion-atom neutralisation model follow the same trends as was found in the experimental data for the oxygen adsorbed Ni(100) surface. The model includes the effect of adsorption on substrate atoms on the neutralisation. Using this model, it has been possible to achieve reasonable agreement between experiment and theory for the two known surface structures studied in this work, namely the Ni(100)($\sqrt{2}$x$\sqrt{2}$)R45°-O and the Ni(100)(2x2)-C surfaces.

It is clearly important to establish the experimental conditions where the variation in the ion yield caused by ion-atom neutralisation is dominant. The ISS studies on the (110) surface

suggest that the major anisotropy in the experimental data can be interpreted by considering elastic shadowing effects (1). A possible reason may be seen by considering the Ag(110)(2x1)-O surface, which was taken as an example in Chapter 2. For the (110) surface, there are alternate open rows of atoms along the $\langle 110 \rangle$ azimuth. It is likely that the adsorbate oxygen atoms will be placed in these open rows. It can be seen that ions scattered along these rows will be able to collide with the oxygen atoms. In contrast, it is very unlikely that the oxygen atoms will be able to contribute to the scattering along the $\langle 100 \rangle$ azimuth. Clearly, if it is not possible for scattering to take place then no ISS signal due to oxygen will be seen. Thus, it is not necessary to consider ion-atom neutralisation effects. This has the result that elastic shadowing arguements will allow a clear distinction between the surface sites which have been proposed. It is for this reason that the ISS studies on the (110) surface were able to perform surface structure analysis without considering ion-atom neutralisation effects.

Other major experimental conditions which may effect the relative contributions of ion neutralisation and elastic scattering to the ion yield are the scattering angle, the type of incident ion and its energy. These variables will effect the sizes of the impact parameters for the collision and will also effect the rate of neutralisation. Thus, by experimentally varying these properties, it may be possible to establish a region where elastic scattering dominates on the (100) surface. Such experiments to investigate the areas where ion-atom neutralisation is important are at present being carried out within the Surface Physics group at the University of Warwick.

The need to consider ion-atom neutralisation effects increases the difficulty of carrying out surface structure analysis with ISS. As the neutralisation probability can no longer be assumed as

constant, it is necessary to calculate the relative strengths of the elastic effects and of the neutralisation effects in order to predict the comparative ion yields. The shadow cone model and 'chain' calculations reported in Chapter 2 allow the elastic scattering effects to be estimated with a large degree of certainty. However, the model developed for the ion-atom neutralisation is only able to produce qualitative results. There are two major reasons for this. Firstly, there are a number of simplifications inherent in the present model. For example, the neutralisation probability has been derived from considering collisions involving small scattering angles. However, this result has then been used to calculate the neutralisation probability due to the major collision. Secondly, there are a number of parameters involved in the model which are not well known. Although the exact values of these constants do not effect the relative ion yield to a large extent, it does effect the absolute value predicted from the neutralisation model (see Table 5.1).

Thus, at present it is not possible to provide a quantitative model for ion scattering which takes into account the two processes which cause the incident ion to be elastically scattered and remain charged. In order to achieve this, it would be necessary to compute the trajectories of each ion path and calculate the probability of neutralisation and the possibility of elastic scattering. It is hoped that further experimental and theoretical study of the neutralisation processes will allow such a model to be developed. This type of model would enable ISS to be applied to surface structure analysis with a greater level of certainty.

An alternative approach to performing surface structure analysis with ISS is to limit the application of the technique to experimental conditions where the anisotropy in the neutralisation is not dominant in the resulting ion yield. As has been noted, this is probably the case for lower symmetry surfaces (e.g. the (110) surface) with low

energy helium and neon ions. The problem of neutralisation can be removed by detecting both the scattered ions and the scattered neutrals. This type of work, using time of flight measurements (T.O.F.) has been performed by Buck et al (3). Although this is experimentally difficult, it does hold a number of advantages. Firstly, using ISS in the form described in the present work, the majority of the information of the scattered particles is lost. This is because the neutralisation probability for the experimental conditions used in ISS is often greater than 99.99% (4). Experiments involving T.O.F. measurements have been performed at higher energies than those found in ISS (greater than 8.0 keV). In this region, a similarity is observed between the spectra obtained from detecting ions plus neutrals compared with those obtained from ions alone. T.O.F. measurements have also been made for neon ions of approximately 3.0 keV. It has been shown that much of the surface sensitivity of ISS is due to the high neutralisation probabilities. This causes ions which penetrate below the surface layer to have an extremely high probability of losing their charge. Thus, the ions detected in ISS have interacted predominantly with the top layer. In contrast, T.O.F. measurements will include neutrals which have penetrated deeply into the lattice. This technique has not been applied to surface structure analysis as yet. However, as it allows both the neutral and charged particles to be detected, it has the advantage that the problem of neutralisation is removed. Thus, it might be hoped that surface structural analysis would be more straight forward using this technique.

Another development of ISS is in the use of alkali metal ions ($Na^+$) instead of inert gas ions (5). The alkali metal ions are more likely to remain ionised during scattering events. Again the problem of ion neutralisation is removed. However, in both cases, the probability of detecting collisions which involve multiple scattering

is increased. Computer simulations of multiple scattering using chain calculations for low angles of incidence have been carried out, and these have been successful in predicting the relative ion yields for higher energy (3.0 keV and above) neon and argon ions (6). Hence, it is likely that such calculations will be applicable to lower energy beams in situations where neutralisation is not crucial in predicting relative ion yields.

For the reasons given in this chapter, it has not been possible to achieve unambiguous surface structure analysis on the Ni(100)-$(\sqrt{2}x\sqrt{2})R45^{\circ}$-O, Ni(100)(2x2)-C or Cu(100)$(\sqrt{2}x2\sqrt{2})R45^{\circ}$-O surfaces from the ISS data which has been collected. However, if the surface sites for the first two structures are assumed, then qualitative understanding of the relative trends of the ISS work can be achieved. Applying the ion-atom neutralisation model to the oxygen adsorbed Cu(100) surface is more difficult. The reason for this is that the surface order in the copper case is not so good as the nickel surface. Further, the sites proposed for the Cu(100)$(\sqrt{2}x\sqrt{2})R45^{\circ}$-O and the Cu(100)$(\sqrt{2}x2\sqrt{2})R45^{\circ}$-O surfaces are not well known. It is known that the $(\sqrt{2}x2\sqrt{2})R45^{\circ}$-O surface is present to some extent in the ISS data which has been collected. The surface structure which has been proposed by Onuferko et al (7) for the $(\sqrt{2}x2\sqrt{2})R45^{\circ}$-O surface is complex, involving a mixture of two fold bridge sites and four fold coplanar sites. It is unlikely that such a structure would be completely formed on the surface. Thus, it is unlikely that the simplified model of ion-atom neutralisation which has been developed would be sufficient to enable structural determination to be carried out. However, qualitative statements can be made concerning the structure by analogy with the oxygen and carbon adsorbed Ni(100) surfaces. From such considerations, tentative support can be given to the site proposed by Onuferko et al. However, further experimental work using ISS as well as other

surface sensitive techniques is required before this surface arrangement can be accepted for the Cu(100)($\sqrt{2}$x2$\sqrt{2}$)R45°-O surface with a reasonable level of certainty.

In conclusion, although it has not been possible to perform surface structure analysis on the (100) surface with ISS in isolation, in attempting to carry out this analysis, a number of important effects have been found. Many of these effects can be understood by considering the localised ion-atom neutralisation model, which has been developed in this work. In previous ISS surface structure studies, the interpretation of the experimental data has relied on elastic effects, whilst assuming a constant neutralisation level. The results of this present work have shown that ion-atom neutralisation plays an important role in determining the experimental data. This localised neutralisation is implicit in the study of oscillatory ion yields mentioned in Chapter 2. However, the importance of such a process in producing crystallographic and, hence, surface structural effects is new, as is the observation of these effects in low energy ion scattering.

## References.


### Preface.

(1) e.g. J.J. Lander, Surface Sci. 1, 125 (1964)

(2) F. Yarwood, High Vacuum Techniques, Chapman and Hall, London (1967)

(3) M. Prutton, Surface Physics, Oxford University Press (1975)

(4) A.G.J. de Wit, R.P.N. Bronckers and J.M. Fluit, Surface Sci. 82, 177 (1979)

(5) W. Heiland, F. Iberl, E. Taglauer and D. Menzel, Surface Sci. 53, 383 (1975)

(6) R.L. Erickson and D.P. Smith, Phys. Rev. Letts. 34, 297 (1975)

(7) J. Demuth, D.W. Jepsen and P. Marcus, Phys. Rev. Letts. 31, 540 (1973)

(8) J.H. Onuferko, D.P. Woodruff and B.W. Holland, Surface Sci. 87, 357 (1979)

(9) D.R. Lloyd, C.M. Quinn and N.V. Richardson, Surface Sci. 68, 419 (1977)

(10) S. Kono, S.M. Goldberg, N.F.T. Hall and C.S. Fadley, Phys. Rev. Letts. 41, 1831 (1978)

(11) P. Hofmann, R. Unwin, W. Wyrobisch and A.M. Bradshaw, Surface Sci. 72, 635 (1978)

(12) J.R. Noonan, D.M. Zehner and L.H. Jenkins, Surface Sci. 69, 731 (1977)

(13) S.P. Holland, B.J. Garrison and N. Winograd, Phys. Rev. Letts. 43, 220 (1979)

(14) J.H. Onuferko and D.P. Woodruff, to be published.

### Chapter 1.

(1) M.P. Seah, Surface Sci. 17, 132 (1969)

(2) C.J. Davisson and L.H. Germer, Phys. Rev. 30, 705 (1927)

(3) J.C. Riviere, Contem. Phys. 14, 573 (1973)

(4) F. Jona, Surface Sci. 68, 204 (1977)

(5) M.B. Webb and M.G. Lagally, Solid State Phys. 28, 301 (1973)

(6) P. Heilmann, E. Lang, K. Heinz and K. Muller, Appl. Phys. 9, 247 (1976)

(7) J. Demuth, D.W. Jepsen and P. Marcus, Phys. Rev. Letts. 31, 540 (1973)

(8) P. Auger, J. Phys. Radium 6, 205 (1925)

(9) E. Harris, Appl. Phys. 39, 1419 (1968)

(10) T.E. Gallon and J.A.D. Matthews, Rev. Phys. Technol. 3, 31 (1972)

(11) M.F. Chung and L.H. Jenkins, Surface Sci. 22, 479 (1970)

(12) M. Perdereau, Surface Sci. 24, 239 (1971)

(13) C.C. Chang, Surface Sci. 25, 53 (1971)

(14) P.W. Palmberg, Handbook of Auger Electron Spectroscopy, Physical Electronics Industries Inc., Minnesota (1972)

(15) P.W. Palmberg, G.K. Bohn and J.C. Tracy, Appl. Phys. Letts. 15, 254 (1969)

(16) S.H.A. Begemann, A.L. Boers, Surface Sci. 30, 134 (1972)

(17) W. Heiland and E. Taglauer, J. Vac. Sci. Technol. 9, 620 (1972)

Chapter 2.

(1) B.V. Panin, Sov. Phys. JETP 42, 313 (1962)

(2) E.S. Mashkova and V.A. Molchanov, Radiation Eff. 16, 143 (1972)

(3) D.P. Smith, Appl. Phys. 38, 340 (1967)

(4) A.L. Boers, Surface Sci. 63, 475 (1977)

(5) H.H. Brongersma, J. Vac. Sci. Technol. 11, 231 (1974)

(6) D.P. Smith, Surface Sci. 25, 171 (1971)

(7) W.L. Baun, Appl. of Surface Sci. 1, 81 (1977)

(8) R.L. Erickson and D.P. Smith, Phys. Rev. Letts. 34, 297 (1975)

(9) B. Poelsema, L.K. Verhey and A.L. Boers, Surface Sci. 64, 537 (1977)

(10) H. Niehus and E. Bauer, Surface Sci. 47, 222 (1975)

(11) N. Bohr, Mat. Fys. Medd. Dan Vid Selk. 8, 18 (1948)

(12) A.A. Abrahamson, Phys. Rev. 178, 76 (1969)

(13) T.M. Buck in "Methods of Surface Analysis" A.W. Czanderna, Elsevier Publ. Co. (1975)

(14) M.T. Robinson, ORNL-4556 (1970)

(15) D.J. Ball, T.M. Buck, D. MacNair and G.H. Wheatley, Surface Sci. 30, 69 (1972)

(16) E. Everhart, G. Stone and R.J. Carbone, Phys. Rev. 99, 1287 (1955)

(17) W. Heiland and E. Taglauer, J. Vac. Sci. Technol. 9, 620 (1971)

(18) H.D. Hagstrum, Phys. Rev. 96, 336 (1954)

(19) H.H. Brongersma and T.M. Buck, Surface Sci. 53, 649 (1975)

(20) E. Taglauer and W. Heiland, Surface Sci. 47, 234 (1975)

(21) A.G.J. de Wit, R.P.N. Bronckers and J.M. Fluit, Surface Sci. 82, 177 (1979)

(22) Yu.V. Martyenko, Sov. Phys. Solid State 6, 1581 (1965)

(23) L.K. Verheij, J.A. Van den Berg and D.G. Armour, Surface Sci. 84, 408 (1979)

(24) H.H. Brongersma and P.M. Mul, Surface Sci. 35, 393 (1973)

(25) M.L. Tarng and G.K. Werner, Appl. Phys. 42, 2449 (1971)

(26) H.H. Brongersma and J.B. Theeten, Surface Sci. 54, 519 (1974)

(27) W. Heiland, F. Iberl, E. Taglauer and D. Menzel, Surface Sci. 53, 383 (1975)

(28) W. Heiland, W. Englert and E. Taglauer, J. Vac. Sci. Technol. 15, 419 (1978)

(29) S. Prigge, H. Niehus and E. Bauer, Surface Sci. 65, 141 (1977)

(30) J.E. Demuth, J. Coll. and Interface Sci. 58, 184 (1977)

(31) W. Heiland and E. Taglauer, Surface Sci., to be published

Chapter 3.

(1) J.T. Tate and P.T. Smith, Phys. Rev. 39, 270 (1932)

(2) L.G. Pittaway, Proc. Int. Conf. on Ion Sources, Sacley, 449 (1969)

Chapter 4.

(1) L. McDonnell and D.P. Woodruff, Surface Sci. 46, 505 (1974)

(2) C. Argile and G.E. Rhead, Surface Sci. 53, 659 (1975)

(3) D.P. Smith, Surface Sci. 25, 171 (1971)

(4) D.J. Ball, T.M. Buck, D. MacNair and G.H. Wheatley, Surface Sci. 30, 69 (1972)

(5) H. Niehus and E. Bauer, Rev. Sci. Instrum. 46, 1275 (1975)

(6) P. Hofmann, R. Unwin, W. Wyrobisch and A.M. Bradshaw, Surface Sci. 72, 635 (1978)

(7) J.H. Onuferko and D.P. Woodruff, to be published

(8) E. Taglauer and W. Heiland, Surface Sci. 47, 234 (1975)

Chapter 5.

(1) P.M. Marcus, J.E. Demuth and D.W. Jepsen, Surface Sci. 53, 501 (1975)

(2) J.H. Onuferko, D.P. Woodruff and B.W. Holland, Surface Sci. 87, 357 (1979)

(3) C. Argile and G.E. Rhead, Surface Sci. 53, 659 (1975)

(4) A.L. Boers, Surface Sci. 63, 475 (1977)

(5) W. Heiland, F. Iberl, E. Taglauer and D. Menzel, Surface Sci. 53, 383 (1975)

(6) R.L. Erickson and D.P. Smith, Phys. Rev. Letts. 34, 297 (1975)

(7) H.D. Hagstrum, Phys. Rev. 96, 336 (1954)

(8) L.K. Verhey, B. Poelsema and A.L. Boers, Nucl. Instrum. Methods 132, 565 (1976)

(9) N.H. Tolk, J.C. Tully, W. Heiland and C.W. White (Eds.) Inelastic Ion-Surface Collisions, Academic Press (1977)

(10) L. McDonnell and D.P. Woodruff, Surface Sci. 46, 505 (1974)

Chapter 6.

(1) L. McDonnell and D.P. Woodruff, Surface Sci. 46, 505 (1974)

(2) P.M. Marcus, J.E. Demuth and D.W. Jepsen, Surface Sci. 53 501 (1975)

(3) D.R. Lloyd, C.W. Quinn and N.V. Richardson, Surface Sci. 68, 419 (1977)

(4) S. Kono, S.M. Goldberg, N.F.T. Hall and C.S. Fadley, Phys. Rev. Letts. 41, 1831 (1978)

(5) P. Hofmann, R. Unwin, W. Wyrobisch and A.M. Bradshaw, Surface Sci. 72, 635 (1978)

(6) J.H. Onuferko and D.P. Woodruff, to be published

(7) W. Heiland, F. Iberl, E. Taglauer and D. Menzel, Surface Sci. 53, 383 (1975)

(8) J.R. Noonan, D.M. Zehner and L.H. Jenkins, Surface Sci. 69, 731 (1977)

(9) S.P. Holland, B.J. Garrison and N. Winograd, Phys. Rev. Letts. 43, 220 (1979)

Chapter 7.

(1) e.g. W. Heiland and E. Taglauer, J. Vac. Sci. Technol. 9, 620 (1971)
W. Heiland, F. Iberl, E. Taglauer and D. Menzel, Surface Sci. 53, 383 (1975)

(2) P.M. Marcus, J.E. Demuth and D.W. Jepsen, Surface Sci. 53 501 (1975)

(3) T.M. Buck, W.F. Van der Weg, Y.S. Chen and G.H. Wheatley, Surface Sci. 47, 244 (1975)

(4) H.H. Brongersma, J. Vac. Sci. Technol. 11, 231 (1974)

(5) I. Terzic, D. Ciric and B. Perovic, Surface Sci. 85, 149 (1979)

(6) A.L. Boers, Surface Sci. 63, 475 (1977)

(7) J.H. Onuferko and D.P. Woodruff, to be published